

# **Development and Characterization of Silicon Drift Detector based X-ray spectrometer for the Space-borne experiments**

A Thesis submitted by

**M. Shanmugam**  
(12PH03)

For the partial fulfillment of the award of the degree

of

**Doctor of Philosophy (Ph. D)**

Under the guidance of

**Dr. Y. B. Acharya (Guide) and Dr. H. S. Mazumdar (Co-guide)**



Department of Electronics and Communication Engineering  
Faculty of Technology  
Dharmsinh Desai University, Nadiad, Gujarat.

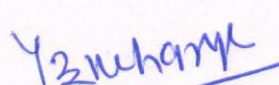
January, 2016

# DHARMSINH DESAI UNIVERSITY, INDIA

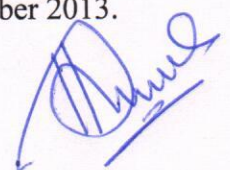
## Certificate of Course Work

This is to certify that Mr. M. Shanmugam (12PH03, registered on 25th September, 2012) is pursuing his Ph. D. on the topic entitled "Development and Characterization of Silicon Drift Detector based X-ray spectrometer for the Space-borne experiments" and has successfully completed the suggested course work as follows.

- 1) Course title : Advanced Digital Signal Processing  
Offered by : Faculty of Technology, DDU  
Faculty Coordinator : Prof. Hardip Shah  
Duration : July 2013 - December 2013.
  
- 2) Course title : Research Methodology  
Offered by : Self Study Course  
Faculty Coordinator : Under the guidance of Dr. Y. B. Acharya  
Duration : January 2013 - December 2013.

  
Dr. Y. B. Acharya, Ph. D.  
Research Guide  
Physical Research Laboratory

Date: 9<sup>th</sup> December, 2016

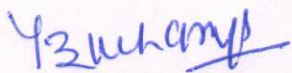
  
Dr. H. S. Mazumdar, Ph. D.  
Research Co-guide  
D. D. University

Date: 9<sup>th</sup> December, 2016



## CERTIFICATE

This is to certify that the content of this thesis titled "Development and Characterization of Silicon Drift Detector based X-ray spectrometer for the Space-borne experiments" is the original work of Mr. M. Shanmugam (12PH03) carried out under our supervision. We further certify that the work has not been submitted either partly or fully to any other university or body - in quest of a degree, diploma and/or any other kind of academic award.



Dr. Y. B. Acharya, Ph. D.  
Research Guide  
Honorary Engineer  
Physical Research Laboratory  
Ahmedabad - 380 009

Date: 09/12/2016  
Place: Nadiad



Dr. H. S. Mazumdar, Ph. D.  
Research Co-guide  
Professor, E.C and Head R&D Center  
D. D. University  
Nadiad - 387 001

Date: 09/12/2016  
Place: Nadiad

## CANDIDATE'S DECLARATION

The work described in this thesis entitled "Development and Characterization of Silicon Drift Detector based X-ray spectrometer for the Space-borne experiments" is carried out solely by me under the guidance of Dr. Y. B. Acharya (Guide) and Dr. H. S. Mazumdar (Co-guide), except for those colleagues and other workers referred/acknowledged in the text. I hereby declare that no part of this thesis has been previously submitted to this or any other university as part of the requirement of a higher degree.



**M. Shanmugam**  
(12PH03)

**Date:** 09/12/2016  
**Place:** Nadiad





9<sup>th</sup> December, 2016

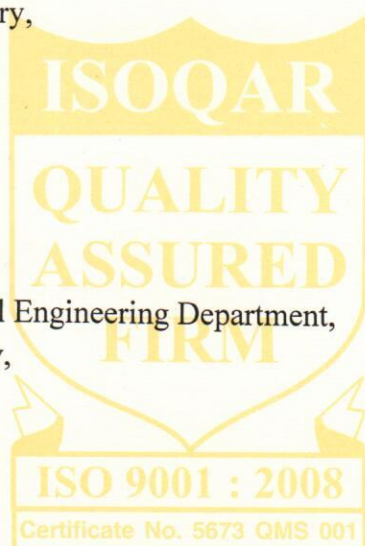
## Ph. D. Viva Voce Examination Report

Based on the Ph. D. evaluation report received from external examiners, Mr. M. Shanmugam (12PH03) has been examined for his Ph. D. Viva Voce on 09/12/2016. He has successfully defended his thesis titled "Development and Characterization of Silicon Drift Detector based X-ray spectrometer for the Space-borne experiments" and completed all the requirements for the award of Ph. D. Degree of Dharmsinh Desai University, Nadiad, Gujarat.

Prof. A. R. Rao (Examiner),  
Department of Astronomy & Astrophysics,  
Tata Institute of Fundamental Research,  
Homi Bhabha Road,  
Colaba, Mumbai - 400 005.

Dr. Y. B. Acharya (Guide),  
Honorary Engineer,  
Physical Research Laboratory,  
Ahmedabad - 380 009.

Dr. M. S. Rao (Observer),  
Professor & Head, Chemical Engineering Department,  
Dharmsinh Desai University,  
Nadiad - 387 001.



## Dharmsinh Desai University

College Road, Nadiad 387 001, India. Ph : 91 0268 2520502 Fax : 91 0268 2520501 Website : [www.ddu.ac.in](http://www.ddu.ac.in)



NAAC ACCREDITED

### To whomsoever it may concern

This is to certify that Mr. M Shanmugam (ID No.12PH03), a Ph.D. student of this University has completed all the requirements for the award of Ph.D. Degree. His viva-voce examination was held on 9<sup>th</sup> December 2016 and he has successfully defended his thesis titled “Development and Characterization of Silicon Drift Detector based X Ray Spectrometer for the Space-borne experiments”. After getting the approval from the Academic Council to the recommendations of all the referees for the award of Ph D for his research work done under the guidance of Dr Y B Acharya , Honorary Engineer, Physical Research Laboratory, Ahmedabad , he will be formally awarded the Ph D Degree at the next convocation of the University in May 2017.

  
Registrar(I/C)

9<sup>th</sup> December, 2016



**Dharmsinh Desai University**



## **DEDICATION**

To my Mother and Father

Wife, Son and Daughter

and

To all my well wishers

## ACKNOWLEDGEMENTS

This thesis could not have been completed without the help and support from many people.

I would like to sincerely express my gratitude to my supervisor Dr. Y. B. Acharya, for his continuous support and guidance. Without his valuable advice and suggestions, none of this work would have been achieved. His efforts and encouragement will be never be forgotten.

I would like to sincerely express my gratitude to my co-supervisor Dr. H. S. Mazumdar for his guidance and support. His critical questioning and suggestions immensely helped me in my research work.

I would like to thank Dr. Santosh Vadawlae for his help and continuous guidance during my research activity in understanding the scientific aspects of the research problems and its importance.

I would like to thank Mr. S. K. Goyal for his help in GEANT4 simulation, Mr. Arpit Patel for his help in measurements during irradiation tests and Mr. Tinkal Ladiya for his help in fabrication and testing of electronic designs.

I would like to thank the Director and Dean, PRL for allowing me to carry out my research and also helping me in providing the required resources for the research. I also would like to thank Prof. J. N. Goswami, Prof. S. V. S. Murty and Dr. D. Banerjee for their encouragement and support.

I would like to thank the Vice Chancellor DDU for giving me this opportunity to carry out to carry out my research at DDU. I would like to thank the Dean, Registrar, HOD of ECE, HOD of IC, HOD CE, DDU for their support and guidance.

I would like to thank Prof. Hardip Shah for his guidance in ADSP course work. Mr. Himanshu purohit, Mr. Pretik patel and Shri. Vitul patel are thanked for their support.

At last, I would like to thank all the PLANEX and PRL colleagues who have directly or indirectly helped me in my research activity.



## ABSTRACT

This thesis focuses on the design and characterization of Silicon Drift Detector (SDD) based X-ray spectrometer for the upcoming lunar mission, Chandrayaan-2 ensuring high energy resolution to meet the scientific objectives of Solar X-ray Monitor (XSM) and Alpha Particle X-ray Spectrometer (APXS). The main topic of interests are, the development of SDD based X-ray spectrometer using commercial equivalent of space qualified components, the use of SDD leakage current as a calibration tool for onboard SDD based X-ray spectrometers and the study of radiation damage effects to the SDDs onboard Chandrayaan-2 spectrometer instruments during the Earth to Moon transit and also in the lunar orbit for the mission life of 2 years. Chapter 1 gives brief objective of the research goal and Chapter 2 reviews various detectors and detector technologies used for X-ray spectrometry in the past several decades and at the end focussing on the semiconductor detectors, specially on silicon detectors. Chapter 3 discusses the working principle of SDD based on the sideward depletion concept and various SDD configurations available for the research and other applications. This chapter also gives the details of various SDD types and their use in the space missions. Chapter 4 gives the design details of the SDD based X-ray spectrometer and its performance results. Chapter 5 discusses the use of a new and simple technique to measure the leakage current in SDD devices and its use as a calibration tool for onboard space/planetary missions to evaluate any performance degradation in the space environment. Chapter 6 describes the irradiation tests conducted on the SDD modules planned for Chandrayaan-2 experiments with gamma rays to study the space radiation effects by measuring the leakage current, energy resolution and the noise. The noise performance of the SDD and the electronics is also characterized in terms of equivalent noise charge. Chapter 7 gives the summary of the research work and future plans.

# TABLE OF CONTENTS

CERTIFICATE-----	(i)
DECLARATION-----	(ii)
DEDICATION-----	(iii)
ACKNOWLEDGEMENT-----	(iv)
ABSTRACT-----	(v)
CONTENTS-----	(vi)
LIST OF FIGURES-----	(vii)
LIST OF TABLES-----	(viii)
LIST OF ABBREVIATIONS-----	(ix)
<b>1. INTRODUCTION-----</b>	<b>1</b>
1.1. Brief of SDD based X-ray Spectrometers Flown in the Space Missions---	2
1.2. Research Objectives and Results-----	3
1.3. Plan of Thesis Chapters-----	6
<b>2. X-RAY SPECTROMETER AND REVIEW OF X-RAY DETECTORS----</b>	<b>10</b>
2.1. X-ray Spectrometer-----	10
2.2. X-ray Generation-----	11
2.3. X-ray Spectrometer Instrumentation-----	13
2.4. Review of X-ray Detectors-----	16
2.4.1. The Proportional Counter-----	18
2.4.2. Scintillation Detectors-----	20
2.4.3. Scintillator Readout Systems -----	24
2.4.3.1. Photomultiplier Tubes-----	24
2.4.3.2. Photodiodes-----	25
2.4.3.3. Silicon Photomultipliers-----	27
2.4.4. Semiconductor Detectors-----	30
2.4.5. Silicon Detectors-----	31
2.4.6. Detection of X-rays Using Silicon-----	32
2.4.6.1. Interaction of X-ray Photons-----	32
2.4.6.2. Detection Efficiency-----	37



2.4.6.3.	Signal Formation and Charge Collection-----	39
2.4.6.4.	Energy Resolution-----	41
2.4.7.	Principle of Operation of Silicon Diode Detectors-----	45
2.4.8.	Si PIN Diode Detector-----	49
2.4.9.	Si (Li) Detectors-----	51
2.4.10.	Silicon Strip Detectors (SSD)-----	52
2.4.11.	Pixel Detectors-----	54
2.4.11.1.	Hybrid Active Pixel Sensors (HAPS)-----	55
2.4.11.2.	Monolithic Active Pixel Sensors (MAPS)-----	56
2.4.11.3.	DEPFET Pixel Detector-----	56
2.4.12.	Fully Depleted p-n CCD-----	58
2.4.13.	Silicon Drift Detector (SDD)-----	61
2.5.	Summary-----	61
<b>3.</b>	<b>REVIEW OF SILICON DRIFT DETECTORS AND THEIR USE IN</b>	
	<b>SPACE APPLICATIONS-----</b>	<b>62</b>
3.1.	Introduction-----	62
3.2.	Working Principle of SDD-----	63
3.3.	SDD for X-ray Measurements-----	65
3.4.	Type of SDD Configurations-----	67
3.4.1.	SDD with Discrete External FET-----	67
3.4.2.	SDDs with On-chip FET-----	68
3.4.3.	SDDs with ASIC Readout-----	71
3.4.4.	Silicon Drift Detector Droplet (SD <sup>3</sup> )-----	72
3.4.5.	Large Area and Multi Element SDDs-----	74
3.5.	SDD Modules-----	76
3.6.	SDD Manufacturers-----	78
3.7.	Application of SDDs-----	79
3.8.	SDDs in Space Missions-----	80
3.8.1.	Mars Exploration Rover (MER)-----	80
3.8.2.	Rosetta Mission-----	83
3.8.3.	Mars Science Laboratory (MSL)-----	83
3.8.4.	Chang'e-3 Mission-----	84

3.8.5. Chandrayaan-2 Mission-----	86
3.8.5.1. Alpha Particle X-ray Spectrometer (APXS)-----	86
3.8.5.2. Solar X-ray Monitor (XSM)-----	88
3.8.6. Large Observatory For X-ray Timing (LOFT) Mission-----	89
3.9. Comparison of SDD Based X-ray Spectrometers Flown/Planned in the Various Space/Planetary Missions-----	90
3.10. Summary-----	92
<b>4. DESIGN AND PERFORMANCE EVALUATION OF SDD BASED X-RAY SPECTROMETER-----</b>	<b>93</b>
4.1. Objectives and Specifications of APXS-----	94
4.2. Objectives and Specifications of XSM-----	96
4.3. Design of SDD Based X-ray Spectrometer-----	97
4.3.1. SDD Module for Chandrayaan-2 Instruments-----	98
4.3.2. Charge Readout Techniques-----	102
4.3.3. Design of Charge Sensitive Pre-Amplifier (CSPA)-----	109
4.3.4. Shaping Amplifier-----	112
4.3.5. Pole-Zero Compensation-----	115
4.3.6. Base Line Restorer-----	116
4.3.7. High Voltage Bias Generation for SDD-----	116
4.3.8. Event Trigger Generator-----	118
4.3.9. Peak Detector-----	119
4.3.10. Analog to Digital Converter-----	120
4.3.11. FPGA Based Data Acquisition and Control System-----	121
4.4. Experimental Setup-----	122
4.5. Characterization of the SDD Based X-ray Spectrometer-----	123
4.5.1. Energy Resolution-----	124
4.5.2. System Linearity-----	125
4.5.3. Dependence of Energy Resolution with Temperature-----	126
4.5.4. Energy Resolution Versus Pulse Shaping Time-----	127
4.5.5. Spectrometer Performance at High Count Rates-----	127
4.6. Summary-----	133



<b>5. LEAKAGE CURRENT AS A CALIBRATION TOOL FOR SPACE-BORNE EXPERIMENTS-----</b>	<b>134</b>
5.1. Onboard Calibration Requirement-----	135
5.2. Leakage Current-----	138
5.3. Leakage Current Measurement Technique-----	142
5.4. Measurement Results-----	144
5.4.1. Measurement of Feedback Capacitance ( $C_f$ )-----	144
5.4.2. Measurement of Leakage Current-----	147
5.4.3. Performance Comparison Between Small and Large area SDDs----	152
5.4.4. Energy Resolution Dependence on Leakage Current -----	155
5.4.5. Leakage Current Due to Spurious Radiation-----	156
5.4.6. Leakage Current - Theoretical Comparison-----	158
5.4.6.1. Estimation of Ideality Constant and Its Temperature Dependence-----	161
5.5. Summary-----	164
<b>6. RADIATION EFFECTS ON THE PERFORMANCE OF THE SDD BASED X-RAY SPECTROMETER ONBOARD CHANDRAYAAN-2 MISSION-----</b>	<b>165</b>
6.1. Introduction-----	165
6.2. Performance Requirement-----	166
6.3. Space Radiation Environment-----	167
6.4. The Radiation Damage Mechanisms -----	169
6.5. Displacement Damage and Its Effects-----	171
6.5.1. Displacement Damage-----	171
6.5.2. Increase in the Leakage Current-----	176
6.5.3. Effect of Doping Concentration-----	178
6.5.4. Charge Collection Efficiency-----	179
6.5.5. Defects-----	179
6.6. Ionization Damage-----	180
6.7. The Non Ionizing Energy Loss (NIEL) Scaling Hypothesis-----	181
6.8. Estimation of Total Proton Fluence for Chandrayaan-2 Mission-----	183
6.9. Estimation of Compton Electron Spectrum with GEANT4 Simulation-----	188

6.10.	Gamma Ray and X-ray Irradiation-----	190
6.10.1.	Gamma Ray Facility and Experimental Procedure-----	190
6.10.2.	X-ray Irradiation Setup and Experimental Procedure-----	192
6.11.	Experimental Results-----	194
6.11.1.	Spectrometer Performance before Irradiation-----	194
6.11.2.	Performance after Gamma Ray Irradiation-----	196
6.11.3.	Performance after X-ray Irradiation-----	200
6.12.	Noise Performance of the Spectrometer: Pre and Post Irradiation Tests-----	203
6.12.1.	Introduction to System Noise-----	203
6.12.2.	Basic Noise Mechanisms-----	204
6.12.2.1.	Thermal Noise-----	205
6.12.2.2.	Short Noise-----	206
6.12.2.3.	Flicker Noise-----	207
6.12.2.4.	Detector Capacitance and Signal to Noise Ratio-----	207
6.12.2.5.	Noise in JFET-----	209
6.12.2.6.	Pulse Shaping and Noise-----	209
6.12.3.	Equivalent Noise Charge (ENC)-----	210
6.12.4.	Noise Performance before Irradiation-----	213
6.12.5.	Noise Performance after Gamma Ray Irradiation-----	215
6.12.6.	Noise Performance after X-ray Irradiation-----	217
6.13.	Summary-----	218
<b>7.</b>	<b>SUMMARY AND FUTURE PLAN-----</b>	<b>219</b>
7.1.	Summary of the Research Work-----	219
7.2.	Future Plan-----	221
	<b>REFERENCES-----</b>	<b>223</b>
	<b>PUBLICATIONS-----</b>	<b>240</b>

## LIST OF FIGURES

Fig. 2.1: The relative probabilities of X-ray emission and Auger electron emission with atomic number-----	12
Fig. 2.2: Schematic representation of characteristic X-ray emission and Auger electron emission processes-----	12
Fig. 2.3: Characteristic X-ray and the bremsstrahlung continuum obtained for tungsten target for various tube voltages-----	13
Fig. 2.4: Generic block schematic of an X-ray spectrometer-----	13
Fig. 2.5: Sample spectrum showing energy resolution in FWHM measured using $^{55}\text{Fe}$ source-----	15
Fig. 2.6: Schematic representation of production of charge carriers in direct and indirect conversion type detectors-----	17
Fig. 2.7: Schematic representation of a cylindrical proportional counter-----	19
Fig. 2.8: X-ray fluorescence spectra measured with a gas filled proportional counter---	20
Fig. 2.9: Schematic representation of working principle of scintillation detector-----	20
Fig. 2.10: Schematic representation scintillator coupled with PMT for charge readout---	22
Fig. 2.11: A typical spectral performance comparison between NaI(Tl) scintillator and high purity germanium detector-----	23
Fig. 2.12: Spectral performance comparison of Lanthanum bromide with sodium iodide and high purity germanium detector-----	23
Fig. 2.13: Schematic representation of SPM pixel arrays with quenching resistor and summed output-----	28
Fig. 2.14: Schematic representation of making of silicon planar technology, a) Oxidation of silicon, b) Selective removal of oxide layer, c) Introduction of	

dopant atoms and d) Diffusion of dopant atoms into silicon-----	32
Fig. 2.15: Linear attenuation coefficient for silicon as a function of photon energy up to 10 MeV-----	34
Fig. 2.16: Variation in the bandgap energy of silicon with operating temperature-----	36
Fig. 2.17: Absorption efficiency for various thicknesses of silicon detector-----	38
Fig. 2.18: Change in the absorption efficiency due to silicon insulation ( $SiO_2$ ) and metal layers at low X-ray energies-----	39
Fig. 2.19: Schematic representation of signal formation and charge collection-----	40
Fig. 2.20: Statistical broadening of the photon energy peak centered at $E_o$ and Full-Width-at-Half-Maximum (FWHM) of the detected peak is commonly used indication of the energy resolution of spectrometer system-----	42
Fig. 2.21: Contribution of Fano factor in the spectrometer energy resolution of Si detector with incident photon energy-----	43
Fig. 2.22: A sample spectra acquired from SDD based X-ray spectrometer with ASIC based readout-----	44
Fig. 2.23: Working principle of a reverse biased silicon PIN diode-----	45
Fig. 2.24: The electric field distribution inside the PIN diode for the detector thickness of 500 microns-----	46
Fig. 2.25: Schematic representation of constituents of Si PIN detector module-----	50
Fig. 2.26: A sample spectrum of Si PIN detector with 500 micron thick and compared with CdTe detector of 1mm thick-----	51
Fig. 2.27: Si(Li) detector efficiency for 3 and 5 mm thick detectors-----	52
Fig. 2.28: Single side silicon strip detector used in the CMS experiment-----	53
Fig. 2.29: Layout of double sided (2D) silicon strip detector-----	54

Fig. 2.30: Schematic representation of hybrid active pixel sensor-----	55
Fig. 2.31: Schematic representation of monolithic active pixel sensor-----	56
Fig. 2.32: Schematic representation of monolithic DEPFET pixel detector-----	57
Fig. 2.33: ATLAS experiment (left) and CMS experiment (right) with hybrid Si pixilated detectors-----	57
Fig. 2.34: ALICE experiment with hybrid Si pixilated detectors-----	58
Fig. 2.35: Schematic representation of p-n CCD cut through view-----	58
Fig. 2.36: Inside view of p-n CCD indicating charge transfer direction to the readout electronics-----	59
Fig. 2.37: The photographic view of p-n CCD built with sensitive area of $6 \times 6 \text{ cm}^2$ , flown in XMM-Newton satellite missions-----	60
Fig. 3.1: Schematic representation of sideward depletion concept-----	63
Fig. 3.2: Schematic representation of working principle of SDD-----	64
Fig. 3.3: The electron guiding potential distribution in the drift region of the SDD pointing towards the anode-----	64
Fig. 3.4: Schematic representation of a circular SDD with anode at the center-----	66
Fig. 3.5: The possible electron path (field line) inside the SDD with 300 micron thickness-----	66
Fig. 3.6: Quantum efficiency of a 450 and 900 micron thick SDDs with thin dead layer-----	67
Fig. 3.7: Schematic representation of discrete FET mounted near to the SDD chip-----	68
Fig. 3.8: Schematic of a circular SDD with on-chip JFET-----	69
Fig. 3.9: Section of the SDD layout where readout transistor is interfaced with the charge collecting anode-----	70



Fig. 3.10: Spectrum measured using 10 mm <sup>2</sup> area, 450 micron thick SDD with on-chip FET by cooling the detector to -20°C-----	70
Fig. 3.11: Spectral energy resolution measured for various incident photon rates up to 1.2 x 10 <sup>5</sup> counts/s-----	71
Fig. 3.12: Schematic view of CUBE ASIC mounted close to the SDD chip (Pre is the CUBE)-----	72
Fig. 3.13: Spectrum obtained with CUBE ASIC for <sup>55</sup> Fe X-ray source, pulse peaking time of 1.5 μs-----	72
Fig. 3.14: Schematic design of Silicon Drift Detector Droplet (SD <sup>3</sup> ). The black region is the on-chip FET placed at the edge of the device which can shielded from the radiation-----	73
Fig. 3.15: Comparison of spectra obtained from a circular SDD and SD <sup>3</sup> with 5 mm <sup>2</sup> area-----	74
Fig. 3.16: Photographic view of large area SDDs, 100 / 150 mm <sup>2</sup> area on the same footprint from KETEK, GmbH (left), 100 mm <sup>2</sup> area from PN Sensor (right)-----	75
Fig. 3.17: Photographic view of multiple element large area SDD assemblies from KETEK (left) and from PN Sensor (right)-----	75
Fig. 3.18: Transmission efficiency of low energy X-rays through various thicknesses of Be windows-----	77
Fig. 3.19: Transmission efficiency of low energy X-rays through thin polymer (AP3.3) window in comparison with 8 micron thick Be window-----	77
Fig. 3.20: Schematic representation of SDD based APXS instrument onboard MER-----	81
Fig. 3.21: Photographic view of APXS flown in MER-----	82
Fig. 3.22: Spectra measured by MER rover for two samples-----	82
Fig. 3.23: Schematic representation of SDD based APXS instrument onboard MSL-----	84

Fig. 3.24: Spectral response comparison of APXS instruments flown in MSL and MER-	84
Fig. 3.25: Photographic view of the APXS onboard Chang'e-3 mission-----	85
Fig. 3.26: The calibration and the lunar soil spectra measured on the lunar surface by APXS onboard Chang'e-3-----	85
Fig. 3.27: Photographic view of the functional model of APXS developed for Chandrayaan-2 rover mission-----	87
Fig. 3.28: Spectra acquired from APXS working model using $^{55}\text{Fe}$ X-ray source for the pulse peaking time of $\sim 3.3 \mu\text{s}$ by cooling the SDD to $-40^\circ\text{C}$ -----	87
Fig. 3.29: Photographic view of the functional model of XSM sensor package-----	89
Fig. 3.30: Spectra acquired for $^{55}\text{Fe}$ source for the pulse peaking time of $0.8 \mu\text{s}$ by cooling the SDD to $\sim -40^\circ\text{C}$ -----	89
Fig. 3.31: Conceptual scheme of LOFT mission-----	90
Fig. 4.1: Block schematic of the SDD based spectrometer system design-----	97
Fig. 4.2: Schematic view of SDD module-----	99
Fig. 4.3: Photographic view of $40 \text{ mm}^2$ area SDD module, b) Internal view (right)-----	99
Fig. 4.4: Internal electrical interconnection diagram of SDD module-----	100
Fig. 4.5: Transmission efficiency of the 450 micron thick SDD with $8 \mu\text{m}$ Dura Be window-----	100
Fig. 4.6: Charge collection and signal integration, a) Velocity of charge carriers, b) Rate of induced charge on sensor electrodes, c) Signal charge-----	104
Fig. 4.7: Basic charge sensitive amplifier configuration-----	104
Fig. 4.8: Schematic representation of RC feedback type CSPA-----	106
Fig. 4.9: Schematic representation of reset type CSPA with typical output signal-----	107

Fig. 4.10: Energy resolution measured for various count rates in self reset and pulsed reset modes-----	108
Fig. 4.11: Change in the peak energy position as a function of count rate with pulsed reset and self reset modes-----	109
Fig. 4.12: Block schematic of pulsed reset type Charge Sensitive Pre-Amplifier (CSPA) design-----	110
Fig. 4.13: CRO screen shot of a CSPA output which is in the form of ramp signal in the absence of photon interaction when the SDD is cooled to -40°C. The ramp signal amplitude is electronically set between -2 V to 4 V-----	111
Fig. 4.14: CRO screen shot of CSPA output showing step pulses indicating the interaction of X-ray photons for the SDD operating temperature at -40°C-----	111
Fig. 4.15: Simulated shaping amplifier output for equal CR-RC time constants-----	113
Fig. 4.16: Simulated shaping amplifier output with one CR and multiple RC stages-----	114
Fig. 4.17: Block schematic of $CR-(RC)^2$ type shaping amplifier-----	114
Fig. 4.18: Ramp signal–input to shaping amplifier (above), Shaping amplifier output for four signal pulses with different amplitudes (below)-----	115
Fig. 4.19: Schematic representation of SDD with HV bias filtering requirement-----	117
Fig. 4.20: The block schematic of HV generation circuit-----	118
Fig. 4.21: Event trigger generation sequence-----	119
Fig. 4.22: Timing diagram representing signal and conversion at various stages of the SDD based X-ray spectrometer-----	121
Fig. 4.23: LABVIEW window panel used for instrument operation commanding and data acquisition-----	122
Fig. 4.24: Photographic view of the front-end electronics coupled with the SDD module-----	123

Fig. 4.25: Photographic view of FPGA based data acquisition, control system and part of FEE circuits-----	123
Fig. 4.26: Spectra obtained from the developed SDD based X-ray spectrometer for three radioactive X-ray sources-----	124
Fig. 4.27: Spectra obtained from the commercial off-the-shelf SDD based X-ray spectrometer for three radioactive X-ray sources-----	125
Fig. 4.28: Linearity plot of peak ADC channel versus known X-ray energies-----	126
Fig. 4.29: Energy resolution versus SDD detector temperature-----	126
Fig. 4.30: Pulse shaping time versus energy resolution-----	127
Fig. 4.31: Experimental setup for high count rate measurements using $^{55}\text{Fe}$ source-----	128
Fig. 4.32: Energy resolution measured for the pulse shaping time of $0.8\ \mu\text{s}$ -----	128
Fig. 4.33: Spectra acquired for various count rates using $^{55}\text{Fe}$ X-ray source for the pulse shaping time of $0.8\ \mu\text{s}$ -----	129
Fig. 4.34: Measured energy resolution versus count rate-----	130
Fig. 4.35: Change in the peak energy position (ADC channel number) for various incident X-ray rates using $^{55}\text{Fe}$ X-ray source-----	130
Fig. 4.36: Photographic view of SDD based X-ray spectrometer testing with X-ray gun-	131
Fig. 4.37: Spectra obtained for various count rates from X-ray gun for the pulse shaping time of $0.8\ \mu\text{s}$ -----	132
Fig. 4.38: Change in the peak energy position (ADC channel number) for various incident X-ray rates using X-ray gun for the pulse shaping time of $0.8\ \mu\text{s}$ -----	132
Fig. 4.39: Different between the incident and detector count rates for both $^{55}\text{Fe}$ X-ray source and X-ray gun for the pulse shaping time of $0.8\ \mu\text{s}$ -----	133
Fig. 5.1: Block schematic of pulsed reset type Charge Sensitive Pre-Amplifier (CSPA)	

design-----	143
Fig. 5.2: Gain calibration of CSPA gain amplifier stage using tail pulse generator-----	145
Fig. 5.3: Gain calibration of three stage filter amplifier using tail pulse generator-----	145
Fig. 5.4: Measured value of feedback capacitance for three different X-ray energies----	146
Fig. 5.5: Feedback capacitance value measured for three X-ray energies for small and large area SDDs (The serial number starts with VS series are small area SDDs and VX series are large area SDDs)-----	147
Fig. 5.6: Ramp signal frequency measured for different detector temperatures by setting three different ramp signal amplitudes-----	148
Fig. 5.7: Ramp signal frequency measured for small and large area SDDs for different temperatures-----	149
Fig. 5.8: Leakage current measured for three different ramp signal amplitudes with temperature-----	150
Fig. 5.9: Leakage current measured for various environmental conditions-----	151
Fig. 5.10: Leakage current measured for small and large area SDDs for various operating temperatures-----	152
Fig. 5.11: Spectra measured for a small and large area SDD using $^{55}\text{Fe}$ and $^{241}\text{Am}$ X-ray sources-----	153
Fig. 5.12: Spectra acquired for small area detector for various detector temperatures----	154
Fig. 5.13: Energy resolution measured for small and large area SDDs at various detector operating temperatures using $^{55}\text{Fe}$ X-ray source-----	155
Fig. 5.14: Leakage current measured for large sample of SDDs versus measured energy resolution-----	156
Fig. 5.15: Change in the ramp signal frequency for various incident photon rates using $^{55}\text{Fe}$ and $^{241}\text{Am}$ X-ray sources-----	157



Fig. 5.16: Measured and theoretically estimated leakage current for small area SDD with ideality factor $\eta = 1.46$ for various detector operating temperatures-----	159
Fig. 5.17: Measured and theoretically estimated leakage current for large area SDD with ideality factor $\eta = 2.14$ for various detector operating temperatures-----	159
Fig. 5.18: Measured slopes for small and large area SDDs using leakage current ratio method-----	160
Fig. 5.19: Natural logarithm of leakage current versus the reciprocal of temperature for small and large area SDDs-----	161
Fig. 5.20: Ideality constant ( $\eta$ ) versus temperature for small area SDDs-----	163
Fig. 5.21: Ideality constant ( $\eta$ ) versus temperature for large area SDDs-----	163
Fig. 6.1: Cutaway drawing of two radiation belts around the Earth, Red-Inner radiation belt, Blue-Outer radiation belt-----	168
Fig. 6.2: Solar wind and radiation belt around the Earth-----	168
Fig. 6.3: Flow diagram of effects radiation damages or various radiations-----	170
Fig. 6.4: Schematic representation of defect caused by damage from an incident particle-----	171
Fig. 6.5: The point and cluster defects in silicon due to fast neutrons-----	172
Fig. 6.6: The point defects in silicon due to gamma ray radiation-----	172
Fig. 6.7: Schematic representation of cluster defects created by an 1 MeV neutron imparting recoil energy of 50 keV on a silicon atom-----	173
Fig. 6.8: Spatial distribution of vacancies created by a 1 MeV neutron imparting recoil energy of 50 keV on a silicon atom. The insert shows the traverse projection-	174
Fig. 6.9: Leakage current due to displacement damage as a function of particle fluence for different types of detectors-----	177

Fig. 6.10: Effect of doping concentration versus particle fluence-----	178
Fig. 6.11: Process of gate oxide under ionization radiation-----	181
Fig. 6.12: Harness factor for various radiations-----	183
Fig. 6.13: Proton flux estimated using AP-8 model for the Chandrayaan-1, orbit 299 to 25481 km-----	185
Fig. 6.14: Electron flux estimated using AE-8 model for the Chandrayaan-1, orbit 299 to 25481 km-----	185
Fig. 6.15: The estimated 10 MeV equivalent trapped and solar proton fluence for various aluminum shielding thicknesses-----	187
Fig. 6.16: SDD module modelled in GEANT4-----	188
Fig. 6.17: GEANT4 simulation for $10^3$ gamma ray photons using $^{60}\text{Co}$ gamma ray source-----	189
Fig. 6.18: Scattered Compton spectrum observed for $10^9$ gamma ray photon interactions with SDD detector using GEANT4-----	189
Fig. 6.19: Schematic representation of the cross sectional view of gamma ray irradiation chamber with $^{60}\text{Co}$ -----	191
Fig. 6.20: X-ray irradiation experimental setup using $^{55}\text{Fe}$ X-ray source-----	193
Fig. 6.21: Energy resolution measured for both the SDD modules (VS0629 and VS0592) before irradiation for various detector operating temperatures-----	195
Fig. 6.22: Energy resolution measured for various shaping time constants at two temperatures for both VS0592 and VS0629 SDD modules-----	196
Fig. 6.23: Leakage current measured for various gamma ray doses versus detector operating temperatures-----	197
Fig. 6.24: Measured energy resolution for various gamma ray doses versus detector operating temperatures-----	198

Fig. 6.25: Measured energy resolution for various detector operating temperatures and compared with gamma ray dose of 547 krad at -20°C-----	199
Fig. 6.26: Energy resolution measured before and after gamma ray irradiation for the detector operating temperature of -20°C (4M - four months after gamma ray irradiation) compared with before irradiation at -40°C-----	199
Fig. 6.27: Leakage current measured for various X-ray doses versus detector operating temperature-----	201
Fig. 6.28: Measured energy resolution (shaping time 3.3 $\mu$ s) for various X-ray doses versus detector operating temperatures (Energy resolution is plotted for fewer doses for clarity)-----	201
Fig. 6.29: Leakage current versus energy resolution for various X-ray doses-----	202
Fig. 6.30: Signal and base line fluctuation for small signal variance and large base line noise fluctuation-----	203
Fig. 6.31: Schematic representation of the detector capacitance and the charge readout amplifier-----	208
Fig. 6.32: Total equivalent noise charge and the contribution of series, parallel and $1/f$ noises-----	213
Fig. 6.33: Equivalent noise charge measured at 5.9 keV for various shaping time constants with temperature for both VS0592 and VS0629 SDD modules before irradiation-----	214
Fig. 6.34: The value of ENC measured before and after gamma ray irradiation for a detector operating temperature of -20°C (4M - four months after gamma ray irradiation)-----	215
Fig. 6.35: The ENC in rms electrons derived from the measured energy resolution before irradiation for a detector operating temperature of -20°C-----	216
Fig. 6.36: The ENC in rms electrons derived from the measured energy resolution after irradiation for a detector operating temperature of -20°C-----	216

Fig. 6.37: Equivalent noise charge measured before and after X-ray irradiation for three  
different SDD operating temperatures----- 217

## LIST OF TABLES

Table-2.1: Comparison of various scintillation detectors and its properties-----	24
Table-2.2: Comparison various characteristics of scintillator readout devices such as PMT, Photo diode and SPM-----	29
Table-3.1: Comparison of SDD with other Silicon detectors-----	78
Table-3.2: Comparison of SDD manufacturers and their device characteristics-----	78
Table-3.3: Comparison of SDD based X-ray spectrometers flown/planned in the space/planetary missions-----	91
Table-4.1: list of major rock forming elements expected on the planets with their energies-----	94
Table-4.2: APXS instrument specifications-----	95
Table-4.3: XSM instrument specifications-----	96
Table-4.4: Specifications of the SDD module planned for Chandrayaan-2 mission-----	101
Table-4.5: Electrical characteristic of the SDD module-----	101
Table-4.6: SDD HV bias voltage, current and filtering on each HV lines-----	117
Table-4.7: Energy resolution at different source energies obtained from developed and the commercial off-the-shelf spectrometers-----	125
Table-5.1: Measured energy resolution for various detector operating temperatures-----	154
Table-5.2: Measured slopes and slope ratios for small and large area SDDs using leakage current ratio method-----	161

Table-6.1: X-ray spectrometer performance requirement onboard Chandrayaan-2-	167
Table-6.2: Qualitative indication of defects created by different types of radiations-----	175
Table-6.3: Relative displacement damage for various particles and energies-----	176
Table-6.4: Measured values of feedback capacitance and the leakage current for SDD modules before irradiation tests-----	195



## LIST OF ABBREVIATIONS

Abbreviation	Full form
COTS	Commercial Off The Shelf
SDD	Silicon Drift Detector
XSM	Solar X-ray Monitor
APXS	Alpha Particle X-ray Spectrometer
CLASS	Chandra Large Area Soft x-ray Spectrometer
ENC	Equivalent Noise Charge
JFET	Junction Field Effect Transistor
$C_T$	Total input capacitance
$g_m$	Transconductance
MER	Mars Exploration Rover
MSL	Mars Science Laboratory
LOFT	Large Observatory for X-ray Timing
ESA	European Space Agency
SPENVIS	Space Environment Information System
ASIC	Application Specific Integrated Circuits
Z	Atomic number
E	Incident photon energy
$\phi$	Binding energy of electron
CSPA	Charge Sensitive Pre-Amplifier

ADC	Analog to Digital Converter
FPGA	Field Programmable Gate Arrays
FWHM	Full Width Half Maximum
e-h	Electron-Hole pair
eV	electron Volts
PMT	Photo Multiplier Tube
SPM	Silicon Photo Multiplier
NaI (Tl)	Sodium Iodide (Thallium)
CsI (Tl)	Caesium Iodide (Thallium)
BGO	Bismuth Germonate
LaBr <sub>3</sub> (Ce)	Lanthanum Bromide (Cerium)
Si	Silicon
Ge	Germanium
KV	Kilo Volts
CdTe	Cadmium Telluride
CdZnTe	Cadmium Zinc Telluride
GaAs	Gallium Arsenide
HgI <sub>2</sub>	Mercury Iodide
CCD	Charge Coupled Device
F	Fano factor
CCE	Charge Collection Efficiency
SSD	Silicon Strip Detector

LN <sub>2</sub>	Liquid Nitrogen
HAPS	Hybrid Active Pixel Sensor
MAPS	Monolithic Active Pixel Sensor
MOS	Metal Oxide Semiconductor
SD <sup>3</sup>	Silicon Detector Droplet
XRF	X-Ray Fluorescence
PIXE	Particle Induced X-ray Emission
FEE	Front End Electronics
BLR	Base Line Restorer
Kcts	Kilo count per second
EOF	End OF Life
PKA	Primary Knock on Atom
NIEL	Non Ionizing Energy Loss
ALICE	A Large Ion Collider Experiment
CMS	Compact Muon Solenoid
LHC	Large Hardon Collider
ATLAS	A Toroidal LHC Apparatus
GLAST	Gamma-Ray Large Area Space Telescope

# **Chapter 1:**

## **INTRODUCTION**

Ever since the start of space age, the information provided by the deep space/planetary missions have proved to be important in understanding various aspects of the space/planetary objects. Measurements from the space platform eliminate the interference caused by the Earth's atmosphere and allowing the detailed observation of these objects that would be difficult to observe/measure through ground based observations. However, the deep space and planetary missions introduce new challenges such as placing the satellite in the desired orbit, its stability during the observation, required power generation and the data transmission to the ground station. The other challenges involve the spacecraft and the scientific instruments used for the observation should be capable of withstanding very hostile space environmental conditions.

Developing a space-borne instrument is a challenging task as the instrument has to survive very hostile space environment. Any instrument onboard spacecraft is expected to encounter harsh radiation environment, large temperature excursions and high vacuum conditions. The instrument should also withstand launch vehicle vibration levels. Care needs to be taken for the above aspects at various levels of the instrument design such as selecting components/devices with space qualification, desired radiation testing, design and packaging of the instrument. Instruments developed with Commercial Off-The-Shelf (COTS) components will not survive the hostile space environment and satellite launch loads. For these reasons "Space instruments are custom-designed one-of-

a-kind and building such unique instrument depends on mission and the instrument configuration required for the scientific application”.

X-ray spectrometer is an instrument used for the measurement of planets and space objects in the X-ray region. In the planetary missions, X-ray spectrometers are generally used for the measurement of elemental composition either from an orbiting satellite or on a lander/rover platform. Instruments onboard orbiting satellite gives global measurements and onboard lander/rover gives in-situ measurements. X-ray spectrometers onboard lander/rover generally carries radioactive sources which are used to induce the X-ray fluorescence from the planetary surface and detecting these X-rays gives the elemental composition. Intensity of the X-ray line gives the quantity. Semiconductor based X-ray spectrometers are found to be superior due to improved signal to noise ratio. Silicon detectors are widely used in X-ray spectroscopy due to wide bandgap and the advancements in the processing technology. Recently, Silicon Drift Detector based X-ray spectrometers are preferred over Si PIN detectors due its low detector capacitance which enables to operate at high incident X-ray rates with superior energy resolution.

### **1.1. BRIEF OF SDD BASED X-RAY SPECTROMETERS FLOWN IN THE SPACE MISSIONS:**

In recent years, Silicon Drift Detector (SDD) based X-ray spectrometers are being flown and considered for onboard space/planetary missions due to its superior spectroscopic performance. Mars rovers such as Mars Exploration Rovers (MER) Spirit and Opportunity and recent Mars Science Laboratory (MSL) have carried SDD based X-ray spectrometer for in-situ elemental composition measurements on Martian surface. The comet mission Rosetta has also carried SDD based X-ray spectrometer onboard

PHILAE lander for the comet 67P/Churyumov-Gerasimenko for in-situ measurements. Recent lunar mission from China, Change'3 also carried SDD for in-situ elemental composition measurements on the lunar surface.

There are planetary/space missions in the near future plan to use scientific instruments having SDD as a sensor. Chandrayaan-2, the second Indian mission to Moon is slated for launch in the year 2017 uses SDD detector in two X-ray spectrometer instruments. The space mission, Large Observatory for X-ray Timing (LOFT) is being developed by European Space Agency (ESA) with large number of large area SDDs with total effective area of  $\sim 10 \text{ m}^2$  for astronomical observations. This mission is slated for launch in the year 2022.

## **1.2. RESEARCH OBJECTIVES AND RESULTS:**

In this research activity, we focused in developing Silicon Drift Detector (SDD) based X-ray spectrometer using commercial equivalent of space qualified components, essentially to use in the upcoming Chandrayaan-2 mission, the second Indian mission to Moon. Chandrayaan-2 mission is configured with Orbiter, Lander and Rover to carry out various scientific experiments. The developed SDD based X-ray instrument is configured as Solar X-ray Monitor (XSM) and Alpha Particle X-ray Spectrometer (APXS) onboard Chandrayaan-2 Orbiter and Rover respectively. The Solar X-ray monitor onboard Chandrayaan-2 orbiter will provide high resolution real time solar X-ray spectrum to the companion instrument named Chandra Large Area Soft x-ray Spectrometer (CLASS), which will measure the global elemental composition of the Moon from the lunar orbit. The Alpha Particle X-ray Spectrometer onboard Chandrayann-2 rover will measure the in-situ elemental composition from the high latitude region of the Moon. Developed SDD based X-ray spectrometer provides energy

resolution of  $\sim 150$  eV at 5.9 keV for the detector operating temperature of  $\sim -40^\circ\text{C}$  and the pulse peaking time of  $\sim 3.3$   $\mu\text{s}$ . The instrument is also characterized for various performance requirements such as energy resolution and its temperature dependence, energy resolution and peak energy position shift for various count rates etc. The test results show that the developed instrument provides the desired performance meeting the scientific requirements of both the instruments.

Another important aspect of any onboard X-ray spectrometer is its calibration. Various techniques including carrying a radioactive source onboard have been used earlier. The second research goal is focused at measuring the leakage current from the SDDs using a simple and novel technique and proposed to use the measured leakage current as an onboard calibration tool for the space applications. This has been demonstrated through the measurement of leakage current for large sample of SDDs. It is experimentally shown that the energy resolution degrades from  $\sim 150$  eV for the detector leakage current of  $\sim 1$  pA to 200 eV at 10 pA and 400 eV at 100 pA. It is also shown that the energy resolution does not improve for the leakage currents  $< 1$  pA. For the smaller leakage currents  $< 1$  pA, the spectrometer system noise is dominant and hence the spectral energy resolution does not improve.

In a space mission, onboard sensors and electronics are continuously exposed to highly ionizing particles which can degrade their performance and/or permanently damage them. Radiation damage effects of critical components must be performed because no replacement is possible once the instrument is in the space. The third research goal is aimed to study the space radiation effects on the SDD modules (SDD chip and the electronic components associated with the module for charge readout) planned for Chandrayaan-2 mission by simulation and experimentation. The radiation effects were studied by irradiating these SDD modules for various doses of gamma rays ( $^{60}\text{Co}$ ,



gamma ray source) and X-rays ( $^{55}\text{Fe}$ , X-ray source). The gamma ray irradiation is to study the space radiation effects on the SDD modules during the transfer (Earth to Moon) and in-orbit (lunar orbit) operations. The X-ray irradiation is to study the X-ray fluence up to which the SDD provides stable energy resolution as the XSM instrument is exposed to very high intensities of solar X-rays in the lunar orbit. It is shown that the energy resolution of these modules does not degrade for the gamma ray dose up to 3 krad and for 10 krad, the energy resolution degraded from  $\sim 160$  eV to  $\sim 210$  eV at 5.9 keV for the detector operating temperature  $\sim -40^\circ\text{C}$ . Extended irradiation result shows that these SDD modules can withstand the space radiation levels for the period of 20 years (100 krad) with desired energy resolution of  $\sim 250$  eV. We have also carried out X-ray irradiation using  $^{55}\text{Fe}$  X-ray source to study the fluence level up to which the SDD detector provides the stable energy resolution as these detector modules are used for X-ray photon detection. It is shown that the energy resolution does not degrade up to the fluence level of  $\sim 2 \times 10^{13}$  photons which corresponds to  $\sim 64$  krad.

The signal from the detector includes several noise sources, such as current, voltage and thermal noise. Noise worsens the performance of the spectrometer by means of degrading its energy resolution. As most of the radiation detectors rely on the measurement charge carriers produced by the ionization events and hence the most commonly used parameter to characterize the noise performance is by means of Equivalent Noise Charge (ENC). The ENC is defined as the input charge that produces the output signal amplitude equal to rms value of noise. It is the minimum charge detectable by the system, making the signal to noise ratio is equal to 1. The noise performance of the spectrometer has been characterized by means of Equivalent Noise Charge (ENC) before and after radiation tests and quantified the degradation to electronic components associated with the SDD module after irradiation. Measuring the

change in the transconductance ( $g_m$ ) value of JFET in the quantification of ENC is not possible as JFET is part of the SDD module and hence we quantified the change in the value of  $C_T^2/g_m$  ratio ( $C_T$  is the total input capacitance). It is shown that the ratio increases from  $\sim 1.34 \times 10^{-21}$  to  $\sim 2.52 \times 10^{-21}$  for the gamma ray dose of  $\sim 547$  krad.

### **1.3. PLAN OF THESIS CHAPTERS:**

Chapter-1 describes briefly about the introduction to the space instruments and the challenges involved in their development for space use. Subsequently, the research goals and the short outcome of each activity are given.

Chapter-2 reviews the various detector technologies adapted over past several decades in the X-ray studies, their working principle and possible readout techniques. The suitability of these detectors for the desired energy range is described by comparing their performances and also giving their merits and demerits. The advancement in the silicon detector technology allows us to develop the X-ray spectrometer instruments with energy resolution close the Fano limit. The use of silicon detectors in various applications (both ground and space based) is also described.

Chapter-3 discusses the working principle of SDD from sideward depletion concept and the availability of various SDD configurations developed over few decades giving their merits and demerits. Improved readout techniques give the energy resolution close to Fano limit. There are several manufacturers of such SDDs which are described in chapter-3 and their use in the space/planetary missions by various space agencies.

Chapter-4 describes the scientific objective and the performance requirement of SDD based X-ray spectrometers onboard Chandrayaan-2. This chapter also gives the concept and the design details subsystems of the SDD based X-ray spectrometer. The SDD based X-ray spectrometer has been developed using commercial equivalent of

space qualified components and shown to provide the energy resolution of  $\sim 150$  eV at 5.9 keV when the SDD is cooled to  $\sim -40^\circ\text{C}$  for the pulse shaping time of  $\sim 3.3$   $\mu\text{s}$ . This meets the performance requirement of APXS instrument. The energy resolution of the developed spectrometer is also measured for various pulse shaping time constants to identify suitable pulse shaping time for the XSM experiment to accommodate count rates up to  $\sim 10^5$  counts/s with reasonably good energy resolution. The count rate performance is tested using both X-ray source and X-ray gun. It is shown that the energy resolution and peak energy position is stable up to 70 k counts/s for the pulse shaping time  $\sim 0.8$   $\mu\text{s}$  with energy resolution of  $\sim 200$  eV at 5.9 keV. The low energy threshold of 1 keV is achieved in both cases.

Chapter-5 describes the necessity of having onboard calibration for the X-ray instruments to have knowledge of any performance degradation due to very hostile space environment. In the space environment, the radiation damage to the SDD leads to increase in the detector leakage current and results in the degradation of energy resolution. We proposed to use SDD leakage current as a calibration tool to establish any performance degradation in the space environment. A new and simple technique of measuring the leakage current by counting the ramp signal frequency at the output charge sensitive pre-amplifier is presented. Leakage current and the energy resolution is measured for large sample of SDD modules for various detector operating temperatures and shown to have good correlation. The experimental technique, method and results are discussed in detail in chapter-5.

Chapter-6 describes the space radiation damage effect to the SDD modules planned for Chandrayaan-2 mission. The interaction of high energy particles in the space environment with the SDD will result in the displacement damage and hence the degradation in the energy resolution. The X-ray instruments onboard Chandrayaan-2 will

encounter severe radiation levels during the Earth to Moon transit and also during the operational period on/around the Moon. The radiation levels were estimated using a web-based European Space Agency (ESA) software suit SPENVIS (Space Environment Information System) for the Chandrayaan-1 orbital profile, assuming that the Chandrayaan-2 mission also will follow the same orbital profile. The effect of space radiation environment on the SDD module has been studied using  $^{60}\text{Co}$  gamma ray source. In this case, displacement damage is due to the Compton electron interactions and the relative damage due to 1 MeV electron is about two order magnitudes less than 10 MeV protons. Performance of the SDD module is also studied for various X-ray doses using  $^{55}\text{Fe}$  X-ray source as the XSM experiment onboard will encounter large intensities of Solar X-ray photons during flare conditions. The noise performance of the spectrometer has been evaluated before and after radiation tests.

Chapter-7 gives the conclusions of the research activity and the future scope. We plan to extend the research activity in the following areas. Proton irradiation tests on the SDD module could not be carried out due to lack of availability of proton irradiation facility which will through some more light on the device characterization. Thus, more experiments are necessary in order to investigate the detector and its complete behaviour in the space. The proton irradiation study will be extended to larger area SDD modules to study the radiation damage effects to the SDD chip and the internal FET in collaboration with the manufacturer for its use in the future space/planetary missions. This is in view of the future plan to develop large area SDD based X-ray spectrometer with large number of such devices.

Hybridization/ASIC development for the SDD readout electronics will be another step forward in developing large area SDD based X-ray spectrometers for the future planetary/astronomy missions.

In recent times, the research is focused at developing thicker silicon detectors with large active area aimed to use in the future space missions for imaging applications. The present X-ray CCDs imaging systems has two major disadvantages: depletion thickness is small (50 micron) resulting in reduction in detection efficiency and low count rate capability due to frame readout. Alternate silicon technologies such as DEPFET and fully depleted pn-CCD also have the issue of faster readout. To overcome these issues, multi-linear SDD configurations were proposed. One such SDD with one dimensional position sensing is planned in the LOFT mission with segmented anodes for linear electron drift. We also propose to extend our future research towards the development of multi-linear SDDs with two dimensional readout with segmented anodes and cathodes in both the sides of the SDD for electron and hole signal readouts to accurately measure the position interaction. In this case, the readout will be faster and provide depletion thickness ranging from few hundreds of microns to 1 mm. This will be a major device level research work. We also propose to develop ASIC based readout for these devices.

## **Chapter 2:**

### **X-RAY SPECTROMETER AND REVIEW OF X-RAY DETECTORS**

The aim of this chapter is to introduce the X-ray spectrometer and the review of suitability of various X-ray detectors for the modern X-ray spectroscopy applications such as measurement of X-ray fluorescence from planetary surfaces and the measurement of solar X-rays with high energy resolution.

#### **2.1. X-RAY SPECTROMETER:**

X-ray spectroscopy is one of the spectroscopic techniques used for the characterization of unknown materials by using X-ray excitation sources. In this process, the incident photon removes an electron from the inner shell of an atom and the rearrangement of electrons releases a photon whose energy is characteristic to the element. Analysis of the characteristic X-ray emission spectrum gives the qualitative elemental composition of the sample under test. Quantitative measurements can be obtained by comparing the X-ray spectrum with spectrum obtained from the standards samples. This can be obtained after the mathematical corrections for absorption, fluorescence and atomic number. X-ray spectrometer is an instrument, capable of detecting X-rays in the energy range of interest. X-rays are keV energy photons, classified loosely into three types based on their energies namely, soft X-rays with energy  $< 1$  keV, medium X-rays and hard X-rays with energy  $> 20$  keV. In our

experimental measurements, we are interested in detecting medium energy X-rays with the energy range of 1 - 25 keV. The frequency of such electromagnetic radiation ranges between  $10^{17}$  -  $10^{19}$  Hz.

## **2.2. X-RAY GENERATION:**

X-ray photons are a form of electromagnetic radiation produced following the ejection of an inner orbital electron and subsequent transition of atomic orbital electrons from states of high to low energy. X-ray tubes were/are generally used to produce X-ray photons in most of the laboratory studies including scientific and medical applications. In the X-ray tube, a filament is heated to produce electrons which are then accelerated in vacuum by a high electric field towards the target. When the high energy electron strikes the target atom, will result in

1. Photon emission - Characteristic X-rays, more likely for high  $Z$  elements,  $Z > 32$ .
2. Auger electron - Radiation less internal rearrangement, more likely for low  $Z$  elements,  $Z < 32$ .

The relative probabilities of X-ray emission and Auger electron emission with atomic number is shown in figure 2.1. The schematic representation of characteristic X-ray emission and Auger electron emission is shown in figure 2.2. In the first process, X-rays are emitted when an electron from the inner shell of the atom is knocked out by the incident photon with a kinetic energy  $E - \phi$ , where  $E$  is the incident particle energy and  $\phi$  is the binding energy of electron.



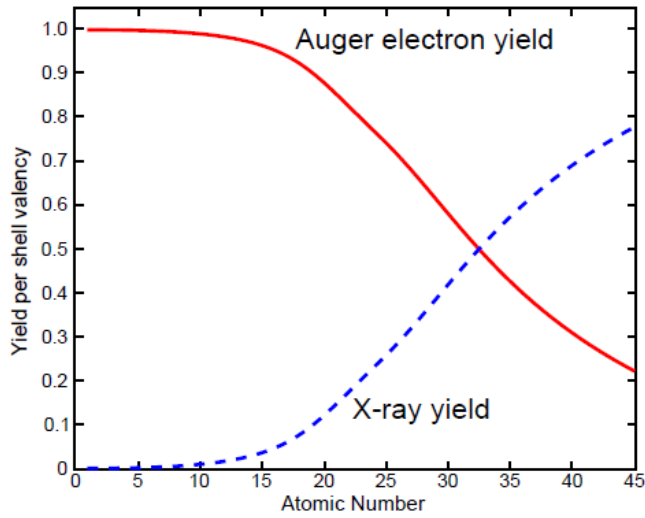


Fig. 2.1: The relative probabilities of X-ray emission and Auger electron emission with atomic number [1].

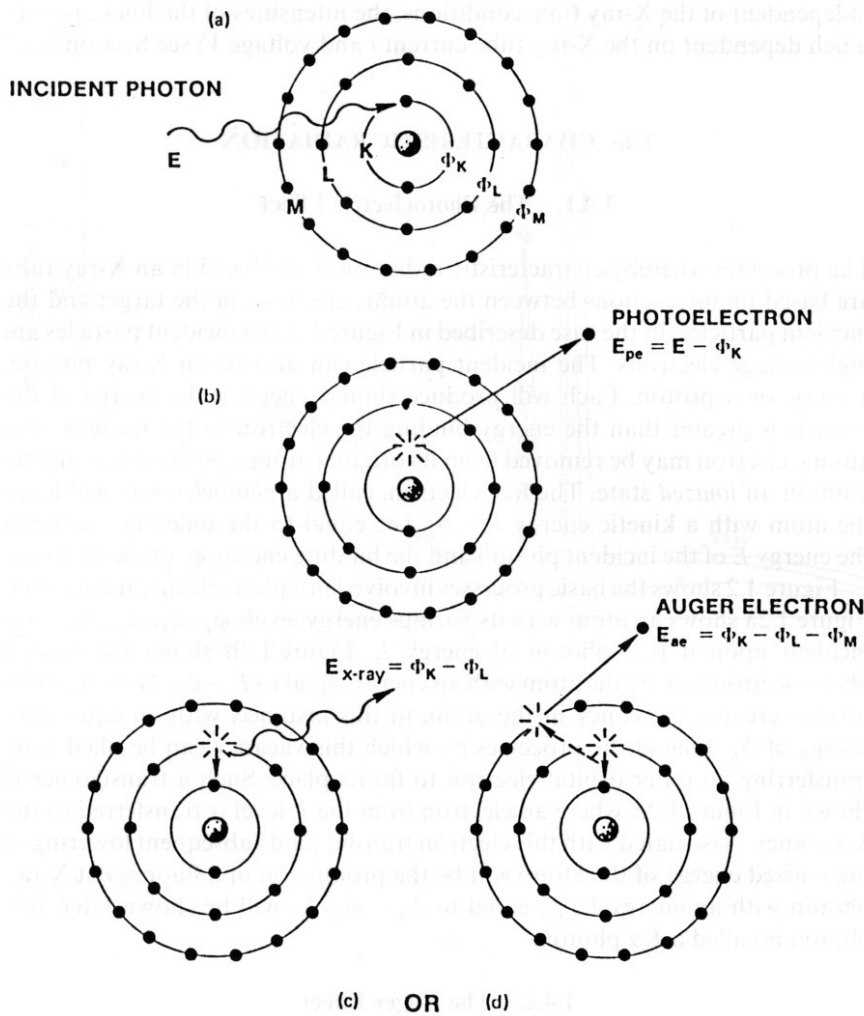


Fig. 2.2: Schematic representation of characteristic X-ray emission and Auger electron emission processes [1].

The electron from the higher energy orbit fills the vacancy and releasing a photon which has a wavelength that is characteristic to the target element. The auger process is a three electron process and leaves the atom doubly-ionized resulting emission of auger electron. The electron beam interaction on the target material also produces continuum of energies called bremsstrahlung which is due to the deceleration of the electrons inside the material. The spectrum having characteristic X-ray and the bremsstrahlung continuum obtained for tungsten target is shown in figure 2.3.

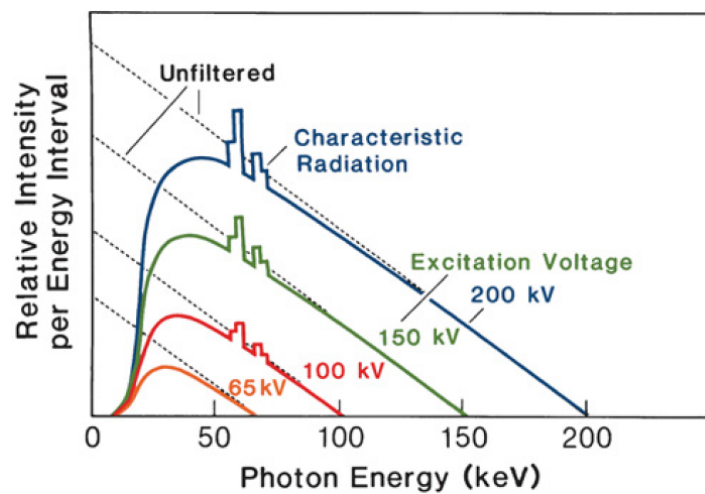


Fig. 2.3: Characteristic X-ray and the bremsstrahlung continuum obtained for tungsten target for various tube voltages (taken from Lippincott Williams and Wilkins).

### 2.3. X-RAY SPECTROMETER INSTRUMENTATION:

The block schematic of the X-ray spectrometer instrumentation is shown in figure 2.4.

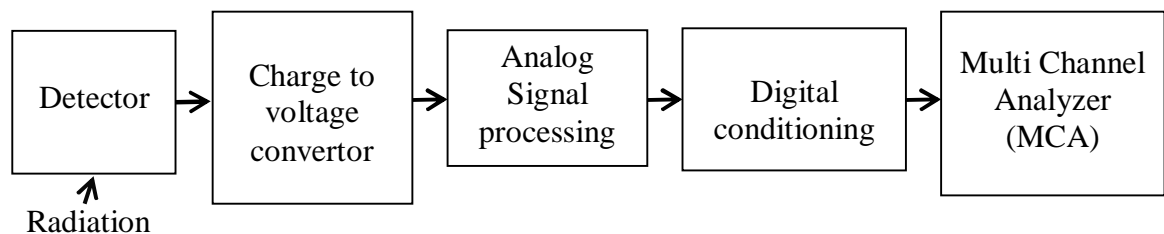


Fig. 2.4: Generic block schematic of an X-ray spectrometer.

X-ray spectrometer consists of a detector which converts the X-ray photon into an electrical signal due to photoelectric effect. A feeble charge signal at the detector electrode is converted into voltage by a Charge Sensitive Pre-Amplifier (CSPA). The output of the CSPA is of the order of few mV. Further signal processing can be carried out either by traditional analog pulse processing technique or by using digital algorithms known as digital pulse processing. In case of analog pulse processing, the output of CSPA is further amplified using a shaping amplifier which is a combination of high and low pass filters. Shaping amplifier provides necessary amplification to cover the desired energy range with improved signal to noise ratio by reducing the signal bandwidth. The output of the shaping amplifier is given to peak & hold detector and then converted into digital bits using Analog to Digital Converter (ADC). The ADC output is then readout by personal computer (PC) based software for data storage and display. The ADC channel number is then converted into energy to identify the incident photon energy. The ADC channel number to energy conversion is carried out after proper gain calibration of the electronics with known source energies. In the analog pulse processing, the peak position changes with incident X-ray rate which is due to base line shift. This peak shift depends on the shaping time, energy shift increases rapidly with increase in the pulse shaping time. To minimize these effects in the resultant spectra at high count rates, new pulse processing technique is adapted in recent years known as digital pulse processing. In digital pulse processing, the output of the CSPA after high pass filter is digitized directly by using high speed sampling ADC and all other signal processing is carried out digitally using Field Programmable Gate Array (FPGA) based algorithms.

The performance of the spectrometer system is evaluated by its energy resolution i.e., how good the spectrometer can resolve the closely spaced electromagnetic radiations. The energy resolution is usually defined by Full-Width-at-Half-Maximum

(FWHM). Lower the FWHM, better the energy resolution of the spectrometer. The sample spectra acquired from the spectrometer showing the energy resolution in FWHM is shown in figure 2.5. Ideally, there should be a single line in the spectra for the monochromatic electromagnetic radiation detected by the spectrometer. But in real case, there will be spread in the spectrum which is due to various processes involved in the spectrometer system such as Fano statistics and the noise due to readout electronics. X-ray spectrometer instruments are very common in all the recent space/planetary missions.

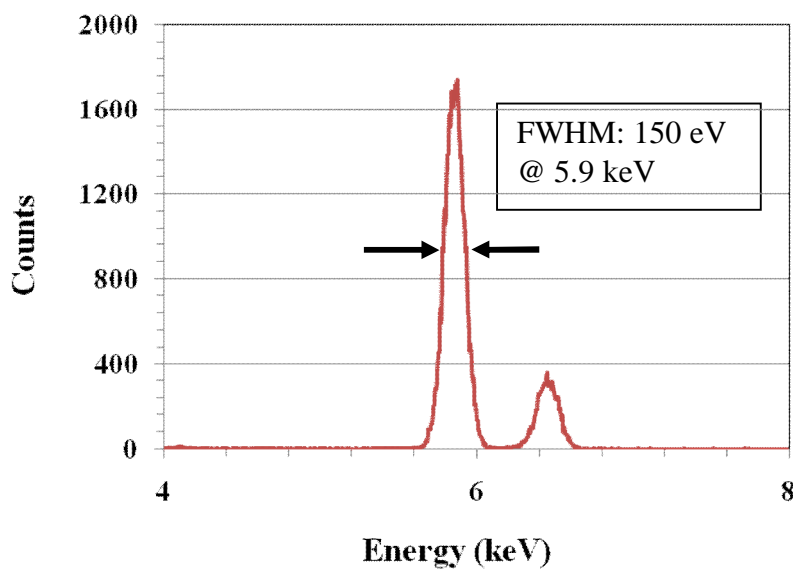


Fig. 2.5: Sample spectrum showing the energy resolution in FWHM measured using  $^{55}\text{Fe}$  source.

These instruments are aimed to study the elemental composition of the planetary surfaces by measuring the X-ray fluorescence either from the orbit (remote sensing) or on the surface (in-situ) of the planet. Measurement of X-ray fluorescence from the orbit requires simultaneous measurement of solar X-ray spectrum, as the intensity of X-ray fluorescence vary with intensity of solar X-rays falling on the planet. For in-situ measurement, radioactive sources are generally carried along with the instrument to irradiate the sample surface and then measure the X-ray fluorescence. There are independent X-ray instruments for solar studies with high energy resolution which was

not possible earlier. X-ray spectrometers with very high spatial and spectral energy resolution using latest detector technologies are also widely used in the space astronomy.

The review of various types of detectors suitable for the X-ray spectrometry, the interaction mechanisms, contribution of various detector parameters to the spectrometer performance and the use of these spectrometer systems in field of space research are discussed in the subsequent sections.

## **2.4. REVIEW OF X-RAY DETECTORS:**

The aim of this section in chapter-2 is to introduce various types of detectors used in X-ray detection with emphasis on semiconductor detectors and, in particular, the silicon detectors. X-ray detector is a transducer which converts the X-ray photon energy into voltage pulses. The interaction of an X-ray photon within the active volume of the detector produces charge carriers (electron-hole pairs) through photo ionization process. The current pulse produced by these charge carriers is converted to a voltage pulse, by a charge to voltage conversion amplifier known as charge sensitive pre-amplifier. The voltage amplitude of the pulse is proportional to energy of the incident X-ray photon. The signal is then processed by a suitable low noise electronics chain to obtain the energy and other required parameters such as arrival time, angle of arrival, position of interaction etc. X-ray detectors are also used to detect other types of electromagnetic radiations such as electrons, protons and alphas etc., but the discussion in this chapter is limited to their use as photon detectors in the low energy X-ray region.

The energy of the photon released in the detector material during the interaction is converted into an electrical signal by means of direct or indirect process [2], with a conversion factor which depends on the type of the detector used. Hence, the radiation detectors are broadly classified in to two types

1. Direct conversion type
2. Indirect conversion type

A direct conversion type detector is the one in which the incoming photon is directly converted into an electrical signal, whereas in indirect conversion type detector, the conversion takes place in two steps. The first step involves conversion of a photon into visible light and the second step involves the conversion of visible light into an electrical pulse. The schematic representation of production of charge carriers in direct and indirect conversion type detectors is shown in figure 2.6.

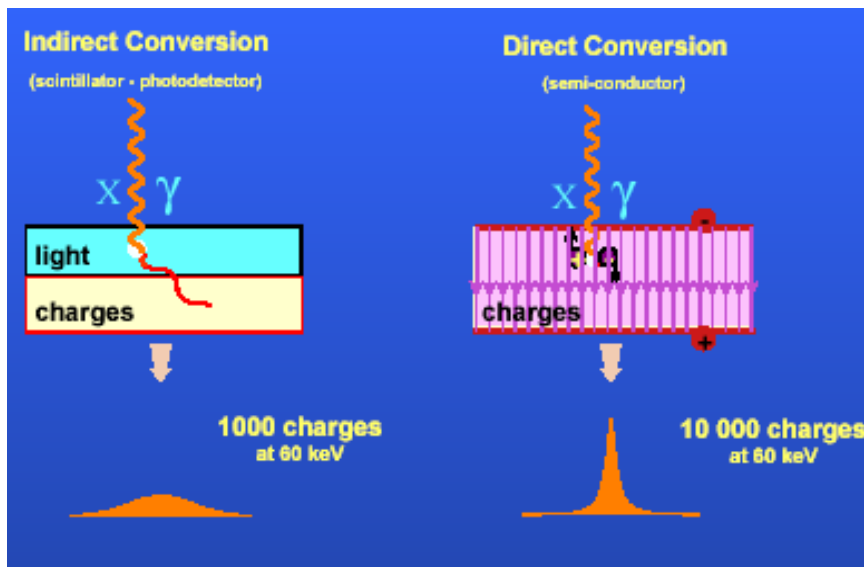


Fig. 2.6: Schematic representation of production of charge carriers in direct and indirect conversion type detectors [2].

The indirect conversion approach induces loss of information in the process particularly at very low radiation inputs. The gas-filled detectors and the semiconductor detectors are of direct conversion type where the incident photon energy is directly converted into a certain amount of charge which is then collected at the output electrode of the device. In direct conversion type, there is no charge loss and hence provides good energy resolution. The energy required to create one electron-hole ( $e-h$ ) pair in gas-filled

detectors varies from 25 – 35 eV and in case of semiconductor detector; it is of the order of few eVs (for silicon, 3.6 eV and for germanium, 2.9 eV).

Scintillation detectors are indirect conversion type, where in the incident radiation is converted into shower of optical photons (visible and near visible region). These photons are then collected and converted into electrical charge by using photo detectors. The photo detector could be photomultiplier tube (PMT) or silicon photo detector or very recent technology device known as silicon photomultipliers (SPM). Due to two step conversion mechanism in the indirect conversion process, there is loss of signal due to light coupling, resulting in poor energy resolution. The average energy required to create one  $e-h$  pair in scintillators is of the order of 25 eV.

In early days, people employed different types of X-ray detectors like gas proportional counters, scintillators and liquid nitrogen/Peltier cooled semiconductor detectors. A brief description of each type of X-ray detector is given in the following subsections.

#### **2.4.1. The Proportional Counter:**

The concept of proportional counter was introduced in the late 1940's. Proportional counter is gas filled device, used as X-ray detector with moderate energy resolution by operating at room temperature [3]. Proportional counters are generally made in cylindrical form and the internal volume is filled with gas as shown in figure 2.7. The most commonly used gases are high purity argon, xenon, neon and krypton. The surface outside the cylinder acts as a cathode and a wire along the axis of the cylinder acts as an anode. The anode is positively biased with respect to cathode. These detectors are generally made in large detection area with high count rate capability. The working principle of the proportional counter is that, the electrons produced by X-ray photon in



the gas which is mainly due to photoelectric effect are accelerated towards the anode by applying suitable voltage across the electrodes and thus producing ionization by their collision with the atoms of the gas.

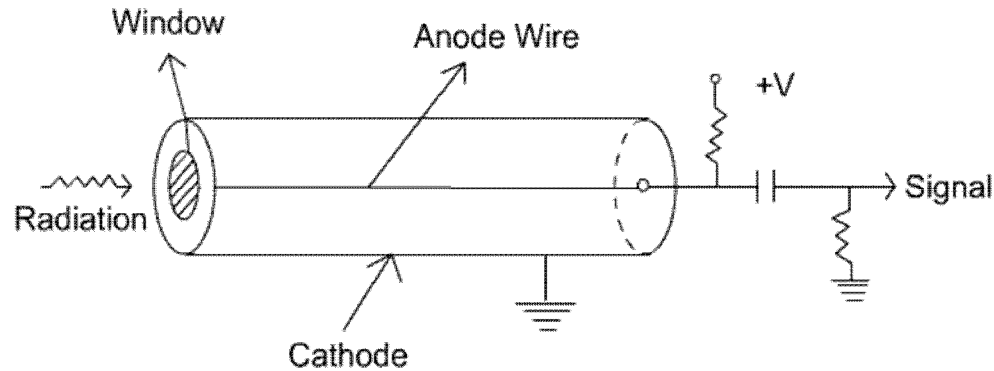


Fig. 2.7: Schematic representation of a cylindrical proportional counter [3].

The amplitude of the resulting signal is therefore proportional to the energy of the X-ray photon by means of electrons generated by the ionization and the multiplication factor ( $M$ ) for these electrons due to collisions. These detectors require typically  $\sim 25\text{--}35$  eV/e-h pair. The value of multiplication factor could vary between 10 and  $10^4$  depending on the applied voltage. The diameter of proportional counter typically ranges from 2 to 5 cm. The efficiency of these detectors in low and medium X-ray energies is small compared to other detectors discussed in the subsequent sections. For example, 5 cm thick proportional counter filled with  $Ar$  gives 50% transmission at 10 keV and for  $Xe$  gas, the same transmission could be achieved at 40 keV at room temperature. The energy resolution of these detectors is poorer than semiconductor detectors and better than scintillators detectors. The energy resolution of a gas proportional is in the order of 10 - 15% at 5.9 keV. A sample spectra obtained from the proportional counter is shown in figure 2.8.

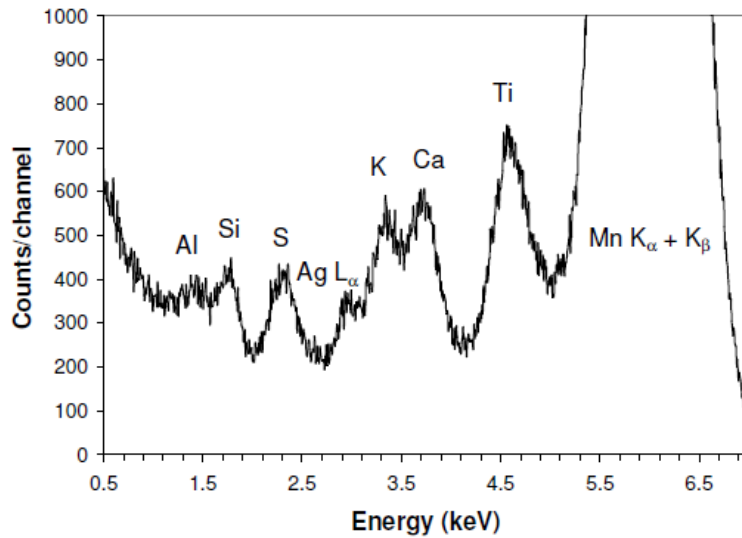


Fig. 2.8: X-ray fluorescence spectra measured with a gas filled proportional counter [3].

#### 2.4.2. Scintillation Detectors:

The scintillation detector is a type of luminescent material which produces scintillation light on photon interaction. The process of fluorescence is the prompt emission of visible light from the material following its excitation by some means. Small amounts of impurities are generally added to all scintillators to enhance the emission of visible light photons. The schematic representation of scintillator working principle is shown in figure 2.9.

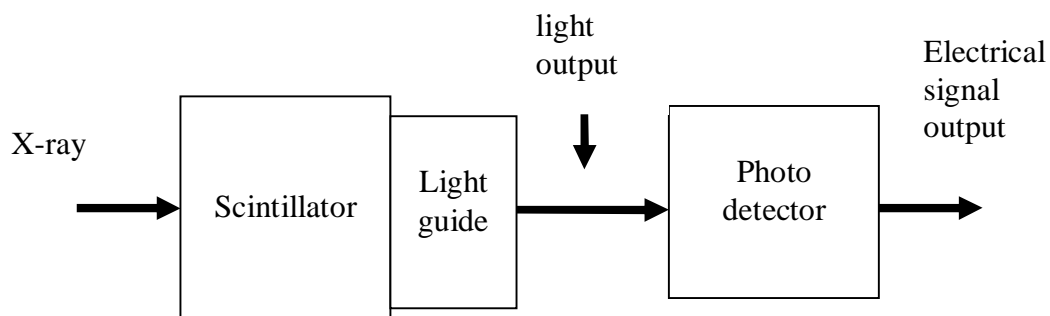


Fig. 2.9: Schematic representation of working principle of scintillation detector.

Scintillation detectors are broadly classified into two types based on the scintillation mechanism [4], they are

1. Organic scintillators

## 2. Inorganic scintillators

In case of organic scintillators, the fluorescence process arises from the transition in the energy level structure of a single molecule and therefore can be observed from a given molecular species independent of its physical state. Some examples of the organic scintillators are plastic scintillators, pure organic crystals and liquid organic crystals. These scintillators are generally used for timing applications.

In case of inorganic scintillators, the scintillation mechanism depends on the structure of the crystal lattice. In a pure inorganic crystal such as NaI, the electrons are only allowed to occupy selected energy bands. The absorption of incident photon energy in pure crystals can elevate the electrons from the valence band to the conduction band leaving gap in the valence band. The return of an electron with the emission of a photon is an inefficient process, only few photons are released by decay and the energy is released by some other mechanisms. Also, the bandgap in the pure crystals are such that the emitted photon energy is too high to lie in the visible range and therefore, some small amounts of impurities are added to the crystal in trace amounts. These impurities are called activators and they create special sites in the lattice which modifies the bandgap structure at that site. The energy structure of the overall crystal remains unchanged. Some of the inorganic scintillators are Sodium Iodide (NaI(Tl)), Cesium Iodide (CsI(Tl)), Bismuth Germanate (BGO) and Lanthanum Bromide (LaBr<sub>3</sub> (Ce)) [4]. Inorganic scintillators are generally used for spectroscopy.

Ideal scintillators material should have the following properties

1. High scintillation efficiency
2. Linear conversion – light yield proportional to the deposited energy for wide energy range
3. Transparent medium for good light collection

4. Short decay time for fast signal pulses
5. Good optical quality with refractive index near to that of glass ( $\sim 1.5$ ).

In comparison to the gas detectors, the scintillation detectors are based on higher Z material with high density. These detectors are often available in larger thickness. Due to these factors, the scintillation detectors have high probability of detecting photons in the wider energy range. However, the energy resolution of these detectors is poorer in the low energy X-ray region, which is of the order of  $\sim 20 - 30\%$  at 5.9 keV. These detectors are widely used in the low resolution applications where the large area is required covering wide energy range from few tens of keV up to hundreds of keV or even few MeV. Scintillators can be operated in the room temperature conditions and even at higher temperature without much degradation in the spectral performance [4]. Schematic representation of a scintillator coupled with Photo Multiplier Tube (PMT) for charge readout is shown in figure 2.10.

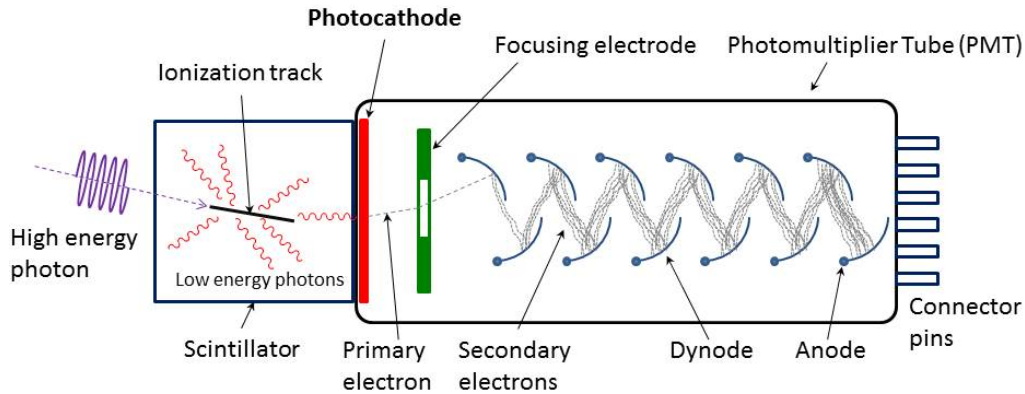


Fig. 2.10: Schematic representation scintillator coupled with PMT for charge readout [5].

Even at higher energies, these detectors provide poor energy resolution compared to semiconductor radiation detector. The comparison of one such spectra obtained from NaI(Tl) scintillator and from high purity germanium is shown in figure 2.11. In case of Scintillator (NaI(Tl)), the FWHM is  $\sim 75$  keV at 1173 keV, but in Germanium the

resolution is  $\sim 2.35$  keV at 1173 keV. This shows that any gamma ray line which is within 75 keV from 1173 keV line will not be resolved using NaI(Tl).

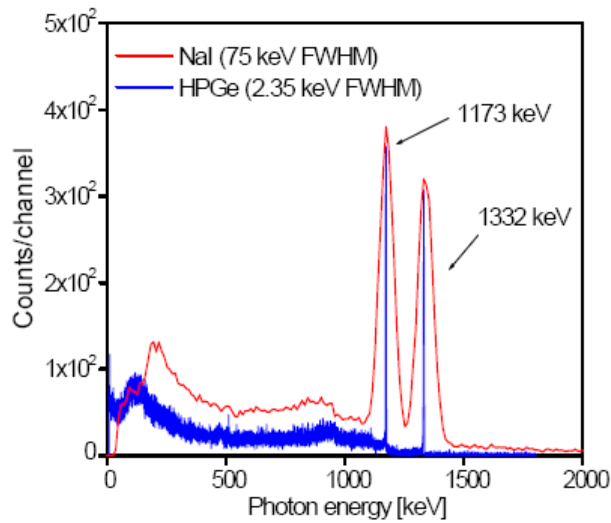


Fig. 2.11: A typical spectral performance comparison between NaI(Tl) scintillator and high purity germanium detector [6].

The latest technology scintillation detector, Cerium doped Lanthanum Bromide ( $\text{LaBr}_3$  (Ce)) [7, 8] has shown to provide reasonably good energy resolution comparable to that of semiconductor detectors by operating in room temperature conditions as shown in figure 2.12.

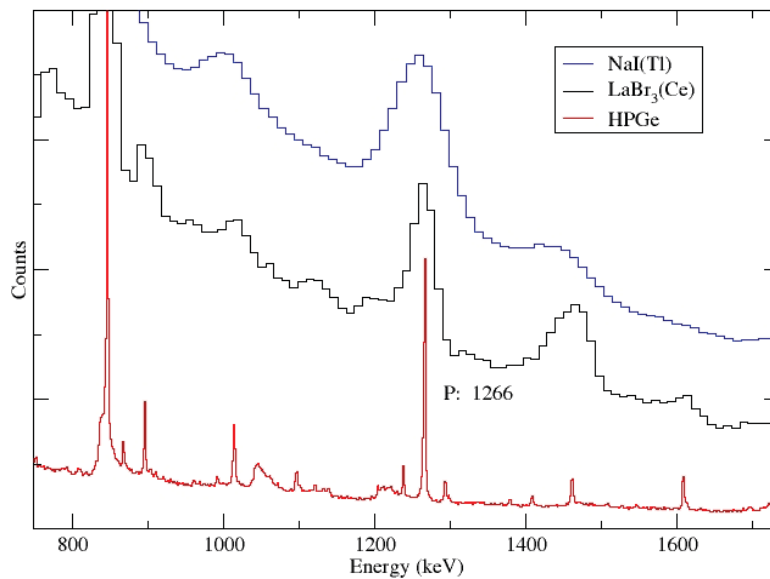


Fig. 2.12: Spectral performance comparison of Lanthanum bromide with sodium iodide and high purity germanium detector [9].

However there are drawbacks to lanthanum Bromide detectors, which include internal radioactivity that contributes to spectral counts and a low-energy response that can cause detector resolution to be lower than that of NaI(Tl) below 100 keV. However resolving very closely spaced lines could be possible only with semiconductor detectors. Table-2.1 gives characteristics of scintillation detectors generally used in the scientific measurements.

**Table-2.1:** Comparison of various scintillation detectors and its properties.

<b>Crystal</b>	<b>Density (g /cm<sup>3</sup>)</b>	<b>Light yield (photon/keV)</b>	<b>Decay time (ns)</b>	<b>Emission wavelength (nm)</b>	<b>FWHM (%) at 662 keV</b>
<b>CsI (Tl)</b>	4.51	66	800	550	6.6
<b>NaI (Tl)</b>	3.67	41	230	410	5.6
<b>LaBr<sub>3</sub> (Ce)</b>	5.3	61	35	358	2.9
<b>BGO</b>	7.1	8.6	300	480	9.0

#### **2.4.3. Scintillator Readout Systems:**

Scintillation detectors provide output in the form of light, which needs to be converted into electrical form to identify the incident photon energy. The following devices are generally used to convert the visible photons into electrical signal.

1. Photomultiplier tubes (PMT)
2. Photo diodes
3. Silicon photomultipliers (SPM)

##### **2.4.3.1. Photomultiplier Tubes:**

Photo multiplier tubes (PMTs) are still the workhorse and generally used to convert the low level light output into electrical signal by coupling the PMTs with

scintillation detectors. PMTs are generally coupled with scintillators using optical compound for better light coupling. The optical light from the scintillators is made to fall on the photocathode of the PMT which converts the light in to electron cloud. These electron clouds are further multiplied by means of acceleration using dynodes which are applied with successively higher potential. The multiplication stages of the PMTs give the gain of the order of  $\sim 10^6$ . The charge output is read out in the final anode with suitable high voltage coupling capacitor to decouple the high voltage reaching the readout electronics. PMTs are generally bulky and require high voltage ranging from hundreds of volts to few kilo volts (KV) for its electrodes (photocathode and dynodes). PMTs can be operated either in counting mode or current mode due to larger signal output. The use of photomultiplier still continues and the size and shape [10] of these tubes are made small due to advancement in the PMT technologies. The quantum efficiency of the PMT varies from  $\sim 10$ -50%. PMTs are sensitive to the magnetic field and hence require proper shielding for its operation. Figure 2.10 gives the schematic representation of the photomultiplier tube.

#### **2.4.3.2. Photodiodes:**

A photodiode is a PN junction diode, produces charge carriers when the incident photon with sufficient energy strikes the junction. On the application of the suitable electric field, charge carriers are collected at the electrodes which produces electrical signal. Photodiodes are mainly operated in two different modes namely, photovoltaic mode and photoconductive mode. In photovoltaic mode, zero bias is applied across the diode and the flow of photocurrent is restricted leads to voltage build up. It is used in a system with low noise and where precision is more important than speed. It is similar to solar cells except that the solar cells have large area.

### ***Photoconductive mode:***

Photoconductive mode of the photodiode is used for light detection. In this mode, the PN junction is reverse biased, which increases the depletion width and reduces the junction capacitance and used in a system where speed is more important than precision. When the light falls on the photodiode,  $e-h$  pairs are generated similar to that of ionizing radiation. Photons corresponding to typical scintillation light carries about 3-4 eV of energy, which is sufficient to create  $e-h$  pairs in the semiconductor with bandgap energy of 1-2 eV. The quantum efficiency of the conventional photodiodes offer as high as 80% which is several times higher than PMTs and hence provides better energy resolution by operating at very low bias voltages. However, photodiode does not provide charge amplification/multiplication as in PMTs and hence the output signal is orders of magnitude smaller than PMT signal. Photodiodes offer compact size and ruggedness compared to PMTs and the performance does not change with the magnetic field.

### ***Avalanche mode:***

Avalanche photodiode is a highly sensitive, has similar structure to photodiodes and operated relatively at very high reverse bias voltage. It makes use of internal amplification to achieve the gain due to impact ionization. The charge carriers are accelerated sufficiently between the collations to create the additional charge of  $e-h$  pairs along the collection path. This process is similar to one described in proportional counters and thereby provides internal charge amplification. The internal multiplication helps to distinguish the signal from the noise level and hence improves the energy resolution in pulse mode. This property allows operating avalanche photodiode at lower energies



compared to that of photoconductive mode of photodiodes. In this case, the gain multiplication factor is very sensitive to temperature and applied bias high voltage and thereby requiring regulated bias voltage and stable operating temperature. Avalanche photodiodes also provides the quantum efficiency as high as 80%.

#### **2.4.3.3. Silicon Photomultipliers (SPM):**

The silicon photomultiplier is a multipixel semiconductor photodiode, where the pixels are connected in parallel on common silicon substrate. Each pixel operates in Geiger mode with bias voltage of  $\sim 20\%$  more than the breakdown voltage. When a sufficiently high electric field is generated within the depletion region of the silicon, the charge carriers generated in this region will be accelerated to point where it carries sufficient kinetic energy to create secondary charge carriers through impact ionization [11]. In this way, a single photoelectron can trigger self induced ionization cascade. The silicon will breakdown and become conductive, effectively amplifying the signal. This process is called Geiger discharge [12].

Each SPM pixel is operated in Geiger mode to achieve high gain. The PN junctions in SPM are designed to withstand the reverse bias beyond its breakdown voltage, creating the necessary high field gradients across the junction. The current flowing through the junction is stopped or quenched using series quenching resistors which limit the current drawn during the breakdown and lowers the reverse voltage below the breakdown voltage. The gain of the each pixel is determined by the charge accumulated in the pixel capacity, which is  $\sim 10^6$ . The pixel size varies from 15 to 70  $\mu\text{m}$  and the total number of pixels varies from 100-10000 pixels/device [13]. As all the pixels in the SPM works on a common load and each pixel works as a binary device resulting

as an analog detector giving measurement of light intensity. The schematic representation of SPM is shown in figure 2.13.

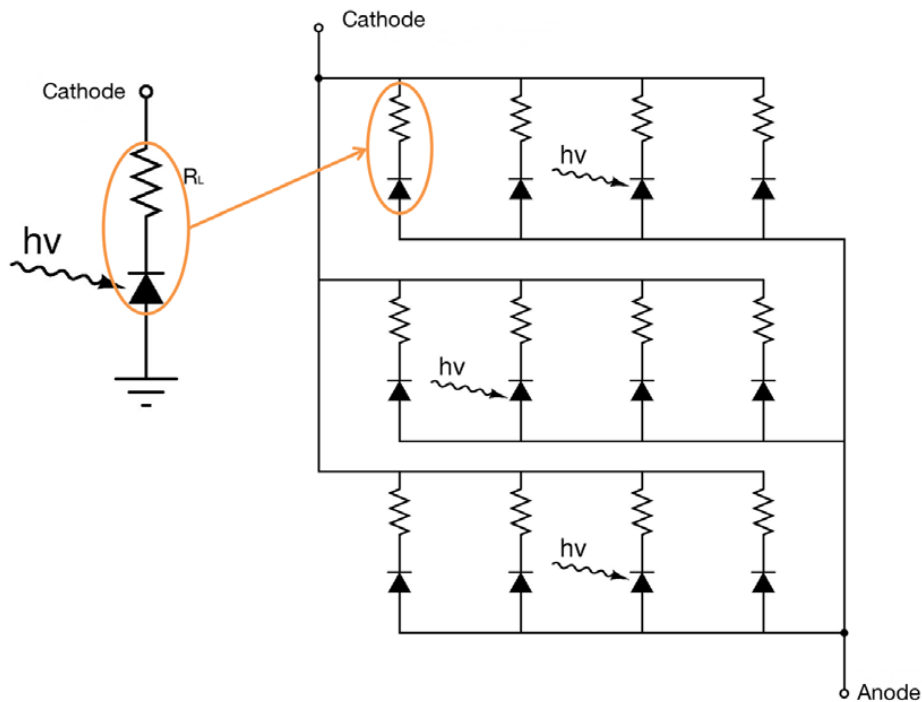


Fig. 2.13: Schematic representation of SPM pixel arrays with quenching resistor and summed output (Courtesy SensL).

Therefore, SPM is capable of detecting low light signal with capabilities of PMT while offering all the benefits of a solid state device. SPM is very hot topic of research in recent years and its usage has gained rapidly in the fields of medical imaging, homeland security and high energy physics. These devices are also planned in the future space missions. SPM is a low cost, robust by the ability to be exposed in room light level without its damage and small physical size. However there are disadvantages which includes large dark noise (10 s of kHz to 1 MHz single photoelectron equivalent), large temperature dependence of breakdown voltage, large cross talk and after pulsing due to charge trapping in silicon substrate. The noise may not be an issue in very high light-level applications or may possibly be mitigated in detector and/or electronics readout design. Thus, there are growing numbers of companies producing these devices and

improvements are being carried out in their design to reduce the crosstalk, noise and also in tuning the optical response of these devices. Table-2.2 gives the comparison of photomultiplier tubes with solid state photo detectors such as photo diode and silicon photomultipliers.

**Table-2.2:** Comparison various characteristics of scintillator readout devices such as PMT, Photo diode and SPM.

	<b>PMT</b>	<b>Photo diode</b>		<b>SPM</b>
		<b>Photoconductive mode</b>	<b>Avalanche mode</b>	
<b>Quantum efficiency</b>	~ 25%	~ 80%	~ 80%	~ 20%
<b>Spectral range</b>	Blue/UV	Red	Red	Green
<b>Internal gain</b>	$10^6$	1	100 - 1000	$10^6$
<b>Response time (ns)</b>	Fast	Medium	Slow	Fast
<b>Multiplication noise</b>	Yes	No	Yes	Yes
<b>Sensitive to magnetic field</b>	Yes	No	No	No
<b>Complexity</b>	High (use of HV)	Low	Medium, low noise electronics	Relatively low
<b>Bias requirement</b>	High (1-2 KV)	Low	100 - 200V	~ 25 V
<b>Temperature sensitivity</b>	Low	Low	High	Low

Each component and combination (scintillator and detector) has its own advantages and disadvantages. One has to use application specific (HEP, Photon Science, Medical Imaging, Industrial Imaging) for his work.

#### 2.4.4. Semiconductor Detectors:

The operation of the semiconductor detector is based on the collection of charge carriers induced in the intrinsic region of the detector due to photon interaction by applying suitable bias voltage. The choice of the semiconductor material as a radiation detector depends on the energy range of interest [4, 14]. Semiconductors as detector material came into use in 1960's. Semiconductors were mainly acknowledged for having much higher density than the gas-filled detectors and intrinsic resolution better than the scintillation detectors. Better intrinsic resolution is due to small Fano factor and very efficient conversion of the incident energy into electrical signal. The ionization energy required for silicon is  $\sim 3.6$  eV and for germanium is  $\sim 2.9$  eV, which is one order magnitude smaller than that of gas-filled and scintillators detectors. Variety of semiconductor materials like Si, Ge,  $\text{HgI}_2$  [15], CdTe [16], CdZnTe [17] and GaAs [18] were considered for nuclear spectroscopy applications and among these detector materials, silicon and germanium are widely used in practice. The compound semiconductor detectors CdTe, CdZnTe are also increasingly used in spectrometry applications in the high energy X-ray region. However, the other semiconductor detectors, scintillators and proportional counters are still being used for various applications based on the experimental requirement and constraints associated with the application.

Semiconductor materials without any impurity are called intrinsic semiconductors. When the dopants are added to the intrinsic semiconductor, the conduction property of the material changes. Adding pentavalent impurities such as Phosphorous or Arsenic with intrinsic semiconductor will increase the conductivity of the material and these dopants are called donors forming *n-type* semiconductors. When

the trivalent impurities such as Boron is added with intrinsic semiconductor resulting in *p-type* semiconductor, also called acceptors.

#### **2.4.5. Silicon Detectors:**

The real use of silicon as photo detector was made possible by the introduction of planar technology which led to the fabrication of silicon detectors by Kemmer in 1980 [19] and Pantazis 1984 [20]. Planar technology consists of series of processing steps on a crystalline silicon wafer and very recently, implants near the top and bottom sides. The planar diode fabrication follows formation of  $SiO_2$  layer on the  $Si$  bulk, selective removal of  $SiO_2$ , introduction of dopant atoms into wafer surface and dopant diffusion into silicon. Combination of these steps can produce any type of complex device on the silicon bulk. The schematic of making planar technology detector is shown in figure 2.14. Silicon planar technology is commonly used in the fabrication of microelectronic circuits [21, 22]. Subsequently, there is lot of development in the last few decades in the silicon detector technologies yielding new detector configurations such as Si PIN, Si Strip and pixilated detectors, charge coupled device (CCD) and Silicon Drift Detector (SDD). These silicon detector configurations are used in vast number of applications and fields. Each of these technologies is briefly described in the following subsections.

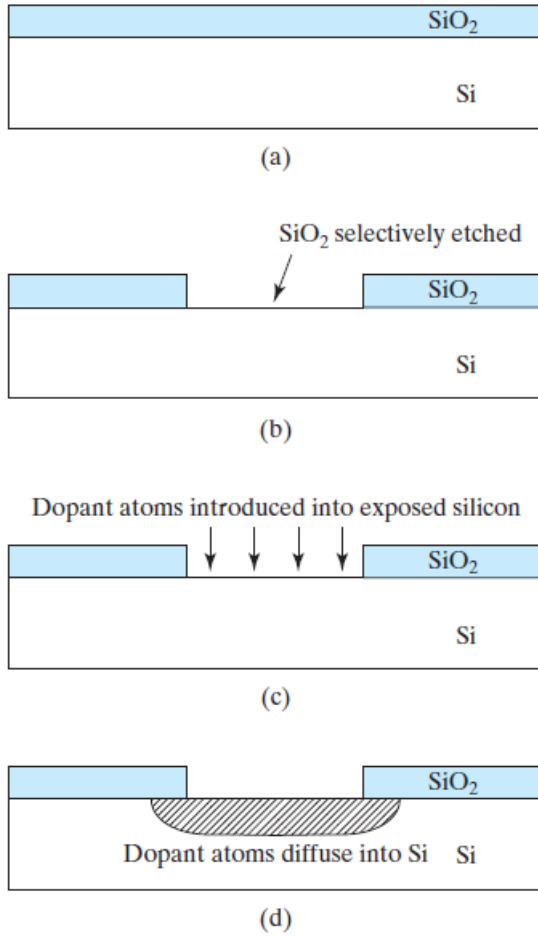


Fig. 2.14: Schematic representation of making of silicon planar technology, a) Oxidation of silicon, b) Selective removal of oxide layer, c) Introduction of dopant atoms and d) Diffusion of dopant atoms into silicon [21].

#### 2.4.6. Detection of X-rays Using Silicon:

Detection of X-ray depends on its interaction with silicon and its detection efficiency. The details of which are discussed below.

##### 2.4.6.1. Interaction of X-ray Photons:

A photon with energy  $E$  is absorbed in a silicon bulk with a probability proportional to the thickness of the silicon. This leads to the exponential transmission given in equation (2.1)

$$I(x) = I_0 e^{-\mu(E)x} \quad (2.1)$$

$I(x)$  - Radiation intensity after passing through the detector

$I_0$  - Radiation intensity before passing through the detector

$x$  - Thickness of the detector

$\mu$  - Attenuation coefficient

The attenuation coefficient ( $\mu$ ) depends on the photon energy and on the absorber material. There are three major mechanisms involved in the interaction of radiation with silicon namely

- a. Photoelectric absorption
- b. Compton scattering and
- c. Pair production

Each of these processes is characterized with individual attenuation coefficients and sum of these gives total attenuation coefficient. The incident photon transfers all its energy to an atomic electron in photoelectric absorption. In case of Compton scattering, the photon transfers only a fraction of its energy to an outer electron and produces a hot electron and a degraded photon. However, in case of pair production, photon with energy above 1.02 MeV interacts within the Coulomb field of the nucleus and produces an electron and positron pair. The photoelectric effect only results in the total absorption of the incident energy and gives information about the photon energy for the accurate energy measurements. The interaction cross section is highly dependent on the atomic number ( $Z$ ) and it varies as  $Z^{4.5}$  for photoelectric absorption,  $Z$  for Compton scattering and  $Z^2$  for pair production. A suitable detector for spectroscopic application must favour

the photoelectric interactions and the semiconductor detectors with a high atomic number are preferred.

The photoelectric absorption is dominant for photon energies up to 100 keV. The Compton scattering dominates for the photon energies  $> 100$  keV and increases linearly with atomic number ( $Z$ ). The pair production becomes realistic for the photon energies  $> 1.022$  MeV. It is necessary to restrict the photon interaction to the photoelectric absorption if any X-ray event has to be detected efficiently. The attenuation coefficient of the silicon detector for various interaction mechanisms is shown in figure 2.15.

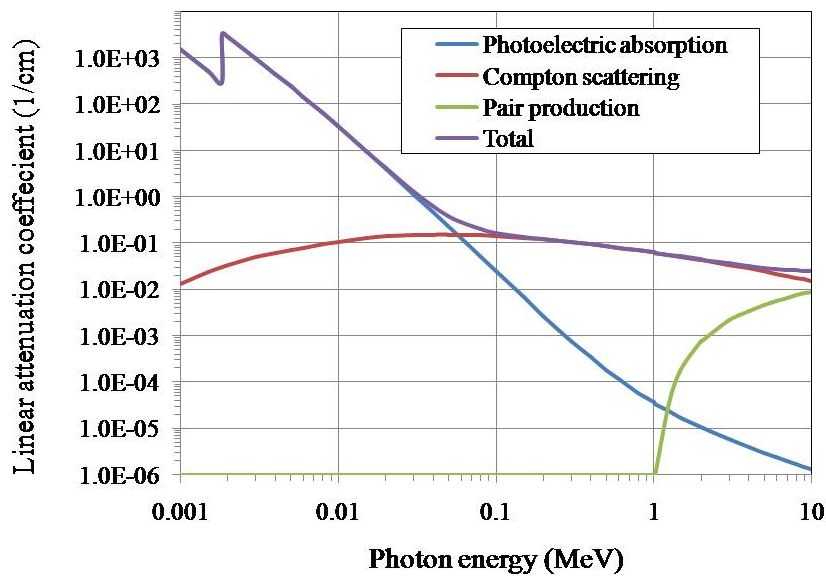


Fig. 2.15: Linear attenuation coefficient for silicon as a function of photon energy up to 10 MeV [23].

The photoelectric absorption is the ejection of photo electron from one of the atom's bound shell when photon interacts with the silicon. The energy of the photo electron is equal to the initial energy of the photon reduced by the binding energy of the photo electron. The vacancy created by the photo electron is quickly filled by electron from the higher orbit and along with this process, the Auger electron or the characteristic X-rays are emitted. These Auger electrons or characteristic X-rays are reabsorbed close to the interaction point. Subsequently, the photo electron causes cascade like process



producing large photo electrons. Equal number of holes are also produced along with the photo electrons. The number of charge carriers  $N_Q$  produced is given in equation (2.2).

$$N_Q = \frac{E}{\varepsilon_i} \quad (2.2)$$

$E$  - Incident photon energy

$\varepsilon_i$  - Energy required to create one  $e-h$  pair

The energy required to create one  $e-h$  pair in silicon detector is  $\sim 3.6$  eV and is  $\sim 2.9$  eV in case of germanium and the corresponding band gap energies are 1.12 eV and 0.72 eV respectively. The mean ionization energy exceeds the band gap due to conservation of momentum which requires excitation of lattice vibrations (phonons). The band gap energy is temperature dependent and hence the energy required to create  $e-h$  pair is also temperature dependent. The energy required to create one  $e-h$  pair increases with decrease in the detector operating temperature, which is given by varshni equation (2.3) [24]

$$E_g(T) = E_g(0) - \frac{\alpha T^2}{(T + \beta)} \quad (2.3)$$

$E_g(T)$  = Band gap energy at temperature T

$E_g(0) = 1.17$  eV, the band gap at temperature 0 K

$\alpha = 4.73 \times 10^{-4}$  eV/K

$\beta = 636$  K for silicon detectors

The change in the bandgap energy with the detector operating temperature is plotted and it varies  $\sim 0.025$  eV in the temperature range of  $-50^\circ\text{C}$  to  $+50^\circ\text{C}$  as shown in figure 2.16.

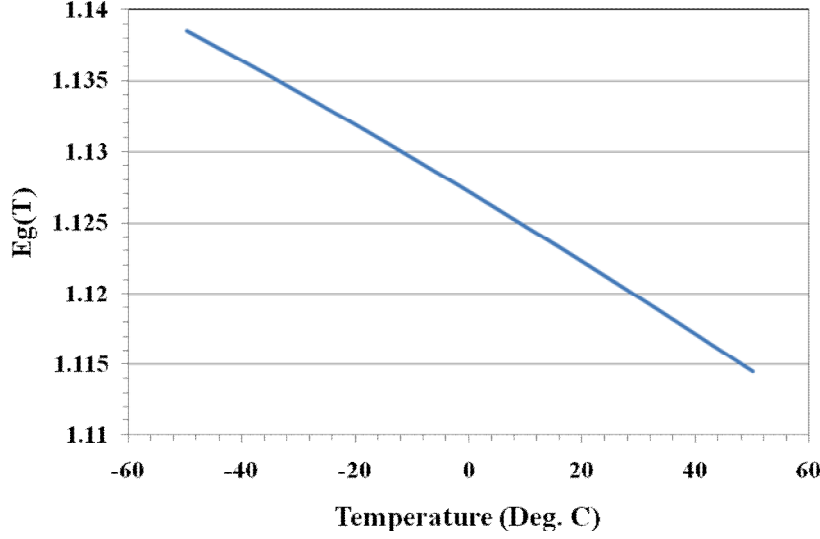


Fig. 2.16: Variation in the bandgap energy of silicon with operating temperature.

The numbers of e-h pairs produced in the silicon detector are not same even for the fixed incident X-rays energies. The fluctuation of charge carrier pair vs. phonon creation is described by Fano factor [25]. The variance  $\sigma_Q$  of number of charge carrier pairs  $N_Q$  created is given in equation (2.4)

$$\sigma_Q = \sqrt{\frac{E_0}{\varepsilon_i}} \sqrt{\frac{E_x}{E_i} \left( \frac{\varepsilon_i}{E_i} - 1 \right)} \quad (2.4)$$

$E_0$  - Absorbed energy

$E_x$  &  $E_i$  - Average phonon and ion pair excitation energies

$\varepsilon_i$  - Average energy required to produce one charge pair

The value of  $E_x$  is 0.037 eV,  $E_i = E_g = 1.12$  eV and  $\varepsilon_i$  is 3.6 eV for silicon detector [4]. The Fano factor for silicon can be estimated using equation (2.5), which is given below

$$F = \frac{E_x}{E_i} \left( \frac{\varepsilon_i}{E_i} - 1 \right) \quad (2.5)$$

The value of Fano factor ( $F$ ) for silicon is 0.11 and the variance in the charge carriers can be written as in the equation (2.6)

$$\sigma_Q = \sqrt{FN_Q} \quad (2.6)$$

Fano factor defines the intrinsic energy resolution of the silicon detector which is the theoretical limit. Engineers around the world strive to achieve the energy resolution close to the theoretical limit.

#### **2.4.6.2. Detection Efficiency:**

The detection efficiency is a ratio of number of photons absorbed in the detector active volume to the total number of incident photons. The absorption coefficient of the detector material varies with detector thickness and the photon energy, limiting the actual number of photon detection. An ideal detector for certain energy range should be able to detect all the photons (absorption efficiency =100%). Generally the high purity silicon wafers have longer recombination life time of charge carriers is of the order of  $\mu s$  and it is reasonable to expect 100% charge collection. Hence the absorption efficiency is not limited by the charge collection efficiency even though this will affect the detection of photons at high count rates. Therefore, the upper energy limit for the given detector material is determined by the absorption efficiency which depends on the thickness of the detector material. The probability an X-ray photon absorbed in the detector varies with detector thickness is given by (2.7)

$$\eta = 1 - e^{-\mu d} \quad (2.7)$$

The change in the absorption efficiency is plotted for various silicon detector thicknesses for the photon energies up to 100 keV. It can be seen that the absorption

efficiency is  $\sim 100\%$  for  $500\ \mu\text{m}$  thick detector for photon energies less than  $20\ \text{keV}$ .

For  $5\ \text{mm}$  thick detector, it is little more than  $30\ \text{keV}$  as shown in figure 2.17.

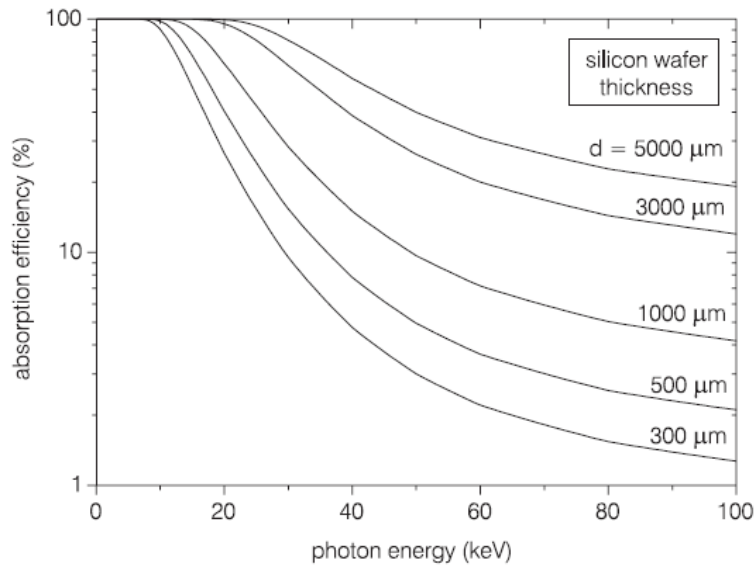


Fig. 2.17: Absorption efficiency for various thicknesses of silicon detector [26].

Fabrication of thicker silicon diodes are possible only with Lithium drifted silicon detectors Si (Li). In planar technology, the detector thickness is limited to  $\sim 500\ \mu\text{m}$  in most of the cases and in recent years, the Si detectors are available up to  $5\ \text{mm}$  thick due to advancement in detector technologies [26]. The low energy (soft X-rays) absorption efficiency in silicon detector is limited due to the presence of thin dead layers which are formed during the detector fabrication process such as  $\text{SiO}_2$  insulating layers and contact layers etc. The absorption efficiency of the  $10\ \text{nm}$  and  $50\ \text{nm}$  thick  $\text{SiO}_2$  layer with photon energy is shown in figure 2.18. Silicon detectors are generally encapsulated to prevent the condensation, where the detectors required to be cooled to lower temperatures. These encapsulation layers also lower the low energy absorption efficiency of the detector. Hence the low energy cut-off of the silicon based X-ray spectrometer is determined by the dead layers associated with the detector fabrication and the encapsulation layer material and its thickness, if the noise level of the readout electronics is superior.

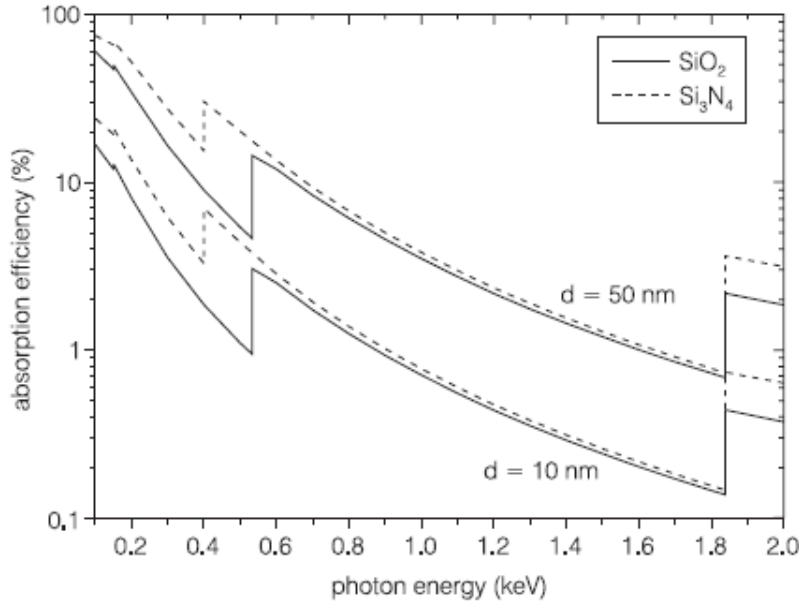


Fig. 2.18: Change in the absorption efficiency due to silicon insulation ( $SiO_2$ ) and metal layers at low X-ray energies [28].

Recently, there are research articles reporting the detection of soft X-rays (up to  $\sim$  keV) using state-of-the-art silicon detectors. It is shown that the X-ray energies down to 50 eV can be measured as reported in refs. [27-30].

#### 2.4.6.3. Signal Formation and Charge Collection:

Semiconductor detectors are direct conversion type ionization chambers, produces  $e-h$  pairs when photon strikes. The number  $e-h$  pairs created in the intrinsic region depends on the energy of the photon and the energy required to create one  $e-h$  pair as given in equation (2.2). Thus generated charge carriers are subject to recombination, if these charge carriers are not collected. The charge carriers move towards the electrode by the influence of the electric field in the detector volume and forms electrical signal. The time required to traverse through the sensitive volume of the detector is called charge collection time. The rise time of the signal charge depends on the detector capacitance  $C_{det}$  and the input resistance of the readout amplifier  $R_i$  and the time constant  $\tau = R_i(C_{det})$

+  $C_i$ ). The operating mode of the readout system depends on the charge collection time of signal charge which is discussed in detail in chapter 4. The representation of signal formation and charge collection is shown in figure 2.19. The charge collection efficiency (CCE) is defined as the total induced charge divided by the charge created  $Q/Q_o$ . For planar detector, the CCE is a function of depth for uniform internal electric field; it is given by Hecht equation (2.8).

$$CCE(x) = \left( \frac{\lambda_e}{L} \right) \left( 1 - e^{-\left( \frac{L-x}{\lambda_e} \right)} \right) + \left( \frac{\lambda_h}{L} \right) \left( 1 - e^{-\left( \frac{x}{\lambda_h} \right)} \right) \quad (2.8)$$

Where  $\lambda_e$  is the drift length/trapping length for electron and  $\lambda_h$  is for holes, which is given by (2.9)

$$\lambda_e = (\mu_e \tau_e) E \quad (2.9)$$

$\mu_e$  and  $\mu_h$  - Mobility of electrons and holes

$\tau_e$  and  $\tau_h$  - Life time/trapping time of electrons and holes

$E$  - Electric field

$x$  - Depth of interaction

$L$  - Detector thickness

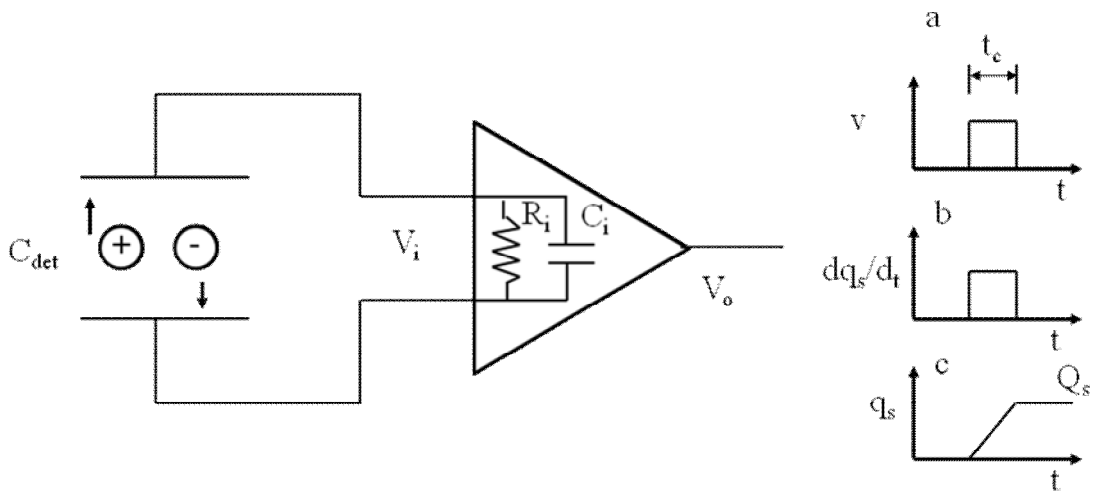


Fig. 2.19: Schematic representation of signal formation and charge collection [31].

The CCE depends not only on drift length, but also on the incoming photon interaction position. The random distribution of the interaction position increases the fluctuations on the induced charge and contributes to the peak energy broadening. Smaller the  $\lambda/L$  ratio reduces the CCE and increases the dependence on the interaction point. The transport properties of the semiconductor detector is characterized by charge carrier mobility and life time product ( $\mu_e\tau_e$  and  $\mu_h\tau_h$ ) which is the key parameter for the development of radiation detector. The product of mobility and life time is called "figure of merit" of the semiconductor material. Poor figure of merit limits the thickness and range of the semiconductor material.

The charge collection efficiency is an important measure of a radiation detector that affects the spectroscopic performance and in particular the energy resolution. High charge collection efficiency improves the energy resolution, which also depends on the statistics of charge generation and the readout electronics noise.

#### **2.4.6.4. Energy Resolution:**

The performance of any spectrometer system is evaluated by its energy resolution. Energy resolution is the measure of how good the spectrometer can resolve the closely spaced electromagnetic radiations. The energy resolution is commonly expressed as Full-Width-at-Half-Maximum (FWHM) of the measured distribution. Ideally, there should be single line in the spectra for the monochromatic X-rays falling on to the detector. In real spectrometer system, the spread in the measured energy is due to intrinsic fluctuation in the charge carrier generation within the detector and also the noise associated with the charge readout & signal processing system. The representation of FWHM is shown in figure 2.20.

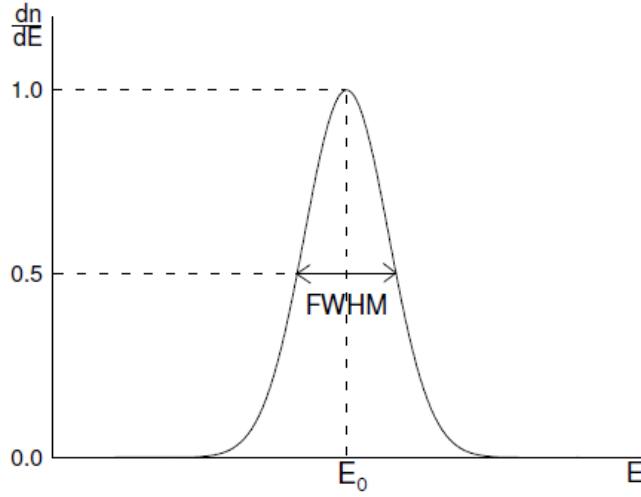


Fig. 2.20: Statistical broadening of the photon energy peak centered at  $E_o$  and Full-Width-at-Half-Maximum (FWHM) of the detected peak is commonly used indication of the energy resolution of spectrometer system [4].

Alternately, the energy resolution can also be expressed in percentage which is the ratio of FWHM value measured to the centroid value of the distribution, as given in equation (2.10).

$$FWHM \text{ (\%)} = \frac{\Delta E_{FEWHM}}{E_o} \times 100 \quad (2.10)$$

Often, the measured distribution can be described by means of Gaussian function, which is expressed by (2.11)

$$G(E) = \frac{N_0}{\sigma \sqrt{2\pi}} e^{\left[ -\frac{(E-E_0)^2}{2\sigma^2} \right]} \quad (2.11)$$

$\sigma$  - Standard deviation

$N_0$  - Area under peak

$E_0$  - Energy peak center

The measured energy resolution is the quadrature sum of FWHM due to Fano statistics and the FWHM due to electronic noise, which is given by the equation (2.12)



$$FWHM (M) = \sqrt{FWHM^2 (Ele) + FWHM^2 (F)} \quad (2.12)$$

where  $FWHM (M)$  - Measured energy resolution

$FWHM (Ele)$  - Contribution of readout electronics noise to the energy resolution

$FWHM (F)$  - Fano statistic contribution to the energy resolution

The Fano noise sets the lowest limit of spectrometer energy resolution, which is given  $FWHM (F) = 2.355 \sqrt{\varepsilon_i F E}$ , where  $\varepsilon_i$  is the  $e-h$  pair production energy (3.6 eV for silicon at room temperature),  $F$  is the Fano factor (0.11 for silicon) and  $E$  is the energy of the absorbed photon. This gives the theoretical limit of  $\sim 120$  eV for the detector based on silicon for the incident energy of 5.9 keV. The Fano factor contribution to the energy resolution of the spectrometer system with incident energy is shown in figure 2.21.

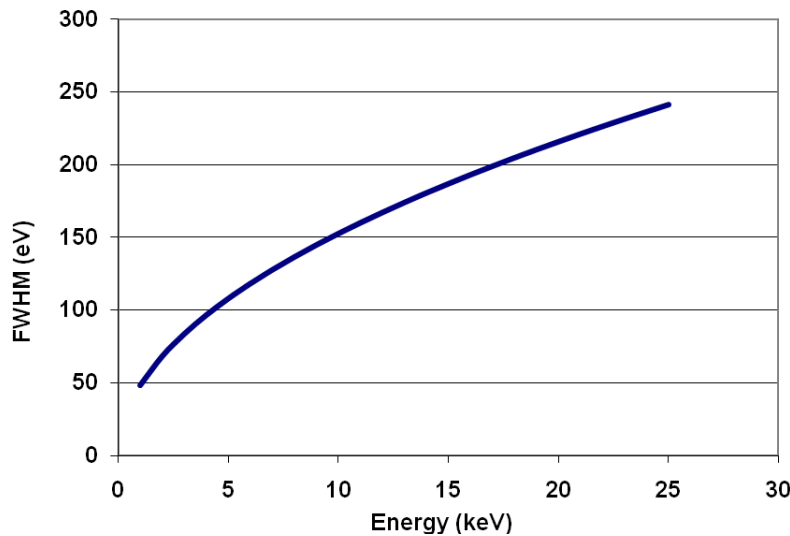


Fig. 2.21: Contribution of Fano factor in the spectrometer energy resolution of Si detector with incident photon energy.

The contribution of readout electronics to the energy resolution is given in equation  $FWHM (Ele) = 2.355 \varepsilon_i \times ENC$ , where ENC is the Equivalent Noise Charge. This noise is independent of incident photon energy, but depends on the detector and signal processing electronics. By substituting the values of measured energy resolution

and the Fano contribution in equation (2.12), one can estimate the equivalent noise charge in electrons rms of the spectrometer system. The noise charge due the detector leakage current and the first stage of the charge readout electronics is expressed as quadrature sum of three independent noise charges such as serial noise, parallel noise and  $1/f$  noise. Detailed discussion of these noise parameters and their contribution to the spectrometer performance can be found in chapter 6. As discussed earlier, the energy resolution of the spectrometer depends on the type of detector, its operating temperature and the noise of the readout system. In the recent years, advancement in the detector and readout technologies, silicon detector, especially Silicon Drift Detector based X-ray spectrometer provides energy resolution of  $\sim 125$  eV at 5.9 keV [37] and a sample spectrum of the same is shown in figure 2.22.

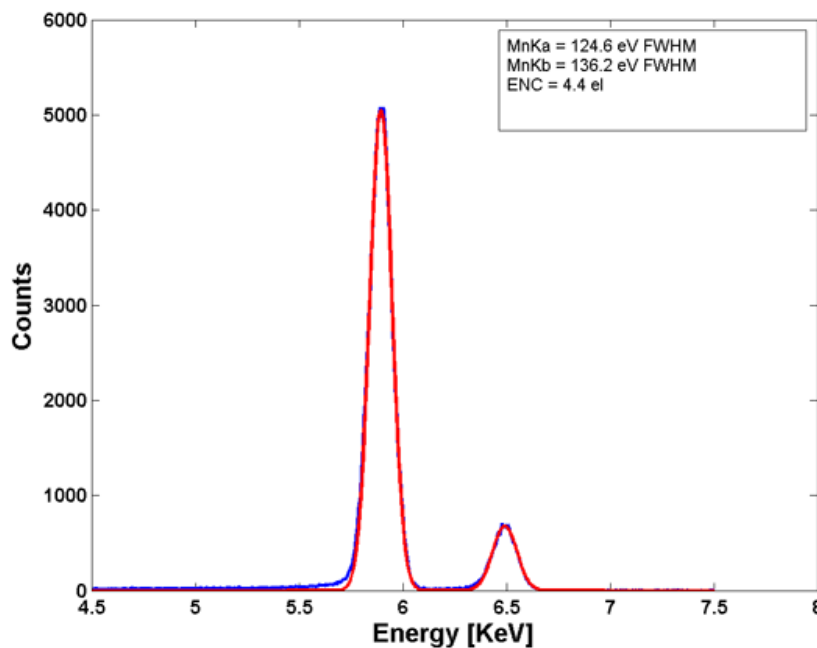


Fig. 2.22: A sample spectra acquired from SDD based X-ray spectrometer with ASIC based readout [32].

#### 2.4.7. Principle of Operation of Silicon Diode Detectors:

The working principle of semiconductor detectors relies on ionization due to the incident photon on the detector material. The absorbed photons excite the valance band electrons into conduction band, creating  $e-h$  pairs. The number of  $e-h$  pairs created depends on the absorbed energy and the bandgap energy. In silicon, the PIN diode is the basic radiation detector with  $p+$  and  $n+$  contacts with n-type bulk as shown in figure 2.23.

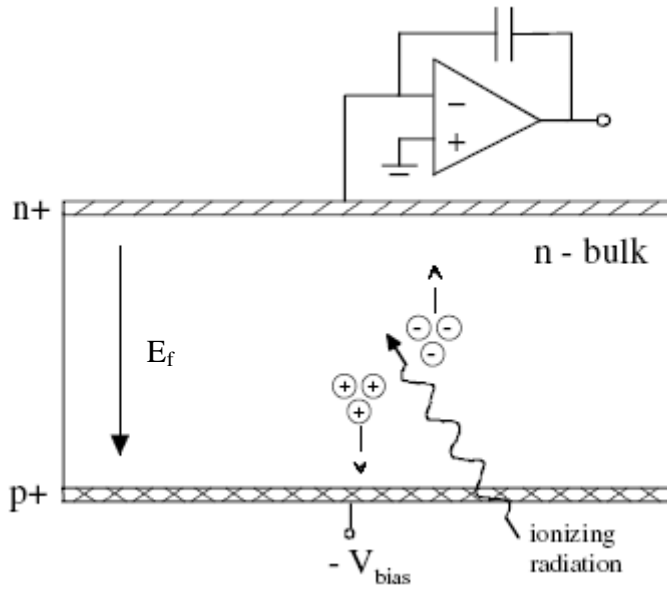


Fig. 2.23: Working principle of a reverse biased silicon PIN diode.

Si PIN diodes are usually made on a high-ohmic resistance ( $> 1 \text{ k}\Omega\cdot\text{cm}$ ) n-type silicon bulk. When the diode is reverse biased, the bulk material is depleted from the free charge carriers. Reverse bias creates an electric field ( $E_f$ ) across the detector which forces the positive and negative charge carriers formed due to ionization to drift in the opposite direction and collected at the electrodes for the further signal processing. The electric field across the 500 micron thick silicon detector is shown in figure 2.24 and the distribution is given in the equation 2.13.

$$E_f = \frac{V_{bias}}{d} \quad (2.13)$$

$E_f$  - Electric field across the detector

$V_{bias}$  - Reverse bias voltage applied across the detector

$d$  - Detector thickness

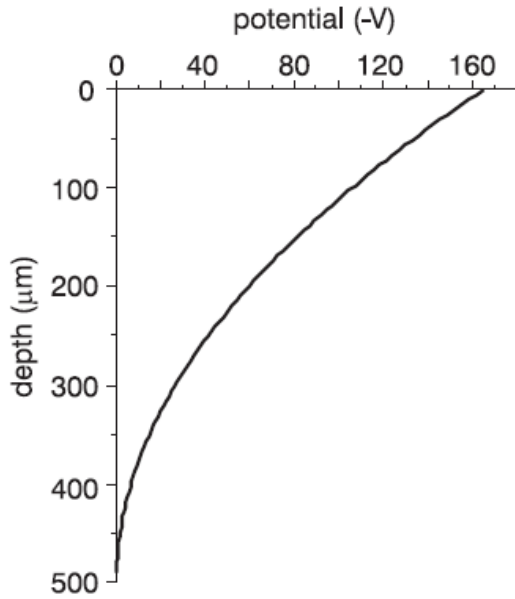


Fig. 2.24: The electric field distribution inside the PIN diode for the detector thickness of 500 microns.

The continuous flow of dark current (reverse current) in the detector is also collected which contributes to the spread in the measured signal charge. The dark current is greatly reduced by cooling the detector to lower operating temperatures. The charge collection time is usually fast in semiconductor detectors and in case of silicon, the charge collection time is  $\sim 10 - 20$  ns. Due to the large electrode capacitance, the signal processing electronics should have longer time constant to achieve the better signal to noise ratio. The large detector capacitance and longer readout time constant forces the spectrometer system to handle only limited count rates.

The noise performance of a PIN diode depends on the detector capacitance and the leakage current at the readout anode along with the noise performance of the charge

readout system. As these detectors are fully depleted by applying reverse bias voltage, the capacitance value of these detectors can be calculated by using parallel plate capacitance approximation, which is given in equation (2.14)

$$C_d = \frac{\epsilon_{si} \epsilon_0 A}{W_d} \quad (2.14)$$

$A$  - Area of the PIN diode

$W_d$  - Depletion thickness

$\epsilon_{si}$  - Permittivity of silicon and the value is about  $10^{-12}$  F/cm<sup>2</sup>

$\epsilon_0$  - Permittivity of air

The parallel plate capacitance of PIN diode detector is estimated to  $\sim 1$  pF/mm<sup>2</sup> for 100 micron thick detector and  $\sim 20$  pF/cm<sup>2</sup> for 500 micron thick detector. The selection of proper material quality is also very important in silicon detector. Generally, the silicon detectors are build on a p-type or n-type bulk with high ohmic resistance. N-type grade silicon material was/is easily available and it is used widely used for the fabrication of silicon detectors and other microelectronics with planar technology. The doping concentration of bulk is also very import and it controls the resistivity of the detector and hence determines the optimal bias voltage required to achieve the full depletion which is essential for radiation detectors. The depletion layer width is proportional to the square root of the applied voltage and inversely proportional to the square root of the doping concentration as given in equation (2.15)

$$W_d \approx \sqrt{\frac{2\epsilon_{si} \epsilon_0 V_{bias}}{q_e N_d}} \quad (2.15)$$

$W_d$  - Depletion width

$\epsilon_{si}$  - Permittivity of silicon and the value is about  $10^{-12}$  F/cm<sup>2</sup>

$\epsilon_0$  - Permittivity of air

$V_{bias}$  - Reverse bias voltage

$N_d$  - Donor concentration

The doping concentration can be expressed in terms of resistivity, which is given in equation (2.16)

$$\rho = (\mu q_e N)^{-1} \quad (2.16)$$

The parameter  $\mu$  gives the relation between the applied voltage and the charge carrier velocity and the depletion width becomes as in equation (2.17) for  $V_{bias} \gg V_{bi}$ . The mobility of electrons approximately 3 times that of mobility of holes. P-type bulk material will have 3 times the resistivity of n-type for the given doping concentration.

$$W_d = \sqrt{2\epsilon_{si}\epsilon_0\mu\rho V_{bias}} \quad (2.17)$$

To achieve the full depletion in the bulk with reasonably low bias voltage, the doping concentration should be as low as possible to get high resistivity. Silicon detectors with 450 micron thick silicon with resistivity of  $\sim 4 \text{ k}\Omega\cdot\text{cm}$  require reverse bias voltage of  $\sim 150 \text{ V}$  to get full depletion. Making a thickest possible detector is limited by the detector capacitance and its contribution to the spectral performance.

The leakage current in a fully depleted PIN diode consists of two leakage currents namely the bulk leakage and surface leakage due to interface layers. The bulk leakage current is due to thermally generated charge carriers in the depleted intrinsic region and this originates from the traps located in the forbidden bandgap. The surface leakage current depends on the  $\text{SiO}_2$  and metal layer interfaces when biased. The modern technologies used in these processes provide leakage current of the order of few tens or hundreds of  $\text{fA}/\text{cm}^2$  at room temperature. Both these leakages are temperature sensitive

and hence by cooling the detector to lower temperature, one can significantly reduce the leakage current contribution to the performance of the spectrometer system.

Silicon detectors are broadly classified into energy dispersive and position sensitive detectors. Both these detectors provide energy information and the later one provides energy along with the position of interaction. Si PIN, Si (Li), p-n junction photo diode and APD are energy dispersive detectors. Silicon Strip Detector (SSD), Si pixel detector and p-n CCD are position sensitive detectors. Working principle, configuration and their usage is briefly described in the following subsections.

#### **2.4.8. Si PIN Diode Detector:**

Silicon detectors were used in the form of Si PIN diode for the radiation detection in 1980's and 1990's as discussed in Kemmer (1980) [19] and Pantazis (1994) [20]. Si PIN diode detectors have been consistently used in various applications including in the space/planetary missions for detecting X-rays in the energy range of 1 - 25 keV until the Silicon Drift Detector technology was available for the researchers. These detectors are available in different sizes starting from 5 mm<sup>2</sup> to 25 mm<sup>2</sup> and thickness ranging from few microns to few hundred microns. Generally, the Si PIN diodes with thickness  $\leq 500$  micron are used for detecting X-rays in the energy range of 1 - 25 keV with reasonably good energy resolution. X-ray spectrometer with 6 mm<sup>2</sup> area, 500 micron thick [33] provides the energy resolution of  $\sim 220$  eV at 5.9 keV (<sup>55</sup>Fe X-ray source) when the detector is cooled to - 40°C for the pulse peaking time of 2.4  $\mu$ s. In case of larger area Si PIN detectors (25 mm<sup>2</sup>), the energy resolution is  $> 300$  eV [33] for the same detector thickness. Si PIN detectors provide good energy resolution relatively at low count rates ( $< 10^4$  counts/s) due to larger detector capacitance and are not generally suitable for high count rate applications.

These detectors are available in the form of standalone modules consisting of Si PIN chip, JFET which is part of first stage of charge readout amplifier to improve signal/noise ratio, and the Peltier cooler to cool the detector to lower operating temperatures. Front side of these detector modules are covered with 8/13/25 micron thick beryllium (Be) window to avoid any stray light falling on to the detector and also helps to maintain conditioned environment inside the module when the detector is cooled to lower temperatures. The 8 micron thick Be window reduces the detector efficiency to 30% for 1 keV X-ray photon. The schematic representation of one such module is shown in figure 2.25 and its spectral performance compared with CdTe having detector thickness of 1 mm is shown in figure 2.26.

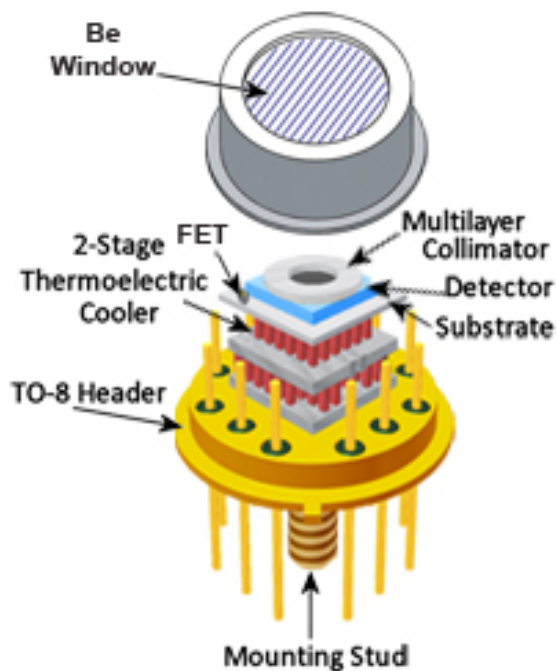


Fig. 2.25: Schematic representation of constituents of Si PIN detector module (Courtesy AMPTEK) [33].



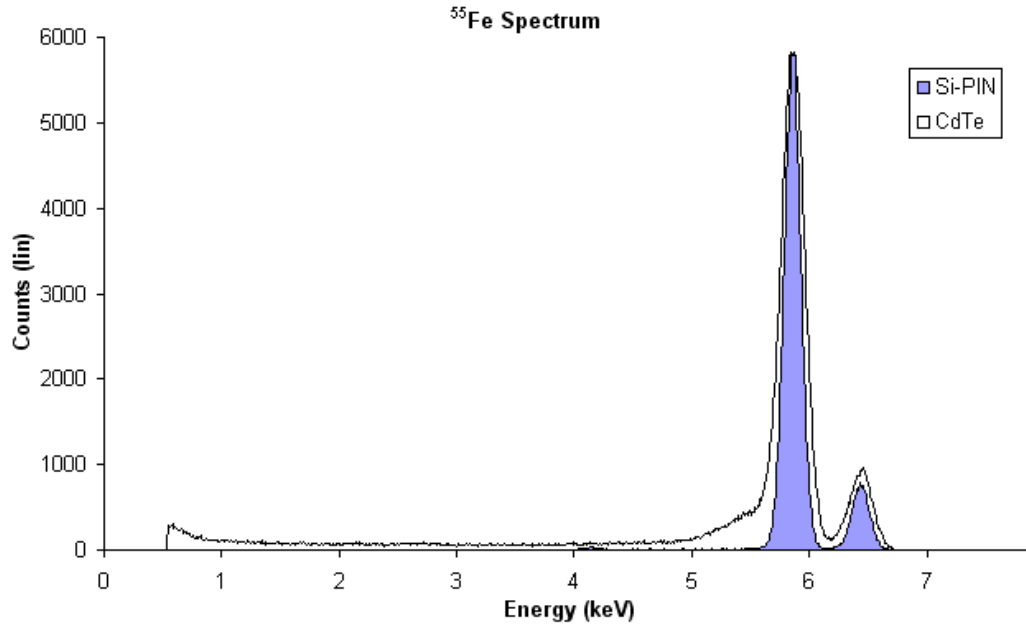


Fig. 2.26: A sample spectrum of Si PIN detector with 500 micron thick and compared with CdTe detector of 1mm thick (Courtesy AMPTEK) [34].

#### 2.4.9. Si (Li) Detectors:

The silicon detectors made with planar technology like Si PIN detector discussed in the earlier section has depletion depth  $< 1$  mm. To achieve the higher depletion depths of 1-5 mm, lithium drifting process in silicon is used. In lithium drifted silicon detector Si (Li), lithium ions acts as donors which are driven through a large volume of silicon crystal (p-type) to obtain an intrinsic like bulk material by means of the compensation of the donor and acceptor impurity concentrations. In a Si (Li) detector, the lithium continues to drift significantly at room temperature and therefore, in order to prevent the undesired redistribution of lithium, the detector must be kept always in the colder environment even when the detector is not used.

Si (Li) detectors provide good energy resolution of  $\sim 150$  eV at 5.9 keV when cooled to liquid nitrogen ( $\text{LN}_2$ ) temperature and this performance closely matches with germanium detector as reported in [35]. These detectors are available in various sizes ranging from  $10 \text{ mm}^2$  to  $80 \text{ mm}^2$  area and the detector thickness is available up to 5 mm.

Due to higher thickness, the efficiency improves at higher energies compared to Si PIN detectors and the efficiency curve for 3 & 5 mm Si (Li) detector is shown in figure 2.27.

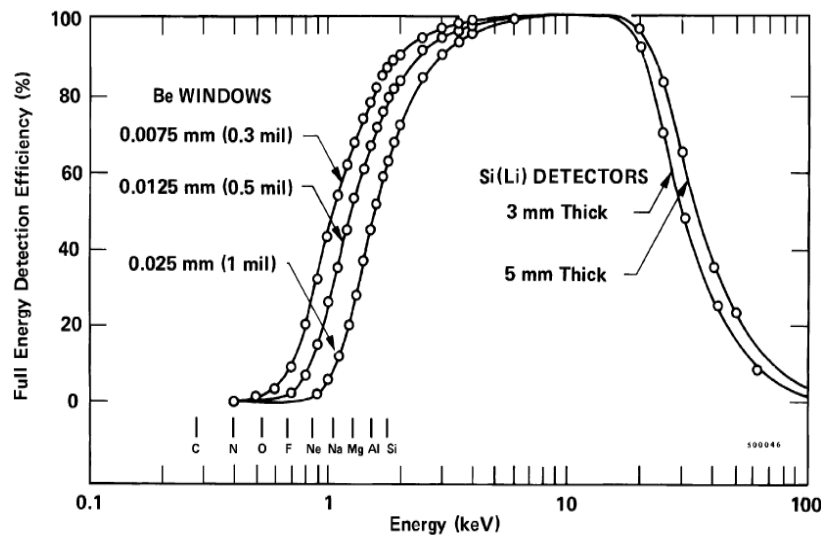


Fig. 2.27: Si (Li) detector efficiency for 3 and 5 mm thick detectors [35].

These detectors work in the energy range of few hundred eV to  $\sim 40$  keV with detection efficiency  $> 25\%$  at 40 keV.

#### 2.4.10. Silicon Strip Detectors (SSD):

Silicon Strip Detector is a type of position sensitive silicon detector obtained by segmenting larger detector into small sub detectors and each sub detectors are connected with individual readout electronics. The charge induced due to photon interaction will be detected in the multiple chains of readout electronics and thereby the position information can be obtained.

In early 1980's, G Lutz and J. Kemmer pioneered the development of silicon strip detectors. The radiation hardened silicon strip detectors were available from 1990's and subsequently, the technology transfer to industry took place for bulk production. The silicon strip detector can be created by patterning larger p-n junction of a PIN diode in to an array of long and narrow strip like structure forming individual p-n junctions as

shown in figure 2.28. The strips usually extend the full length of the sensor. The biasing of the strips is fed from a shared common power supply. When the reverse bias is applied to all the junctions together, individual depletion layers overlap and device behaves like large PIN diode with multiple readout electrodes. The width of the strip is in the order of few tens of microns and the pitch between the strips varies from  $\sim 50 \mu\text{m}$  up to several hundreds of microns [37, 38]. Strips in one side and planar contact on other side forms single sided strip detector (SSSD), which can provide 1D-position sensing capability.

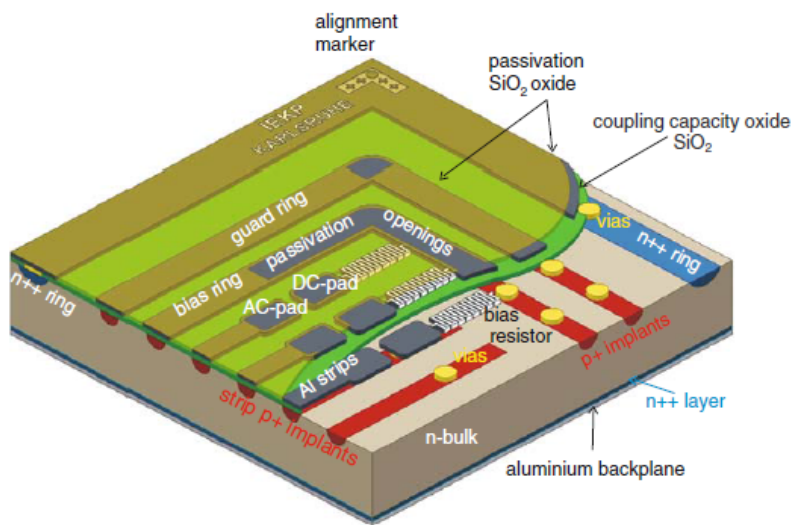


Fig. 2.28: Single side silicon strip detector used in the CMS experiment (3D-model) [36].

If the strip patterns are established on both the sides of the silicon sensor with crossed strips known as double sided silicon strip detector (DSSD). With the crossed pattern, by reading the signal charge due to both electrons and holes in the opposite electrodes, one can estimate the position accurately with 2D-position capability. The layout representation of 2D strip detector is shown in figure 2.29. SSD's are also widely used for tracking charged particles and there are SSD based systems available providing 2D position resolution as low as  $1\mu\text{m}$ . Currently, these detectors are available in wafer size of about 4-5 inches and combining many of such detectors will provide large area, essential for many scientific applications. Making such large size is possible due to simple electrode structures.

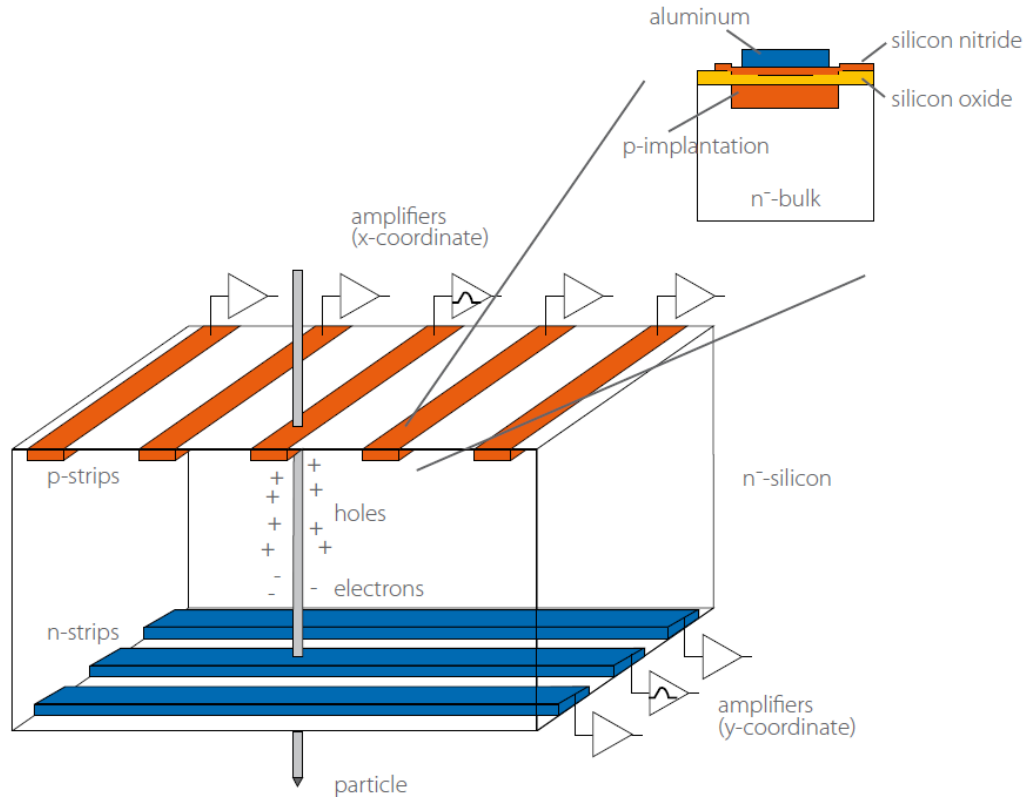


Fig. 2.29: Layout of double sided (2D) silicon strip detector [40].

Large number of these detectors are being used in ATLAS experiment at CERN [39] with silicon active area are  $> 150 \text{ m}^2$  and in CMS experiment of LHC [40] with active area of  $200 \text{ m}^2$ . Silicon strip detectors are also employed as gamma detector in space based Compton telescopes, GLAST with active area of  $\sim 80 \text{ m}^2$  [41]. Strip detectors are seldom used for spectroscopic applications due to larger capacitance of the charge collecting electrodes which results in poor energy resolution.

#### 2.4.11. Pixel Detectors:

In case of silicon strip detector, the detector will not be able to assign the position unambiguously if there are multiple events within the readout period. This drawback is due to the longer electrode structure. In such cases, pixel detectors have to be used. Instead of longer strips, segment the strips in both the sides, becomes pixel detectors.

This configuration increases 2D resolution and also provides better energy resolution due to smaller electrode capacitance. Such pixilated detector calls for large number of readout chains and hence the conventional discrete electronics based readout will be impractical. Hence, it is essential to have Application Specific Integrated Circuit (ASIC) based readout system for the pixilated detectors. There are two configurations widely used in pixel detectors

1. Hybrid active pixel sensor (HAPS)
2. Monolithic active pixel sensor (MAPS)

#### 2.4.11.1. Hybrid Active Pixel Sensors (HAPS):

In HAPS configuration, the pixilated detector and the ASICs are separately fabricated and bonded together. The interface between the detector and ASIC is done by means of bump bonds with low signal loss. The HAPS configuration is shown in figure 2.30. These detectors are available in varies sizes such as  $50 \times 450 \mu\text{m}^2$ ,  $50 \times 400 \mu\text{m}^2$  and  $100 \times 150 \mu\text{m}^2$  (is not the size of single pixel) with thickness up to  $250 \mu\text{m}$  with position resolution of  $\sim 10 \mu\text{m}$ .

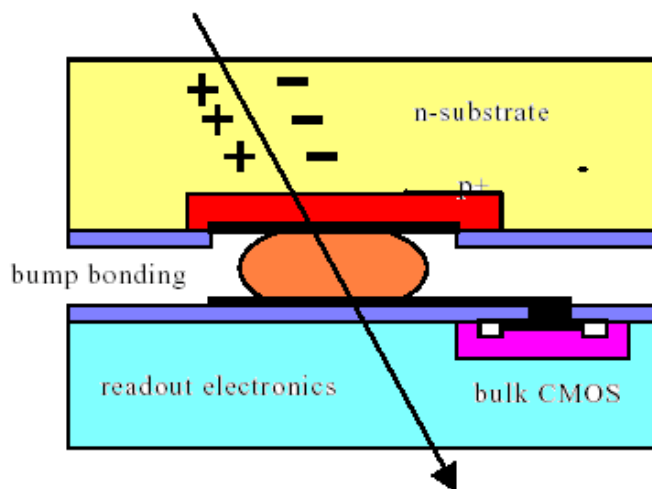


Fig. 2.30: Schematic representation of hybrid active pixel sensor [42].

#### 2.4.11.2. Monolithic Active Pixel Sensors (MAPS):

In this case, the pixilated detector and the ASICs are made on a common silicon substrate. One part of the silicon works as detector and other part is made of microelectronics for charge readout as shown in figure 2.31. Bonding material is not exclusively required in monolithic active pixel sensor. The thickness of these sensors typically varies from 50-75  $\mu\text{m}$  and the size of the pixel varies from 20-50  $\mu\text{m}$  with position resolution of  $\sim 1 \mu\text{m}$  [43, 44].

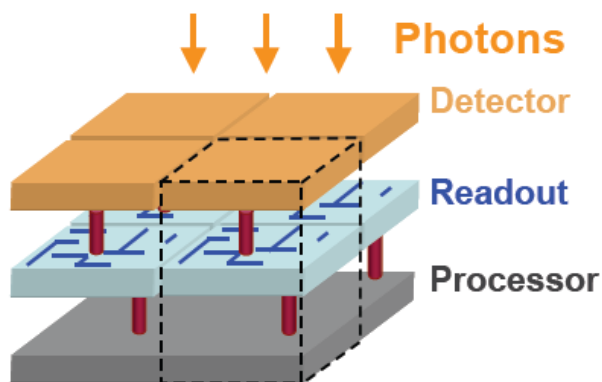


Fig. 2.31: Schematic representation of monolithic active pixel sensor [43, 44].

#### 2.4.11.3. DEPFET Pixel Detector:

Fully depleted field effect transistor (DEPFET) pixel detector is also a type of monolithic pixel detector wherein only front-end amplifying FET transistor is placed along with the fully depleted bulk and subsequent signal processing is carried out external to the detector chip [45]. The schematic representation of the DEPFET pixel detector is shown in figure 2.32.

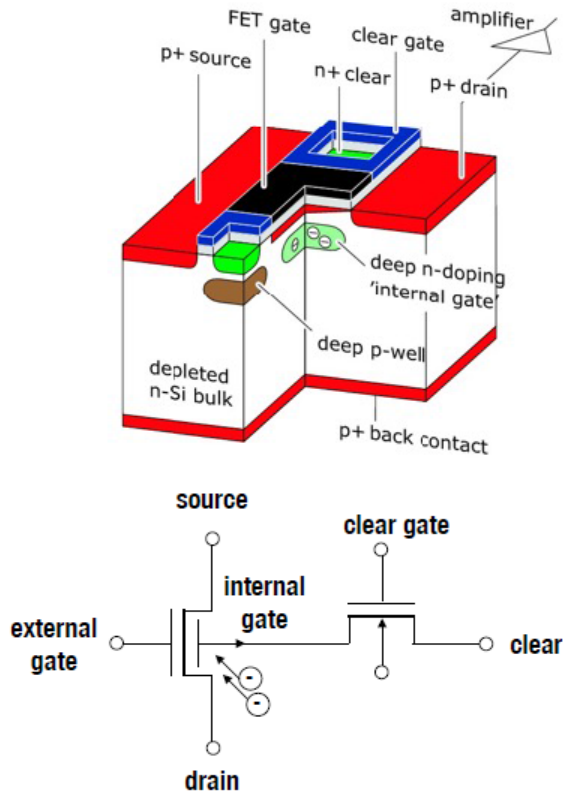


Fig. 2.32: Schematic representation of monolithic DEPFET pixel detector [45].

Some of the scientific experiments (ATLAS and ALICE) which use hybrid pixilated silicon sensors are shown in figure 2.33 and 2.34.

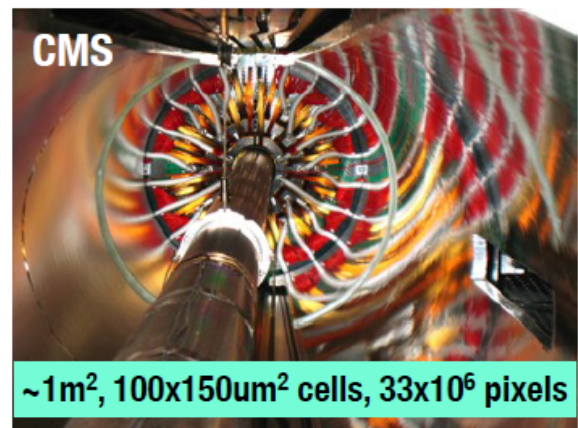
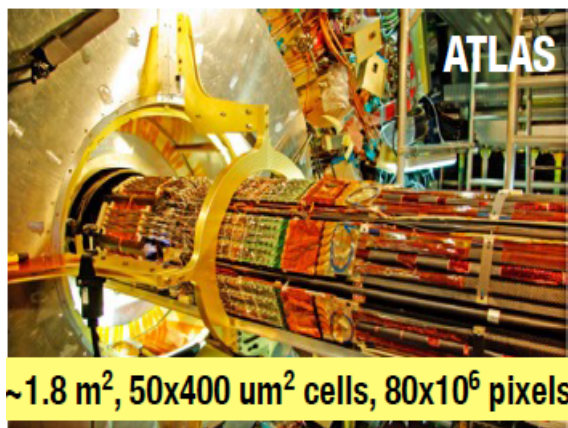


Fig. 2.33: ATLAS experiment (left) [46] and CMS experiment (right) with hybrid Si pixilated detectors [47]

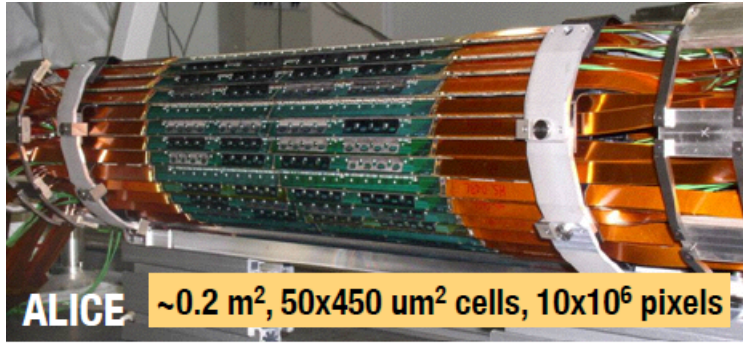


Fig. 2.34: ALICE experiment with hybrid Si pixilated detectors [48].

#### 2.4.12. Fully Depleted p-n CCD:

The concept of charge coupled device (CCD) was originally introduced as a imaging device in video cameras. The principle of operation is based on the storage and transport of charge. Subsequently, the modified version of the CCD was proposed for detecting radiation in the form of fully depleted CCDs [49, 50] with on-chip FET [51]. The basic schematic representation of fully depleted p-n CCD is shown in figure 2.35.

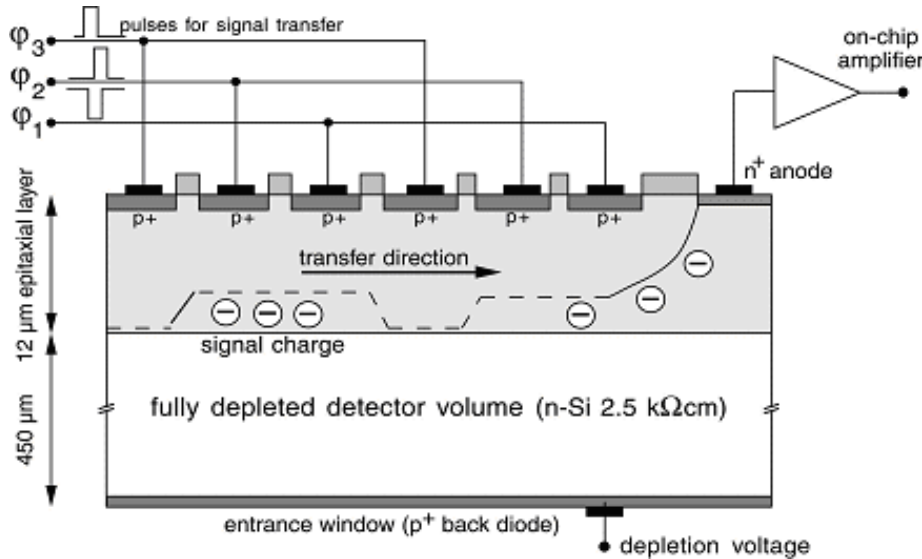


Fig. 2.35: Schematic representation of p-n CCD cut through view (courtesy PN Sensor) [52].

The concept of fully depleted p-n CCD is based on the principle of sideward depletion of high resistivity silicon which was proposed for silicon drift detectors in 1983 and 1984. In the following years, the basic concept was modified and designed to form



p-n CCDs [52]. It is built on a high ohmic n-type silicon bulk as that of other silicon detector with a n-type epitaxial layer and a matrix of  $p+n$  strips and perpendicular  $p+$  implants on the upper surface. When X-ray photon strikes, the electrons are drifted towards potential minimum wells under the  $p+$  contacts called transfer registers (figure 2.36).

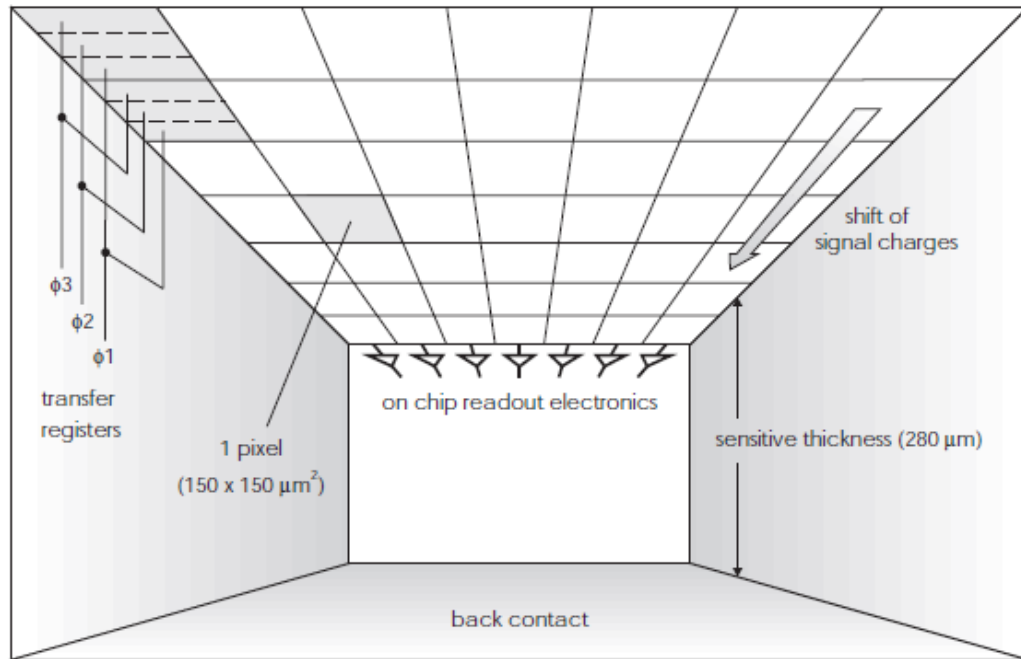


Fig. 2.36: Inside view of p-n CCD indicating charge transfer direction to the readout electronics [53].

The holes are absorbed by the back contact. The electrons in the potential well are then transferred to the readout electrode by changing the biasing conditions of the transfer registers. In this configuration, the charge readout speed is increased as the single phase sequencing is sufficient to transfer the charge to the neighboring register and this is achieved by means of structuring the potential minima for electrons at three different depths in the n-type epitaxial layer. The major advantage of this configuration is that the detector efficiency improves greatly by operating in fully depleted mode compared to MOS CCDs of same thickness. The fully depleted region of the silicon bulk makes it attractive to use in the X-ray spectroscopy. P-n CCDs are generally used for X-

ray imaging as it has the limitation of using in photon counting mode at high count rates due to sequential readout. In X-ray imaging, the position resolution is very important and this is mainly determined by the strip spacing which is of the order few tens of microns. The charge spread during the charge integration and transfer is made negligible in the fully depleted p-n CCDs.

Though the functional p-n CCDs were available in 1993, the first large area and large depletion p-n CCD was made at Max Planck Institute for extraterrestrial physics together with semiconductor laboratory involving PN Sensor. The fabricated sensitive area was  $6 \times 6 \text{ cm}^2$  with pixel size of  $150 \mu\text{m} \times 150 \mu\text{m}$  having depletion thickness of  $300 \mu\text{m}$ . This device provided unprecedented quantum efficiency in the energy range of 100 eV to 15 keV. This sensor was successfully flown in XMM-Newton satellite missions [54] and the photographic view of the same is shown in figure 2.37.

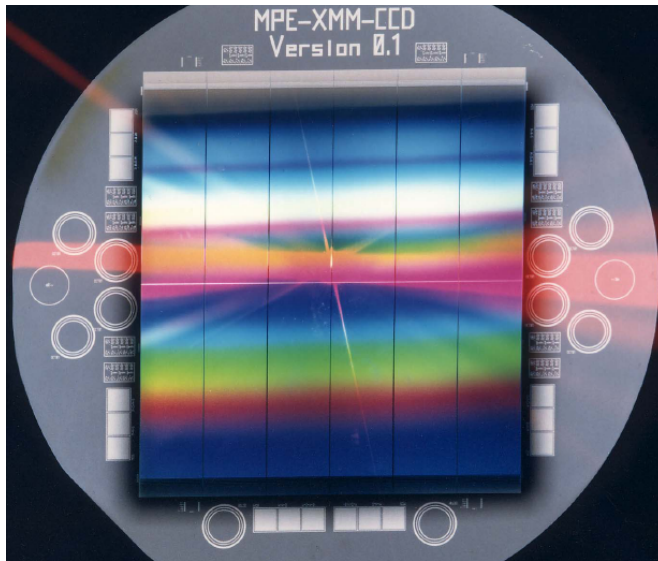


Fig. 2.37: The photographic view of p-n CCD built with sensitive area of  $6 \times 6 \text{ cm}^2$ , flown in XMM-Newton satellite missions [52, 54].

In recent years, p-n CCD are available in multiple pixel sizes from  $36 \mu\text{m} \times 36 \mu\text{m}$  up to  $150 \mu\text{m} \times 150 \mu\text{m}$ , depletion depth up to  $450 \mu\text{m}$  and the active area reaching from  $1 \text{ cm}^3$  to  $3 \text{ cm}^3$ .

### **2.4.13. Silicon Drift Detector (SDD):**

Silicon Drift Detector is a new technology Si detector which provides energy resolution better than exiting Si detector technologies. Though the SDD was invented in 1984, the first working SDD was fabricated in late 1990's and vast improvements have been made in last two decades in terms of detector configurations and readout techniques. These detectors are shown to provide energy resolution of  $\sim 125$  eV at 5.9 keV which is close to the Fano limit, the theoretical limit of spectral energy resolution. The concept, types and advancements in SDD and their use in the space missions are discussed in chapter-3.

### **2.5. SUMMARY:**

In this chapter, the working principle and various subsystems involved in the X-ray spectrometer are discussed. This chapter also describes various detectors and technologies adapted over past several decades in X-ray studies, their working principle, charge formation and readout techniques. The suitability of these detectors for the desired energy range is described by comparing their performances and also giving their merits and demerits. Detailed discussion on the photon interaction mechanisms on the silicon detectors, bandgap and its temperature dependence, charge carrier formation and its variance (Fano factor), detector efficiency, charge collection, energy resolution and its dependence on Fano factor/noise from the readout electronics are described. The advancement in the silicon detector technology allows us to develop the X-ray spectrometer instruments with energy resolution close the Fano limit. The use of silicon detectors in various applications (both ground and space based) is also described.

## **Chapter 3:**

### **REVIEW OF SILICON DRIFT DETECTOR AND THIER USE IN SPACE APPLICATIONS**

#### **3.1. INTRODUCTION:**

Silicon Drift Detector (SDD) is a new technology silicon photo detector with unique electrode structure and offers low detector capacitance compared to planar Si PIN detector of same area. This yields low noise even at shorter shaping times and hence, SDDs can be used at much higher count rates with desired energy resolution. The concept of SDD was introduced in 1984 by Gatti and Rehak who presented the concept and the experimental results [55]. The concept was based on the sideward depletion. SDD was initially proposed for position measurement and considered as a replacement for gas chambers in the form of solid state device. In his work, it was observed that detector capacitance is independent of detector area. In 1985, Rehak and Gatti [56] have shown the use of SDDs for energy measurements rather than position measurement with SDD in circular form. In these SDDs, the drift electrodes are made on both the sides to form the radial electric filed. The planar electrode concept in SDD was introduced in 1987 by Kemmer [57] with planar contact on one side and drift electrodes on the opposite side. As discussed in the earlier chapter, the fabrications of planar contacts are easier to manufacture. This technique also provides very thin dead layer in the entrance window where only X-ray photons are allowed to enter in to the detector, which is

important for X-ray spectroscopy. The first good quality SDD for laboratory application was produced in 1995 for EDS and XRF measurements [58]. In the last two decades, SDDs are being optimized to achieve very good spectral energy resolution in various types and sizes [45, 59-61]. Significant research work has been carried out in the SDD readout techniques [51, 62-64] aiming at improving the energy resolution by reducing the contribution of electronics noise. In recent times, it is shown that SDDs with advanced readout electronics can provide energy resolution close to Fano limit.

### 3.2. WORKING PRINCIPLE OF SDD:

In the conventional PIN photo detector, the ohmic  $n+$  contact extends to the full area of the silicon bulk on one side and the potential distribution is shown in figure 3.1a. In figure 3.1b,  $n+$  contact introduced with  $p+$  electrodes on both the sides to achieve the depletion of the bulk and when the bias at  $n+$  contact is increased, creating a potential minimum at the centre of the bulk with small undepleted zone near the  $n+$  region as shown in figure 3.1c.

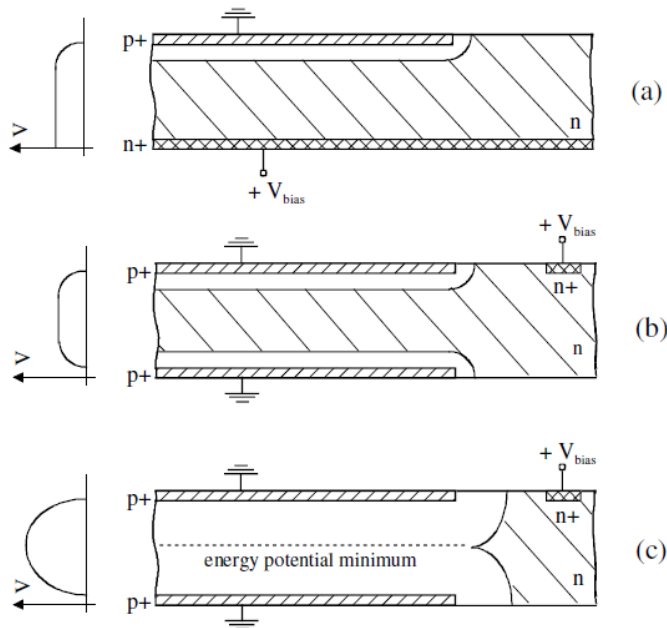


Fig. 3.1: Schematic representation of sidewall depletion concept [55].

The working principle of SDD is understood from the sideward depletion concept. In case of SDD, an additional electric potential is applied on both sides to force the electrons to drift towards the  $n^+$  electrode for the signal readout as shown in figure 3.2. This is achieved by implanting  $p^+$  electrode array on both the sides. These electrodes are suitably biased such that an electric field line is created as shown in figure 3.3.

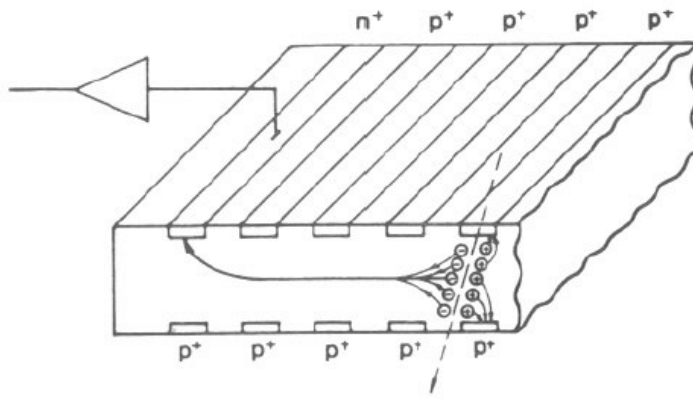


Fig. 3.2: Schematic representation of working principle of SDD [55].

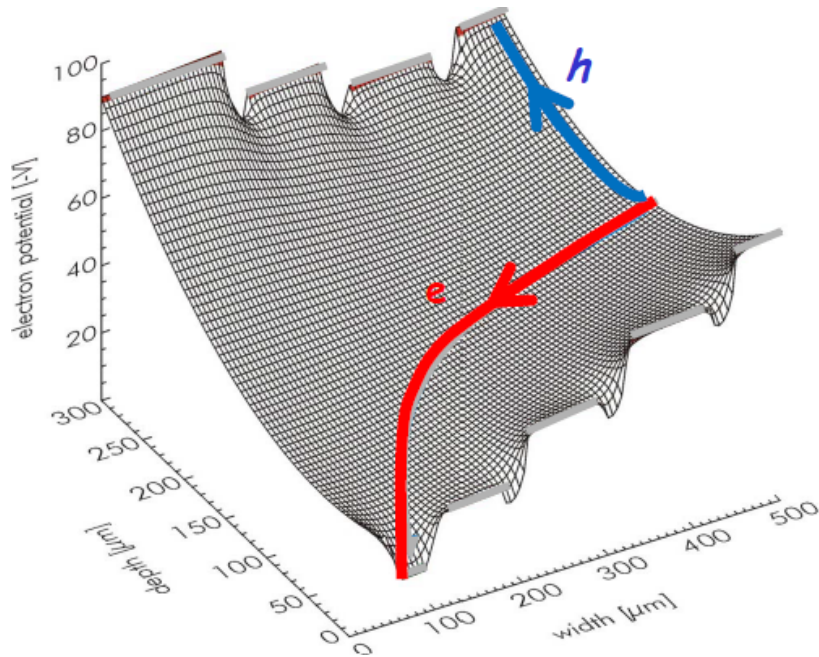


Fig. 3.3: The electron guiding potential distribution in the drift region of the SDD pointing towards the anode [55].

When a photon interacts in the active volume of the detector, the electrons are guided towards the anode and the holes are collected by the nearest  $p+$  electrodes as the  $p+$  electrodes are applied with negative bias. The region close to the collecting anode, the bottom of the potential channel is shifted towards the surface where the anode is present by suitably biasing the opposite electrodes. The electron cloud gives an electric pulse in the anode and the drift time of the electron cloud along with the signal due to holes can be used to derive the measure of the position of the photon interaction [56]. The signal due to electron charge will give the energy of the photon. The important finding of this sideward depletion concept is that the detector capacitance is the anode capacitance whose value is independent of the detector area. The anode capacitance is of the order of few hundred fempto farad. The low detector capacitance provides low noise at lower shaping times and thereby the system can be used for high count rate applications.

### **3.3. SDD FOR X-RAY MEASUREMENTS:**

SDDs are ideally suited for X-ray spectrometry due to its low detector capacitance along with the low noise readout system enables to achieve the energy resolution close to the Fano limit. In the sideward depletion SDD concept, the areas between the  $p+$  strips on the surface are covered with  $SiO_2$  layer. There is fixed positive charges in the  $SiO_2$  layer causing the potential distribution downward from the detector surface creating potential minima. These sites could collect the signal electrons generated during the photon interaction, in the low energy range  $< 5$  keV [65]. To overcome this limitation at lower X-ray energies, a suitable design topology has been implemented with a thin continuous entrance window without oxide layer gaps [57]. Also, the point anode is kept in the centre forming a circular detector that minimizes any

signal loss due to the travel length of the signal electrons. The circular SDD optimized for energy measurement is shown in figure 3.4.

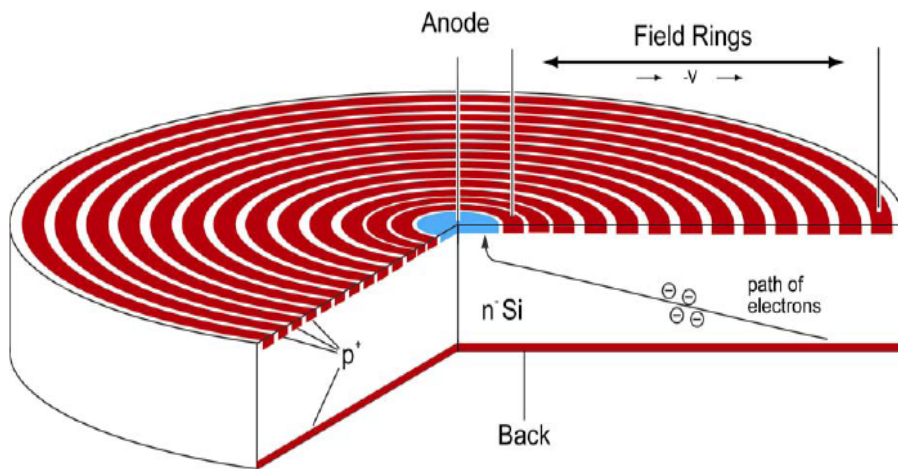


Fig. 3.4: Schematic representation of a circular SDD with anode at the center (courtesy KETEK, GmbH) [66].

Circular SDDs have concentric rings around the point anode, which are applied with progressively higher reverse bias voltages, which guide the photoelectrons into a "point" anode. The drift field with respect to the point anode at the centre is shown in figure 3.5.

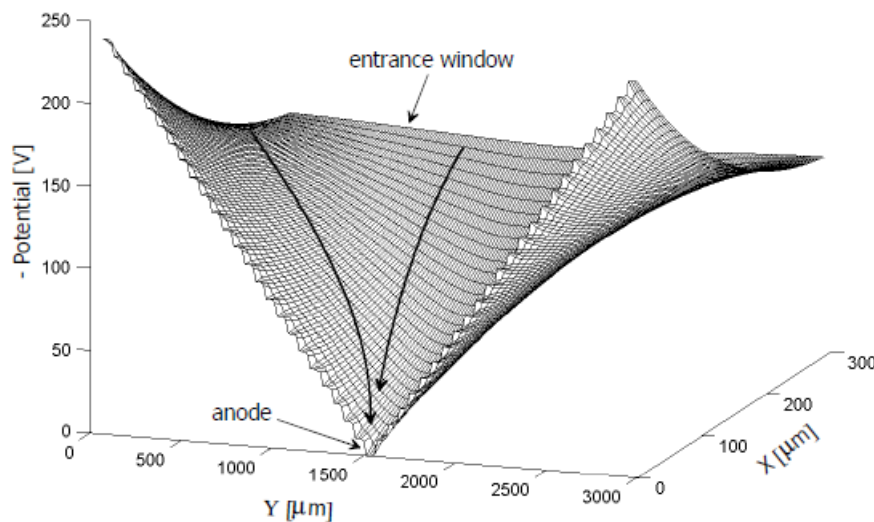


Fig. 3.5: The possible electron path (field line) inside the SDD with 300 micron thickness [66].



The bias voltage required for the successive  $p+$  electrodes are derived from a single high voltage applied at the outer electrode by using resistive divider which is part of the SDD chip. The inner ring close to the anode and the back contacts are applied with separate bias voltages. The capacitance of the point anode is  $\sim 200$  fF. The  $p+$  back contact acts as entrance window for the radiation to be detected is made of a shallow  $p+$  implantation with thickness of the order of few tens of nano meters [67] which allows to achieve the low energy threshold of few hundred eV. The quantum efficiency of such SDD with few tens of nm of dead layer for 450 and 900 micron thick detector is reported in [68]. It is shown that the quantum efficiency of  $> 40\%$  could be achieved for incident energies more than 200 eV as shown in figure 3.6.

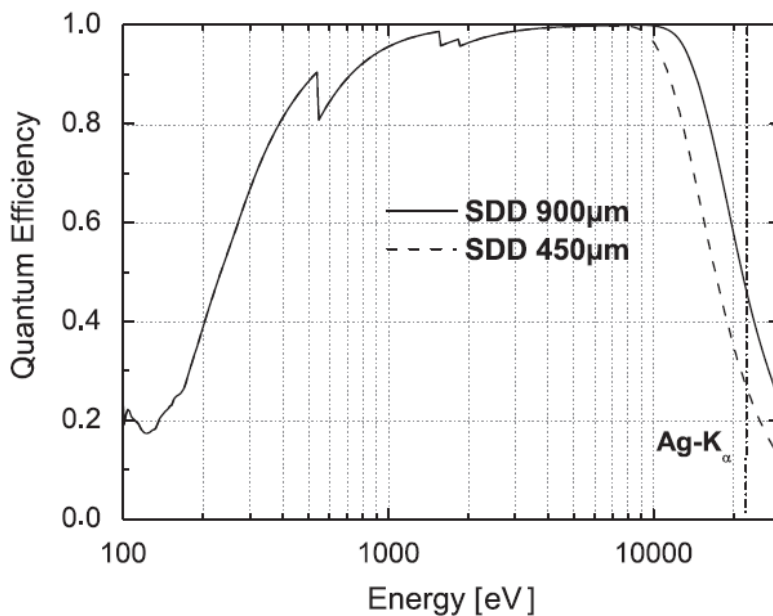


Fig. 3.6: Quantum efficiency of a 450 and 900 micron thick SDDs with thin dead layer [68].

### 3.4. TYPES OF SDD CONFIGURATIONS:

#### 3.4.1. SDD with Discrete External FET:

The major advantage of SDD over Si (Li) detector or Si PIN detector is the possibility to realize an X-ray spectrometer with energy resolution of  $\sim 150$  eV at 5.9

keV for higher count rates with moderate operating temperatures of  $\sim -40^{\circ}\text{C}$ . Such operating temperature can be achieved using Peltier coolers. Generally, a low noise field effect transistor (FET) is used in the first stage of the charge readout system to minimize the capacitance of the readout electronics to exploit the low anode capacitance of the SDD to achieve the good energy resolution. Initially, SDD modules were made available with a discrete FET mounted close to the point anode to reduce the total input and stray capacitance contribution due to the wires connected between the anode and the charge readout system as shown in figure 3.7.

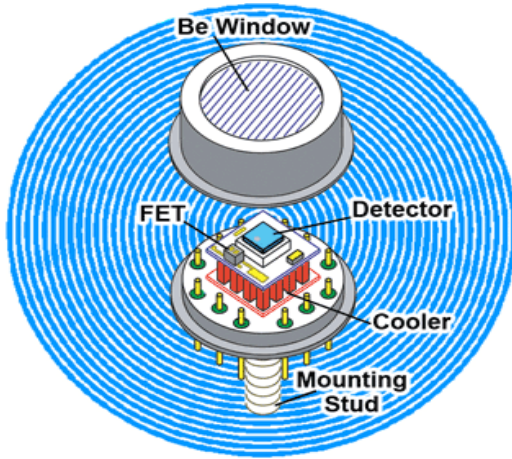


Fig. 3.7: Schematic representation of discrete FET mounted near to the SDD chip (Courtesy to AMPTEK, USA) [69].

Initial version of such detectors was shown to provide the energy resolution of  $\sim 180$  eV at 5.9 keV [70]. In recent years, with the improvement in the detector fabrication technologies and also in the readout systems, energy resolution of  $\sim 130$  eV @ 5.9 keV has been achieved [71].

### 3.4.2. SDDs with On-chip FET:

The concept of implementation of readout electronics part of silicon was introduced in 1993 by Pinnoti for p-n CCDs. Since then, implementation of FET on-chip

is being used in most of the devices and applications. The main advantage of implementing FET on a SDD chip further reduces the input and stray capacitances between the anode and the charge readout system [51, 72-74]. The schematic representation of SDD with on-chip FET is shown in figure 3.8.

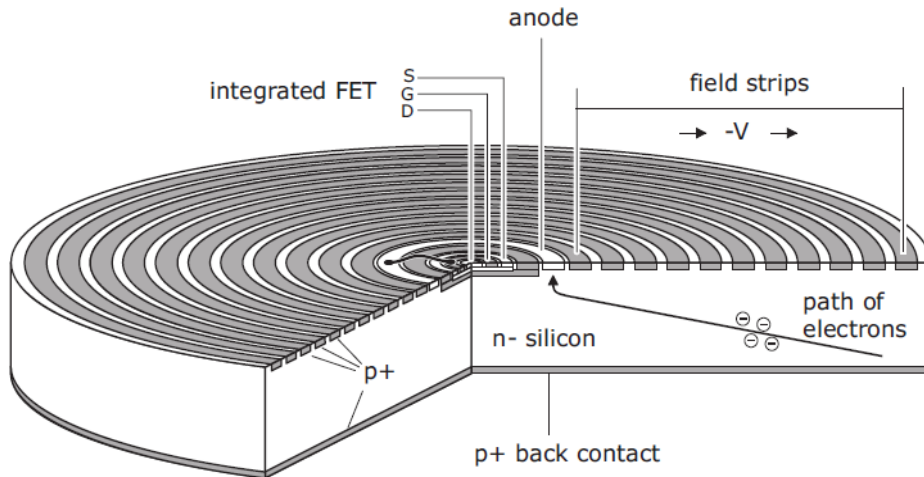


Fig. 3.8: Schematic of a circular SDD with on-chip JFET [59].

As the FET is made on the silicon substrate, the capacitance matching between the SDD and FET ( $C_{det} = C_{FET}$ ) can be achieved easily and this also greatly reduces the micro phonic, cross talk and electric pickup noises which could happen in case of discrete FET based or external readout systems. The FET transistor is n-channel JFET which is designed to be operated on a fully depleted silicon bulk placed inside the ring type anode, against point anode as discussed earlier. A narrow metal strip connects the JFET gate with SDD anode. A circular  $p$  implantation, biased through a guard ring divides the JFET region with SDD. The gate of the JFET collects the charge carriers from the anode via a metal strip as shown in figure 3.9. The discharge of the anode will be carried out using reset diode. The concept of discharge mechanism and the use of reset diode is discussed in chapter-4. SDDs with on-chip FET can be operated either in source-follower [75] or charge sensitive pre-amplifier modes [76, 77] with internal self adapting discharge mechanism [76] (which does not require external reset circuit) or

pulse reset technique with external reset circuit [78, 79]. These reset techniques are also discussed in detail in chapter-4.

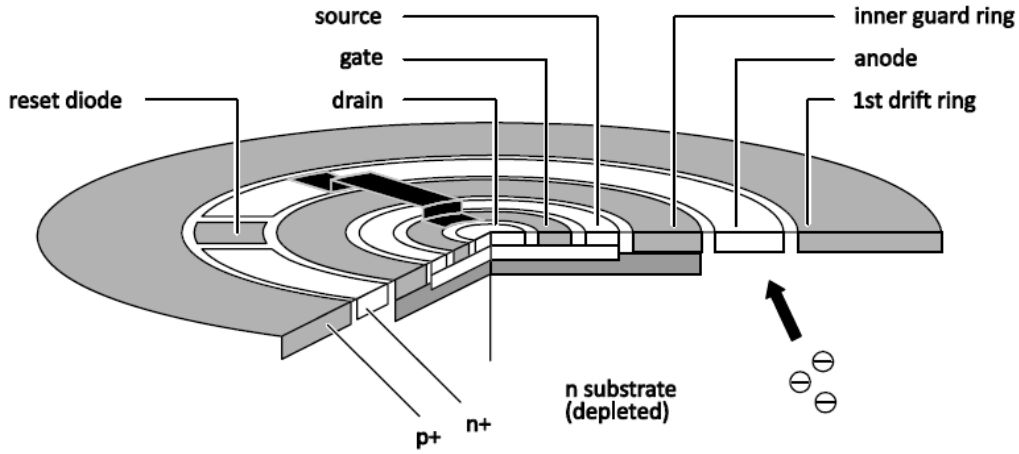


Fig. 3.9: Section of the SDD layout where readout transistor is interfaced with the charge collecting anode [51].

The X-ray spectrometers with such SDDs are shown to provide the energy resolution of  $\sim 130$  eV at 5.9 keV for the detector area of  $10 \text{ mm}^2$  with 450 micron thick silicon, by cooling the detector to  $\sim -20^\circ\text{C}$  [80] as shown in figure 3.10.

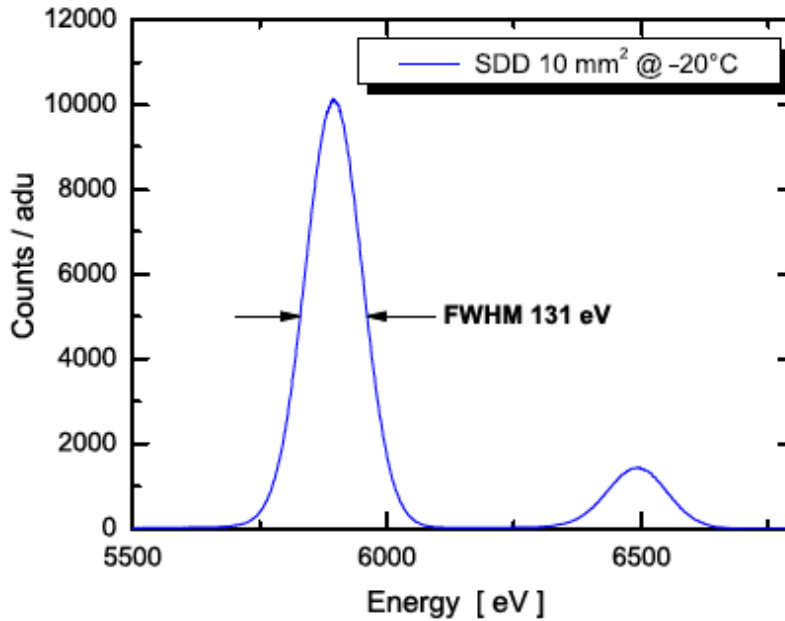


Fig. 3.10: Spectrum measured using  $10 \text{ mm}^2$  area, 450 micron thick SDD with on-chip FET by cooling the detector to  $-20^\circ\text{C}$  (courtesy PN Sensor) [80].

It is also shown that the same energy resolution is maintained for the count rates up to  $\sim 10^5$  counts/s as shown in figure 3.11. This is possible due to the small detector capacitance and low noise readout electronics.

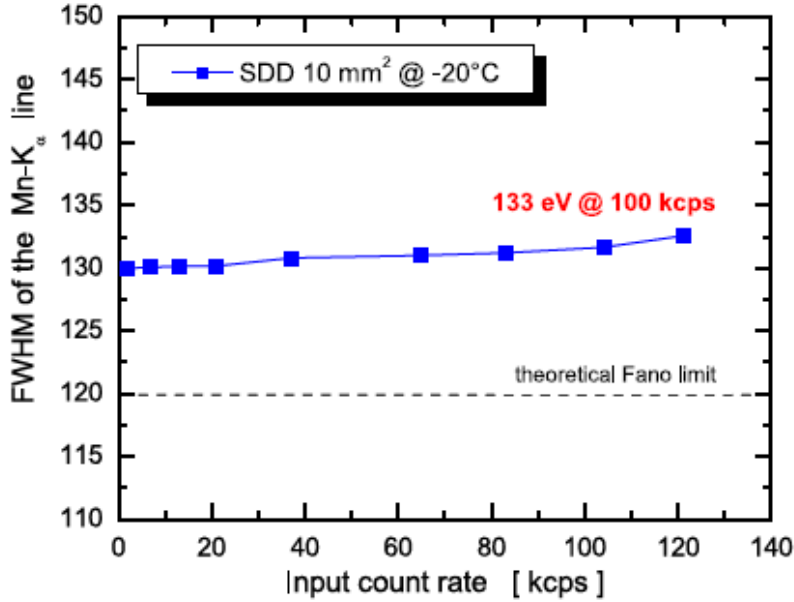


Fig. 3.11: Spectral energy resolution measured for various incident photon rates up to  $1.2 \times 10^5$  counts/s [80].

### 3.4.3. SDDs with ASIC Readout:

In the recent years, instead of using discrete or integrated on-chip FET, researchers have developed Application Specific Integrated Circuit (ASIC) based readout electronics named CUBE containing full charge readout amplifier [81]. The CUBE ASIC is mounted close to the SDD chip. The schematic representation of the SDD with CUBE ASIC is shown in figure 3.12. The CUBE ASIC is designed with physical size of  $< 1 \text{ mm} \times 1 \text{ mm}$  consuming  $< 6 \text{ mW}$  power. Using this ASIC, it is shown that the SDD with  $10 \text{ mm}^2$  area provides energy resolution of  $\sim 125 \text{ eV}$  at  $5.9 \text{ keV}$  when the SDD is cooled to  $-40^\circ\text{C}$  as shown in figure 3.13.

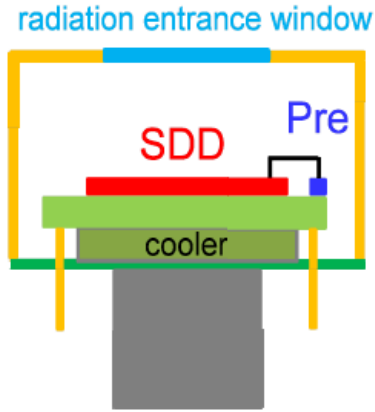


Fig. 3.12: Schematic view of CUBE ASIC mounted close to the SDD chip (Pre is the CUBE) [81].

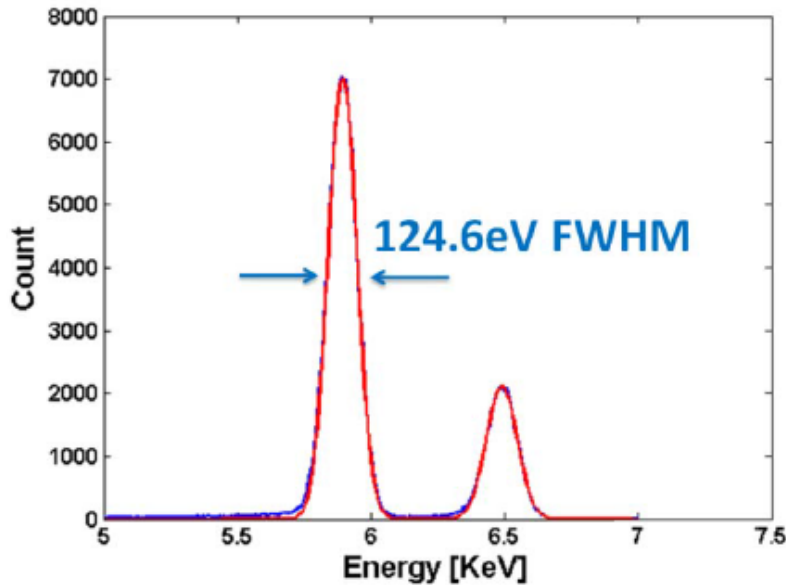


Fig. 3.13: Spectrum obtained with CUBE ASIC for  $^{55}\text{Fe}$  X-ray source, pulse peaking time of  $1.5\ \mu\text{s}$  [81].

#### 3.4.4. Silicon Drift Detector Droplet ( $\text{SD}^3$ ):

The Silicon Drift Detector Droplet ( $\text{SD}^3$ ) is a modern SDD design wherein the on-chip FET is fabricated on the edge of the silicon bulk and hence the charge readout anode is offset close to the FET [63, 82]. This configuration is often referred as "tear drop" or "droplet" SDD as shown in figure 3.14.

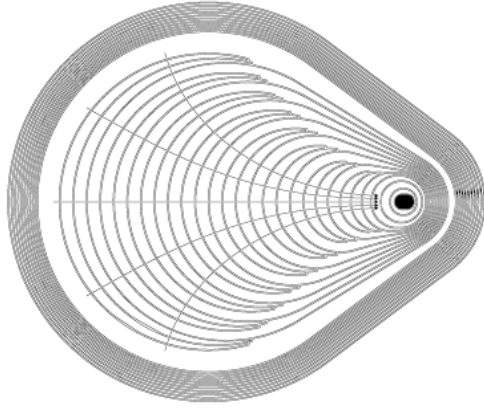


Fig. 3.14: Schematic design of Silicon Drift Detector Droplet ( $SD^3$ ). The black region is the on-chip FET placed at the edge of the device which can shielded from the radiation [63].

In this detector concept, the charge carriers are guided towards the point anode by applying suitable electric field to the bow-shaped electrodes.  $SD^3$  architecture has two main advantages compared to that of circular SDDs. When the FET is integrated at the center of the SDD, FET is susceptible to radiation damage and also the X-ray interactions close the FET site will result in partial loss of the signal electrons and hence increase in the background contribution to the resultant spectrum. Additionally, the electrostatic field around the centre FET resulting in the performance degradation. By moving the FET outside the active area, one can easily protect it from the radiation by means of collimator and additional shielding. This configuration improves the peak/background ratio (3000 to 5000) with collimator (dia. 2 mm) by eliminating the partial events that occur close to the centre FET.

The  $SD^3$  configuration also offers the designer to design the readout anode with different shape and size as the direction of the charge carriers are known. This results in further reduction of total input capacitance seen by the readout electronics and the reduction in capacitance is found to be  $\sim 120$  fF from  $\sim 200$  fF [83]. The measured energy resolution is  $\sim 128$  eV at 5.9 keV for  $5 \text{ mm}^2$  area  $SD^3$  when the detector is cooled to  $-10^\circ\text{C}$  as shown in figure 3.15.

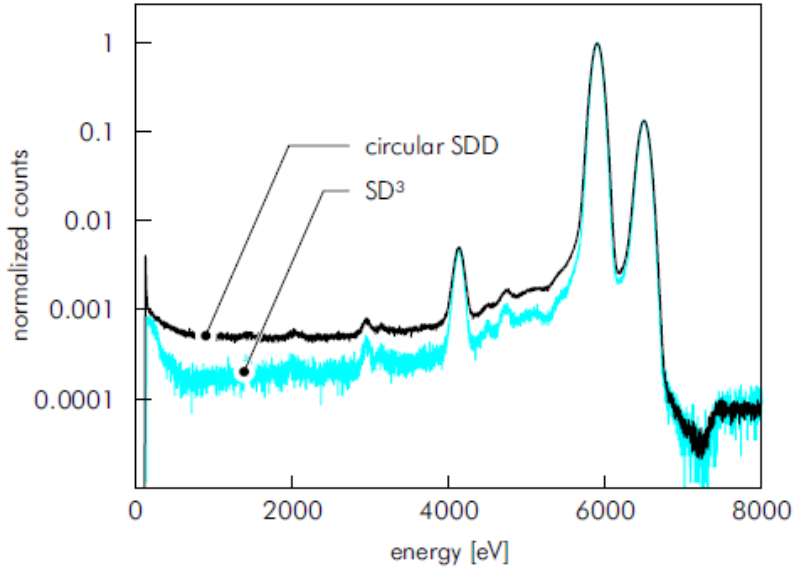


Fig. 3.15: Comparison of spectra obtained from a circular SDD and  $SD^3$  with  $5 \text{ mm}^2$  area [83].

The disadvantage of this detector concept is that the path length of the charge carrier doubles when compared to that of center readout anode and this constraints making a large area detector using this concept. In recent times, the energy resolution of  $\sim 125 \text{ eV}$  has been reported using Application Specific Integrated Circuit (ASIC) based readout system even with circular SDDs [84].

### 3.4.5. Large Area and Multi Element SDDs:

Single element large area SDDs are now available with active area up to  $150 \text{ mm}^2$  [33] from KETEK, GmbH. These detectors provide energy resolution of  $\sim 135 \text{ eV}$  at  $5.9 \text{ keV}$  when cooled to  $\sim -40^\circ\text{C}$ . The internal photographic view of large area SDDs from KETEK, GmbH [85] and PN Sensor, GmbH [86] is shown in figure 3.16. For large area based spectrometer applications, multiple numbers of individual SDDs are combined in a particular fashion with minimal dead area between them to achieve the desired total active area [87-91] as shown in figure 3.17.



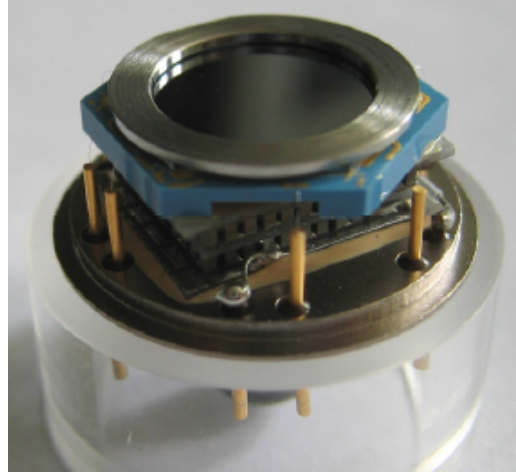
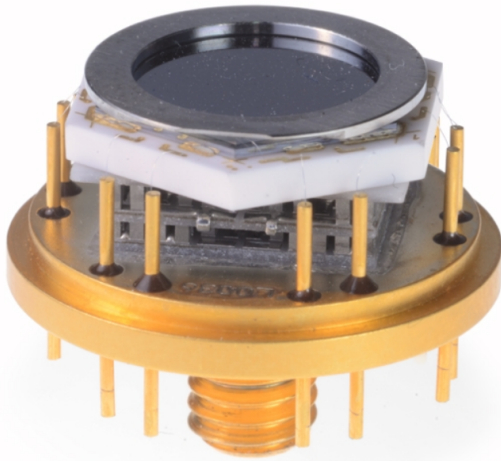


Fig. 3.16: Photographic view of large area SDDs, 100 / 150 mm<sup>2</sup> area on the same foot print from KETEK, GmbH (left), 100 mm<sup>2</sup> area from PN Sensor (right) (Courtesy KETEK GmbH and Courtesy PN Sensor, GmbH).

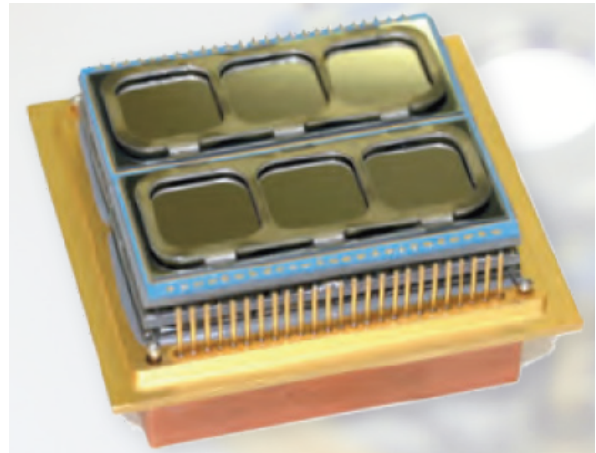
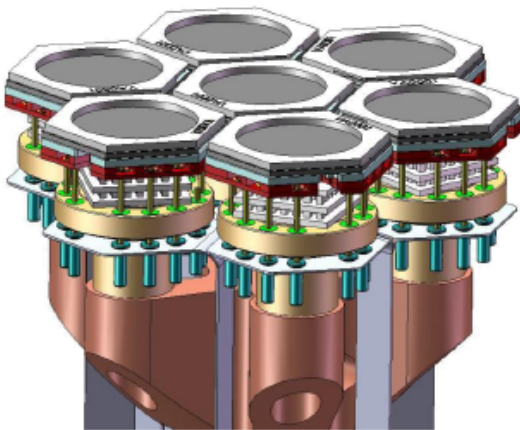


Fig. 3.17: Photographic view of multiple element large area SDD assemblies from KETEK (left) [87] and PN Sensor (right) [88] (Courtesy KETEK GmbH and Courtesy PN Sensor, GmbH).

Combining multiple detectors will be constrained by the type of readout electronics as it is necessary to have readout electronics placed close to the detector to achieve the best possible energy resolution. It is also essential to have suitable heat sink to keep the detectors at the desired temperature during the operation, especially when the large numbers of SDDs are put together.

### 3.5. SDD MODULES:

SDDs are generally made in the form of modules accommodating bare SDD chip with Peltier cooler enclosed using a very thin beryllium (Be) window. The whole assembly is fitted in TO-8 package with necessary electrical connections which are made available in the form of pins. This makes it easy to handle and develop the SDD based instruments. The package also incorporates either first stage of the charge readout amplifier (JFET) or CSPA itself in the form of ASIC and other devices such as reset diode (diode in the form die mounted inside the module or part of the SDD chip layout), temperature monitor (thermistor or diode) etc. The Be window acts as entrance window for X-rays and also protects the SDD chip from dust and stray light. Such packaging also enables to maintain the desired environment inside the module to achieve the desired operating temperature. In early days, people have used dry nitrogen filling inside the module and in recent times, the cooling efficiency of the Peltier is improved by means of high vacuum sealing inside the SDD modules. The low energy detection threshold for such a SDD module is determined by the thickness of the Be window placed in front of the detector. For small area SDDs, Be window thickness could be as low as 8 micron thick and it varies from 12 - 25 microns for large area SDDs. The transmission efficiency of various thicknesses of Be window is shown in figure 3.18. The 8  $\mu\text{m}$  thick Be window gives transmission efficiency of  $\sim 40\%$  at 1 keV and  $< 10\%$  for 25  $\mu\text{m}$  thick Be window. An alternate window made of thin polymer (AP3.3) is available in recent times which provide good transmission efficiency at lower energies. A comparison of AP3.3 polymer with 8  $\mu\text{m}$  thick Be is shown in figure 3.19. The thin polymer AP3.3 provides  $\sim 60\%$  transmission efficiency at 0.5 keV and can go down to  $< 0.2$  keV with  $> 20\%$ . The polymer provides  $\sim 90\%$  transmission efficiency at 1 keV. The efficiency at higher X-ray energies depends on the detector thickness.

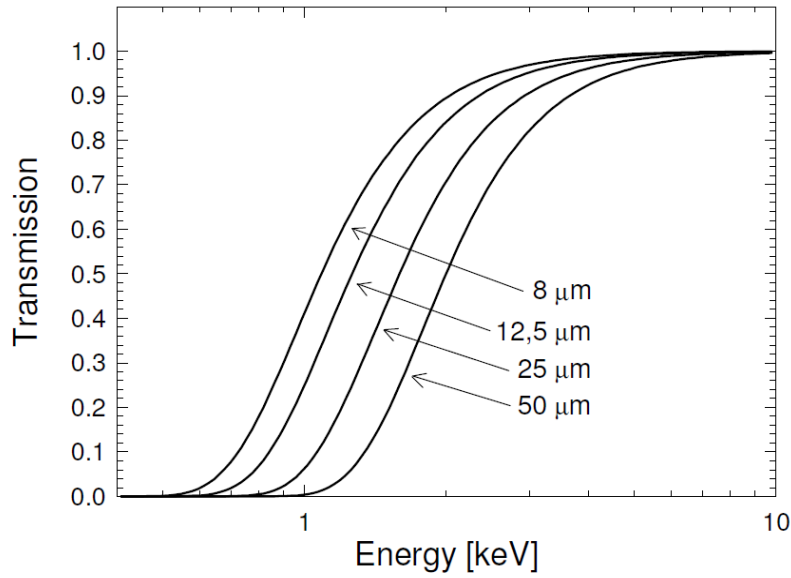


Fig. 3.18: Transmission efficiency of low energy X-rays through various thicknesses of Be windows [30].

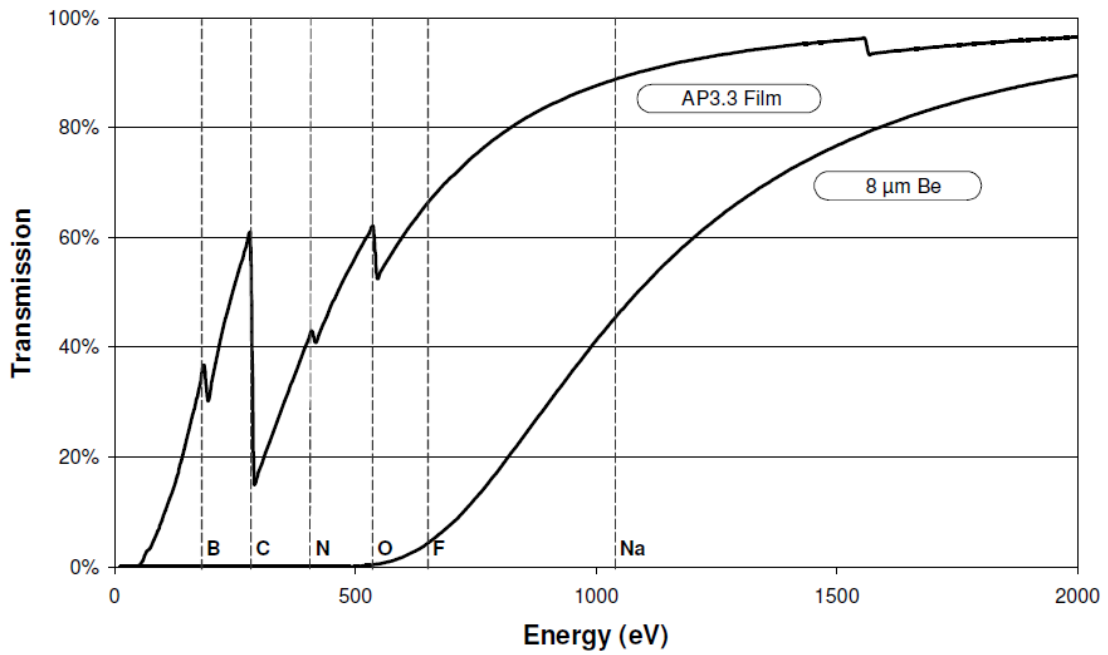


Fig. 3.19: Transmission efficiency of low energy X-rays through thin polymer (AP3.3) window in comparison with 8 micron thick Be window (Courtesy to MOXTEK Inc).

Comparison of various characteristics of SDD with other silicon detectors is given in table-3.1.

**Table-3.1:** Comparison of SDD with other Silicon detectors.

	<b>Si (Li)</b>	<b>Si PIN</b>	<b>SDD</b>
<b>FWHM @ 5.9 keV</b>	~ 130 eV	~ 150 eV	~ 125 eV
<b>Thickness</b>	up to 5 mm	up to 1 mm	up to 775 $\mu\text{m}$
<b>Count rate</b>	$< 10^5$ cts/s	$< 10^4$ cts/s	up to $10^6$ cts/s
<b>P/B ratio</b>	up to 20000:1	up to 5000:1	up to 15000:1
<b>Active area</b>	up to 80 $\text{mm}^2$	up to 25 $\text{mm}^2$	up to 150 $\text{mm}^2$
<b>Cooling requirement</b>	$\text{LN}_2$	-40°C	-40°C

### 3.6. SDD MANUFACTURERS:

There are several manufacturers who make SDDs with various shapes, sizes and types. The SDDs which are widely in use for research and other applications are manufactured by KETEK (GmbH), PN Sensor (GmbH) and AMPTEK (USA). The size and configuration of SDDs produced by these manufacturers are listed in table-3.2.

**Table-3.2:** Comparison of SDD manufacturers and their device characteristics.

<b>Manufacturer</b>	<b>KETEK</b>	<b>PN Sensor</b>	<b>AMPTEK</b>
<b>Parameters</b>	<b>GmbH</b>	<b>GmbH</b>	<b>USA</b>
<b>Size (<math>\text{mm}^2</math>)</b>	7/10/15/20/30/50/ 80/100/ 150	5/10/20/30 /60/100	7/25
<b>Thickness (<math>\mu\text{m}</math>)</b>	450	450	500
<b>FWHM @ 5.9keV for small area SDDs</b>	~ 130 eV with external FET, ~ 125 eV with ASIC	~ 128 eV	~ 125 eV
<b>Shape</b>	Circular	Circular, Square, Droplet	Circular
<b>FET</b>	Discrete FET and also ASIC based readout	on-chip	Discrete
<b>Be and AP3.3</b>	Yes	Yes	Yes
	Used in Mars Exploration		

<b>Space mission</b>	Rover, Mars Science laboratory, Rosetta comet mission, Planned for Chandrayaan-2 mission	Not known	Not known
----------------------	--	-----------	-----------

There are other manufacturers such as thermo scientific-USA, Oxford instruments, Hitachi-USA formerly known as SII nano technology and SGX Sensortech-UK are also producing SDDs with various shapes and sizes.

### **3.7. APPLICATIONS OF SDDs:**

SDDs are used in variety of scientific and laboratory applications. SDD based X-ray spectrometers are widely used in the ground based and space based applications for measuring the elemental compositions with high energy resolution which is essential to resolve the closely spaced X-ray fluorescence lines with their intensity. SDD based X-ray spectrometer is ideally suited for high count rate measurements with count rates up to  $10^6$  counts/s. These instruments are used to produce spatially resolved elemental maps with wide dynamic range [92].

SDDs are also used as photo detector to detect the scintillation light in high energy X-ray and gamma ray applications along with the scintillator [93]. Compared to PMTs, SDDs are compact with high quantum efficiency. SDDs offer low noise compared to other photodiodes such as Si PIN. This thesis is aimed at use of SDDs in the space applications. Hence, we briefly describe the space/planetary missions which have carried the SDD based X-ray spectrometers onboard for various scientific studies.

### **3.8. SDDs IN SPACE MISSIONS:**

Several space missions in the past decade have carried Silicon Drift Detector (SDD) based X-ray spectrometer onboard for various scientific measurements due to its superior spectroscopic performance. Mars rover experiments such as Mars Exploration Rovers (MER) Spirit and Opportunity and recent Mars Science Laboratory (MSL) have carried SDD based X-ray spectrometer for in-situ elemental composition measurement of Martian surface. The comet mission Rosetta has also carried SDD based X-ray spectrometer onboard PHILAE lander for the comet 67P/Churyumov-Gerasimenko to carry out in-situ elemental composition measurements. Recent lunar mission from China, Change'3 also carried SDD for in-situ elemental composition measurements on the lunar surface.

There are planetary/space missions in the near future plan to use scientific instruments having SDD as a sensor. Chandrayaan-2, the second Indian mission to Moon is slated for launch in the year 2017 uses SDD detector in two X-ray spectrometer instruments. The space mission, Large Observatory for X-ray Timing (LOFT) is being developed by European Space Agency (ESA) with large number of large area SDDs with total effective area of  $10 \text{ m}^2$  for astronomical observations. This mission is slated for launch in the year 2022. The instrument details with the scientific requirement are discussed briefly in the following subsections.

#### **3.8.1. Mars Exploration Rover (MER):**

The SDD based X-ray spectrometer named Alpha Particle X-ray spectrometer (APXS) was flown in two Mars Exploration Rovers (MER) namely Spirit and Opportunity. The objective of the instrument was to determine the major and minor

elemental composition of Martian rocks, soils and other geological materials near the landing sites. The working principle of APXS is based on the measurement of characteristic X-rays emitted from Martian surface due to alpha Particle Induced X-ray Emission (PIXE) and X-ray Fluorescence (XRF) processes by irradiating the sample surface with alphas and X-rays emitted from the radioactive alpha sources ( $^{244}\text{Cm}$ ). The instrument was configured with six alpha sources, each with activity of  $\sim 5$  mCi giving the total activity of  $\sim 30$  mCi [94].

APXS onboard MER carried a SDD with active area of  $10\text{ mm}^2$ , 450 micron thick silicon covered with 5 micron thick Beryllium window. This instrument is configured as cylinder with 53 mm dia and 84 mm length accommodating SDD, six numbers of alpha sources and six numbers of alpha detectors as shown in figure 3.20.

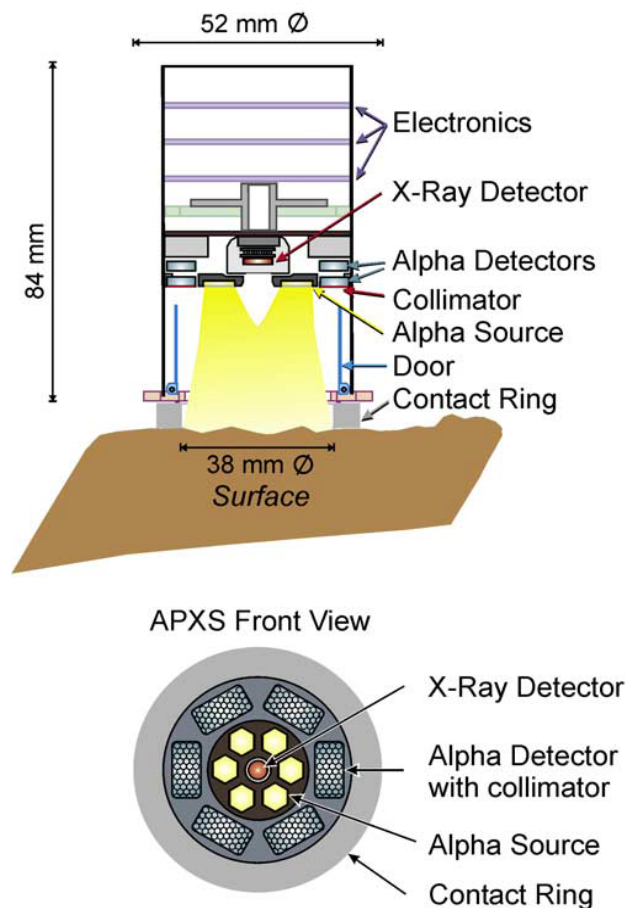


Fig. 3.20: Schematic representation of SDD based APXS instrument onboard MER [94].

The photographic view of the instrument is shown in figure 3.21. The APXS onboard MER provided the energy resolution of  $\sim 160$  eV at 5.9 keV by cooling the SDD to  $\sim -35^{\circ}\text{C}$  when operated during the Martian night time and the resolution degraded to  $\sim 200$  eV during day time operating for the operating temperatures greater than  $-10^{\circ}\text{C}$ . The fluorescence spectra measured by the APXS onboard MER rover is shown in figure 3.22.

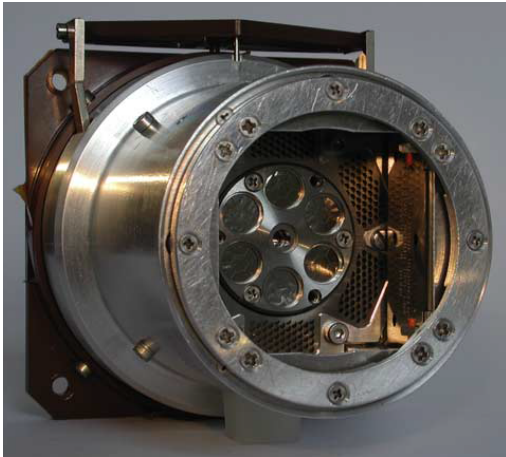


Fig. 3.21: Photographic view of APXS flown in MER [94].

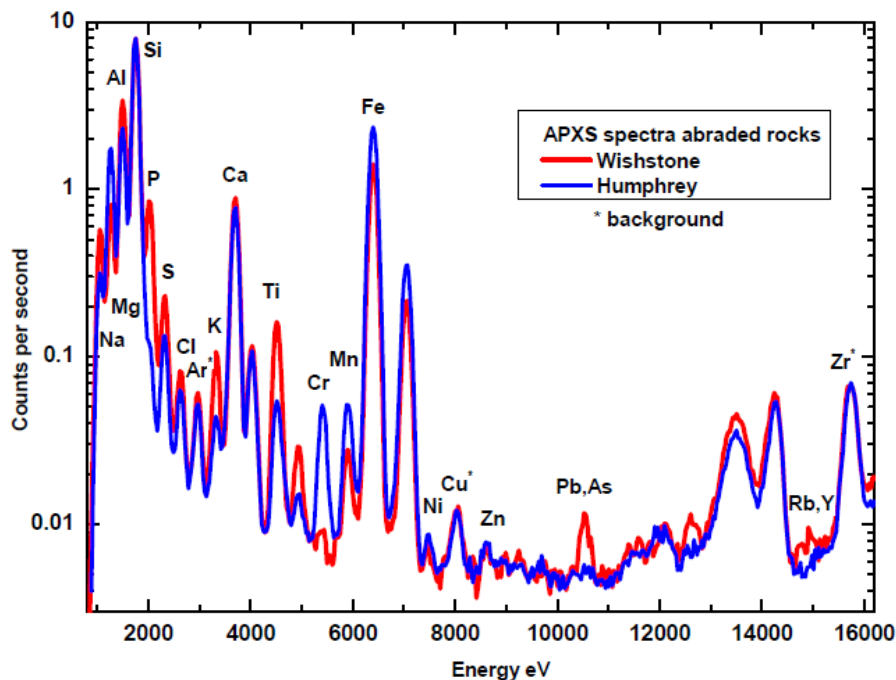


Fig. 3.22: Spectra measured by MER rover for two samples [95].



### **3.8.2. Rosetta Mission:**

APXS instrument onboard Rosetta mission was the first mission planned with SDD for the space use, though the Rosetta mission was launched in 2004 after the landing of MER rovers in 2003. Rosetta is a space probe built by the European Space Agency. Rosetta mission landed on the comet on 12<sup>th</sup> November, 2014. The objective of the Rosetta APXS instrument is to carry out elemental composition studies on the comet, 67P/Churyumov-Gerasimenko by mounting it on the PHILAE lander. The APXS instrument on Rosetta lander was delivered to the mission team in mid 2002 and it underwent all the environmental tests as desired before its integration with lander. This instrument provides energy resolution of  $\sim 180$  eV at 6.4 keV when the SDD cooled to  $-40^{\circ}\text{C}$ . This instrument configuration is very similar to the APXS flown in MER [96].

### **3.8.3. Mars Science Laboratory (MSL):**

The improved version of the SDD based Alpha Particle X-ray Spectrometer (APXS) that flew in MER was flown in Mars Science Laboratory (MSL) with similar scientific objectives. The new configuration reduces the total integrating time from several hours to few hours by taking the SDD and alpha sources close to the sample surface as shown in figure 3.23. In this instrument, the improved version of the SDD module was used, which provides the energy resolution of  $\sim 150$  eV at 5.9 keV by cooling the detector to below  $-15^{\circ}\text{C}$ . This allows larger temperature operational time window for continuous data collection compared to APXS onboard MER [97]. The improved spectral response of APXS instrument onboard MSL in comparison with the APXS instrument flown in MER is shown in figure 3.24 for a Basalt Columbia River (BCR), a geochemical standard reference.

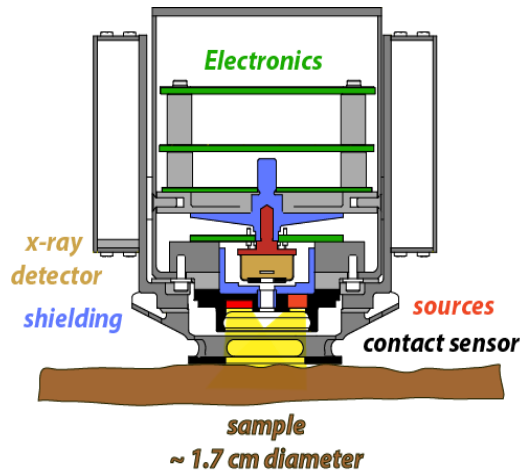


Fig. 3.23: Schematic representation of SDD based APXS instrument onboard MSL [97].

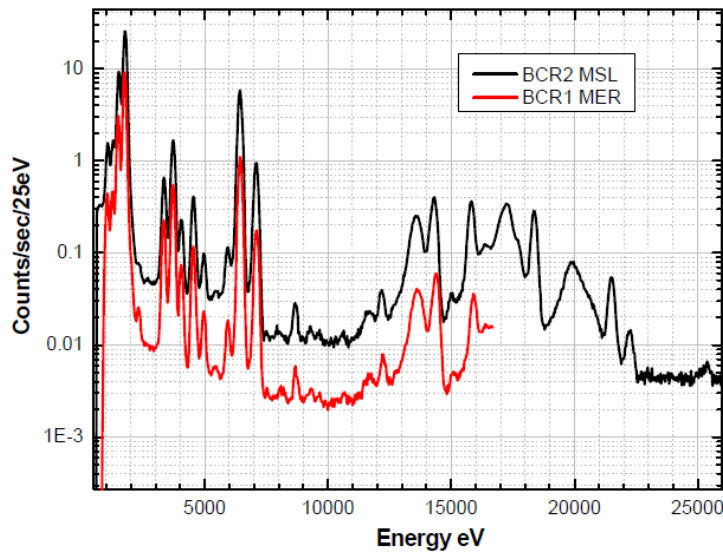


Fig. 3.24: Spectral response comparison of APXS instruments flown in MSL and MER [97].

#### 3.8.4. Chang'e-3 Mission:

Chang'e-3 is the first mission to carry SDD onboard lunar mission to carry out in-situ X-ray fluorescence measurement onboard Yutu rover to determine the elemental composition of lunar rock and soil around the landing site. Though the instrument is named as APXS, but it carried only X-ray sources. It carried four number of  $^{55}\text{Fe}$  with activity of  $\sim 70$  mCi each and four number of  $^{109}\text{Cd}$  with  $\sim 5$  mCi each. The APXS onboard Chang'e-3 rover was shown to be providing the energy resolution of  $\sim 135$  eV

at 5.9 keV by cooling the SDD to  $-30^{\circ}\text{C}$  [98]. The SDD used in the experiment has the active area of  $7\text{ mm}^2$  with 2 micron thick beryllium window in the front. The photographic view of the instrument is shown in figure 3.25.

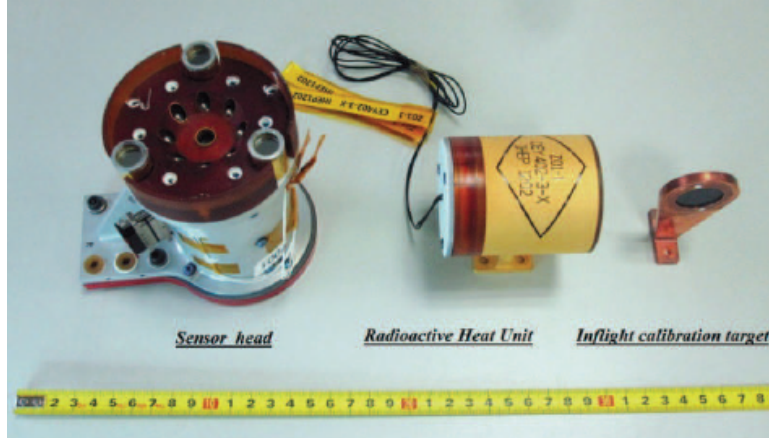


Fig. 3.25: Photographic view of the APXS onboard Chang'e-3 mission [98].

The instrument was first powered and the calibration measurement was carried out on 22<sup>nd</sup> December, 2013. The first lunar soil measurement was carried out on 24<sup>th</sup> December, 2013 for more than two hours. Subsequently, the second APXS measurement was carried out on 14<sup>th</sup> January for one hour after the lunar night. The measured calibration spectra and the XRF on the lunar surface is shown in figure 3.26.

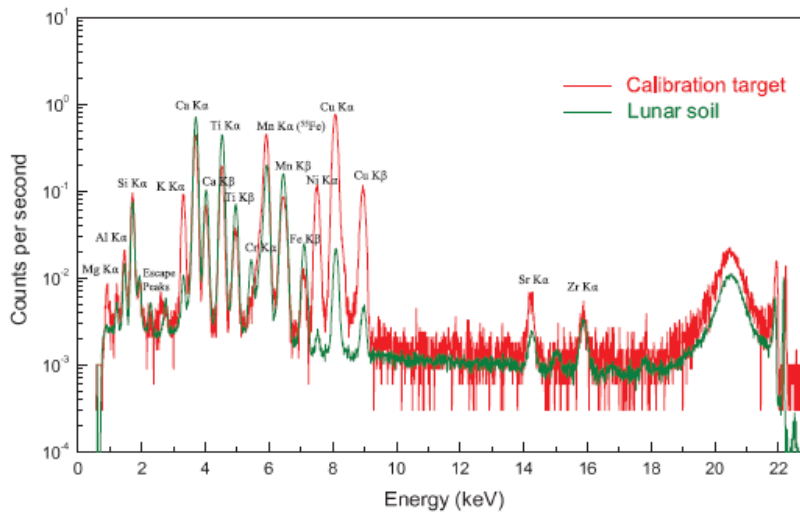


Fig. 3.26: The calibration and the lunar soil spectra measured on the lunar surface by APXS onboard Chang'e-3 [98].

### **3.8.5. Chandrayaan-2 Mission:**

Chandrayaan-2, the second Indian mission to Moon will have Orbiter, Lander and Rover and slated for launch in the year 2017. There are several instruments onboard on these three platforms to carryout various scientific measurements. There are two SDD based X-ray instruments planned onboard Chandrayaan-2 mission namely Alpha Particle X-ray Spectrometer (APXS) on the rover and Solar X-ray Monitor (XSM) on the orbiter.

#### **3.8.5.1. Alpha Particle X-ray Spectrometer (APXS):**

The objective of Alpha Particle X-ray Spectrometer onboard Chandrayaan-2 rover is to analyze several rock/soil samples around the high latitude landing site on the lunar surface for the elemental composition studies, covering the energy range of 1 - 25 keV. APXS instrument onboard Chandrayaan-2 will carry six number of  $^{244}\text{Cm}$  alpha sources with  $\sim 5$  mCi activity each [99]. This is the first time such measurement is planned, though the Chang'e-3 APXS was flown in 2013, but carried only X-ray sources and hence only XRF measurements were carried out. Earlier in-situ measurements were carried out on the lunar surface in late 1960s through the detection of back scattered alpha particles with Surveyor lander [100]. Both the earlier and recent in-situ measurements were carried out in the equatorial region of the Moon. APXS onboard Chandrayaan-2 rover will study the lunar surface in the high latitude polar region for the first time.

The laboratory working model of the APXS instrument has been completed and tested for the performance requirement to meet the science goal. The photographic view of the APXS package is shown in figure 3.27. APXS package consists of SDD module surrounded by six  $^{244}\text{Cm}$  alpha sources. The readout electronics is accommodated in three Printed Circuit Boards (PCB) which are stacked one over another. The SDD

module planned for this experiment will have the total active is of  $40 \text{ mm}^2$  collimated to  $30 \text{ mm}^2$  with 450 micron thick silicon. A beryllium window of 8 micron thick is placed in front of the detector.

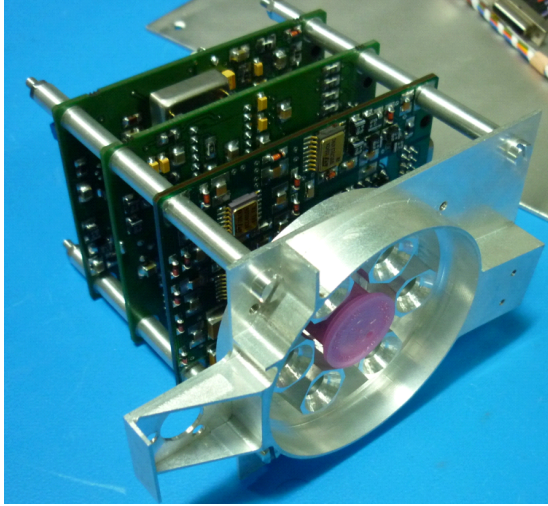


Fig. 3.27: Photographic view of the functional model of APXS developed for Chandrayaan-2 rover mission [101].

The developed system provides the energy resolution of  $\sim 150 \text{ eV}$  at  $5.9 \text{ keV}$  when the SDD is cooled to  $\sim -40^\circ\text{C}$  for the pulse peaking time of  $\sim 3.3 \mu\text{s}$  as shown in figure 3.28.

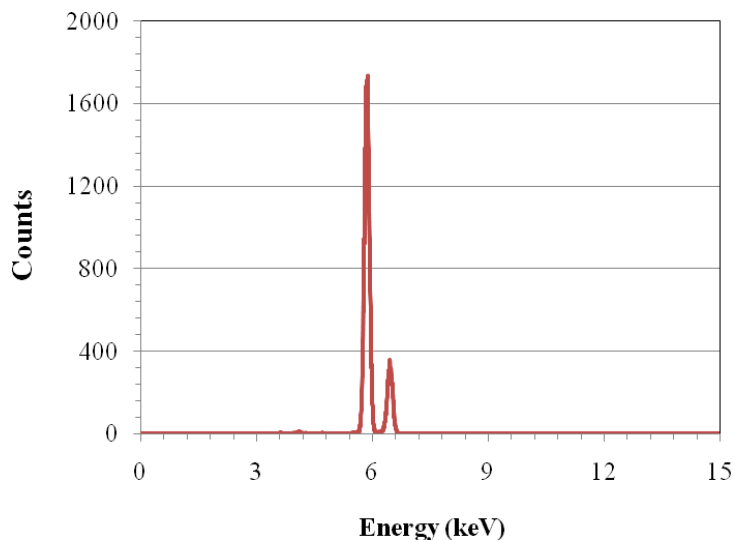


Fig. 3.28: Spectra acquired from APXS working model using  $^{55}\text{Fe}$  X-ray source for the pulse peaking time of  $\sim 3.3 \mu\text{s}$  by cooling the SDD to  $-40^\circ\text{C}$ .

### **3.8.5.2. Solar X-ray Monitor (XSM):**

It is well known that the remote X-ray fluorescence spectroscopy is widely used to investigate the elemental composition of the atmosphere-less bodies from the orbiting satellite. The experiment involves measuring X-ray fluorescent spectra from the planetary surface and simultaneous measurement of solar X-ray spectrum is essential as the intensity of XRF from the planetary surface critically depends on the intensity of solar X-rays. In the context of Moon, this technique has been employed by several missions to determine the global elemental composition of the lunar surface. However, so far the global elemental composition could not be obtained due to various reasons. So therefore, it is planned to continue the remote X-ray fluorescence spectroscopy experiment onboard Chandrayaan-2. There are two separate instruments are required for this purpose. The lunar X-ray observations will be carried out by Chandra Large Area Soft x-ray Spectrometer (CLASS) experiment (developed at ISRO Satellite Centre, Bangalore); whereas the solar X-ray observations will be carried out by Solar X-ray Monitor (XSM) which is being developed at Physical Research Laboratory (PRL).

Solar X-ray Monitor onboard Chandrayaan-2 orbiter is designed to provide high resolution real time solar X-ray spectrum in the energy range of 1–15 keV. The laboratory working model of the payload has been completed. XSM is designed with two packages namely XSM sensor package and XSM processing electronics package. The photographic view of XSM sensor package is shown in figure 3.29. The laboratory working model of the XSM instrument provides the energy resolution of  $\sim 200$  eV at 5.9 keV for the pulse peaking time of  $0.8 \mu\text{s}$  when the SDD is cooled to  $-40^\circ\text{C}$  [48] as shown in figure 3.30.

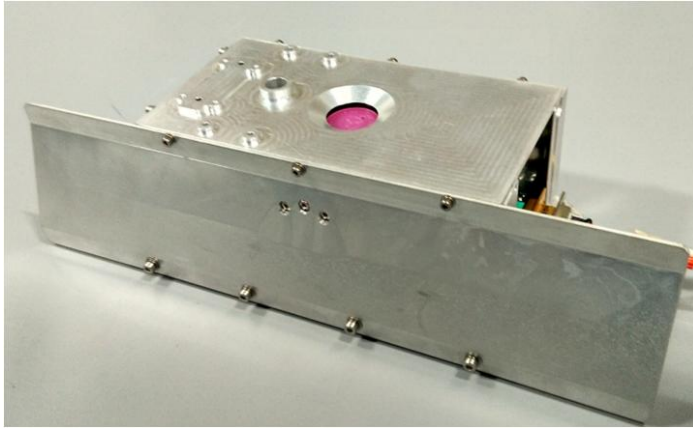


Fig. 3.29: Photographic view of the functional model of XSM sensor package [102].

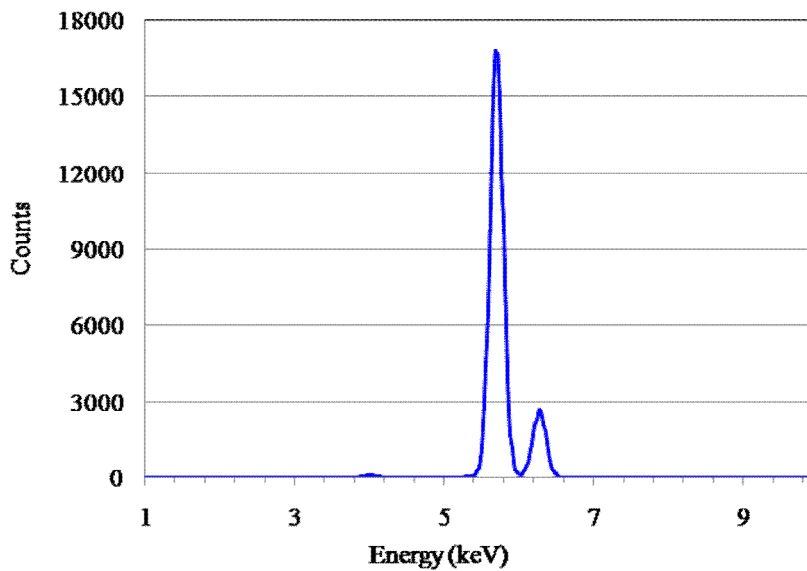


Fig. 3.30: Spectra acquired for  $^{55}\text{Fe}$  source for the pulse peaking time of  $0.8 \mu\text{s}$  by cooling the SDD to  $\sim -40^\circ\text{C}$ .

### 3.8.6. The Large Observatory For X-ray Timing (LOFT) Mission:

The large Observatory For X-ray Timing (LOFT) is one of the ESA's space mission devoted for the observation of Galactic and extra-Galactic sources in the X-ray domain. This is a medium sized space mission planned by ESA within the contest of the Cosmic Vision Program 2015 - 2025. The LOFT mission is slated to be launched in the year 2022 into a low Earth equatorial orbit. The LOFT instrument comprises of Large Area Detector (LAD) and a Wide Field Monitor (WFM).

The LAD instrument is a non-imaging instrument and will be used for pointed X-ray observations in the energy range of 2 - 30 keV. LAD instrument uses large number of large area SDDs, configured with six panels having 21 modules each [103, 104]. Each module consists of 16 SDDs giving total sensitive area of  $\sim 76 \text{ cm}^2$ . A total of 2016 detectors are used for LAD instrument giving the total geometric area of  $18 \text{ m}^2$ . The schematic view of the LOFT mission is shown in figure 3.31.

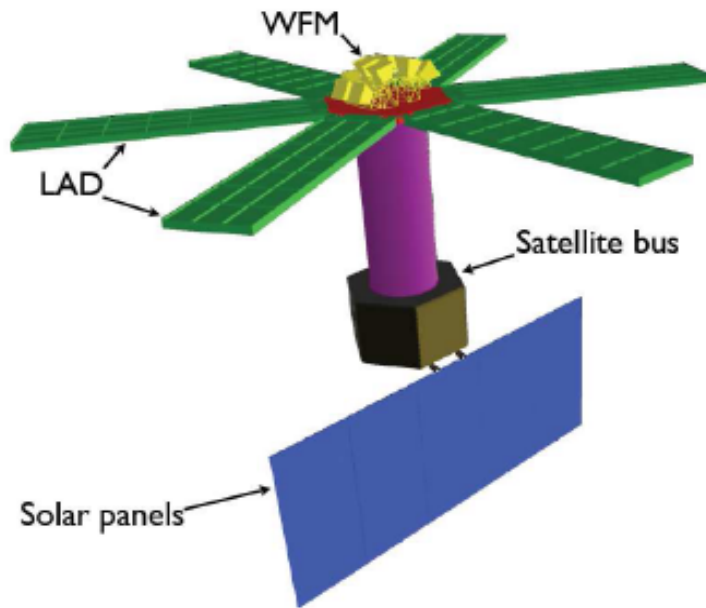


Fig. 3.31: Conceptual scheme of LOFT mission [103].

The SDDs used in the LAD - LOFT mission provides the energy resolution of  $\sim 200 \text{ eV}$  at  $6 \text{ keV}$  for the detector operating temperature of  $-10^\circ\text{C}$  and will carry out the measurements for  $\sim 4.25$  years in the low Earth orbit.

### **3.9. COMPARISON OF SDD BASED X-RAY SPECTROMETERS FLOWN/PLANNED IN VARIOUS SPACE/PLANETARY MISSIONS:**

Table-3.3 gives comparison of SDD based X-ray spectrometers flown/planned in various space/planetary missions.



**Table-3.3:** Comparison of SDD based X-ray spectrometers flown/planned in the space/planetary missions.

<b>Mission and year</b>	<b>Scientific objective</b>	<b>SDD specification</b>	<b>Energy resolution</b>	<b>References</b>	<b>Remarks</b>
<b>Mars Exploration Rover (MER), 2003</b>	Elemental composition of Martian surface for both light and major elements	SDD with active area of 10 mm <sup>2</sup> , covered with 5 micron thick Be window	160 eV at 5.9 keV, -35°C	Rieder et al., 2003, Gellert et al., 2006.	Carried 6 numbers of <sup>244</sup> Cm alpha sources with total activity of 30 mCi
<b>Mars Science Laboratory, 2012</b>	Elemental composition and also trace elements on the Martian surface	SDD with active area of 10 mm <sup>2</sup> , covered with 5 micron thick Be window	150 eV at 5.9 keV, -15°C	Gellert et al., 2009, Campbell et al., 2012.	Carried 6 numbers of <sup>244</sup> Cm alpha sources with total activity of 30 mCi
<b>Rosetta PHILAE lander mission, 2004</b>	Elemental composition of comet 67P/Churyu mov-Gerasimenko	SDD with active area of 10 mm <sup>2</sup> , covered with 5 micron thick Be window	180 eV at 5.9 keV, -40°C	Klingelhofe et al. 2007	Carried 6 numbers of <sup>244</sup> Cm alpha sources with total activity of 30 mCi
<b>Chang'e-3, 2013</b>	Elemental composition of lunar surface	SDD with active area of 7 mm <sup>2</sup> , covered with 2 micron thick Be window	135 eV at 5.9 keV, -30°C	X. H. Fu et al., 2014.	Carried X-ray sources, 4 numbers of <sup>55</sup> Fe (70 mCi each) and 4 numbers of <sup>109</sup> Cd (5 mCi each)
	APXS -		150 eV at	Shanmugam	Six number

<b>Chandrayaan-2, 2017</b>	Elemental composition of high latitude lunar surface	SDD with active area of 30 mm <sup>2</sup> , covered with 8 micron thick Be window	5.9 keV, peaking time 3.3 $\mu$ s, -40°C	et al., 2013	of <sup>244</sup> Cm with total activity ~ 30 mCi
	XSM – To measure the high resolution solar X-ray spectrum		200 eV at 5.9 keV, peaking time 0.8 $\mu$ s, -40°C	Santosh et al., 2013	<sup>55</sup> Fe calibration source planned with activity of ~ 50 $\mu$ Ci
<b>LOFT mission, 2022</b>	Astronomical observation of Galactic and extra-Galactic sources	Total area of 18 m <sup>2</sup> Each SDD 1 sq. Inch	200 eV at 6 keV, -40°C	Del Monte et al., 2014	-

### 3.10. SUMMARY:

This chapter briefly describes about the invention of SDD from sidewall depletion concept and its working principle. Though the SDD concept was invented in 1984, the first spectroscopy grade SDD was available only in late 1990's. Since then, lot of research has taken place in this field producing the SDDs in various forms, types and sizes, which are available for research and commercial applications. This chapter also briefly describes about all the SDD types with merits and demerits and the selection of the suitable SDD for the Chandrayaan-2 experiments. The use of SDDs in the space/planetary missions by various space agencies is also described.

## **Chapter 4:**

### **DESIGN AND PERFORMANCE EVALUATION OF SDD BASED X-RAY SPECTROMETER**

The use of Silicon Drift Detector (SDD) based X-ray spectrometers are gaining importance in most of the space/planetary missions due to its superior spectroscopic performance. Several planetary missions [95-98] have employed SDD based X-ray spectrometer to measure the X-ray fluorescence from the planetary surfaces. The SDD based X-ray spectrometers are also planned for the upcoming Indian Chandrayaan-2 mission to detect X-ray fluorescence [99] from the lunar surface onboard rover and also incident solar X-rays [102] from the orbiting satellite. The SDD based X-ray spectrometer has been developed using commercial version of the space qualified components and successfully demonstrated the performance characteristics that meets the desired scientific goals for the spectrometers onboard Chandrayaan-2 mission. In the actual payload, these components will be replaced with qualified ones.

SDD based X-ray spectrometers are commercially available for laboratory/field experiments which are designed with Commercial Off-The-Shelf (COTS) components. These instruments are not space worthy and are not designed to survive very hostile space environment such as radiation, large temperature excursions and high vacuum conditions. These instruments are not designed to survive the satellite launch loads and design must have low mass and high strength. Hence it is essential to design a custom SDD based X-ray spectrometer using space qualified components with required quality levels to meet the scientific requirement as well as can survive the hostile space environment. For all these reasons “Space instruments are custom-designed, one-of-a-

kind and building such unique instrument depends on the mission and the instrument configuration required for the given scientific application”. As a part of this research activity, SDD based X-ray spectrometer has been developed and shown that the developed X-ray spectrometer provides energy resolution of  $\sim 150$  eV at 5.9 keV when the SDD is cooled to  $-40^{\circ}\text{C}$  for the pulse shaping time of  $\sim 3.3$   $\mu\text{s}$ . The developed instrument is configured for two different applications onboard Chandrayaan-2 mission as described in the following subsections.

#### 4.1. OBJECTIVES AND SPECIFICATIONS OF APXS:

The major scientific objective of the Alpha Particle X-ray Spectrometer (APXS) onboard Chandrayaan-2 rover is to analyze several rocks/soil samples for the major elemental composition around the landing site by irradiating the sample surface with radioactive source ( $^{244}\text{Cm}$ , alpha source) and measuring the X-ray fluorescence [99]. This measurement gives the quantitative elemental composition. Typically, most of the planetary bodies expected to have major rock forming elements as listed in table-4.1 with their characteristic X-ray emission line.

**Table-4.1:** List of major rock forming elements expected on the Moon with their energies.

Element	Energy
Mg	1.24 keV
Al	1.49 keV
Si	1.74 keV
Ca	3.69 keV
Ti	4.51 keV
K	3.31 keV
Fe	6.49 keV

From table-4.1, it is clear that the low energy threshold requirement of the APXS instrument should be well below 1 keV to unambiguously detect 1.24 keV Mg line. Most of the major elements are covered within the energy range of 1-8 keV, but there may be some minor elements (Strontium, Yttrium and Zirconium) above 8 keV which may be present at the lunar surface. The APXS instrument has therefore been designed to cover the energy range up to 25 keV. The energy resolution requirement of the APXS should be better than 200 eV to resolve the closely space lines such as Mg-Al-Si with energy difference of ~ 250 eV. However, we aim to achieve the best possible energy resolution with a low noise system design by using discrete space qualified electronic components based readout electronics. The design of the APXS instrument is aimed to meet the specification listed in the table-4.2. The design and the performance details are described in the subsequent subsections.

**Table-4.2:** APXS instrument specifications.

Parameters	Values
Detector area/thickness	SDD with 30 mm <sup>2</sup> , 450 micron thick
Energy range	1-25 keV
FWHM at 5.9 keV	~ 150 eV
Detector operating temperature	-40°C
Radioactive source, Activity	<sup>244</sup> Cm, 30 mCi
Integration time	1 hour to few hours*

\*Integration time would depend on the location and final configuration of sensor package mounting.

#### 4.2. OBJECTIVES AND SPECIFICATIONS OF XSM:

The primary objective of Solar X-ray Monitor (XSM) is to provide the real time measurement of solar X-ray spectrum for quantitative interpretation of the lunar X-ray fluorescence spectra obtained by the companion instrument Chandra Large Area Soft X-ray Spectrometer (CLASS). Data from both instruments are essential to obtain the global elemental composition of the Moon from the lunar orbit. XSM instrument will accurately measure the solar X-ray spectrum in the energy range of 1-15 keV. It is well known that the intensity of the solar X-rays is highly variable in time and can reach  $\sim 10^6$  counts/s/mm<sup>2</sup> for large class (X-class) flares. The intensity of solar X-rays can increase by orders of magnitude within a minute. One of the major challenges of the XSM design is to accommodate dynamic variation in the count rate and maintaining the sensitivity requirement at small class flares. Hence, it is essential to choose the optimal pulse shaping time for the readout electronics to accommodate the desired count rates with good energy resolution. The energy resolution desired for the XSM instrument is targeted at  $\sim 200$  eV at 5.9 keV for the count rates close to  $10^5$  counts/s. During large class flare conditions, the incident count rate on the SDD is limited to  $< 10^5$  counts/s using a 250 micron thick beryllium window which is mounted on a motor based mechanism [102]. Specifications of the XSM instrument are given in table-4.3.

**Table-4.3:** XSM instrument specifications.

Parameters	Values
Detector area/thickness	SDD with 30 mm <sup>2</sup> , 450 micron thick
Aperture	0.2 mm <sup>2</sup>
Energy range	1-15 keV
FWHM at 5.9 keV	200 eV
Detector operating temperature	-40°C

Count rate	up to $10^5$ counts/s
Spectral data integration time	1 second

#### 4.3. DESIGN OF SDD BASED X-RAY SPECTROMETER:

The spectrometer system design consists of front-end electronics and FPGA (Field Programmable Gate Array) based data acquisition system interfaced with computer through Universal Serial Bus (USB) for data readout and display using LABVIEW software. The USB based interface and the LABVIEW software are developed for ground testing. The LABVIEW software also simulates the spacecraft in receiving the serial spectral data from FPGA and also in providing necessary commands for the payload operation. The block schematic of the spectrometer system design is shown in figure 4.1. It is divided into two parts namely Front-End Electronics (FEE) and FPGA based control, readout and signal conditioning system.

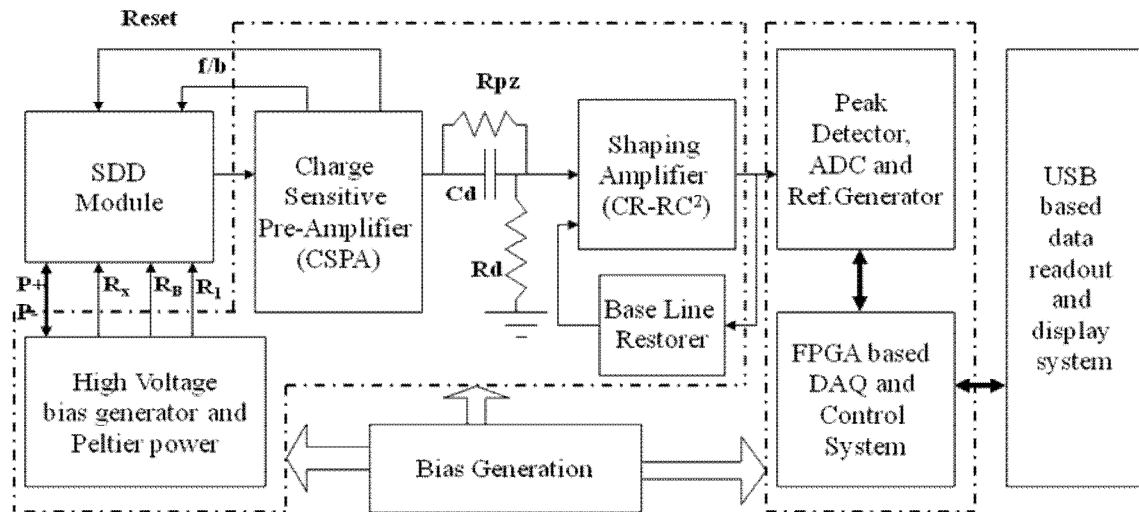


Fig. 4.1: Block schematic of the SDD based spectrometer system design [105].

The Front-End Electronics consists of Charge Sensitive Pre-Amplifier (CSPA), Shaping amplifier with base line restorer and High Voltage (HV) bias generator circuits interfaced with the SDD detector module. The FPGA based control, data acquisition and

signal conditioning system consists of programmable FPGA interfaced with reference generator, peak detector and A/D converter. The reference generator provides a reference signal to FPGA on occurrence of X-ray interaction with the SDD. FPGA initiates the analog signal peak detection and A/D conversion on occurrence of the reference signal and makes the spectrum [105]. The spectral data is acquired by the LABVIEW software through USB interface in the computer.

The FEE electronics and the peak detector designs are similar for both APXS and XSM instruments. In case of APXS, serial 12 bit ADC is planned due to low count rate of X-ray fluorescence expected from the lunar surface and a common FPGA will be shared by all the subsystems on the rover. In case of XSM, 12 bit parallel ADC is planned and the spectra will be made using 10 bit data from the ADC which is good enough to achieve the targeted energy resolution of  $\sim 200$  eV at 5.9 keV. This reduces the onboard memory requirement by 4 times. The developed spectrometer system uses commercial equivalent of the space qualified components except FPGA. The FPGA used in the design is programmable FPGA and the FPGA planned for the XSM instrument is one time programmable device and it is selected due to its space quality and heritage. Design of individual subsystem is described in detail in the following subsections.

#### **4.3.1. SDD Module for Chandrayaan-2 Instruments:**

As discussed in chapter-3, the choice of the X-ray detector for the desired energy range of APXS and XSM instruments essentially comes from silicon detector family i.e., Silicon Drift Detector (SDD). The X-ray spectrometers onboard Chandrayaan-2 uses SDDs with active area of  $30 \text{ mm}^2$  with 450 micron thick silicon. These detectors are available in the form of modules and are procured from KETEK, GmbH due to their space heritage in the recent Mars missions [106]. These SDD modules consist of SDD chip,



JFET, charge integration feedback capacitor, reset diode, temperature sensor diode and Peltier cooler. In these modules, JFET, feedback capacitor and the reset diode are external to the SDD chip in die form and are mounted inside module close to the SDD anode. The Schematic and photographic view of the SDD module is shown in figure 4.2 and figure 4.3.

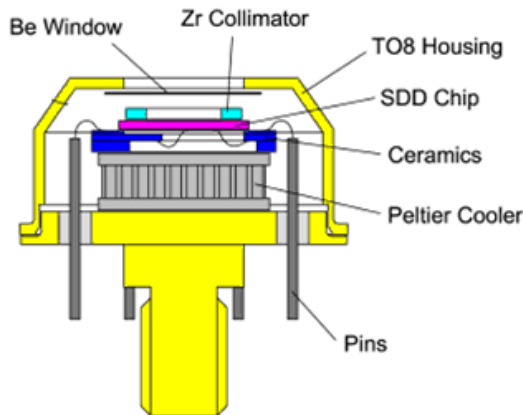


Fig. 4.2: Schematic view of SDD module [71](Courtesy KETEK, GmbH).

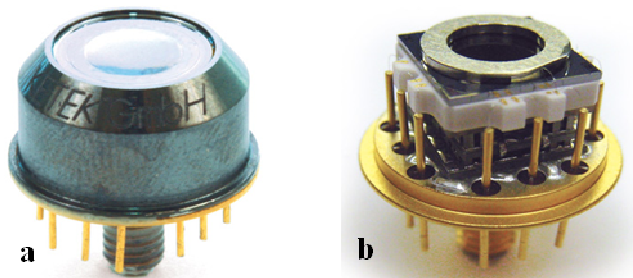


Fig. 4.3: a) Photographic view of 40 mm<sup>2</sup> area SDD module, b) Internal view (right) [85] (Courtesy KETEK, GmbH).

The SDD module is provided with 12 pins for necessary electrical interfaces and the internal electrical interconnection diagram of SDD module is shown in figure 4.4. These SDD modules are encapsulated with tungsten shield and the front face of the detector is covered with think 8  $\mu\text{m}$  thick Dura Be window, which allows the X-rays to penetrate. The SDD efficiency at lower energies,  $< 1$  keV is determined by the thickness of Be window and the shallow back contact of the SDD.

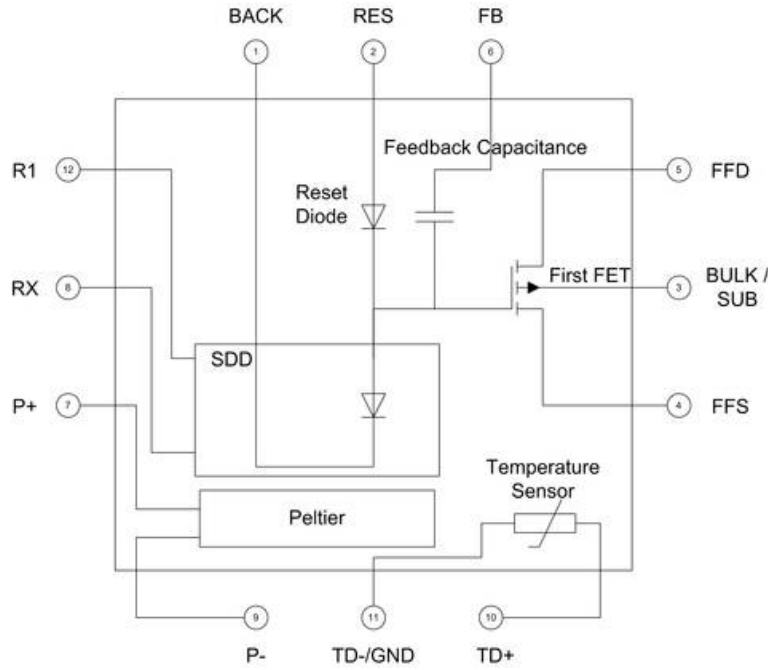


Fig. 4.4: Internal electrical interconnection diagram of SDD module [85] (courtesy KETEK, GmbH).

The efficiency curve for 8  $\mu\text{m}$  thick Dura Be window is shown in figure 4.5. Internal to the SDD module, there is a circular Zr collimator with a opening of  $4.5 \text{ mm}^2$  that reduces the probability of split events at the edges of the sensitive area.

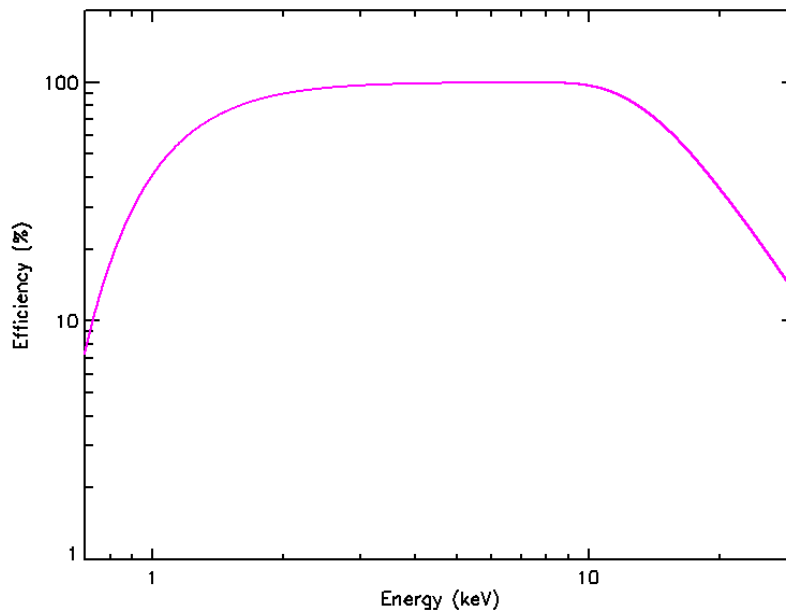


Fig. 4.5: Transmission efficiency of the 450 micron thick SDD with 8  $\mu\text{m}$  Dura Be window.

By the choice of the material, undesired fluorescent lines are avoided. The SDD module also has metallic body made of kovar with M4 threaded rod for its mounting and also heat removal. A suitable mechanical interface needs to be provided to drain out the heat from the hot junction of the Peltier cooler when the detector is cooled to lower operating temperatures. These SDD modules are commercially available in a standard TO-8 package with a diameter of 15 mm and a height of 16 mm. The housing is hermetic vacuum sealed and also tested for leakage with specification MIL 883C meth. 1014. The X-ray window being an 8  $\mu\text{m}$  Dura Be foil mounted on a Zr collimator. The specification of the 30  $\text{mm}^2$  area SDD module is given in table-4.4. Table-4.5 gives the electrical characteristics of the SDD module with min, max and typical values for all the I/O pins.

**Table-4.4:** Specifications of the SDD module planned for Chandrayaan-2 mission.

S. No	Parameter	Values/components
1	Area	30 $\text{mm}^2$
2	Absorption Depth	450 $\mu\text{m}$
3	Windows	8 $\mu\text{m}$ Be (with 1 micron thick Dura Coat)
4	Cooling Performance	$\Delta T > 70 \text{ K}$
5	HV ( $R_1$ , $R_X$ and $R_{\text{BACK}}$ )	-20 V, -130 V and -60 V
6	Peltier Element	4 V, 1 A
7	Temperature Monitor	Thermister, 10 $\text{K}\Omega$ at 20°C

**Table-4.5:** Electrical characteristic of the SDD module.

Parameter	Minimum	Typical	Maximum	Tolerance	Unit
<i>Voltages</i>					
$R_1$	-25	-20	-5	$\pm 1$	V
$R_X$ ( $R_{18}$ )	-160	-130	-80	$\pm 5$	V
$R_{\text{BACK}}$	-100	-65	-35	$\pm 2$	V
FET-Bulk	-7	-4	-2	$\pm 1$	V
Drain	1	3	4	$\pm 0.1$	V

<i>Currents</i>					
<b>R<sub>I</sub></b>	5	10	20	±5	μA
<b>R<sub>X</sub> (R<sub>I8</sub>)</b>	5	10	20	±0.1	μA
<b>R<sub>BACK</sub></b>	<1	1	2	±0.1	nA
<b>Drain</b>	2	3	4	±0.1	mA
<b>Temp. sensor</b>	0.1	1	5	±0.1	μA
<i>Peltier cooler (Thermo Electric Cooler-TEC)</i>					
<i>SDD at -35°C, Heat sink at 20°C</i>					
<b>Voltage</b>	1.6	1.7	1.8	±0.1	V
<b>Current</b>	250	300	350	±10	mA
<i>Maximum possible cooling to SDD, Heat sink at 20°C</i>					
<b>Voltage</b>	3	3.3	3.6	±0.1	V
<b>Current</b>	600	650	700	±10	mA
<i>Sensitivity</i>					
<b>Gain</b>		0.9		±30%	mV/keV

The detector has to be reset by a pulse of 1 V amplitude having pulse width of 1 μs.

#### 4.3.2. Charge Readout Techniques:

The charge carriers (*e-h* pairs) induced in the active volume of the detector are collected in the detector electrodes by applying suitable reverse bias voltage across them. The number of *e-h* pairs created in the active volume of the detector depends on the incident photon energy and the energy required to create one *e-h* pair. The total charge is given in equation (4.1)

$$Q_s = e \left( \frac{E_i}{\varepsilon} \right) \quad (4.1)$$

where  $Q_s$  is the total charge,  $E_i$  is the incident photon energy,  $\varepsilon$  is the energy required to create one *e-h* pair (3.6 eV for Si detector) and  $e$  is the charge of the electron.

The signal output from the semiconductor detector is usually a short current pulse whose duration varies from pico seconds to micro seconds based on the detector material and size. The deposited energy is proportional to the total charge which is the integration of the current pulse over a period of time which is given in equation (4.2)

$$E_i \propto Q_s = \int i_s(t) dt \quad (4.2)$$

The rise time of the signal at the input of charge readout amplifier with input resistance of  $R_i$  and capacitance of  $C_i$  with the detector capacitance of  $C_{det}$ , gives the voltage pulse  $V_{in}$ , which is given by (4.3)

$$V_{in} = \frac{Q_s}{C_{det} + C_i} \quad (4.3)$$

The signal current from the silicon detector is feeble, which is of the order of fA for the incident photon energy range of 1-25 keV. It will be practically difficult to detect such a small signal using voltage sensitive or current sensitive amplifiers. Over and above, the capacitance associated with the detector will vary with the applied bias voltage and the operating temperature etc. leads to additional calibration requirement for each sensitive parameters. It is desirable to have a charge readout system which is independent of the sensor parameters. This could be achieved by means of charge sensitive amplifier. Charge sensitive pre-amplifiers (CSPA) are usually the best choice when designing readout circuitry for pulse detectors. The CSPA design offers low noise, stability, and their integrating nature provides an output proportional to the total charge flowing from the detector during the pulse event. It is for these reasons that the charge sensitive preamplifiers are usually adapted in radiation detection applications, where the individual pulses need to be measured with high precision. The output voltage pulse amplitude is proportional to charge integrating capacitor in the feedback path of the amplifier and independent of any variations in the detector characteristics. The schematic

representation of charge generation, collection and signal formation is shown in figure 4.6. The basic configuration of a charge sensitive amplifier is shown in figure 4.7.

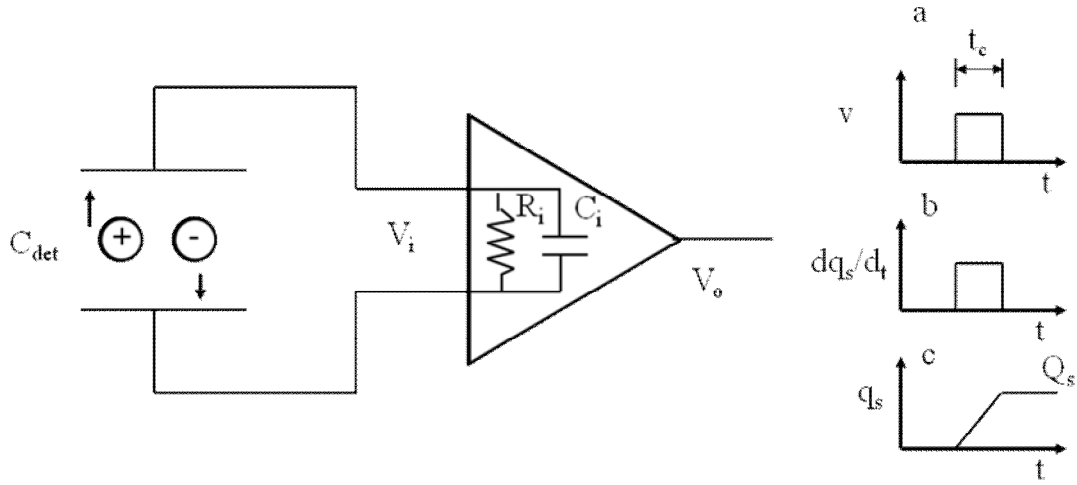


Fig. 4.6: Charge collection and signal integration, a) Velocity of charge carriers, b) Rate of induced charge on sensor electrodes, c) Signal charge.

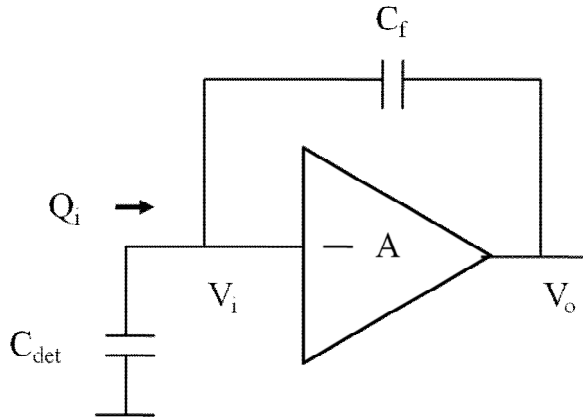


Fig. 4.7: Basic charge sensitive amplifier configuration.

It consists of an inverting amplifier with voltage gain  $-A$  and a feedback capacitor  $C_f$  connected between the input and output. For simplicity, assuming that the amplifier has infinite input impedance and hence no current flows into the amplifier. The voltage at the amplifier output is  $-AV_i$  for the input voltage  $V_i$  and the voltage across the feedback capacitor  $C_f$  is given by equation (4.4) and the charge deposited on  $C_f$  is  $Q_f = C_f V_f = C_f (A+1)V_i$ . Due to high input impedance of the amplifier, the total input charge  $Q_i$  gets integrated into the feedback capacitor which is  $Q_f = Q_i$ .

$$V_f = (A + 1)V_i \quad (4.4)$$

The input capacitance appears at the amplifier is given by (4.5)

$$C_i = \frac{Q_i}{V_i} = C_f (A + 1) \quad (4.5)$$

The voltage signal at the output of the amplifier per unit input charge is given by (4.6)

$$\begin{aligned} A_Q &= \frac{dV_o}{dQ_i} = \frac{AV_i}{C_i V_i} \\ &= \frac{A}{A+1} \cdot \frac{1}{C_f} \end{aligned} \quad (4.6)$$

for the amplifier gain  $A \gg 1$ , the gain of the charge sensitive amplifier will be

$$A_Q = \frac{1}{C_f}$$

So, the gain of the charge sensitive amplifier is determined by the value of feedback capacitor. The charge sensitive amplifier is the first amplifier stage in the detector readout system and hence called as charge sensitive pre-amplifier (CSPA). There are two types of CSPAs differing mainly in the method used to discharge the feedback capacitor, they are

1. *RC* feedback type CSPA
2. Reset type CSPA

#### ***RC feedback type CSPA:***

In *RC* feedback type CSPA, a very high value resistor is connected across the feedback capacitor to discharge the charge stored in the feedback capacitor. The schematic representation of *RC* feedback type CSPA is shown in figure 4.8. The *RC*

feedback type CSPA is generally used for low count rate applications due to larger  $RC$  ( $R_f C_f$ ) time constant in the feedback path which results in pulse-pileup at high count rates. The feedback resistor in the  $RC$  feedback type CSPA introduces intrinsic noise in the signal current resulting in poor energy resolution.

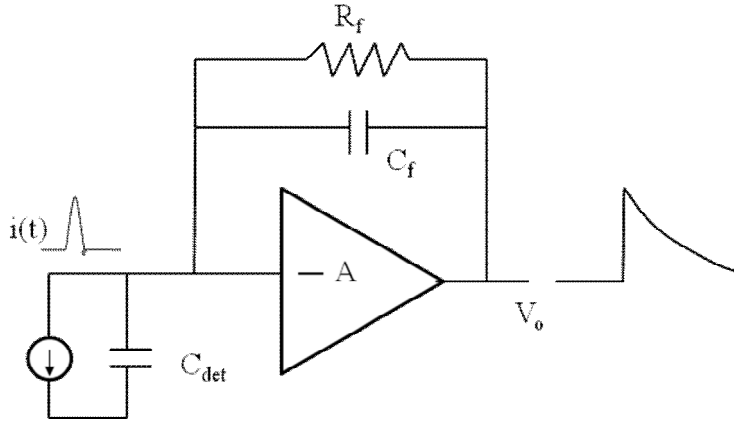


Fig. 4.8: Schematic representation of RC feedback type CSPA.

#### ***Reset type CSPA:***

The reset type CSPA eliminates the shortcomings of RC feedback type by using an active reset switch across the feedback capacitor. The charge due to the photon interacting with the detector and the detector leakage current gets integrated into the feedback capacitor and the feedback capacitor is discharged before it reaches the saturation and the process repeats. Hence the output of the reset type CSPA will be in the form of ramp signal. When there is no photon interacting with the detector, the ramp signal will be smooth and a step pulse appears in the ramp when photon interaction takes place. The schematic representation of reset type CSPA with a typical output wave form is shown in figure 4.9. When there is no photon interacting with the detector, the ramp frequency depends on the detector leakage current. The ramp signal frequency increases with energy of the photons interacting with the detector and also on the rate of interaction.



The charge reset can be of two types; self reset and pulse diode reset. SDDs with on-chip FET uses either self reset or pulse reset techniques to discharge the charge collected at the anode. SDDs with discrete FET generally uses pulse diode reset to discharge. The self reset technique was first introduced in 1970 [107] and 1972 [108] even before the invention of SDD technology. In this method, the discharge of integrated charge is done by means of impact ionization due to accelerated charges carriers in the channel of the FET amplifier.

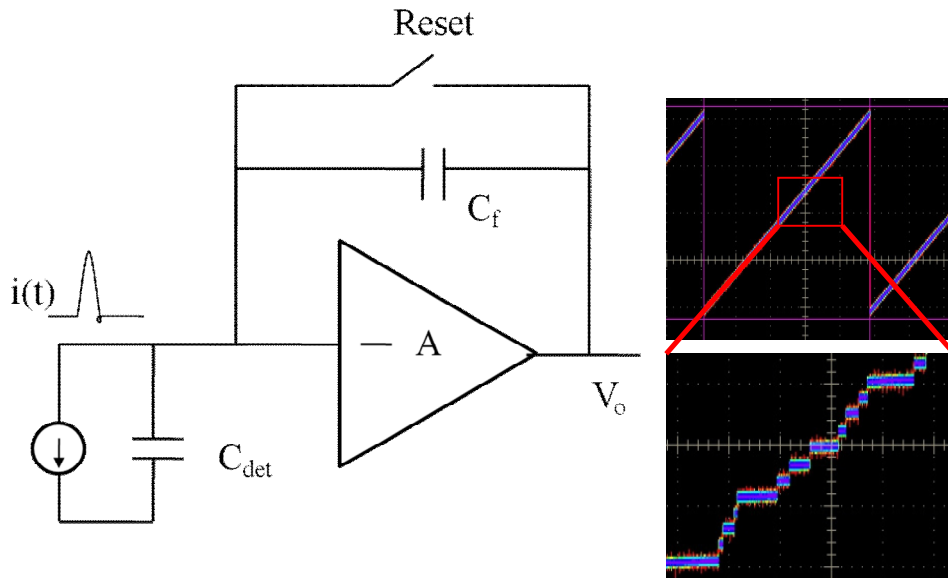


Fig. 4.9: Schematic representation of reset type CSPA with typical output signal.

The same technique is adapted in the SDD detector readout which does not require any additional components for the discharge. With this reset technique, by operating the FET in source follower voltage amplifier mode [74, 76, 77, 79, 109, 110], it has been observed that there is a degradation in the energy resolution with increase in the incident X-ray rate. It is also observed that the peak energy position varies with operating temperature. Using the same self reset technique, operating the FET amplifier in charge sensitive mode [74, 109, 111-113], and the temperature dependence of energy position shift is minimized but the degradation in the energy resolution is still observed.

Alternately, a pulse diode reset technique [79, 112] was introduced and in this method, a positive pulse of very short duration is provided to the anode of the diode which discharges the integrated charge in the feedback capacitor. The discharge was carried out with pulse reset frequency of 1 kHz and shown that energy resolution is stable with higher rates of incident radiation compared to self reset method. In recent times, the pulse reset type uses automated feedback circuit which provides reset pulse before the ramp signal output reaches the saturation level.

The self adapting discharge mechanism removes the charge at the detector anode continuously resulting in increase of noise associated with the reset current at high count rates, where as the pulse reset technique removes the charge at selected time phases. This leads to minimal degradation in the energy resolution and peak position shift at high incident X-ray rates as compared to self adapting discharge mechanism [79]. The change in the energy resolution and the peak energy position with count rate in self reset and pulse reset modes are shown in figure 4.10 and figure 4.11 [79].

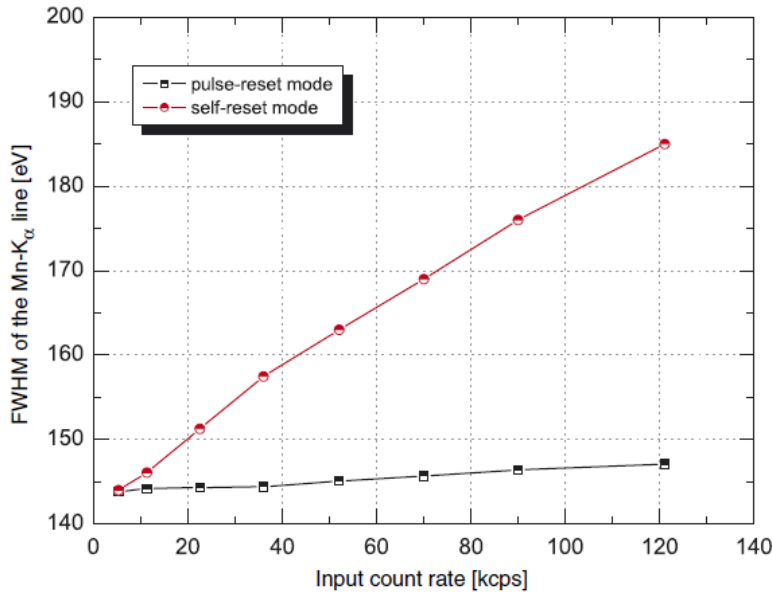


Fig. 4.10: Energy resolution measured for various count rates in self reset and pulse reset modes [79].

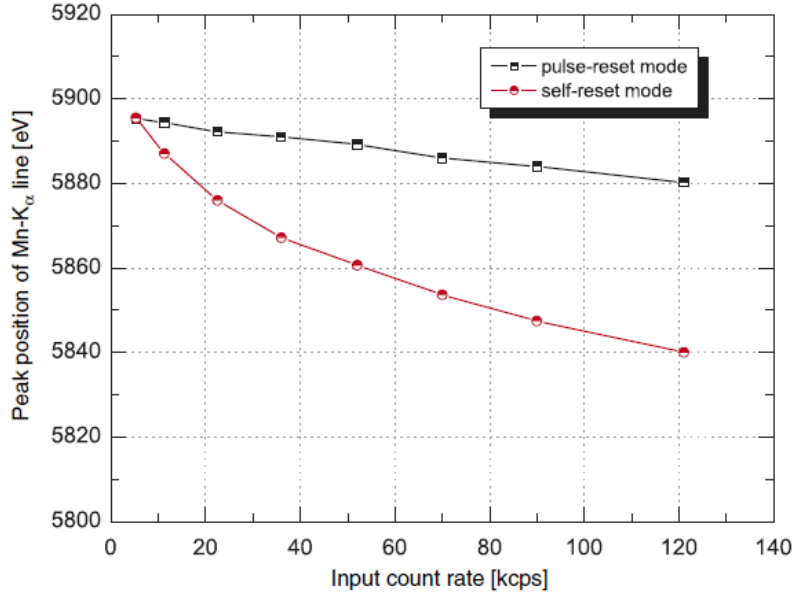


Fig. 4.11: Change in the peak energy position as a function of count rate with pulse reset and self reset modes [79].

By operating the SDD with discrete or on-chip FET in charge sensitive configuration and pulse reset discharge mode, one can achieve stable energy resolution and peak energy position for the count rates greater than  $10^5$  counts/s. The SDD modules planned for Chandrayaan-2 is configured with reset diode for discharge and with a discrete FET at the input inside the SDD module.

#### 4.3.3. Design of Charge Sensitive Pre-Amplifier (CSPA):

The block schematic of the developed charge sensitive pre-amplifier along with SDD is shown in figure 4.12. The first stage of the charge sensitive pre-amplifier is the charge to voltage conversion amplifier, where the internal FET is operated in common source configuration. The internal charge storing capacitor is connected in the feedback path which determines the gain of the charge to voltage conversion amplifier. The output of the charge to voltage conversion amplifier is connected to gain amplifier to provide additional gain to the feeble signal which is of the order of  $< 1$  mV/keV.

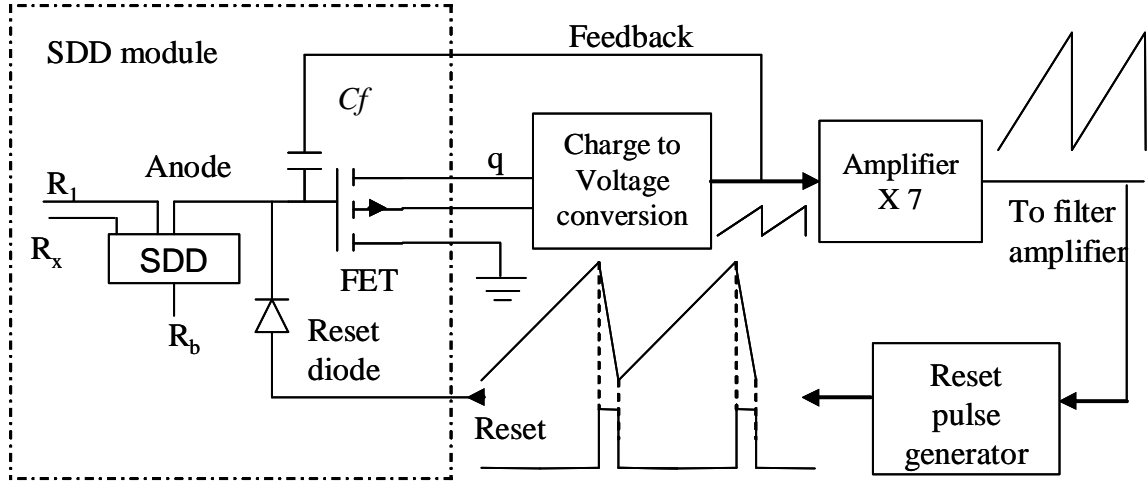


Fig. 4.12: Block schematic of pulse reset type Charge Sensitive Pre-Amplifier (CSPA) design [105].

The feedback capacitor integrates the leakage current and also the current pulses due to photon interaction. The charge integrated in the form of ramp signal and the charge should be removed before the amplifier attains the saturation limits. To generate the reset pulses to remove the charge in the feedback capacitor, the output of the gain amplifier is fed to Schmitt trigger based reset pulse generator which provides reset pulses when the ramp signal amplitude crosses the set threshold limit. The duration of the reset pulse is set  $\sim 1 \mu\text{s}$  which is fed to the reset diode to discharge the charge stored in the feedback capacitor. The selected operational amplifier device for the CSPA design is AD829 which has wide bandwidth of  $\sim 28 \text{ MHz}$ , low input noise  $4 \text{ nV}/\sqrt{\text{Hz}}$  and high slew rate of  $230 \text{ V}/\mu\text{s}$ . The Schmitt trigger is made using comparator LM311. The ramp signal frequency at the output of the CSPA will depend on the magnitude of the leakage current generated by the SDD in the absence of any photon interacting with the detector. One such ramp signal recoded in the cathode ray oscilloscope (CRO) is shown in figure 4.13. In the presence of photon interactions, the ramp signal frequency varies with energy and rate of photon interacting with the detector. Each photon interaction appears

as step voltage pulse on the ramp and the magnitude of the step pulse is proportional to the incident photon energy as shown in figure 4.14.

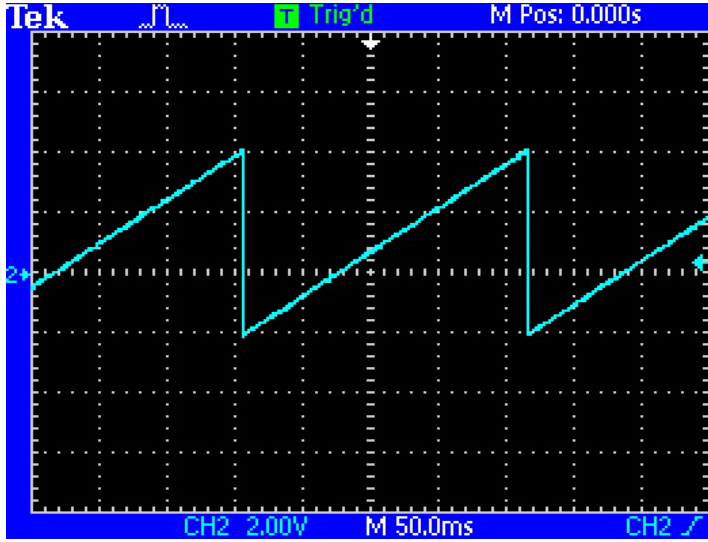


Fig. 4.13: CRO screen shot of a CSPA output which is in the form of ramp signal in the absence of photon interaction when the SDD is cooled to  $-40^{\circ}\text{C}$ . The ramp signal amplitude is electronically set between  $-2\text{ V}$  to  $4\text{ V}$  [105].

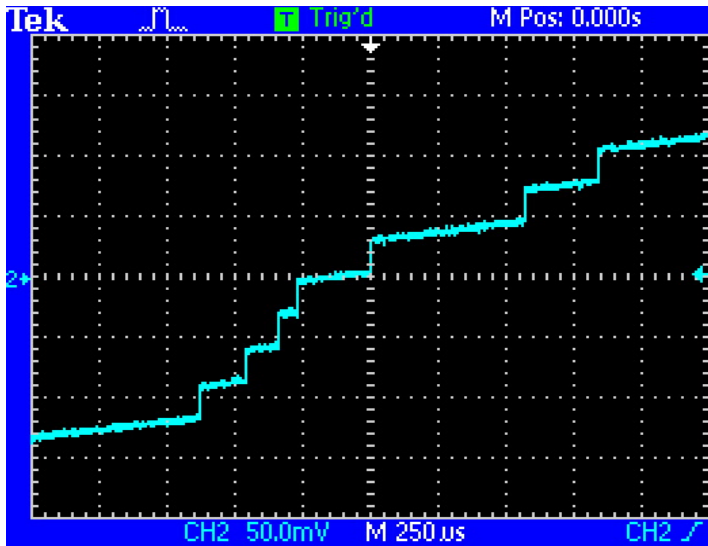


Fig. 4.14: CRO screen shot of CSPA output showing step pulses indicating the interaction of X-ray photons for the SDD operating temperature at  $-40^{\circ}\text{C}$  [105].

The step pulse amplitude at the output of charge to voltage conversion amplifier of CSPA (first stage of CSPA) is  $\sim 0.74\text{ mV/keV}$  (assuming the value of  $C_f$  is  $\sim 60\text{ fF}$ ) and at the final output of CSPA is  $\sim 5\text{ mV/keV}$ . Application Specific Integrated Circuit (ASIC) based charge readout ICs have been developed in recent times [114-116] and

shown to provide the energy resolution of  $\sim 140$  eV at 5.9 keV. Recently, a CMOS based ASIC has been developed [81] which is integrated along with the SDD module and shown to provide the energy resolution of  $\sim 125$  eV at 5.9 keV.

#### 4.3.4. Shaping Amplifier:

Shaping amplifier is generally used following the CSPA stage which performs three functions. First, the shaping amplifier provides an output pulse with faster return to the baseline than the CSPA which has peak to baseline return time of  $\sim$  few tens of micro seconds. This is especially important at high count rates, where pulses from consecutive events can ‘pile up’. Secondly, the shaping amplifier filters the noise from the preamplifier output signal by reducing the signal bandwidth as desired for the application. Finally, the shaping amplifiers also provide necessary gain to amplify the signal from CSPA which is very small (few mV/keV). Shaping amplifier is a combination of high pass and low pass filter amplifiers which reduces the signal bandwidth and thereby improves the signal to noise ratio and also provides necessary gain to match the analog to digital converter (ADC) range. The output of the shaping amplifier will be in the form of semi-Gaussian pulse and one can get close to Gaussian pulse shape by increasing number of low pass filter amplifiers in the design.

The shaping amplifier is designed with three stage amplifier, first stage is  $CR$  high pass filter amplifier which defines the desired fall time of the signal with  $C_I R_I$  time constant. It is represented by the equation (4.7)

$$V_d = V_{in} e^{-\frac{t}{\tau_d}} \quad (4.7)$$

where  $V_d$  is the signal amplitude at the output of the  $C_I R_I$  differentiator and  $\tau_d$  is the differentiator time constant. The amplifier after  $CR$  stage is known as  $CR$  amplifier

providing suitable gain to output signal having fast rise time. The output of the  $CR$  filter amplifier is given to two stage  $RC$  low pass filter amplifiers with time constants of  $R_2C_2$  and  $R_3C_3$  respectively. The two stage  $RC$  filter amplifier defines the rise time or peaking time of the pulse. The equation for one stage  $RC$  filter is given in equation (4.8)

$$V_i = V_d \left( 1 - e^{-\frac{t}{\tau_i}} \right) \quad (4.8)$$

Assuming the  $CR$  differentiator and  $RC$  integrator time constants are equal i.e.,  $\tau_d = \tau_i = \tau$ , then the equation becomes (4.9)

$$V_o = V_{in} \left( \frac{t}{\tau} \right) e^{-\frac{t}{\tau}} \quad (4.9)$$

The output of the  $CR$ - $RC$  type shaping amplifier with step input for  $\tau_d = \tau_i$  is shown in figure 4.15.

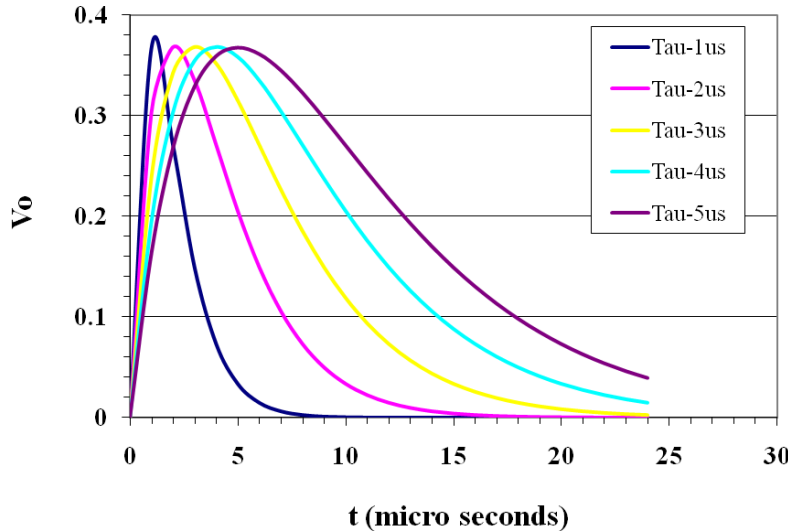


Fig. 4.15: Simulated shaping amplifier output for equal  $CR$ - $RC$  time constants.

To get the shaping amplifier output close to Gaussian, the number of  $RC$  stages has to be increased and the equation becomes (4.10)

$$V_o = V_{in} \left( \frac{t}{\tau} \right)^n e^{-\frac{t}{\tau}} \quad (4.10)$$

where  $n$  is the order of  $RC$  integrator stages and the shaping amplifier output for one stage  $CR$  filter and number of  $RC$  filters is shown in figure 4.16.

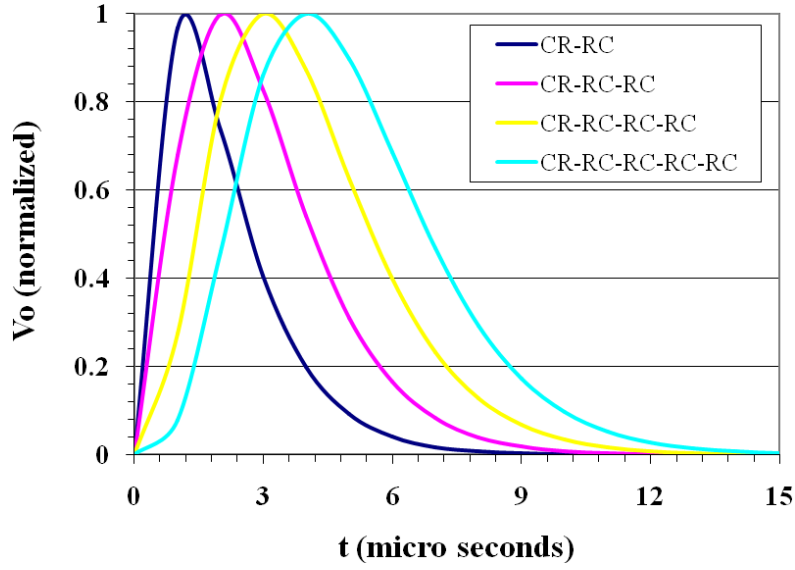


Fig. 4.16: Simulated shaping amplifier output with one  $CR$  and multiple  $RC$  stages.

The shaping amplifier has been designed using AD829 op-amp with three stage  $CR-(RC)^2$  type (5 pole) shaping. Increasing the number of  $RC$  stages will increase the hardware complexity substantially and hence limited to two stage  $RC$  filters. The block schematic and the output waveform are shown in figure 4.17 and figure 4.18. The shaping amplifier gain is decided based on the energy range covered by the spectrometer.

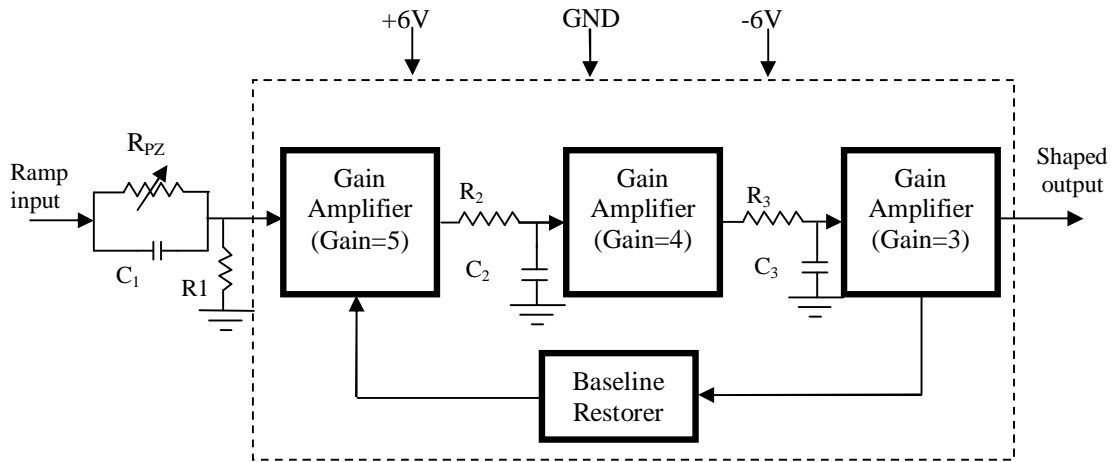


Fig. 4.17: Block schematic of  $CR-(RC)^2$  type shaping amplifier.



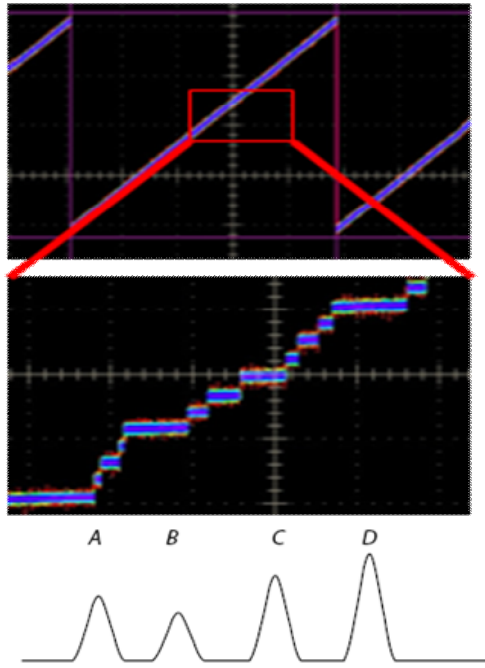


Fig. 4.18: Ramp signal – input to shaping amplifier (above), Shaping amplifier output for four signal pulses with different amplitudes (below).

The shaping time requirement is decided based on the energy resolution versus count rate. In case of APXS, the expected XRF count rate is very small and hence we decided to have shaping time of  $\sim 3.3 \mu\text{s}$  to achieve the best possible energy resolution of  $\sim 150 \text{ eV}$  at  $5.9 \text{ keV}$ . In case of XSM, it is planned with  $\sim 0.8 \mu\text{s}$  shaping time to accommodate count rates of  $\sim 10^5 \text{ counts/s}$  with energy resolution of  $\sim 200 \text{ eV}$  at  $5.9 \text{ keV}$ .

#### 4.3.5. Pole-Zero Compensation:

The signal output from the CSPA is in the form of step (reset type CSPA) or decay pulse with longer fall time (RC feedback type CSPA). When the step signal output is passed through the CR filter, the exponential decay pulse superimposed on the shaper output resulting in undershoot and hence degradation in the energy resolution due to baseline variations. Shaping amplifier has been designed by incorporating pole-zero compensation by adding a resistor  $R_{PZ}$  across the series capacitor  $C_I$  which is part of CR

high pass filter as shown in figure 4.17. The value of  $R_{PZ}$  is decided based on the shaping time constant of the shaping amplifier circuit. The resistor  $R_{PZ}$  is essential to maintain the base line due to undershoot. Under compensated or overcompensated design will distort the signal amplitude resulting in poor energy resolution.

#### **4.3.6. Base Line Restorer:**

Shaping amplifier also incorporates Base Line Restorer (BLR) which is essential to hold the base line when the design is used in high count rates as in the case of XSM. It is well known that, at high count rates, the shaping amplifier signal output goes down below the base line due to the occurrence of adjacent pulse before the settling time of the earlier occurred pulse. The magnitude of the base line shift is based on the incident photon rate and the energy of the photons. The AMPTEK make BLR1 is used in the design and it is connected in the feedback path between third and first stage of the shaping amplifier as shown in figure 4.17. BLR1 is a wide bandwidth trans-conductance amplifier with trans-conductance of  $\sim 17$  mA/volt. It amplifies both the DC baseline component and the pulse component by a large factor with output connected to low resistive load of 20 k $\Omega$ , providing voltage gain at the amplifier output of  $\sim 340$ . This output is then passed through the low pass filter which is fed to the input chain of the shaping amplifier to minimize the base line shift at the output of the amplifier chain.

#### **4.3.7. High Voltage Bias Generation for SDD:**

SDD requires three high voltages for its operation on the terminals namely outer ring  $R_{18}$  ( $R_X$ ), inner ring adjacent to anode  $R_I$  and back contact  $R_{BACK}$ . The high voltage bias and the filtering requirement are listed in the table-4.6.

**Table-4.6:** SDD HV bias voltage, current and filtering on each HV lines.

SDD Ring	Typical voltage, current	Filter requirement
R <sub>1</sub> Voltage, Current	-20 V $\pm$ 1V, 10 $\mu$ A	15 k $\Omega$ , 220 nF
R <sub>18</sub> (R <sub>X</sub> ) Voltage, Current	-130 V $\pm$ 5V, 10 $\mu$ A	500 k $\Omega$ , 47 nF (250 V)
R <sub>BACK</sub> Voltage, Current	-60 V $\pm$ 2V, < 1 nA	1 M $\Omega$ , 47 nF (250 V)

The schematic representation of the high voltage bias pin locations on the SDD module and the filter connections are shown in figure 4.19.

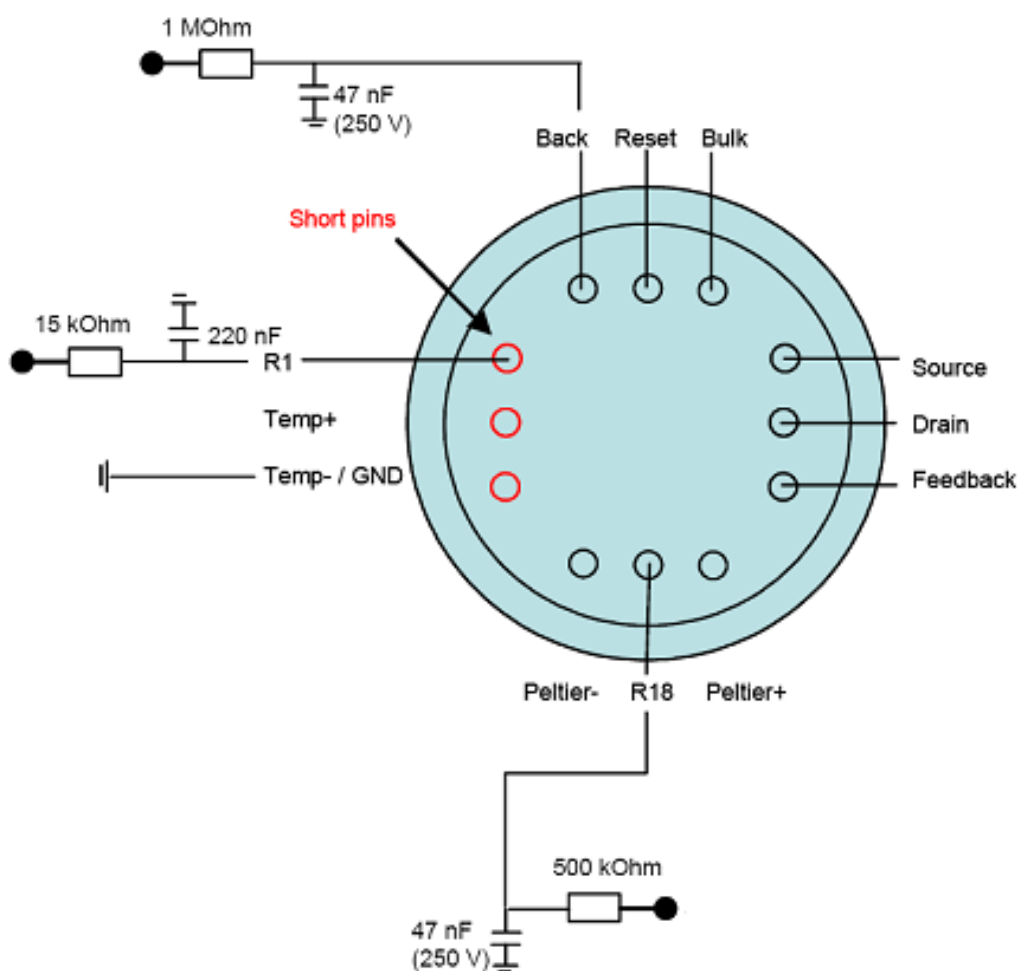


Fig. 4.19: Schematic representation of SDD with HV bias filtering requirement [Courtesy KETEK GmbH].

These high voltage biases are generated using a voltage multiplier based circuit having eleven stages of voltage multiplication with first stage being RC oscillator with frequency of about 100 kHz. Block schematic of the HV bias generation circuit is shown in figure 4.20.

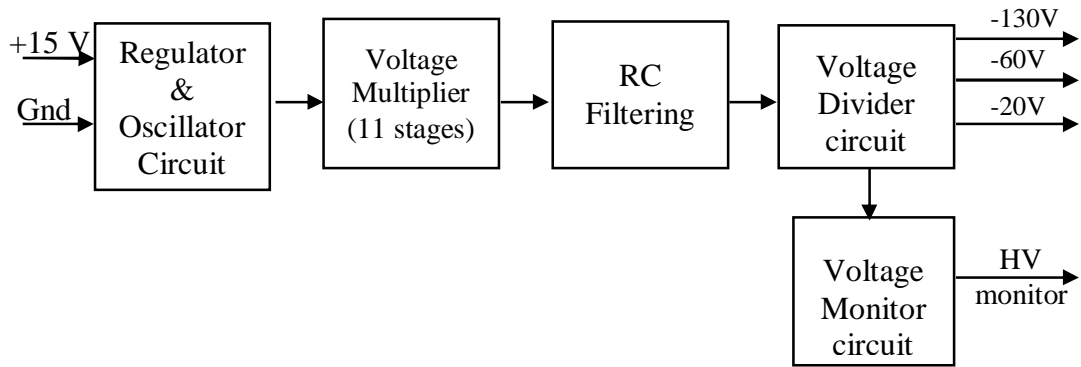


Fig. 4.20: The block schematic of HV generation circuit.

Each stage of the voltage multiplier uses Schmitt trigger buffer with diode-capacitance combination for voltage multiplication. Hex Schmitt trigger inverter CD40106 IC is used for this purpose and the voltage multiplication is carried out with 15 V bias input. Three different voltages required for SDD operation are derived using resistive voltage divider.

#### 4.3.8. Event Trigger Generator:

Event trigger generator is designed to provide indication of X-ray interaction with the detector to the digital electronics to initiate the peak detection, analog to digital conversion and further signal processing. This is done by feeding the shaping amplifier output to a fast voltage comparator, AD8561 which has fast rise time of 7 ns. The waveform representing the generation of event trigger is shown in figure 4.21.

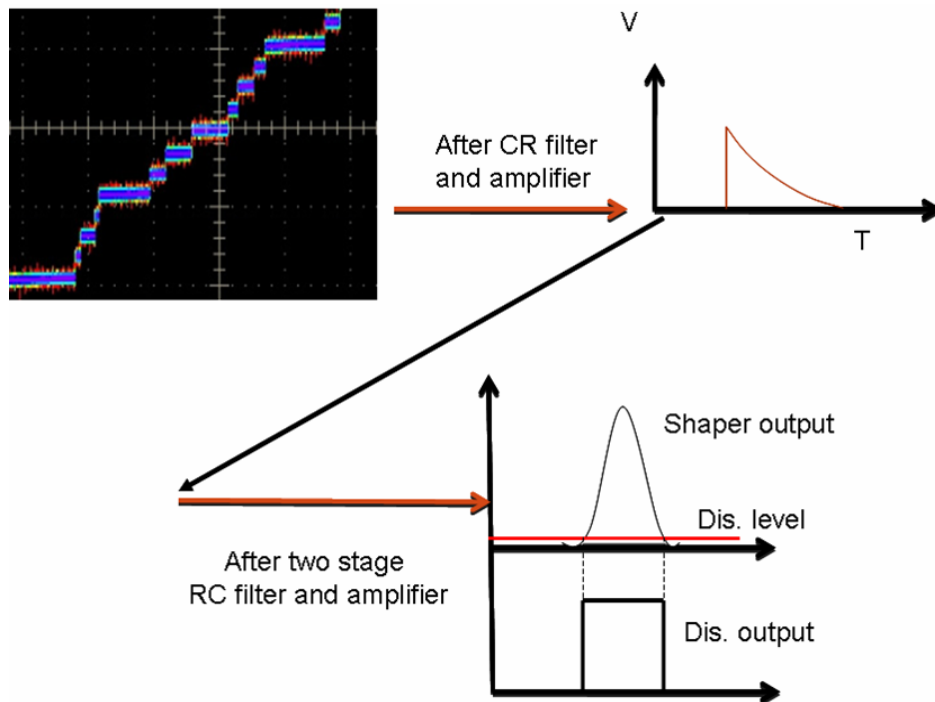


Fig. 4.21: Event trigger generation sequence.

By setting appropriate threshold voltage level to the comparator, the base level noise can be cut-off and any signal pulse above the set threshold level generates the event trigger and hence detected as valid pulse to build the spectrum.

#### 4.3.9. Peak Detector:

The energy of the incoming X-ray photon is determined by the peak amplitude of the shaping amplifier. Peak detector is therefore essential to hold the peak signal voltage amplitude of the signal from the shaping amplifier to convert it into digital value for further signal processing. The AMPTEK make peak detector PH300 is used in this design which is available in the form of hybrid module and it has been used in many space missions. Peak detector PH300 is having the following features

1. Low droop rate (10 nV/ms)
2. High speed (250 ns rise time)
3. Low power consumption (36 mW)

#### 4. Fast discharge

The peak detector PH300 operation is controlled through FPGA. FPGA allows the input signal into the peak detector as and when event trigger occurs by activating the GATE input. PH300 provides active low digital output PKDT indicating that the peak detector has detected the peak value of the input signal. On detecting the active low PKDT, FPGA closes the GATE and starts the analog to digital conversion process and data readout from the analog to digital converter (ADC). Once the conversion is over, the peak signal amplitude is discharged by making RAMP and DUMP signals active low and this is called fast discharge mode. PH300 takes  $\sim 1 \mu\text{s}$  for the discharge. This process repeats for every event and the dead time for each event conversion is the sum of pulse shaping time (peaking time), analog to digital conversion time, signal readout time from the ADC to FPGA (serial or parallel) and the peak detector discharge time (see fig. 4.22).

##### **4.3.10. Analog to Digital Converter (ADC):**

The output of the peak detector is given to ADC to convert the analog signal into digital form for further signal processing. In case of APXS, serial 12 bit ADC, AD7893 is used which is having the conversion time of  $\sim 6 \mu\text{s}$ . In case of XSM, 12 bit parallel ADC, AD7492 is planned with conversion time of  $\sim 880 \text{ ns}$ . In both cases, FPGA initiates the conversion process and readouts the data once the conversion is over. In APXS, 12 bit event data is stored in the solid state recorder onboard rover and in XSM, the instrument uses 10 bit parallel data and makes spectrum inside the FPGA for every second and then transferred to space craft. 10 bit data is shown to be sufficient for the energy resolution of  $\sim 200 \text{ eV}$  and this reduces the onboard memory requirement by 4

times compared to 12 bit data. The timing diagram showing analog to digital conversion for serial ADC is shown in figure 4.22.

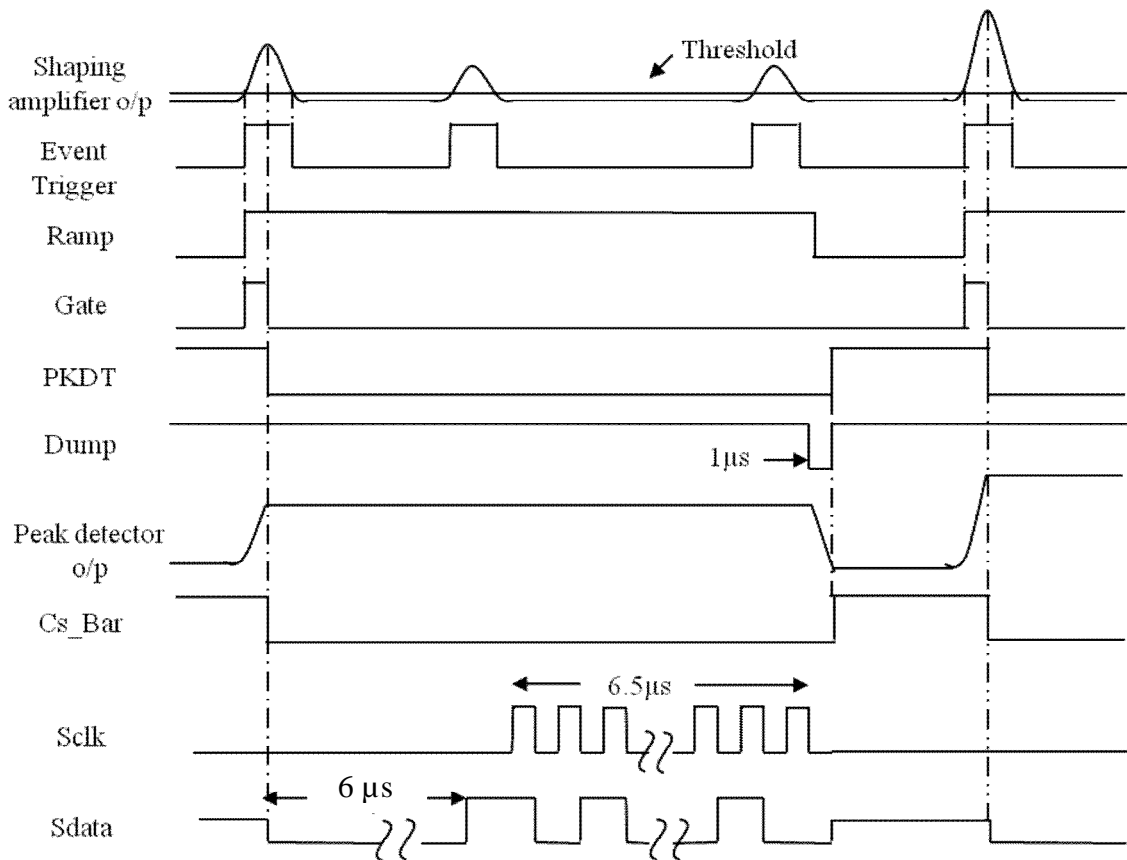


Fig. 4.22: Timing diagram representing signal and conversion at various stages of the SDD based X-ray spectrometer.

#### 4.3.11. FPGA Based Data Acquisition and Control System:

FPGA based data acquisition and control system consists of programmable FPGA A3PE1500 interfaced with reference generator, peak detector and ADC. It also has interfaces with computer through USB port using National Instruments make USB - 6343 module and LABVIEW based data readout and display system. The LABVIEW software is for ground testing and calibration of the developed system and it also has the capability to provide necessary commands for the payload operation. On occurrence of reference pulse due to X-ray interaction with the SDD, FPGA provides necessary control signals to the peak detector to hold the peak signal amplitude and initiates the analog to

digital conversion. After analog to digital conversion, the FPGA reads the digital data and makes spectrum which is then stored in the internal memory. The spectral data is then transferred to the computer for every second using USB module and the LABVIEW software acquires and updates the spectral data for every second. It also has additional capabilities for estimating spectral parameters such as energy resolution (FWHM), total counts under the peak, peak position, energy/channel and the system linearity. The FPGA A3PE1500 is a programmable FPGA used for the ground development and the same will be replaced with qualified FPGA RTAX250 for the flight version. A sample LABVIEW window is shown in figure 4.23.

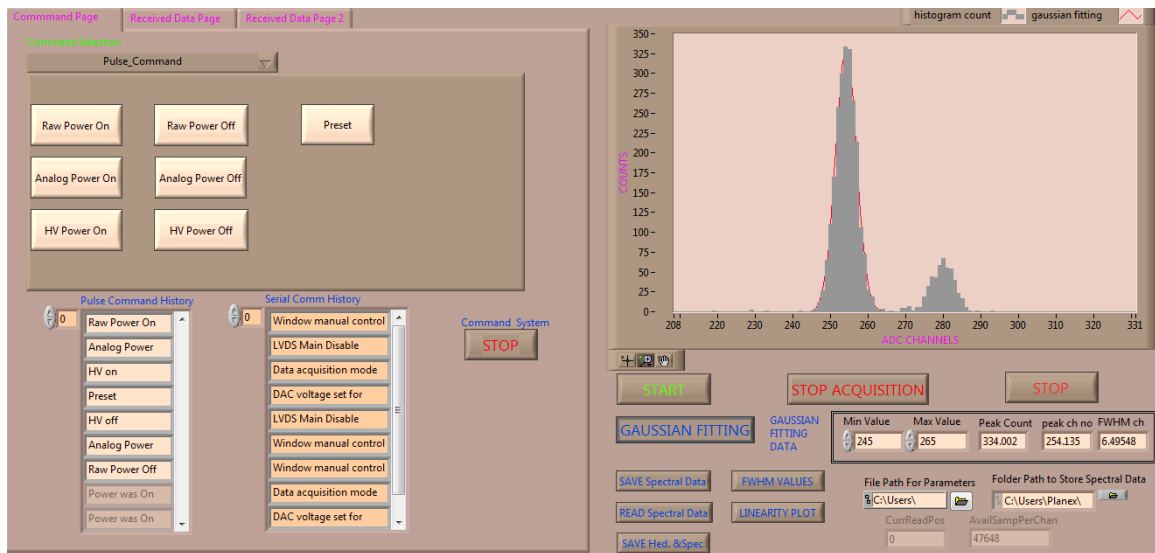


Fig. 4.23: LABVIEW window panel used for instrument operation commanding and data acquisition.

#### 4.4. EXPERIMENTAL SETUP:

The experimental setup consists of two subsystems namely front-end electronics subsystem and FPGA based data acquisition and control subsystem. The photographic view of front-end electronics and FGPA based control and readout system are shown in figure 4.24 and figure 4.25.



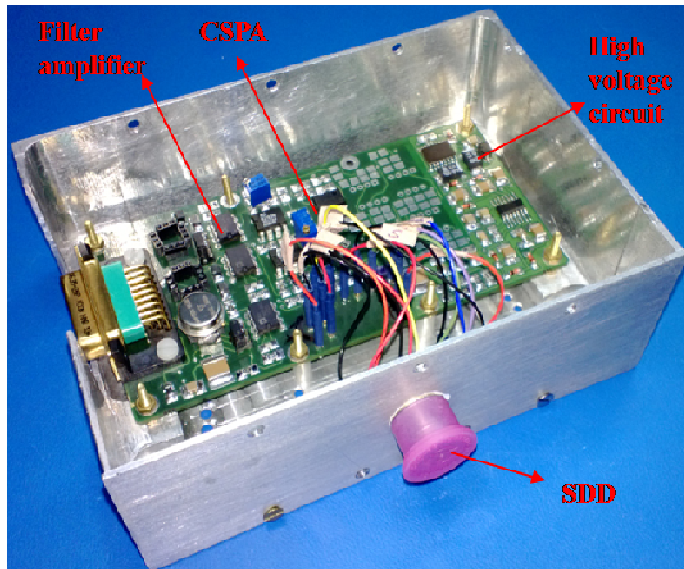


Fig. 4.24: Photographic view of the front-end electronics coupled with the SDD module [105].

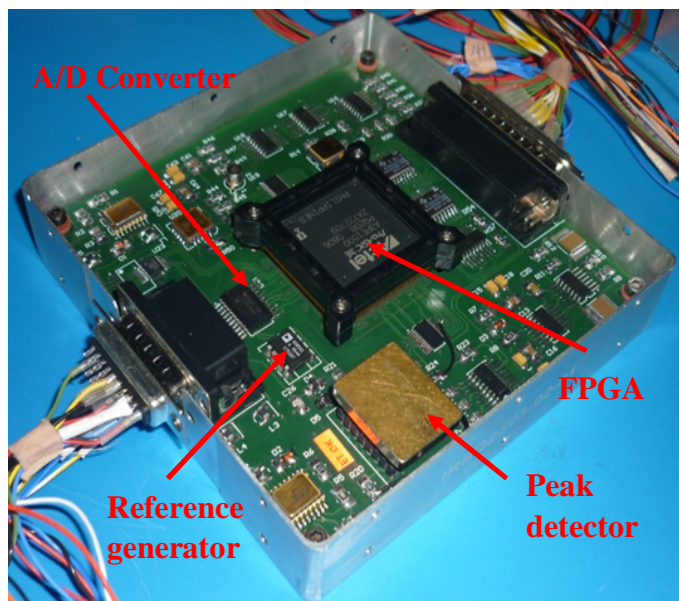


Fig. 4.25: Photographic view of FPGA based data acquisition, control system and part of FEE circuits [105].

#### 4.5. CHARACTERIZATION OF THE SDD BASED X-RAY SPECTROMETER:

The developed SDD based X-ray spectrometer is tested for various performance characteristics and shown that the instrument meets the scientific requirements of the payloads onboard Chandrayaan-2 mission.

#### 4.5.1. Energy Resolution:

The spectral energy resolution is measured from the developed SDD based X-ray spectrometer for different radioactive X-rays sources such as  $^{55}\text{Fe}$ ,  $^{241}\text{Am}$  and  $^{109}\text{Cd}$ . The SDD is cooled to  $-40^\circ\text{C}$  and shown that the spectrometer provides energy resolution of  $\sim 150$  eV at 5.9 keV for the pulse shaping time of  $\sim 3.3$   $\mu\text{s}$ . The combined spectrum is shown in figure 4.26.

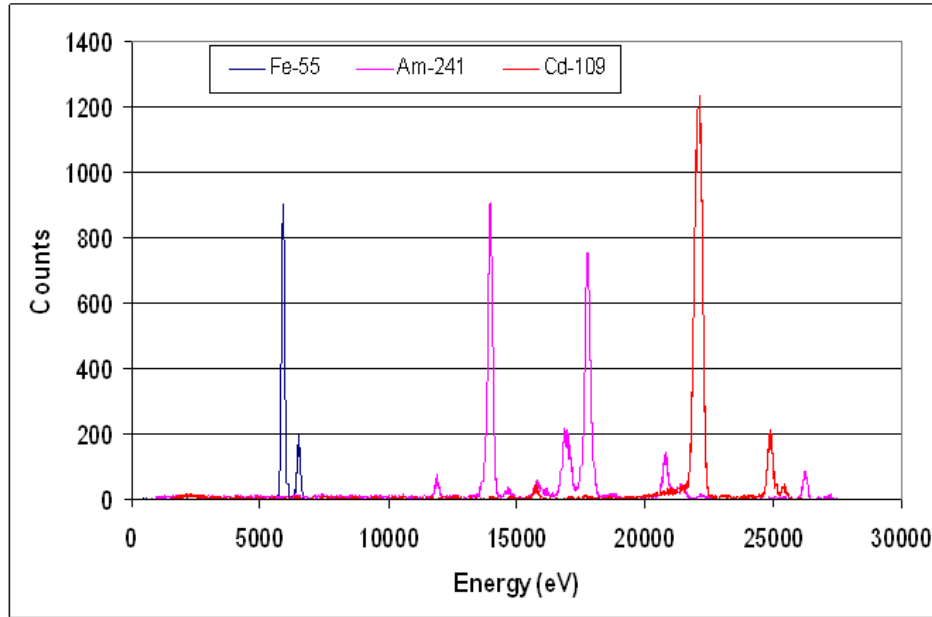


Fig. 4.26: Spectra obtained from the developed SDD based X-ray spectrometer for three radioactive X-ray sources.

The energy resolution of the developed SDD based X-ray spectrometer is compared with off-the-shelf SDD spectrometer procured from KETEK, GmbH and the spectra is shown in figure 4.27. In this case the spectrum is acquired for the pulse shaping time of 4  $\mu\text{s}$  and the detector is cooled to  $-35^\circ\text{C}$ . The FWHM at various X-ray energies for both these X-ray spectrometers are compared and shown to be closely matching as given in table-4.7.

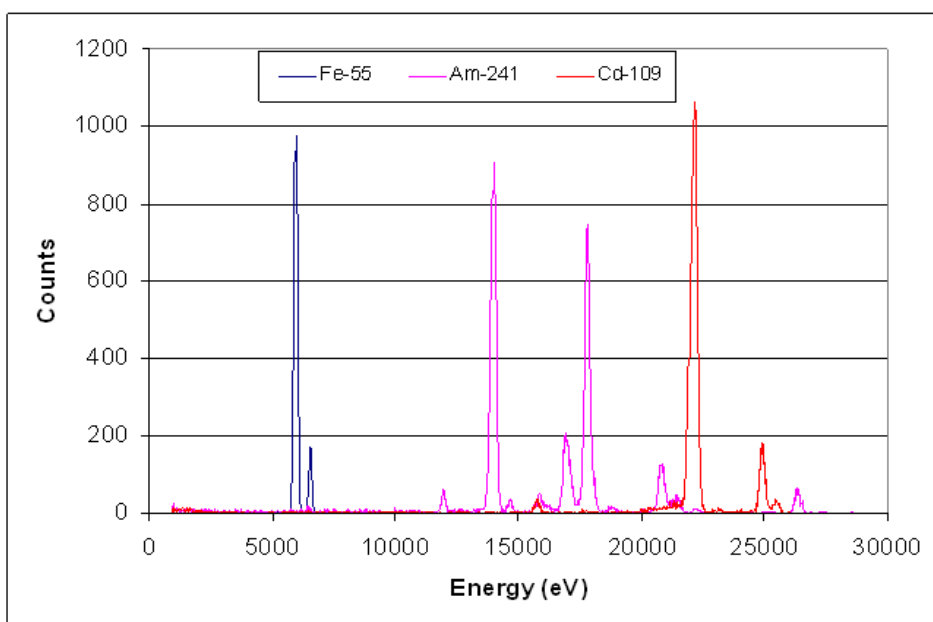


Fig. 4.27: Spectra obtained from the commercial off-the-shelf SDD based X-ray spectrometer for three radioactive X-ray sources.

**Table-4.7:** Energy resolution at different source energies obtained from developed and the commercial off-the-shelf spectrometers.

X-ray line energies	5.9 keV	13.9 keV	17.8 keV	22.1 keV
Resolution from the developed system	149 eV	240 eV	269 eV	341 eV
Resolution from off-the-shelf system	147 eV	237 eV	270 eV	336 eV

#### 4.5.2. System Linearity:

The system linearity is verified by measuring the peak energy channel position for the known X-ray energies and the system is shown to have good channel to energy linearity. The linearity plot is shown in figure 4.28. The energy per channel is obtained using this linearity plot to identify the unknown energy peaks in the spectra when the spectrometer is used for XRF measurements.

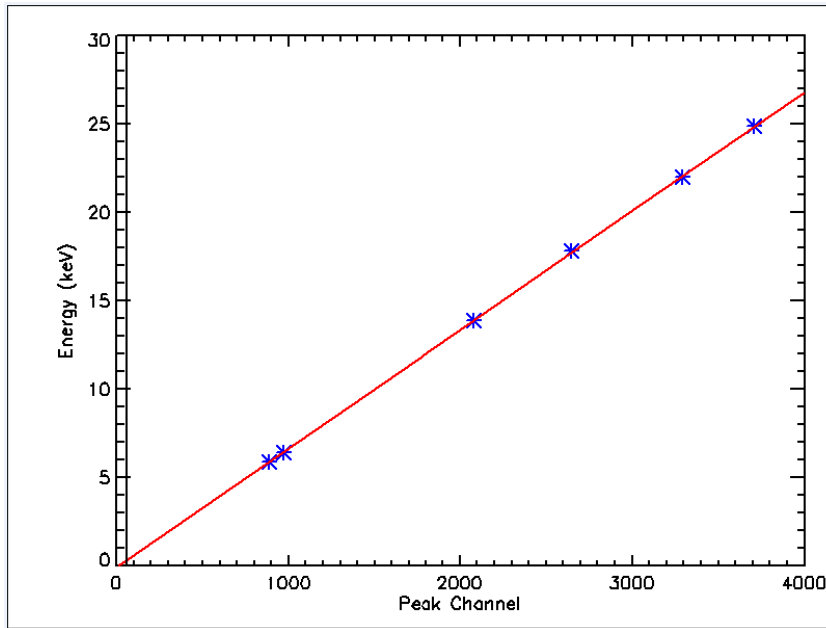


Fig. 4.28: Linearity plot of peak ADC channel versus known X-ray energies.

#### 4.5.3. Dependence of Energy Resolution with Temperature:

The spectrometer energy resolution is measured by varying the SDD operating temperature from  $\sim 20^{\circ}\text{C}$  to  $\sim -40^{\circ}\text{C}$  by maintaining the ambient temperature at  $20^{\circ}\text{C}$ . It is observed that the energy resolution does not improve beyond  $-40^{\circ}\text{C}$  and degrades from 150 eV to  $\sim 180$  eV at  $-10^{\circ}\text{C}$  and to  $\sim 350$  eV at  $10^{\circ}\text{C}$ . The change in the energy resolution with temperature is shown in figure 4.29.

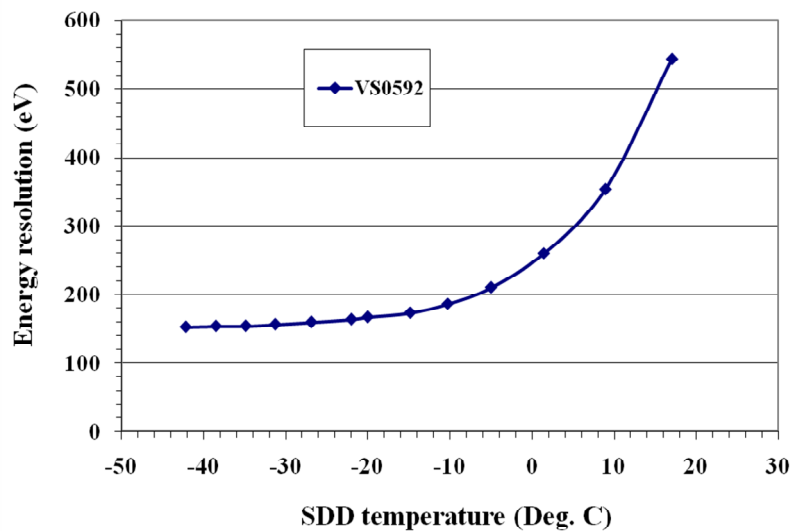


Fig. 4.29: Energy resolution versus SDD detector temperature.

#### 4.5.4. Energy Resolution Versus Pulse Shaping Time:

As discussed earlier, the signal/noise ratio of the spectrometer improves at higher pulse shaping time by reducing the signal bandwidth. It is shown experimentally that the energy resolution improves from  $\sim 200$  eV for the pulse shaping time of  $0.8 \mu\text{s}$ , 165 eV at  $1.2 \mu\text{s}$  to about 142 eV at  $3.3 \mu\text{s}$ . The performance of the developed spectrometer closely matches with the commercial off-the-shelf SDD based spectrometer as shown in figure 4.30.

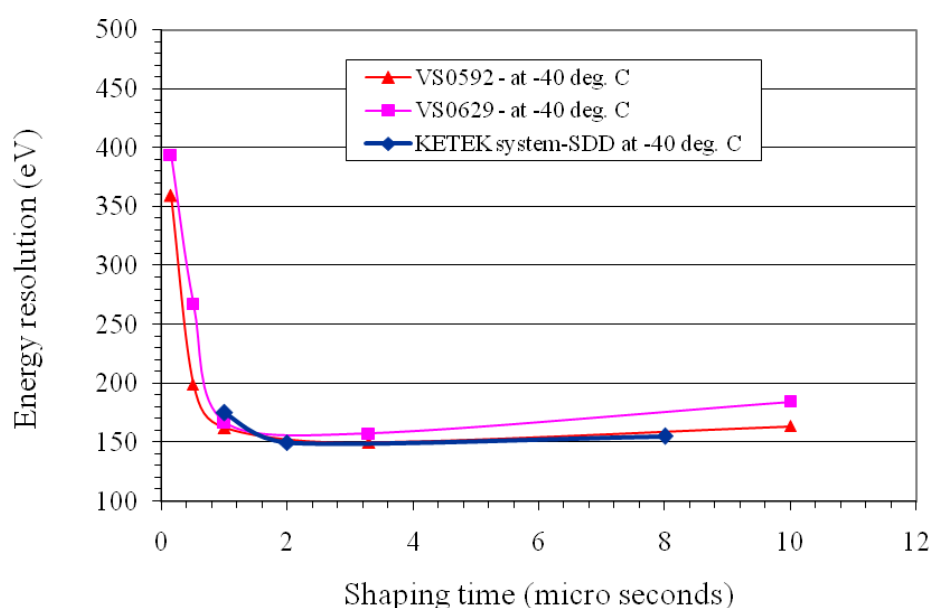


Fig. 4.30: Pulse shaping time versus energy resolution.

#### 4.5.5. Spectrometer Performance at High Count Rates:

The spectrometer performance is tested for various incident X-ray rates using X-ray source and X-ray gun. The performance results are discussed in the following subsections.

**Testing with X-ray source ( $^{55}\text{Fe}$ ):**

The energy resolution is measured for various X-ray count rates for various pulse shaping time constants to identify the suitable pulse shaping time with desired energy resolution and also to accommodate counts rates up to  $10^5$  counts/s. Initially the count rate measurement is carried out using  $^{55}\text{Fe}$  X-ray source by varying the distance between the detector and the source. The experimental setup is shown in figure 4.31. At low count rates, for the pulse shaping time of  $0.8\ \mu\text{s}$ , the observed energy resolution is about 200 eV at 5.9 keV for the detector operating temperature of  $-40^\circ\text{C}$  as shown in figure 4.32.

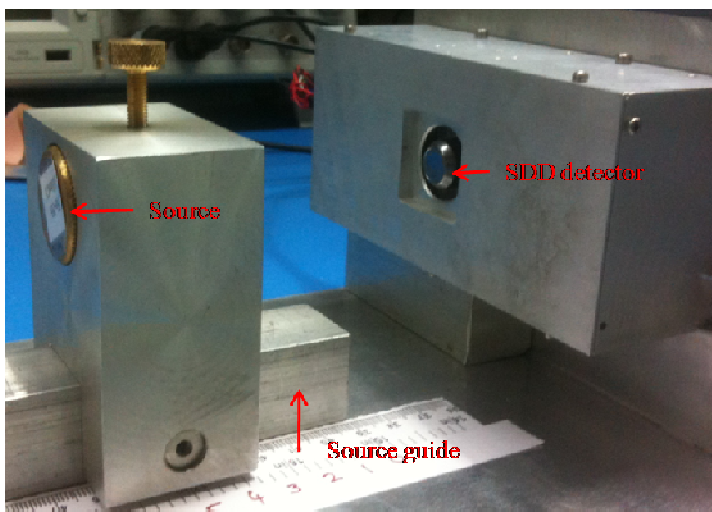


Fig. 4.31: Experimental setup for high count rate measurements using  $^{55}\text{Fe}$  source [117].

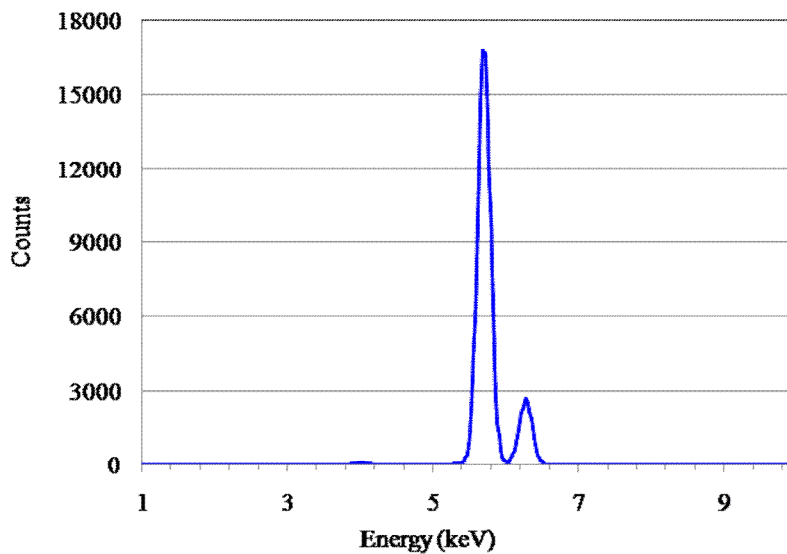


Fig. 4.32: Energy resolution measured for the pulse shaping time of  $0.8\ \mu\text{s}$  [117].

The energy resolution is also measured for the pulse shaping time of  $1.2\ \mu\text{s}$  and system provides the energy resolution of  $\sim 175\ \text{eV}$  at  $5.9\ \text{keV}$ . For both these pulse shaping times, the incident X-ray rate is varied from few hundred counts to  $\sim 150\ \text{kcts/s}$ . The spectra for various count rates for the pulse shaping time of  $0.8\ \mu\text{s}$  is shown in figure 4.33.

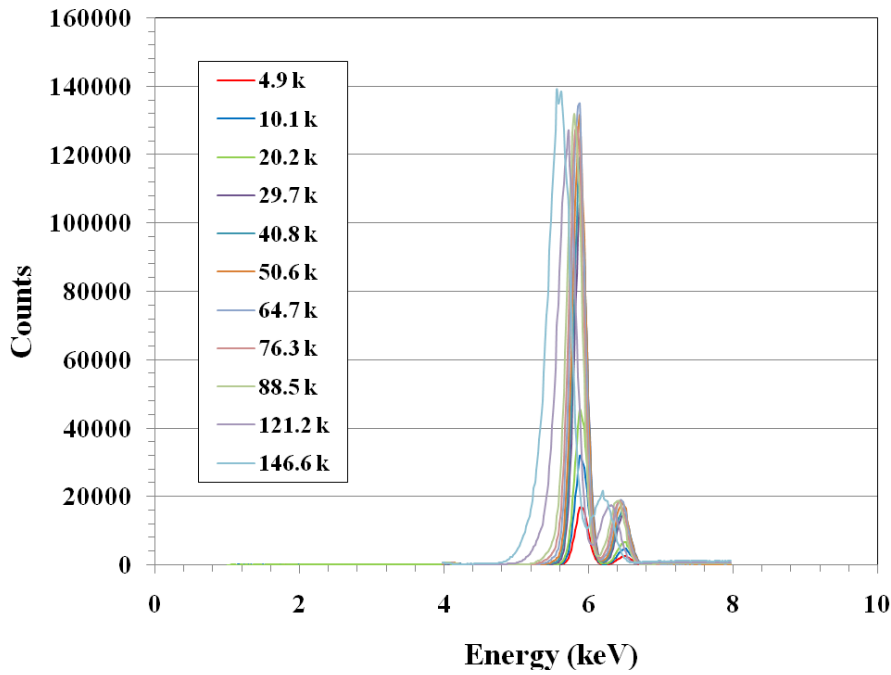


Fig. 4.33: Spectra acquired for various count rates using  $^{55}\text{Fe}$  X-ray source for the pulse shaping time of  $0.8\ \mu\text{s}$  [117].

The difference in counts seen in the spectra is due to varied count rates and the spectra are acquired for unequal times. From this experiment, it is shown that the energy resolution maintained  $\sim 200\ \text{eV}$  at  $5.9\ \text{keV}$  up to  $70\ \text{kcts/s}$  and varies to  $350\ \text{eV}$  at  $150\ \text{kcts/s}$ . For the pulse shaping time  $1.2\ \mu\text{s}$ , the resolution is stable for the count rates up to  $40\ \text{kcts/s}$  and changes drastically at higher count rates as shown in figure 4.34. The change in the peak energy position (ADC channel number) with incident count rate is shown to be fairly constant up to  $\sim 70\ \text{kcts/s}$  for the pulse shaping time of  $0.8\ \mu\text{s}$  as shown in figure 4.35.

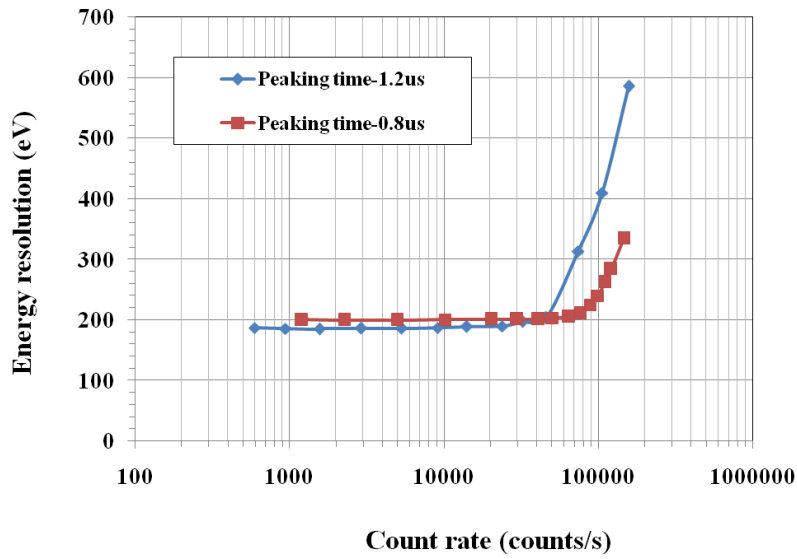


Fig. 4.34: Measured energy resolution versus count rate [117].

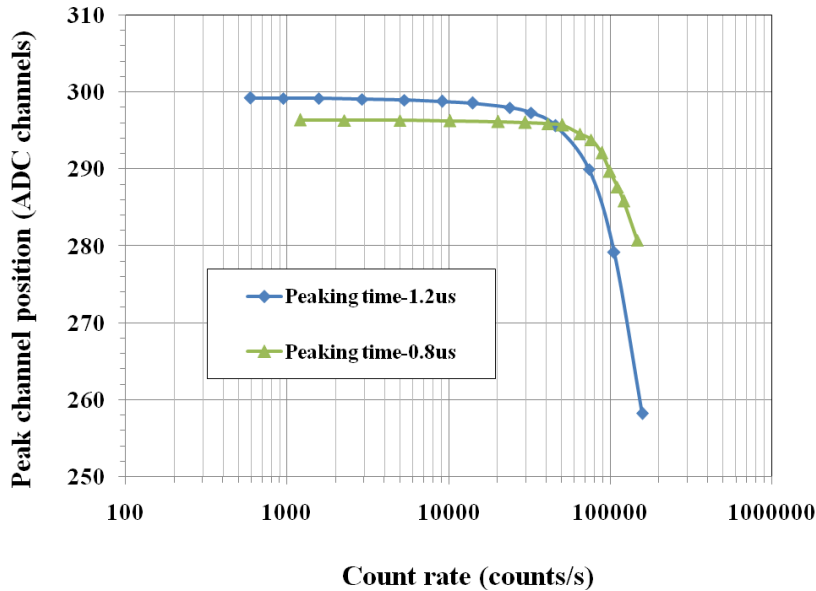


Fig. 4.35: Change in the peak energy position (ADC channel number) for various incident X-ray rates using  $^{55}\text{Fe}$  X-ray source [117].

The peak energy position changes  $< 3$  ADC channels which corresponds to  $< 60$  eV peak energy shift. For the pulse shaping time  $1.2 \mu\text{s}$ , the change in the peak energy position is much faster with incident rate compared to that of  $0.8 \mu\text{s}$ . Based on the XSM specification and performance requirement, we have chosen  $0.8 \mu\text{s}$  pulse shaping time for XSM experiment.



### ***Testing with X-ray gun:***

The spectrometer is also tested for count rates up to 230 kcts/s using X-ray gun.

The photographic view of the experimental set up is shown in figure 4.36.

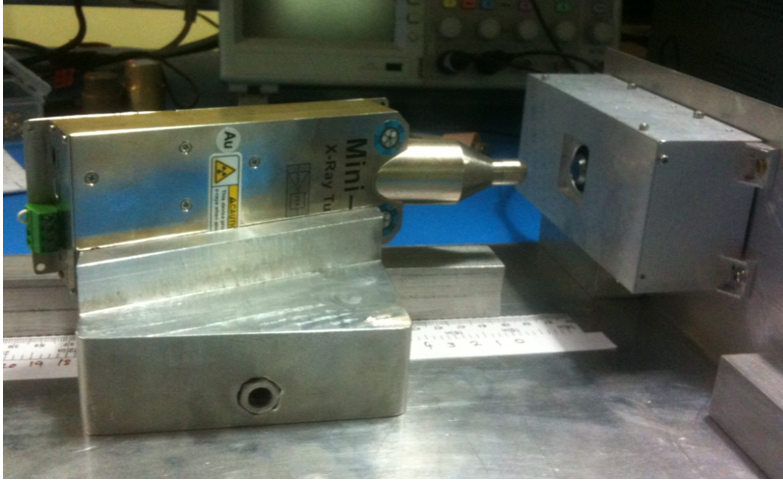


Fig. 4.36: Photographic view of SDD based X-ray spectrometer testing with X-ray gun.

The experiment is carried out by fixing the X-ray gun in a aluminum fixture and guide which has provision to slide back and forth. The incident X-ray rate from the X-ray gun is varied by changing the distance between the X-ray gun and the detector. X-ray gun provides continuum spectrum along with the energy peaks based on the target material used. The count rate and the energy spectrum can be varied by varying the X-ray gun current and the target respectively. The spectra obtained for various count rates using gold target is shown in figure 4.37. In the X-ray gun spectra, one can observe that the energy resolution is stable up to  $\sim 70$  kcts/s and degrades at higher count rates. The peak energy position is also recorded for these incident rates and shown that the peak energy position variation is  $< 4$  ADC channels, as shown in figure 4.38. The detected X-ray count is also monitored at high incident X-ray rates to determine the difference between the incident and detected X-ray events for the dead time of  $\sim 3 \mu\text{s}$ . We used fast channel with shaping time of  $\sim 0.2 \mu\text{s}$  to count the actual X-ray interaction. The experiment is carried out for both X-ray source and X-ray gun.

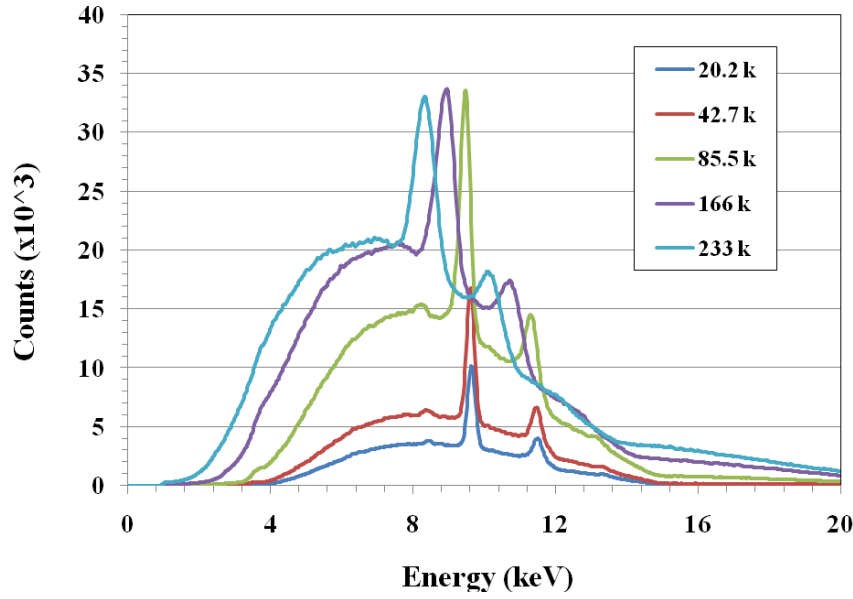


Fig. 4.37: Spectra obtained for various count rates from X-ray gun for the pulse shaping time of  $0.8 \mu\text{s}$  (only five spectrums plotted for clarity).

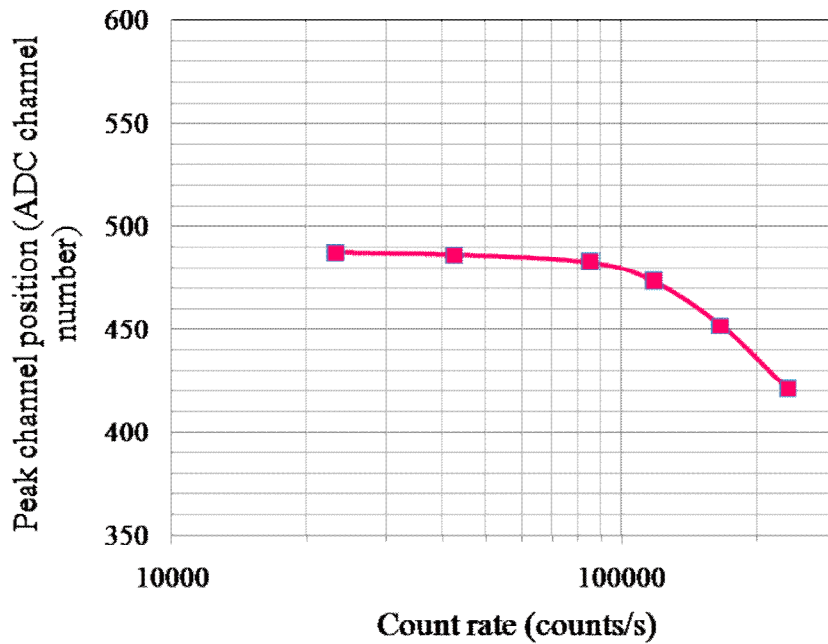


Fig. 4.38: Change in the peak energy position (ADC channel number) for various incident X-ray rates using X-ray gun for the pulse shaping time of  $0.8 \mu\text{s}$ .

It is shown that the difference between the incident rate and the number of detected X-ray events vary  $\sim 15\%$  at  $\sim 70$  kcts/s as shown in figure 4.39.

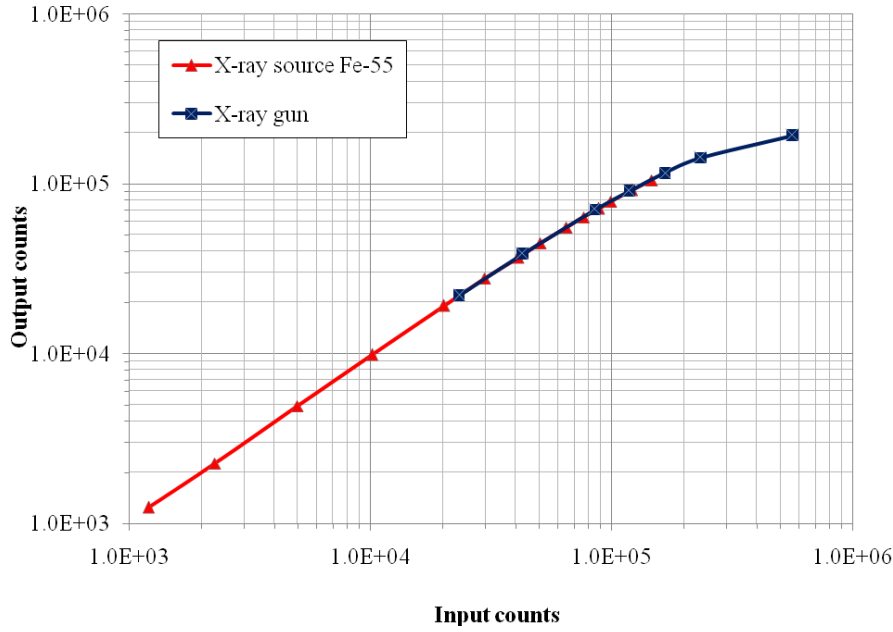


Fig. 4.39: Different between the incident and detector count rates for both  $^{55}\text{Fe}$  X-ray source and X-ray gun for the pulse shaping time of  $0.8\ \mu\text{s}$ .

#### 4.6. SUMMARY:

The SDD based X-ray spectrometer has been developed using commercial equivalent of space qualified components. It is shown that the developed spectrometer provides energy resolution of  $\sim 150\ \text{eV}$  at  $5.9\ \text{keV}$  when the SDD is cooled to  $\sim -40^\circ\text{C}$  for the pulse shaping time of  $\sim 3.3\ \mu\text{s}$ . This meets the performance requirement of APXS instrument. The energy resolution of the developed spectrometer is measured for various pulse shaping time constants to identify suitable pulse shaping time for the XSM experiment and also accommodate count rates close to  $\sim 10^5\ \text{counts/s}$  with reasonably good energy resolution of  $\sim 200\ \text{eV}$  at  $5.9\ \text{keV}$  which is required for the XSM experiment. Based on the experimental results, it is decided to have pulse shaping time of  $\sim 0.8\ \mu\text{s}$  which gives stable energy resolution and peak energy position up to  $\sim 70\ \text{kcts/s}$ . The spectrometer performance is also characterized for various detector operating temperatures, pulse shaping time constants and for various incident X-ray rates. In both cases, the low energy threshold of  $< 1\ \text{keV}$  has been achieved.

## **Chapter 5:**

### **LEAKAGE CURRENT AS A CALIBRATION TOOL FOR SPACE-BORNE EXPERIMENTS**

One important aspect of the X-ray spectrometer onboard spacecraft is its calibration at regular time intervals which is necessary to understand any performance degradation due to very hostile space conditions. In this chapter, a new technique is proposed for measuring the leakage current in the Silicon Drift Detector (SDD) based X-ray spectrometer and described the use of this technique as a tool for onboard performance estimation due to radiation damage to the SDD employed in the space-borne X-ray spectrometers. The leakage current in silicon based detector varies with the detector operating temperature and increases with the radiation dose encountered by the detector in the space environment. The proposed technique to measure detector leakage current involves measurement of the ramp frequency of the reset type charge sensitive pre-amplifier when the feedback capacitor is charged only due to the detector leakage current. Using this technique, the leakage current is measured for large samples of SDDs having two different active areas of 40 mm<sup>2</sup> (small area) and 109 mm<sup>2</sup> (large area) with 450 micron thick silicon. These measurements are carried out in the temperature range of -50°C to 20°C. At each step energy resolution is measured for all SDDs using <sup>55</sup>Fe X-ray source and shown that the energy resolution varies systematically with the leakage current irrespective of the difference among the detectors of the same as well as different

sizes. Thus by measuring the leakage current onboard, it would be possible to estimate the time dependent performance degradation of the SDD based X-ray spectrometer.

### **5.1. ONBOARD CALIBRATION REQUIREMENT:**

Several planetary missions have carried SDD based spectrometer for X-ray fluorescence measurements [94, 97] and there are missions planned with small and large area SDDs for the future planetary and astronomical observations [103]. It is well known that the performance of any silicon detector degrades due to the environmental effects as well as radiation damage and the most important parameter affected by this degradation is the energy resolution of the X-ray spectrometer. Thus in all space-borne experiments employing the silicon detectors, it is customary to include onboard calibration source/target to calibrate the detector before making any scientific measurements and also at regular time intervals to quantify any performance degradation of the detector. Towards this direction, most of the spectrometers flown in the space/planetary missions have carried calibration sources/targets for onboard performance characterization.

The X-ray spectrometers flown in the planetary missions for measuring the X-ray fluorescence requires radioactive sources (typically high strength) onboard for in-situ elemental surface composition. Such instruments always carry a sample target in the form planetary analogue or the target surface coated with the multiple chemical compounds to use it as calibration target. These calibration targets are mounted on a mechanism which brings the target in front of the detector - source assembly in case the spectrometer is mounted permanently on the lander or rover without maneuvering provision. The X-ray fluorescence from these target material due to source excitation is detected by the SDD and used for spectrometer performance calibration. Alternately, the sample targets can be permanently mounted at the desired location onboard lander or

rover where the spectrometer instrument is mounted with maneuvering provision such as robotic arm. In such case, the robotic arm is commanded to carry the instrument near the target as and when the calibration of the instrument is desired.

The X-ray spectrometers flown for remote X-ray fluorescence spectroscopy/astronomical observations in the orbiting satellite carry radioactive source(s) for onboard calibration. These radioactive sources (typically very low strength) are generally mounted on a mechanism which brings the source in front of the detector for the spectrometer calibration. This method requires a moving mechanism which is heavy and consumes more power. The mechanism weighs anywhere between few hundred grams to few kilograms based on the number of detectors used in the spectrometer. Use of moving mechanisms is generally less preferred in the space instruments. If any failure to the mechanism, the spectrometer in that case will not be usable. There are X-ray spectrometer instruments [118] flown with calibration sources mounted on the inner side of the protection doors which are used for one time calibration of the instrument before opening the protection door. In such cases, it would be difficult to find cause of any degradation in the instruments temporal performance.

The energy resolution of the SDD based spectrometer primarily depends on the detector leakage current and the baseline noise associated with the charge readout & signal processing electronics. The SDD leakage current onboard X-ray spectrometer varies with detector operating temperature and increases with radiation dose absorbed by the detector in the space environment. The baseline noise associated with the charge readout and signal processing electronics is not expected to change significantly due to the virtue of using space qualified and radiation hardened electronic components. Any degradation in the performance of readout electronics can be quantified by feeding charge pulses through a small capacitor to the electronic chain through an electronics

switch. Thus the degradation in the energy resolution of the SDD can be estimated if it is possible to measure the detector leakage current.

However, the leakage current measurement typically involves a different measurement setup with access to the bare detector chip. Since the SDD is available module form, the conventional methods of measuring detector leakage current cannot be implemented in the onboard electronics. Thus it becomes essential to have a dedicated calibration source or target, typically requiring a separate moving mechanism, in order to keep track of the performance degradation of the SDD in space. Such mechanism can be implemented in the X-ray spectrometers involving small number of detectors. However, for the future instruments involving large number of SDDs, it would be difficult to implement a separate calibration mechanism for individual detector or a single mechanism which will be very heavy and power consuming. Thus, onboard calibration of the instruments involving large number of detectors, such as the X-ray spectrometer involving 64 SDDs which we are developing for a future mission, will be a major issue.

An alternate technique is proposed for the calibration of the SDD based X-ray spectrometers by measuring the detector leakage current onboard and hence the energy resolution. A simple, novel technique has been adapted to measure the detector leakage current by measuring the ramp frequency of the reset-type charge sensitive pre-amplifier. This technique does not require any additional electronics hardware except a counter which can be part of spectrometer digital data acquisition system and thus can be easily implemented for any number of detectors. It is demonstrated that the energy resolution can be uniquely estimated from the leakage current by measuring the leakage current for two sets of SDDs having the detector area of  $40 \text{ mm}^2$  and  $109 \text{ mm}^2$  for various detector operating temperatures.

## 5.2. LEAKAGE CURRENT:

A small current of the order of microamperes is observed when reverse bias voltage is applied to a diode. This leakage current is commonly described as a combination of diffusion and generation current [119]. The leakage current relationship with device parameters can be derived using basic diode theory. Increase in the leakage current with radiation dose in the space-borne SDDs are due to defects created in the silicon crystal lattice which acts as generation centers for leakage current [120, 121] and degrades the energy resolution. These generation centers are very sensitive to the temperature variations and the detectors need to be operated at much lower temperatures to achieve the stable spectroscopic performances. The device level leakage current in silicon detector depends on the local defects [122], leakage current generated both in the depleted bulk & at the  $Si-SiO_2$  interfaces [123] and the edge effects [124]. Defects in the material are considered to be the main cause of the existence of the current noise which increases with temperature [125]. In a good quality detector system, the noise contribution due to leakage current is negligible with no radiation damage. SDDs produced in recent years use advanced processing techniques to minimize such effects on the overall performance. SDDs with low leakage current can be operated at fast shaping time and hence for high count rate applications.

The theory of p-n junction diode was established by Shockley [126]. The forward current-voltage relation of a  $p-n$  junction diode is given by the Shockley equation (5.1)

$$I = I_o \left( e^{\frac{qV}{\eta kT}} - 1 \right) \quad (5.1)$$



where  $I$  is the forward current,  $I_o$  is the leakage current (reverse saturation current),  $q$  is the electronic charge,  $V$  is the junction voltage,  $k$  is the Boltzmann's constant,  $\eta$  is the ideality constant and  $T$  is the temperature in  $K$ . The  $p$ - $n$  junction diode equation (1) contains two temperature dependant terms; one is the temperature dependence of the leakage current ( $I_o$ ) and another is temperature itself in the exponential term ( $qV/\eta kT$ ). It was later extended to recombination in the  $p$ - $n$  junction depletion region by Sah-Noyce-Shockley [127]. As per the Sah-Noyce-Shockley theory, the forward current is dominated by the recombination of minority carriers injected into the neutral regions of the junction and this type of current gives ideality constant  $\eta=1$ . The deviation of ideality constant ( $\eta>1$ ) is explained by the recombination of carriers in the space charge region mediated by recombination centers located near the intrinsic Fermi level. However, Sah-Noyce-Shockley theory does not account for the ideality constant value greater than 2 reported in AlGaIn/GaN and GaN  $p$ - $n$  junctions [128, 129]. The Shockley-Read-Hall (SRH) theory about the function of impurities, acting not only as traps but also as source of free carriers and it is dependent [130]. In this case, the value of  $\eta$  typically varies between 1 and 2 [131-133].

The leakage current is the noise source and can be used as a indicator of performance of the semiconductor detector and the leakage current is commonly described as a combination of diffusion and generation current [119]. The diffusion current is due to the minority carriers generated in the neutral region and the diffusing is negligible for fully depleted to the edge of the depletion region and therefore, it is independent of the applied reverse bias voltage, at least until the full depletion reached. When  $N_D$  is small, the diffusion current increases. The diffusion current density is given in equation (5.2)

$$J_{Diff} = q \sqrt{\frac{D_p}{\tau_p}} \frac{n_i^2}{N_D} \quad (5.2)$$

where  $D_p$  is the diffusion coefficient,  $\tau_p$  is the minority carrier life time,  $n_i$  is the intrinsic carrier concentration,  $N_D$  is the doping concentration of the substrate. This current is negligible for the fully depleted detector. Generation current is due to the generation of charge carriers in the depletion region. The generation current can be reduced by using pure and defect free material. One has to keep the detector temperature low in a controlled environment. The generation current density is given in (5.3)

$$J_{gen} = q \frac{n_i}{\tau_e} W \quad (5.3)$$

where  $W$  is the depletion width,  $\tau_e$  is the effective life time and  $1/\tau_e$  gives generation rate in the depletion region. Then the total current becomes (5.4)

$$I_o = J_{Diff} + J_{gen} = q \sqrt{\frac{D_p n_i^2}{\tau_p N_D}} + q \frac{n_i}{\tau_e} W \quad (5.4)$$

If the generation centers are distributed uniformly, the generation current is directly proportional to the depletion width from where the generated carriers are collected. The depletion width is given in equation (5.5)

$$W = \sqrt{\frac{2\epsilon_s}{qN_D}} (V_{bi} + V_R) \quad (5.5)$$

where  $V_{bi}$  is the built in reverse bias voltage,  $V_R$  is the applied external reverse bias voltage. For the high resistivity silicon,  $N_D$  is small,  $W$  is large and hence the generation current will increase. The generation current is proportional to  $\sqrt{V_R}$  and the activation energy which is  $\sim 0.6$  to  $0.9$  eV, depending on the energy level of the generation centers. The generation rate is very important factor which is given in (5.6)

$$\frac{1}{\tau_e} \propto \frac{N_t v_{th} \sigma_0 n_i}{2 \cosh \left[ (E_t - E_i) / kT \right]} \quad (5.6)$$

where  $N_t$  is the density of the states of the generation center,  $E_t$  is the energy level of the generation center,  $v_{th}$  is the electron thermal energy,  $\sigma_0$  is the capture cross section. To reduce the generation current, the process should be clean to reduce  $N_t$ . The leakage current in a reverse biased fully depleted junction can be expressed in terms of minority carrier density and carrier diffusion length as given in equation (5.7)

$$I_o = q \left( \frac{D_p p_{n0}}{L_p} + \frac{D_n n_{p0}}{L_n} \right) \quad (5.7)$$

where  $D_{n,p}$  is the diffusion coefficients for the charge carriers,  $L_{n,p}$  is the diffusion length which is  $\sqrt{D_{n,p} \tau_{n,p}}$  and  $n_{p0}$ ,  $p_{n0}$  are the minority carrier density in each side at thermal equilibrium. This leakage current reaches saturation on electrical breakdown as the reverse voltage is increased. The breakdown can be explained by either avalanche mechanisms which is due to the charge multiplication collisions with the lattice or by Zener breakdown, based on the quantum mechanical tunnel effect or by thermal instability. In the reverse bias condition, the free charge carriers density is low in the depleted region (bulk) and thus the recombination is improbable. The main effect is the generation current. Measuring the current in a fully depleted condition is good method to evaluate the radiation damage in the detector as the magnitude of this current is proportional to the density of the defects induced by the radiation. The generation current strongly depends on the temperature as described in equation (5.8)

$$I_o(T) \propto T^2 e^{-\frac{E_g}{\eta kT}} \quad (5.8)$$

where  $I_o(T)$  is the generation current and  $E_g$  is the bandgap energy. The bandgap energy is temperature dependent as given in Varshni equation [24] The magnitude of the current at temperature  $T_2$  compared to the temperature at  $T_1$  is given in equation (5.9)

$$I_o(T_2) = I_o(T_1) \left( \frac{T_2}{T_1} \right)^2 e^{-\frac{E_g}{\eta k} \left( \frac{1}{T_2} - \frac{1}{T_1} \right)} \quad (5.9)$$

where  $I_o(T_1)$  is the leakage current at temperature  $T_1$  and  $I_o(T_2)$  is the leakage current at temperature  $T_2$ . In silicon detectors, the leakage current reduces to half for every 7° decrease in the detector temperature.

### 5.3. LEAKAGE CURRENT MEASUREMENT TECHNIQUE:

The pulse reset type CSPA (discussed in chapter-4) configuration allows us to measure the detector leakage current by directly integrating in to the feedback capacitor. The charge stored in the feedback capacitor is removed by providing reset pulses to the junction of FET gate, detector anode and the feedback capacitor (see figure 5.1) through the reset diode at a time when the charge across the feedback capacitor reaches the predefined threshold level. Hence the output of the reset type CSPA will be in the form of ramp signal. The leakage current of the SDD (in the absence of X-ray interaction) can be obtained by measuring the ramp signal amplitude ( $V_{RAMP}$ ) at the output of charge to voltage conversion stage of CSPA and frequency ( $F_{RAMP} = 1/T_{RAMP}$ ) using equation (5.10) with the known value of charge integrating feedback capacitor  $C_f$ .

$$I_o = C_f \frac{V_{RAMP}}{T_{RAMP}} \quad (5.10)$$

The ramp signal frequency at the output of the CSPA will depend on the magnitude of the leakage current generated by the SDD in the absence of any photon

interacting with the detector. In the presence of photon interactions, the ramp signal frequency varies with energy and rate of photon interacting with the detector and they appear as step pulses on the ramp signal.

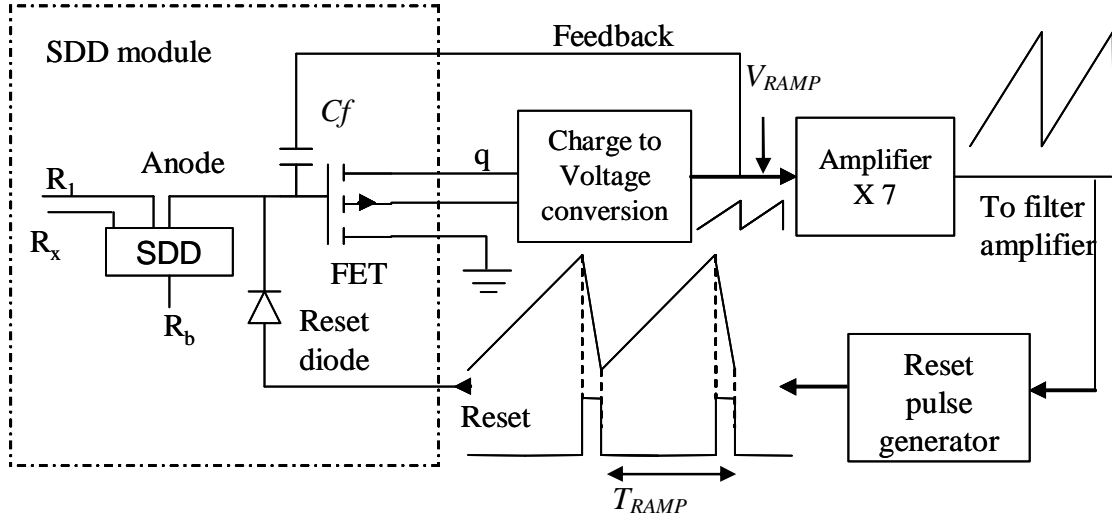


Fig. 5.1: Block schematic of pulse reset type Charge Sensitive Pre-Amplifier (CSPA) design [134].

The leakage current can be measured by counting the reset pulses with fixed ramp signal amplitude and known feedback capacitance. This technique does not require any additional electronics hardware except a counter which can be part of spectrometer digital data acquisition system and thus can be easily implemented for any number of detectors. To estimate the leakage current using equation (5.10), it is essential to know the value of  $C_f$  accurately along with the precise measurement of  $V_{RAMP}$  and  $T_{RAMP}$ . Estimation of  $C_f$  is described in the next sub section.

## 5.4. MEASUREMENT RESULTS:

### 5.4.1. Measurement of Feedback Capacitance ( $C_f$ ):

Accurately measuring the value of charge integrating feedback capacitor is essential to precisely obtain the leakage current of the SDD as given in equation (5.10). The feedback capacitor is part of SDD module which defines the gain of the charge to voltage conversion stage of the CSPA. The value of feedback capacitor is obtained by using standard charge to voltage conversion using equation (5.11).

$$C_f = \frac{Q_{in}}{V_o} \quad (5.11)$$

where  $C_f$  is the value of feedback capacitor,  $Q_{in}$  is the charge induced in the SDD for a given photon energy and  $V_o$  is the amplitude of the step pulse on the ramp signal at the output of charge to voltage conversion stage of the CSPA. The charge  $Q_{in}$  is known for the known X-ray photon energy and the voltage pulse amplitude  $V_o$  can be measured with known value of feedback capacitor. Directly measuring the amplitude of step pulse at the output of charge to voltage conversion amplifier is practically difficult as the step pulse amplitude is  $\sim 0.74$  mV/eV (assuming feedback capacitor value of 60 fF obtained from the manufacturer) and the voltage step voltage output after the gain stage of the CSPA is  $\sim 5$  mV/keV. Hence the output of CSPA is further amplified by the shaping amplifier. The shaping amplifier output is recorded for known X-ray energies (5.9 keV, 13.9 keV and 17.8 keV) using  $^{55}\text{Fe}$  and  $^{241}\text{Am}$ . Dividing these signal amplitudes by the actual system gain (CSPA gain amplifier + shaper amplifier gain) provides the signal amplitude at the output of the charge to voltage conversion stage of the CSPA for these X-ray energies.

The gain stages of CSPA gain amplifier and the shaping amplifier are calibrated separately using tail pulse generator (Berkeley Nucleonic make Model BH-1, Tail Pulse Generator). Though the theoretical gain of each stage is known, it is essential to have real gain numbers to accurately estimate the  $C_f$  and the leakage current. The single stage CSPA gain and the three stage shaping amplifier gain are obtained from the plots shown in figure 5.2 and figure 5.3 respectively.

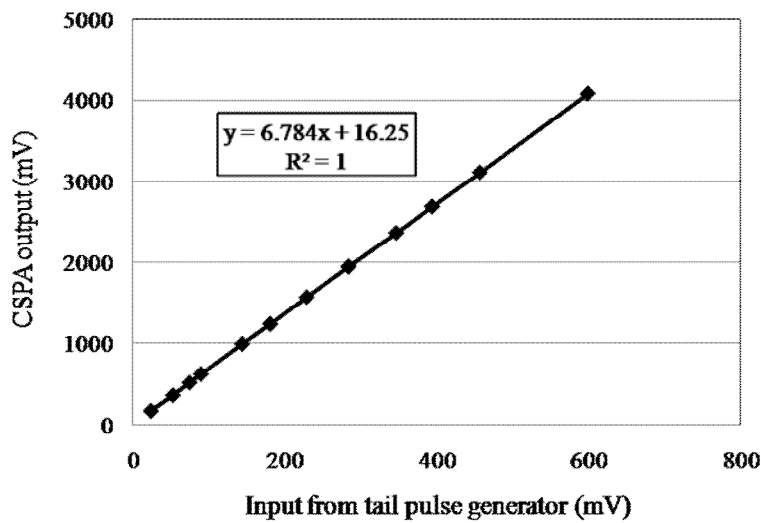


Fig. 5.2: Gain calibration of CSPA gain amplifier stage using tail pulse generator.

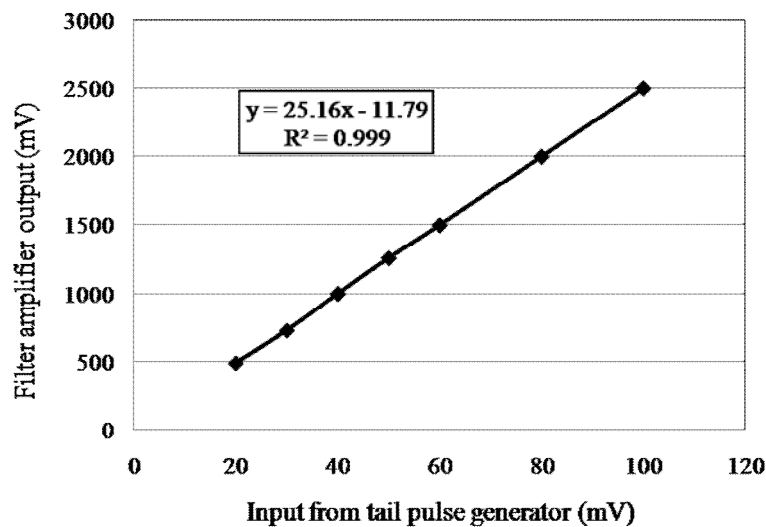


Fig. 5.3: Gain calibration of three stage shaping amplifier using tail pulse generator.

In case of CSPA amplifier calibration, the input from the tail pulse generator is varied from  $\sim 10$  mV to 600 mV and the gain values are obtained by storing the corresponding signal output. From this measurement, it is observed that the gain of the CSPA gain amplifier is  $\sim 6.78$ . Similarly, the input to the shaping amplifier is varied from 20 mV to 100 mV and recorded the corresponding signal output. The gain of the shaping amplifier is found to be  $\sim 25.16$ . The total gain is  $\sim 170.58$ . After the gain calibration, X-ray sources  $^{55}\text{Fe}$  and  $^{241}\text{Am}$  are kept one at a time in front of the SDD based spectrometer and recorded the shaping amplifier output and also measured the energy spectrum. The signal amplitude at the output of the shaping amplifier for the X-ray energies of 5.9 keV, 13.9 keV and 17.8 keV are derived from both recorded data and also from the measured spectrum considering the analog to digital converter range. Both these amplitude measurements closely match. Then dividing the signal amplitude with the total system gain gives the step voltage amplitude at the output of the charge to voltage conversion stage of the CSPA and thereby one can derive the value of  $C_f$  with known charge for the given incident X-ray energy. The value of  $C_f$  derived for three different X-ray energies is found to be  $\sim 63$  fF as shown in figure 5.4.

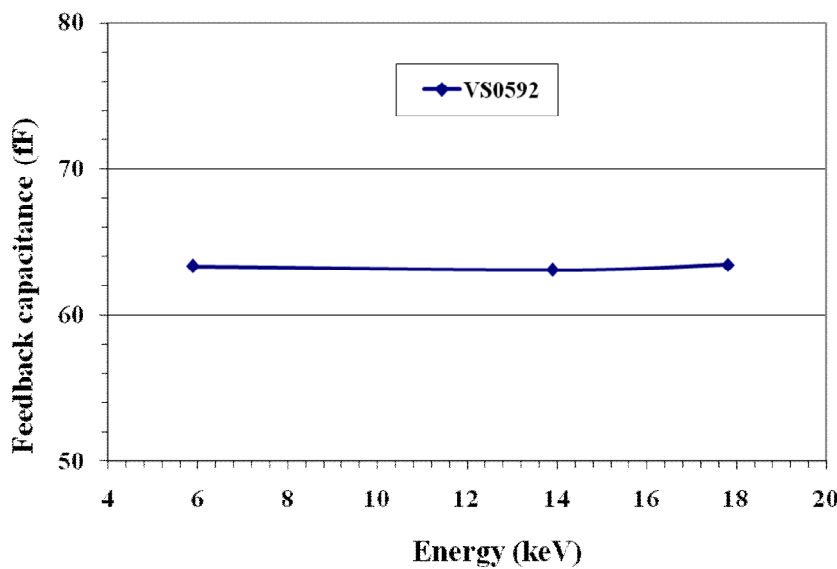


Fig. 5.4: Measured value of feedback capacitance for three different X-ray energies.



The measured value of feedback capacitor for three X-ray energies 5.9 keV, 13.9 keV and 17.8 keV are 63.31 fF, 63.08 fF and 63.43 fF respectively for the one of the small area SDD module. The experiment is repeated for 3 more small area SDDs and 8 large area SDDs in the similar operating condition using the same experimental setup and shown that the feedback capacitance varies from ~ 60 fF to ~ 66 fF between the SDD modules as shown in figure 5.5.

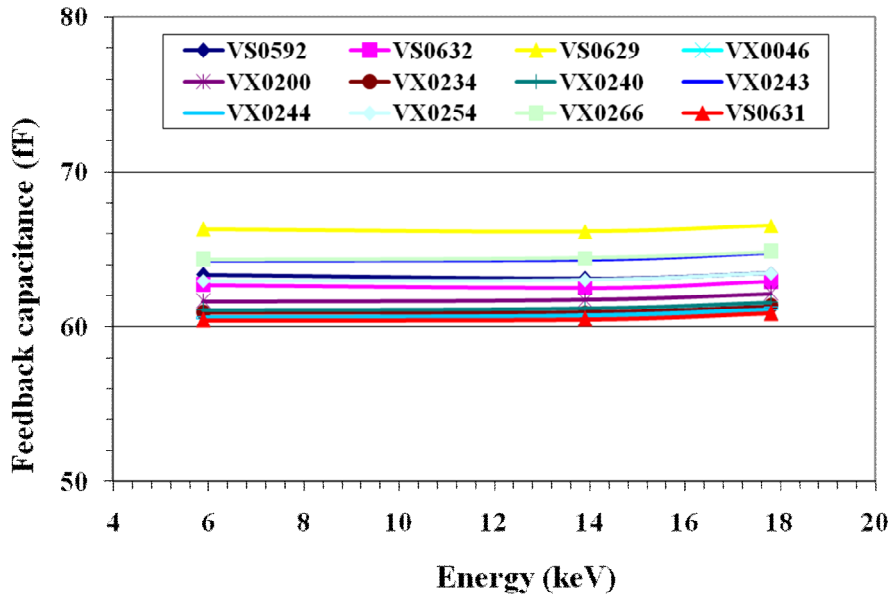


Fig. 5.5: Feedback capacitance value measured for three X-ray energies for small and large area SDDs (The serial number starts with VS series are small area SDDs and VX series are large area SDDs) [105].

The serial number starts with VS series are small area SDDs and VX series are large area SDDs. The variation in the measured value of feedback capacitance is  $< 0.5$  fF for three X-ray energies which is less than 1% for all SDDs and the feedback capacitance is shown to be varying ~ 10% between the SDD modules.

#### 5.4.2. Measurement of Leakage Current:

The ramp signal frequency ( $F_{RAMP} = 1/T_{RAMP}$ ) is measured at the output of CSPA with the fixed ramp signal amplitude in the laboratory environmental condition by

counting the reset pulses. During the measurement, the SDD with readout electronics enclosure is mounted on a thick aluminium plate to maintain the assembly and the SDD at stable temperature. The experiment is carried out in the room temperature of  $\sim 20^{\circ}\text{C}$  without any input flux (dark condition). The ramp signal amplitude is set between  $-2\text{ V}$  to  $+4\text{ V}$  in the CSPA and the temperature of the SDD is varied by varying the Peltier power and measured the ramp signal frequency. At each step, no data is recorded initially for  $\sim 5$  minutes to maintain the SDD at stable temperature and then measured the ramp signal frequency. It is observed that the ramp signal frequency varies from  $\sim 10\text{ kHz}$  at  $20^{\circ}\text{C}$  to  $\sim 5\text{ Hz}$  at  $-40^{\circ}\text{C}$  for one of the small area SDD. The experiment is repeated by changing the peak-peak ramp signal amplitude to  $-4\text{V}$  to  $+4\text{V}$ ,  $0$  to  $+4\text{V}$  and observed that the ramp signal frequency varies systematically with ramp signal amplitude as shown in figure 5.6.

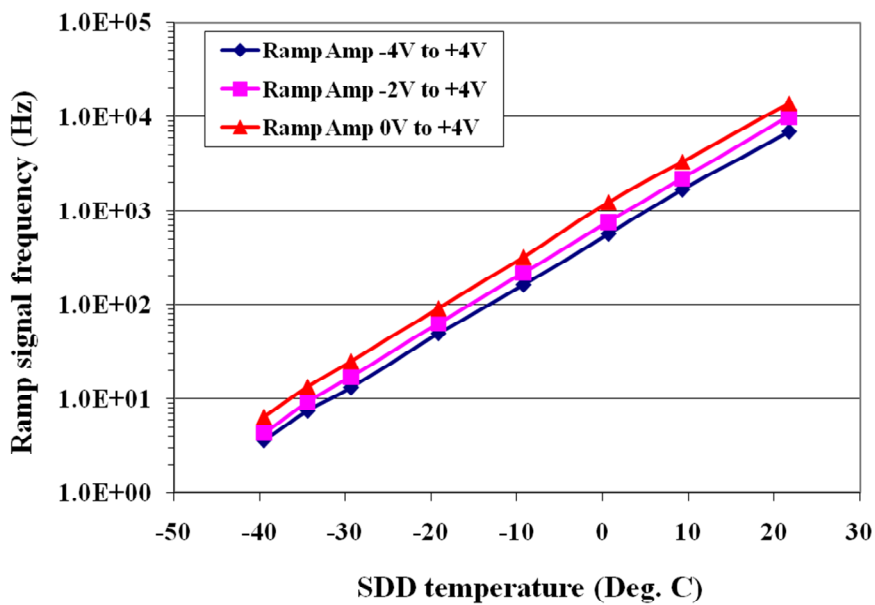


Fig. 5. 6. Ramp signal frequency measured for different detector temperatures by setting three different ramp signal amplitudes [134].

It was observed that at lower SDD operating temperatures, the rate of change of ramp signal frequency did not follow the exponential trend. Later, it was established that the non exponential trend in the ramp signal frequency at lower temperatures is due to

the stray light when the SDD and the readout electronics is kept open during the measurement. The experiment is repeated by covering the experimental setup with aluminium enclosure and observed that the rate of change of ramp signal frequency follows the exponential trend. Similar measurement is also carried out for a large area SDD detector having  $109 \text{ mm}^2$  area (SDD No. VX0234) and observed that the ramp signal frequency varies from  $\sim 13 \text{ kHz}$  at  $20^\circ\text{C}$  to  $20 \text{ Hz}$  at  $-50^\circ\text{C}$ . The comparison between the small and large are SDD is shown in figure 5.7.

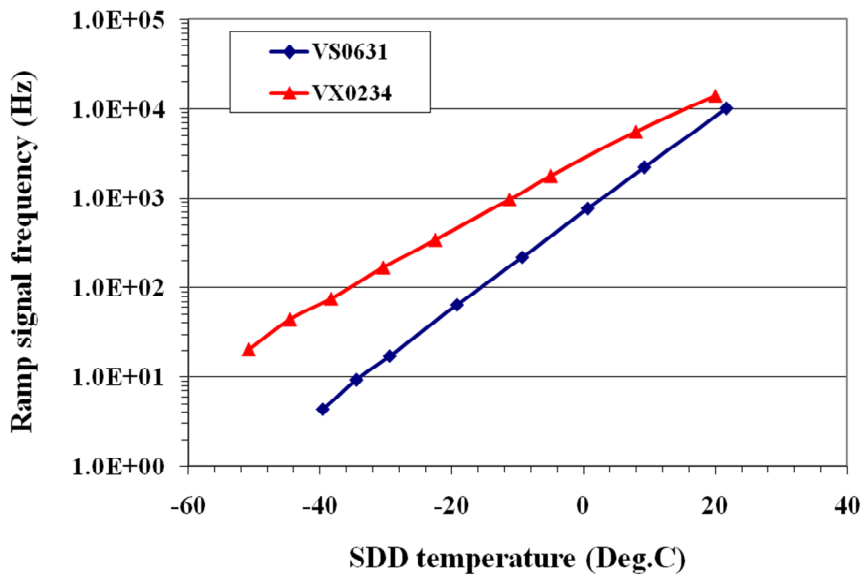


Fig. 5.7: Ramp signal frequency measured for small and large area SDDs for different temperatures [105].

Measurement is repeated for all the SDDs and observed that the ramp signal frequency varies from few kHz to  $\sim 10 \text{ kHz}$  for small area SDDs and  $\sim 13 \text{ kHz}$  to  $\sim 40 \text{ kHz}$  for large area SDDs at room temperature. The ramp signal frequency is about few Hz for small area SDDs at  $-40^\circ\text{C}$  and about few tens of Hz for large area SDDs at  $-50^\circ\text{C}$ . After the measurement of  $C_f$ ,  $V_{RAMP}$  and  $T_{RAMP}$ , one can estimate the leakage current using the equation (5.10). The leakage current is estimated for different sets of ramp signal amplitude and shown that the magnitude of the leakage current obtained is independent of the set ramp signal amplitude. This is due to the smaller set ramp signal

amplitude which increases the ramp signal frequency proportionately. The non-exponential trend is also observed in the leakage current due to the stray light as observed in the frequency measurements. The measured leakage current varies from  $\sim 0.6$  nA at  $20^{\circ}\text{C}$  to  $\sim 0.2$  pA at  $-40^{\circ}\text{C}$  for a  $40\text{ mm}^2$  area SDD as shown in figure 5.8.

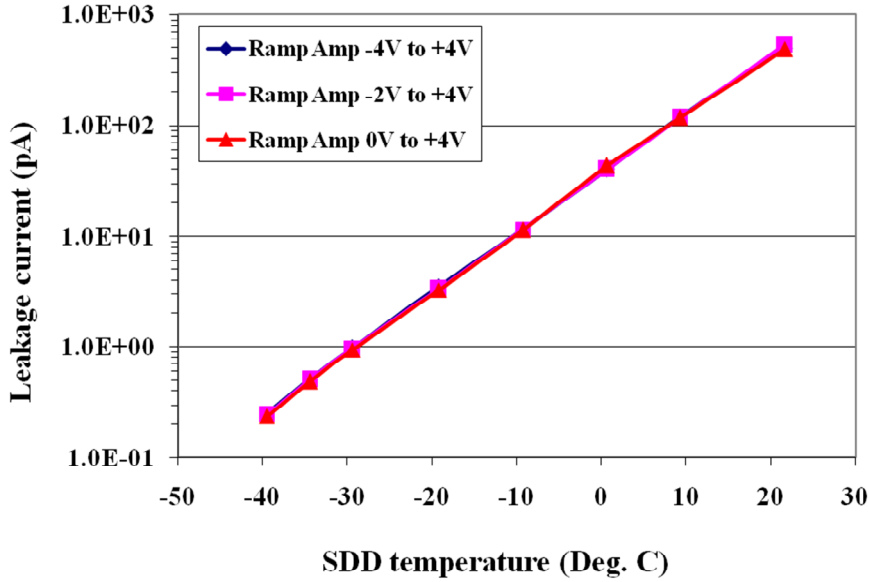


Fig. 5.8: Leakage current measured for three different ramp signal amplitudes with temperature [134].

The leakage current measurement experiment is also conducted inside the thermal chamber to verify the effect of any change in the ambient temperature on the leakage current as the laboratory ambient temperature could vary about few degrees during the measurement. This experiment is also conducted to verify any contribution of readout electronics temperature to the SDD leakage current. Inside the environmental chamber, the measurements were carried out for two conditions, in one case, the ambient temperature is kept at  $20^{\circ}\text{C}$  and the SDD temperature is varied from  $20^{\circ}\text{C}$  to  $-40^{\circ}\text{C}$  by varying the Peltier power. In second case, the Peltier power is switched off and the environmental temperature is varied from  $30^{\circ}\text{C}$  to  $-40^{\circ}\text{C}$ . In both these cases, the ramp signal frequency is measured for various SDD operating temperatures and hence the leakage current. It is shown that there is no difference between the laboratory, constant

amplitude and varying ambient (inside the thermal chamber) conditions as shown in figure 5.9.

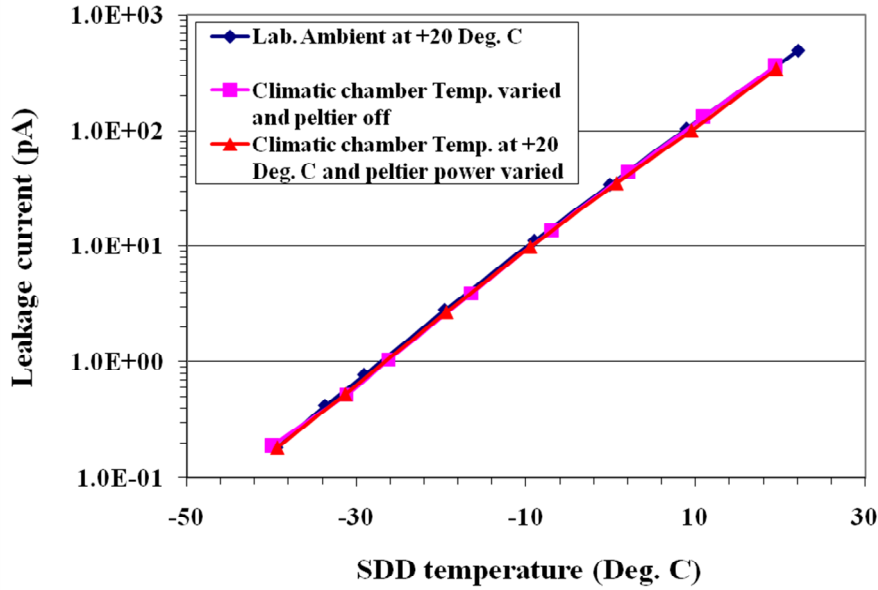


Fig. 5.9: Leakage current measured for various environmental conditions [134].

It is also observed that there is no change in the ramp signal frequency due to minor variations in the ambient temperature as the power to the Peltier is controlled using active PID controller circuit. Any sudden increase in the ambient temperature would require few minutes to attain the stable SDD operating temperature.

Subsequently, the leakage current is measured for all small and large area SDDs in the laboratory environmental conditions by setting the ramp signal amplitude at -2 V to +4 V. The SDD temperature is varied from  $\sim 20^{\circ}\text{C}$  to  $-40^{\circ}\text{C}$  in case of small SDDs and from  $\sim 20^{\circ}\text{C}$  to  $-50^{\circ}\text{C}$  in case of large area SDDs as the large area SDDs require to be operated at much lower temperatures to achieve the same performance as that of small area SDDs. It is shown that the leakage current varies in the range of 0.2 to 1 nA at  $20^{\circ}\text{C}$  and 0.1 to 0.3 pA at  $-40^{\circ}\text{C}$  for small area SDDs and varies in the range of 0.7 to 2 nA at  $20^{\circ}\text{C}$  and 1 to 2.5 pA at  $-50^{\circ}\text{C}$  for large area SDDs as shown in figure 5. 10. It is observed that the rate of change of leakage current with temperature is smaller for large

area SDDs compared to small area SDDs. It was later confirmed that the change in the slope in large area SDDs are due to the presence of diode as temperature monitor. Though the leakage current is measured for various detector operating temperatures, the same technique can be adapted onboard to measure the increase in leakage current with radiation by maintaining the SDDs at constant temperature.

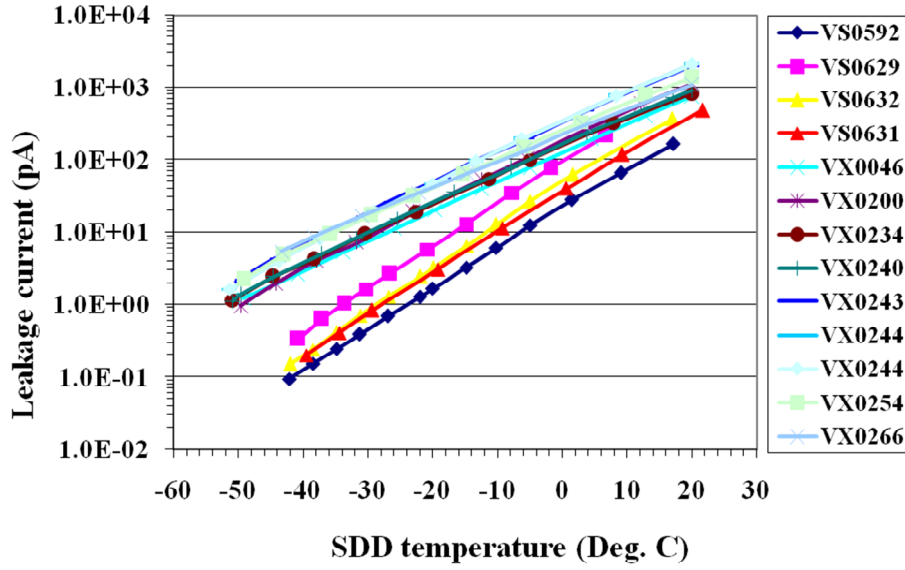


Fig. 5.10: Leakage current measured for small and large area SDDs for various operating temperatures [105].

Knowledge of feedback capacitor value is essential to measure the leakage current onboard which can be obtained through the ground measurements and any change in the feedback capacitance value will result in the gain shift.

#### 5.4.3. Performance Comparison between Small and Large Area SDDs:

The energy resolution is measured for both small and large area SDDs using  $^{55}\text{Fe}$  and  $^{241}\text{Am}$  X-ray sources and the spectrum is acquired for both these X-ray sources individually by keeping one source at a time in front of the detector. The measured value of energy resolution is  $\sim 150$  eV at 5.9 keV for both small and large area SDDs when the

detectors are cooled to  $-40^{\circ}\text{C}$  and  $-50^{\circ}\text{C}$  respectively. A sample spectra acquired for both  $^{55}\text{Fe}$  and  $^{241}\text{Am}$  is shown in figure 5. 11.

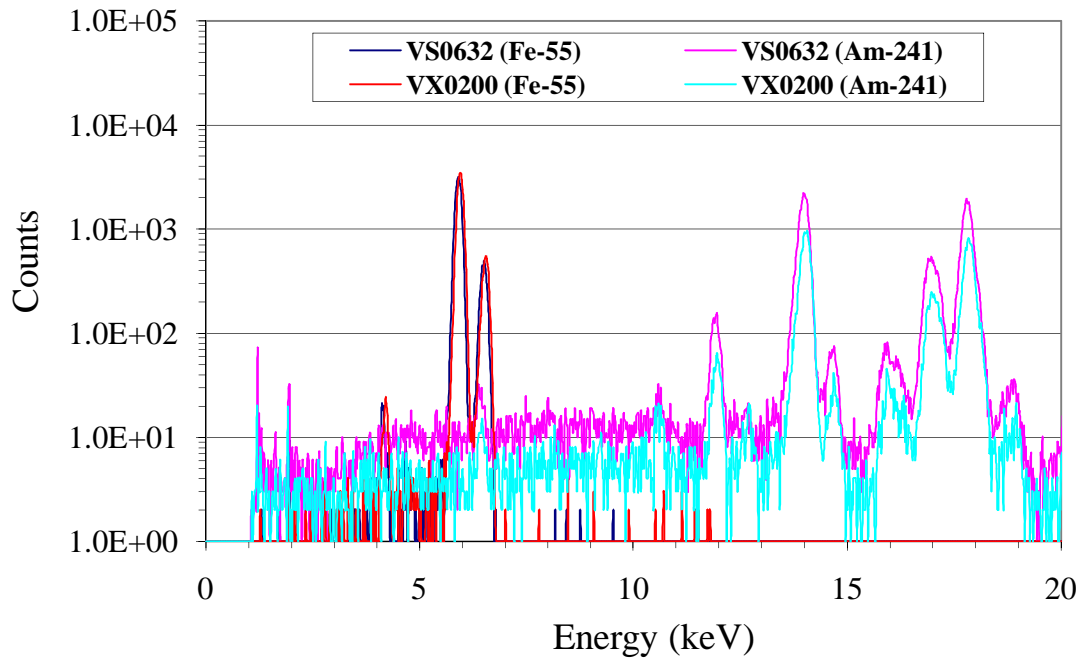


Fig. 5.11: Spectra measured for a small and large area SDD using  $^{55}\text{Fe}$  and  $^{241}\text{Am}$  X-ray sources [105].

The energy resolution is also measured for both small and large area detectors for various detector temperatures. The energy resolution varies from 342 eV at  $2^{\circ}\text{C}$  to  $\sim 150$  eV at  $-40^{\circ}\text{C}$  for small area detector and 431 eV at  $-5^{\circ}\text{C}$  to 152 eV at  $-50^{\circ}\text{C}$  at 5.9 keV. Figure 5.12 shows spectral response of the small area detector for various detector temperatures.

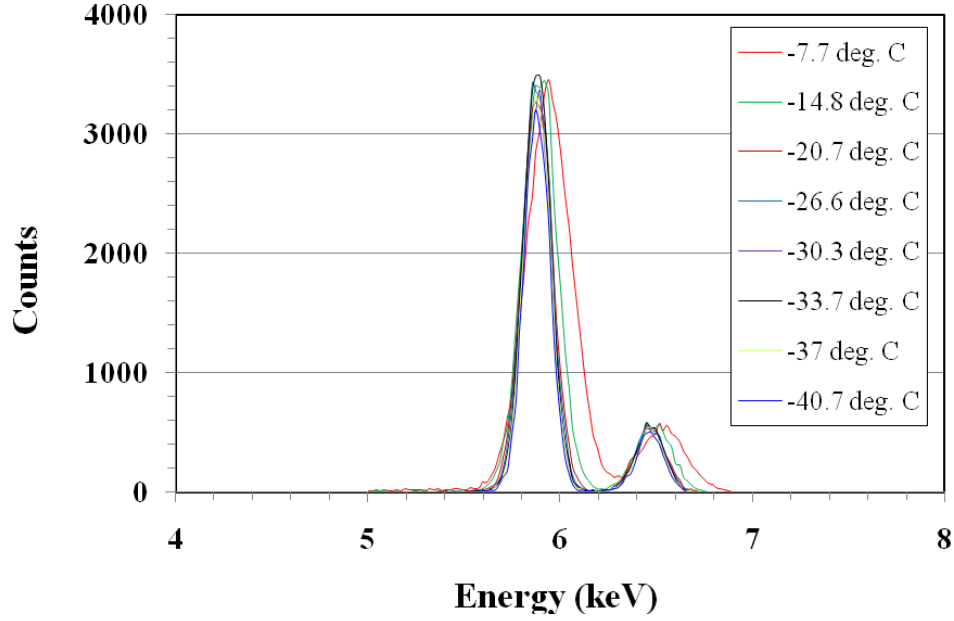


Fig. 5.12: Spectra acquired for small area detector for various detector temperatures [134].

Table-5.1 gives measured energy resolution for a sample small and large area SDDs for various detector operating temperatures using  $^{55}\text{Fe}$  and  $^{241}\text{Am}$ .

**Table-5.1:** Measured energy resolution for various detector operating temperatures.

X-ray source and energy	Small area SDD		Large area SDD	
	-40°C	2°C	-50°C	-5°C
$^{55}\text{Fe}$ , 5.9 keV	150 eV	342 eV	152 eV	431 eV
$^{241}\text{Am}$ , 13.9 keV	240 eV	530 eV	243 eV	695 eV
$^{241}\text{Am}$ , 17.8 keV	270 eV	610 eV	271 eV	768 eV

Energy resolution versus detector operating temperature is plotted for 6 SDDs (small and large area) for clarity even though measurement is carried out for 12 SDDs as shown in figure 5.13. The energy resolution degrades faster in case of large area SDDs with temperature compared to small area SDDs.



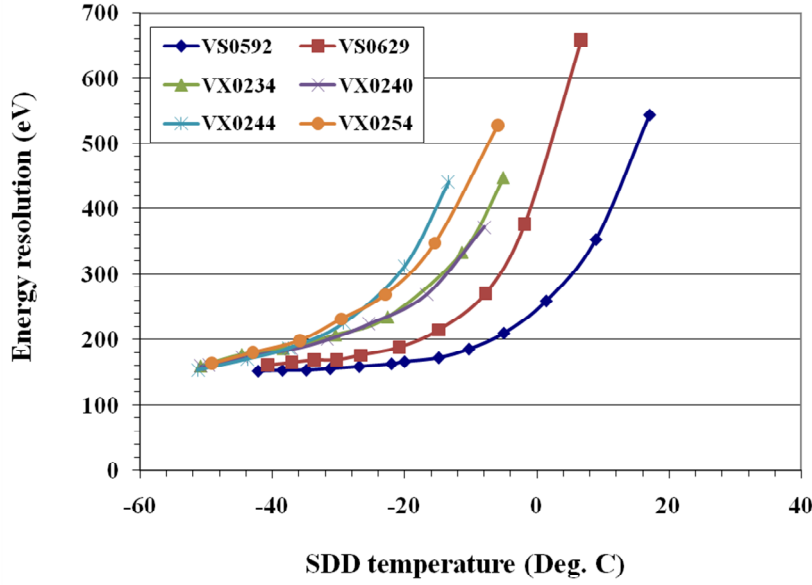


Fig. 5.13: Energy resolution measured for small and large area SDDs at various detector operating temperatures using  $^{55}\text{Fe}$  X-ray source [105].

#### 5.4.4. Energy Resolution Dependence on Leakage Current:

The measured value of leakage current for all the SDDs at various detector operating temperatures are plotted against the measured energy resolution and shown that the energy resolution degrades for the detector leakage currents greater than 1 pA. The energy resolution degrades from  $\sim 150$  eV for the detector leakage current of  $\sim 1$  pA to 200 eV at 10 pA and 400 eV at 100 pA as shown in figure 5.14. It can be clearly seen that the energy resolution does not improve for the leakage currents  $< 1$  pA. For the smaller leakage currents  $< 1$  pA, the spectrometer system noise is dominant and hence the spectral energy resolution is constant at  $\sim 150$  eV at 5.9 keV for the pulse peaking time of  $\sim 3.3$   $\mu\text{s}$ . Figure 5. 14 also give the consistency of the leakage current measurement and also the performance of developed SDD based spectrometer for various detector operating temperatures. By measuring the leakage current onboard, one can estimate any degradation in the energy resolution and it can be carried out by counting number of reset pulses and thereby the ramp signal frequency.

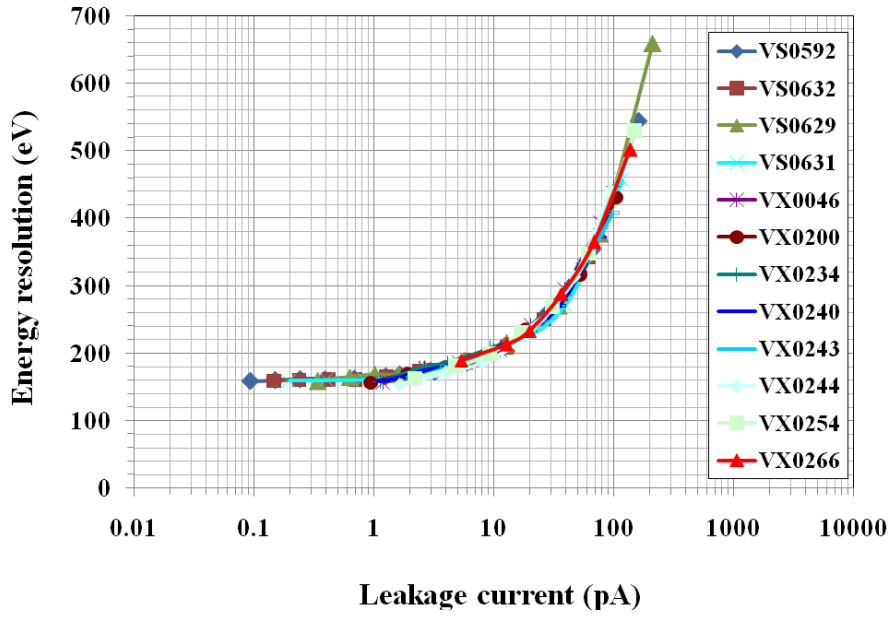


Fig. 5.14: Leakage current measured for large sample of SDDs versus measured energy resolution [105].

The set ramp signal amplitude will remain fairly constant as the onboard instruments uses space qualified and radiation hardened electronic components. One can also optimize the Peltier power required for the SDD cooling using the measured values of leakage current and the known noise performance of the spectrometer system.

#### 5.4.5. Leakage Current Due to Spurious Radiation:

These measurements of the reset frequency are carried out in the absence X-ray interactions. The reset frequency should increase in presence of the actual X-ray photons, which may result in inaccurate measurement of the leakage current during large count rates. In order to estimate the effect of the X-ray interactions on the reset frequency, we also experimentally measured the ramp signal frequency for various X-ray photon rates using  $^{55}\text{Fe}$  and  $^{241}\text{Am}$  X-ray sources for one of the large area SDD (VX0234) at  $-40^\circ\text{C}$ . The reset pulses are counted for every 10 s for the total duration of 100 s and the resultant reset frequency for different incident rate is shown in figure 5.15.

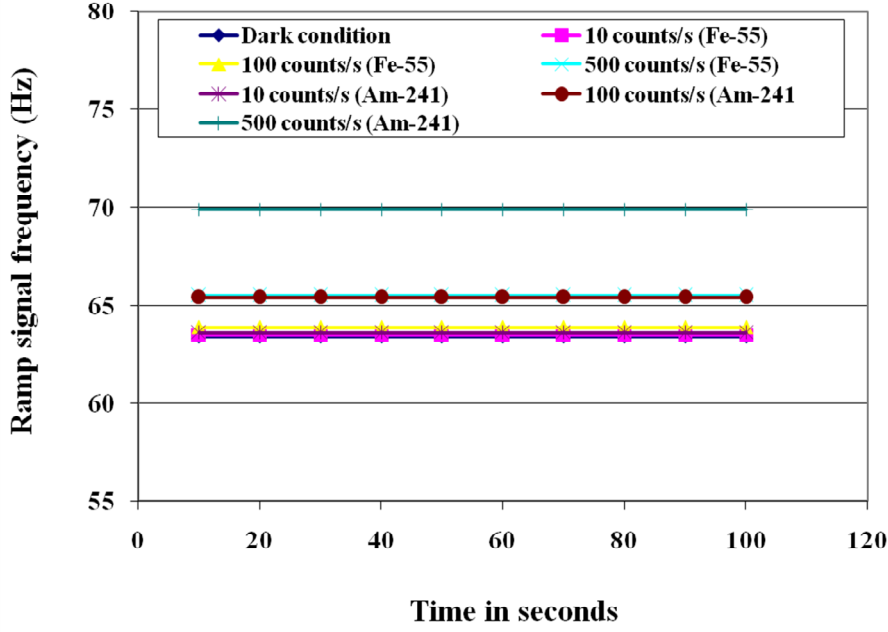


Fig. 5.15: Change in the ramp signal frequency for various incident photon rates using  $^{55}\text{Fe}$  and  $^{241}\text{Am}$  X-ray sources [105].

It can be seen that even for the incident rate of  $\sim 100$  photons per second, the change in reset frequency is only  $\sim 0.5$  Hz ( $\sim 0.8\%$ ) and  $\sim 2$  Hz ( $\sim 3\%$ ) for the X-ray sources  $^{55}\text{Fe}$  (5.9 keV, 6.49 keV) and  $^{241}\text{Am}$  (13.9 keV, 17.8 keV and 59.5 keV) respectively. This shows that, even though ideally leakage current measurement should be carried out without any additional X-ray interactions, a small count rate of ‘spurious’ events would not affect the result significantly. We also calculated the increase in the ramp signal frequency for additional X-ray interactions in the detector. For  $^{55}\text{Fe}$  X-ray source (83% of 5.9 keV and 17% of 6.5 keV photons), incident rate of 100 photons/s results in total 26 fC charge deposition for the  $e-h$  pair creation energy of 3.6 eV. This results in increase of  $V_{RMAP}$  by  $\sim 0.43$  V for the measured feedback capacitance value of 61 fF. This means that for the  $V_{RMAP}$  range of  $\sim 0.9$  V, the total charge deposition of  $\sim 52$  fC will result in increase of reset frequency by 1Hz. This value matches with experimental measurements as shown in figure 5.15.

#### 5.4.6. Leakage Current - Theoretical Comparison:

In the forward current-voltage diode equation (5.1), forward current of the p-n junction diode depends on the term  $\exp(qV/\eta kT)$ . The diode equation contains two temperature dependant terms; one is exponential term  $(qV/\eta kT)$  and another is leakage current ( $I_o$ ). Measuring leakage current gives vital information on the contribution of the current noise by the SDD in the overall spectrometer system performance. The leakage current ( $I_o$ ) is directly proportional to temperature and exponentially related to  $(-qE_g/\eta kT)$ . The leakage current is given by the generalized equation (5.12) [135]

$$I_o = BT^{3/2} e^{-\frac{qE_g}{\eta kT}} \quad (5.12)$$

where  $B$  is the constant,  $E_g$  is the band gap energy which varies with temperature [24] and hence cannot be considered as constant. Researchers have also used  $BT^{3/2}$  [135],  $BT^2$  [136],  $BT^{5/2}$  [126] and  $BT^{3/\eta}$  [137] terms for estimating the leakage current in various p-n junction diodes.

The leakage current is estimated for various detector operating temperatures using various forms of diode equation (5.12). The theoretically estimated leakage current values are compared with the experimental measurements. It is shown that the rate of change of leakage current with temperature closely matches for the ideality factor value of  $\sim 1.5$  for small area SDDs and  $\sim 2$  for large area SDDs (assuming  $B=1$ ) as shown in figure 5.16 and figure 5.17 respectively. The magnitude of the leakage current varies depending on various forms of the product term in equation (5.12) including  $B$  term which is diode junction area. Since the junction of area of two diodes under test is different, the magnitude of leakage current should also be different and the value of  $B$  is device dependant.

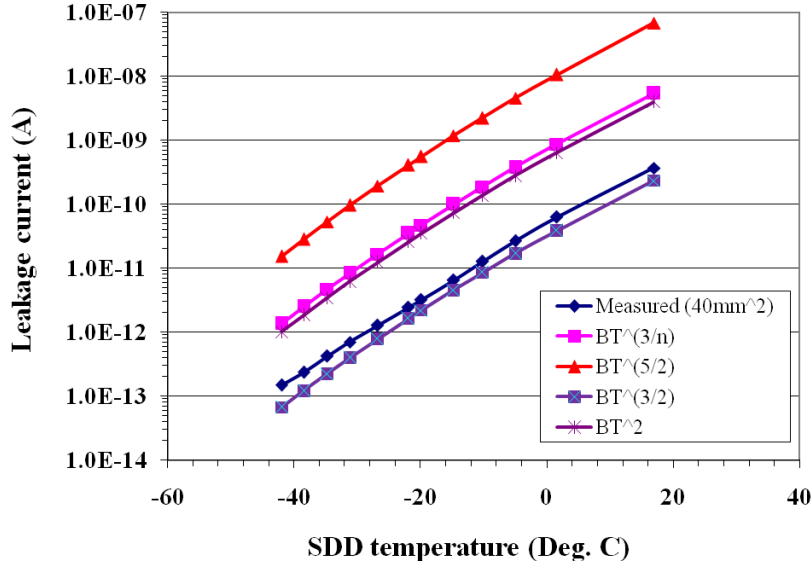


Fig. 5.16: Measured and theoretically estimated leakage current for small area SDD with ideality factor  $\eta = 1.46$  for various detector operating temperatures.

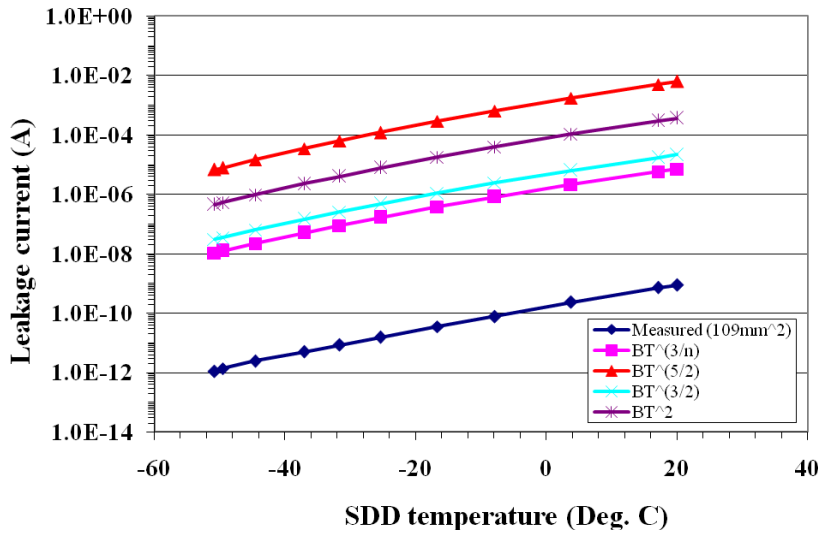


Fig. 5.17: Measured and theoretically estimated leakage current for large area SDD with ideality factor  $\eta = 2.14$  for various detector operating temperatures.

The magnitude of the leakage current dependence on  $B$  is eliminated by dividing leakage current at one temperature with its value at another temperature. The equation (5.9) is rewritten as (5.13) with diode equation of the form given in ref. [137]

$$\ln \left[ \frac{(I_o(T_2) / I_o(T_1))}{(T_2 / T_1)^{3/\eta}} \right] = - \frac{E_g}{\eta K} \left( \frac{T_1 - T_2}{T_1 T_2} \right) \quad (5.13)$$

The slope values derived from the measured leakage current for small and large area SDDs by plotting  $\ln\left[\frac{I_o(T_2)/I_o(T_1)}{(T_2/T_1)^{3/\eta}}\right]$  against  $\left(\frac{T_1-T_2}{T_1T_2}\right)$  for various forms of diode equation. The theoretical slope is estimated by substituting  $E_g$ , measured ideality factor for small and large area SDDs and  $K$  in the slope term  $E_g/\eta K$  from equation (5.13) (see figure 5. 18) and this remains same for all forms of diode equation. The theoretical slope value for  $\eta = 1.46$  is 8900 and for  $\eta = 2.14$  is 6070 which approximately matches with the measured slopes for all forms of diode equation for both small and large area SDDs.

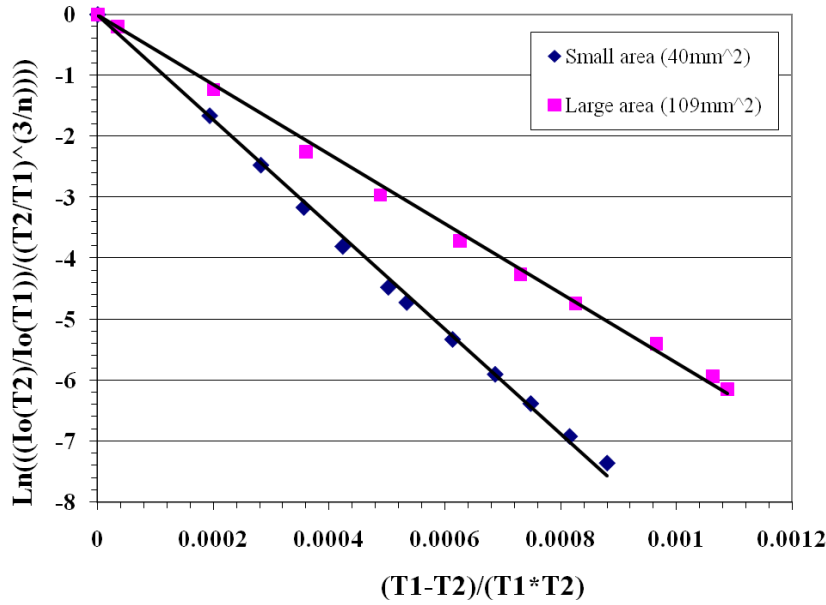


Fig. 5.18: Measured slopes for small and large area SDDs using leakage current ratio method.

However to confirm the suitability of the particular diode equation, we have computed the ratio of slopes measured experimentally for small to large area SDDs using different form of diode equations as given in equation (5.12). The theoretical slope ratio  $\sim (8900/6070)$  i.e. 1.466 is found to be closely matches with the leakage ratio equation of the form  $BT^{3/\eta}$  as given in the table-5.2.

**Table-5.2:** Measured slopes and slope ratios for small and large area SDDs using leakage current ratio method.

	$BT^2$	$BT^{3/2}$	$BT^{5/2}$	$BT^{3/\eta}$
Small area SDD (40 mm <sup>2</sup> )	8411.5	8539.7	8283.2	8397.4
Large area SDD (109 mm <sup>2</sup> )	5577.2	5704.1	5450.3	5729.9
Measured slope ratio	1.508	1.497	1.519	1.465

#### 5.4.6.1. Estimation of Ideality Constant and Its Temperature Dependence:

The natural logarithm of the measured leakage current for small and large area SDDs are plotted against  $1000/T$  as shown in figure 5.19 and the slope of each SDD is estimated by linear square fitting.

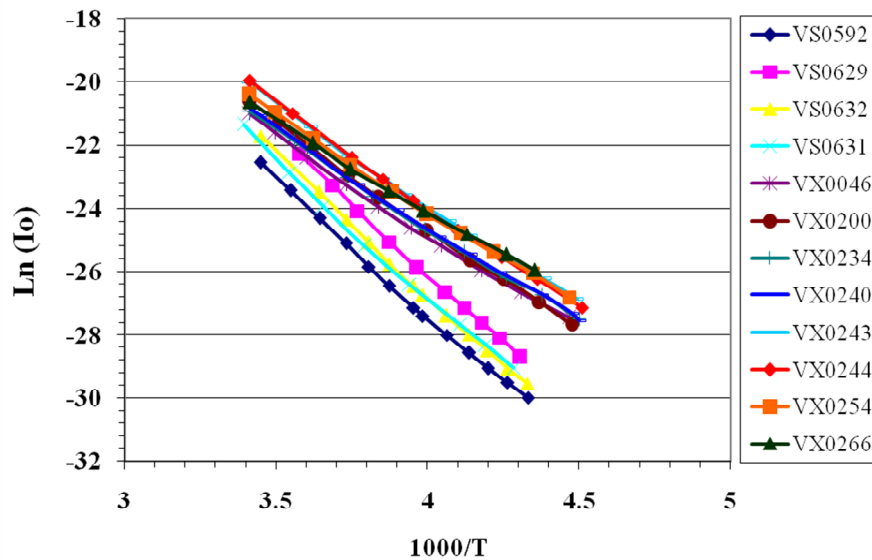


Fig. 5.19: Natural logarithm of leakage current versus the reciprocal of temperature for small and large area SDDs.

The slope of the fitted line for each SDD is equated to  $(11.59 \times (E_g/\eta))$  and the value of ideality constant is derived by substituting  $E_g$  with 1.127 (band gap energy of silicon at 273 K). The derived value of ideality constant for small area SDDs (4 pieces) are 1.53, 1.49, 1.46, 1.53 and for large area SDDs (8 pieces) are 2.13, 1.97, 2.17, 2.14,

2.07, 2.01, 2.16 and 2.34. This shows that the value of  $\eta$  is about 1.5 for 40 mm<sup>2</sup> area SDDs and about 2 for 109 mm<sup>2</sup> area SDDs. The measured values of ideality constant for bulk p-i-n SDDs closely matches with the values reported for silicon based p-n junction diodes. The increase in the value of ideality constant for the larger area SDDs are attributed to the presence of additional p-n junction diode for temperature monitoring. This result is in line with the results reported earlier showing increase in the value of ideality constant with number of p-n junctions [138]. Though the p-n junction is not a part of physical device, the radiative property of the forward biased p-n junction does affect the leakage current values with temperature. The change in the value of ideality constant is also attributed to the recombination enhanced by the larger number of defects in the larger bulk area, contact area and the number of contacts. The change in the value of ideality constant within the small and large area SDDs could be due to the varied bulk material quality.

The temperature dependence of the ideality constant for these SDDs are estimated by substituting the value of band gap energy at different temperatures in the slope term ( $11.59 \times (E_g/\eta)$ ) and the temperature dependent band gap energy is derived from the Varshni equation (24). The estimated value of ideality constant is shown to be varying from 1.548 at ~ 230 K to 1.529 at ~ 290 K for a sample small area SDD (VS0592). Figure 5.20 shows the temperature dependence of ideality constant for all 4 small area SDDs. It is observed that the change in the value of ideality constant is ~ 0.02 in the temperature range of 230 K to 290 K for small area SDDs and ~ 0.03 in the temperature range of 220 K to 293 K for large area SDDs. The value of ideality constant decreases linearly with increase in the SDD operating temperature and the trend is similar to the values reported for Au/n-GaAs, Pt/n-GaN Schottky diodes [139-140] and various types of solar cells [141-144].



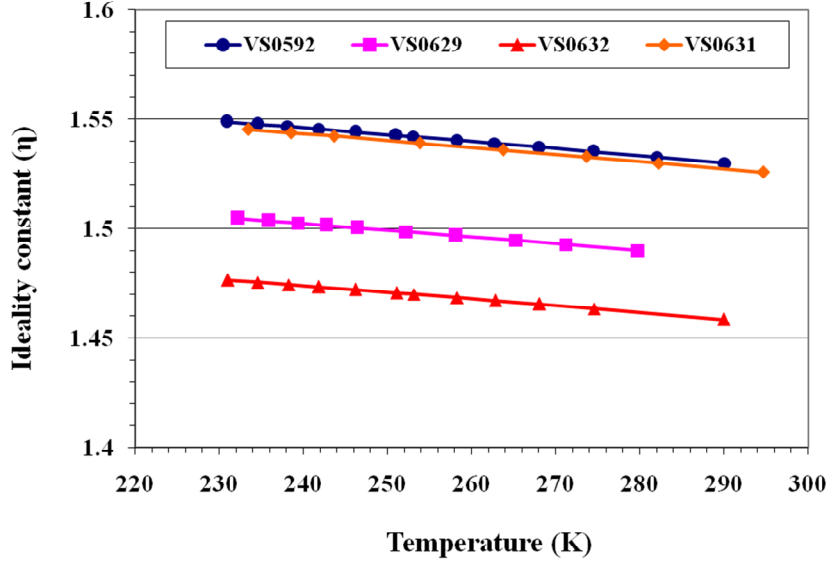


Fig. 5.20: Ideality constant ( $\eta$ ) versus temperature for small area SDDs.

For a sample large area SDD (VX0046), the ideality constant varies from 2.152 at  $\sim 220$  K to 2.121 at  $\sim 293$  K. Figure 5.21 shows the temperature dependence of ideality constant for all 8 large area SDDs.

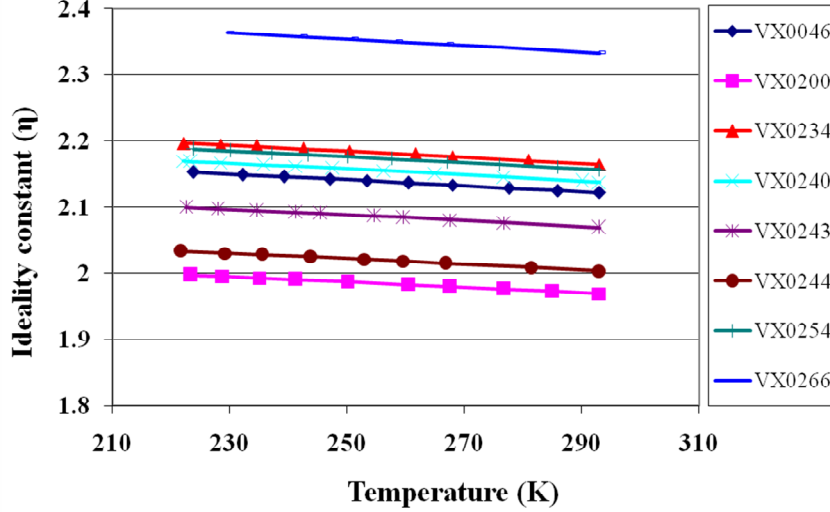


Fig. 5.21: Ideality constant ( $\eta$ ) versus temperature for large area SDDs.

The change in ideality constant value with temperature does not exhibit remarkable temperature dependence and this marginal variation could be attributed to the possible activation of defects which acts as trap and/or recombination centers.

## 5.5. SUMMARY:

In this chapter, a new and simple technique for measuring the leakage current in SDDs is discussed. The measurement technique involves by simply counting the ramp signal frequency at the output of CSPA with known values of charge integrating feedback capacitor and the ramp signal amplitude. The value of feedback capacitance is estimated by independent measurements and the ramp signal amplitude is fixed electrically in the CSPA. The measured value of feedback capacitance is shown to be varying from  $\sim 60$  to  $66$  fF. Using this technique, the leakage current is measured for large sample of SDDs having two different active area of  $40 \text{ mm}^2$  and  $109 \text{ mm}^2$  for various detector operating temperatures. Simultaneously, the energy resolution is also measured for all the SDD modules at each point of leakage current measurement. It has been shown that the energy resolution is  $\sim 150$  eV at  $5.9$  keV for the detector leakage currents  $< 1$  pA and changes to  $\sim 200$  eV at  $10$  pA and  $\sim 400$  eV at  $100$  pA. For the leakage currents  $< 1$  pA, the electronics noise determines the energy resolution and at higher leakage currents, the leakage current is dominant. Using this technique, one can estimate the performance degradation of the space-borne SDD based X-ray spectrometer where the detector is expected to encounter very hostile space radiation environment. The radiation damage to the SDD leads to the increase in the leakage current and hence it degrades energy resolution (discussed in chapter-6). This technique takes care of only the radiation damage to the SDD. It is expected that the components used in the readout electronics should be of space qualified in nature with certain dose levels. Any degradation to the electronic chain can be quantified separately by means of electronic calibration. This may not include the on-chip or discrete JFET used in the SDD modules. The measured leakage current is also compared with theoretical values and shown to have good correlation with respect the ideality (device) constant.

## **Chapter 6:**

# **RADIATION EFFECTS ON THE PERFORMANCE OF THE SDD BASED X-RAY SPECTROMETER ONBOARD CHANDRAYAAN-2 MISSION**

### **6.1. INTRODUCTION:**

Space radiation is a major issue for the satellite based instruments, especially when using sensitive components and detectors such as Silicon Drift Detector. It is essential to have knowledge of the radiation effects on these devices in order to assess the performance degradation due to hostile space radiation environment. The main effects due to space radiation in silicon detector are displacement damage (bulk damage) and ionization damage (surface damage). The displacement damage is caused by the displacement of crystal atoms and the ionization damage covers the effects in the dielectric and interface regions.

Performance of a SDD based X-ray spectrometer degrades due to environmental effects as well as radiation damage resulting in poor energy resolution. The energy resolution of the SDD based X-ray spectrometer mainly depends on the leakage current and the noise contributed by the readout electronics. The leakage current in a semiconductor diode varies with the operating temperature (typically doubles for increase of every  $\sim 7^{\circ}\text{C}$ ) and increases with the radiation dose absorbed by the detector during the transit through radiation belts and in-orbit operations. The electronic noise

associated with the readout system (except internal JFET) will not change significantly as the space instruments are designed using space grade components which are designed to withstand higher ( $> 30$  krad) radiation dose levels. SDDs used in the space experiments are either custom designed [104] which are specific to the scientific study or off-the-shelf devices [85-87] which are readily available in various types and sizes. We plan to use one such off-the-shelf SDD device in two X-ray spectrometer instruments namely Solar X-ray Monitor (XSM) [102] and Alpha Particle X-ray Spectrometer (APXS) [99] for our upcoming Indian mission to Moon, Chandrayaan-2.

Silicon detectors are sensitive to the displacement damage which is produced by the non ionizing energy losses of charged and neutral particles. The displacement damage leads to increase in the detector leakage current and thus degrades the energy resolution. Change in the leakage current and the charge collection efficiency in large area SDDs with proton spectrum centered at 11.2 MeV for the fluence of  $\sim 10^9/\text{cm}^2$  is reported in ref. [120, 145]. Irradiation measurements on various other types of silicon detectors have been reported with protons [146-147], gamma rays [148-149] and neutrons [150-151]. These measurements indicate that the increase in the leakage current is due to bulk damage as well as surface leakages. It is also shown that the change in the leakage current is independent of type of silicon material; low or high resistivity, *p*- or *n*-type and low concentration of carbon and oxygen impurities [152].

## **6.2. PERFORMANCE REQUIREMENT:**

Planetary missions such as Chandrayaan-2 will be passing through the radiation belts around the earth during the transit to the Moon. It is known that the Earth is surrounded by extremely intense radiation regions known as Van Allen radiation belts. These radiation belts are essentially highly energetic electrons and protons trapped

within the Earth's magnetosphere. In the lunar orbit, the majority of the radiation is solar protons. Hence it is necessary to study the radiation damage effects on the SDDs during transit and in-orbit. The performance requirement of SDD based spectrometer onboard Chandrayaan-2 mission is listed in table-6.1.

**Table-6.1:** X-ray spectrometer performance requirement onboard Chandrayaan-2 [153].

Mission and its duration	Chandrayaan-2, 2 years
Orbital altitude around the Moon	100 km
Trapped proton fluence, transit (~ 7 days)	$\sim 3.4 \times 10^7$ protons/40 mm <sup>2</sup>
Lunar orbit solar proton fluence for 2 years	$\sim 4 \times 10^9$ protons/40 mm <sup>2</sup>
Estimated cumulative dose	10 krad
Energy resolution at the start of the mission	$\sim 150$ eV at 5.9 keV for 3.3 $\mu$ s
Required energy resolution at the end of life	< 250 eV
SDD operating temperature	-40°C
Energy range	1-25 keV

### 6.3. SPACE RADIATION ENVIRONMENT:

The spacecraft encounters the space radiation environment surrounding the Earth and these radiations come from four different sources, they are

1. Protons and electrons residing in the Van Allen radiation belts.
2. Heavy ions trapped in the magnetosphere.
3. Protons and heavy ions from the cosmic rays.
4. Protons and heavy ions from solar flares.

All the above phenomenon are intimately dependent on the solar cycle [154]. It is well known that the Earth is surrounded by the extremely intense radiation regions

known as Van Allen radiation belts. The schematic representation of the Van Allen radiation belts is shown in figure 6.1.

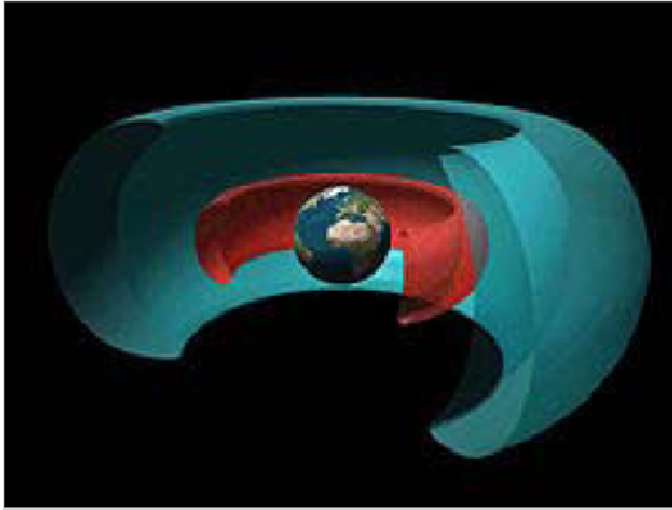


Fig. 6.1: Cutaway drawing of two radiation belts around the Earth, Red-Inner radiation belt, Blue-Outer radiation belt [Courtesy NASA].

These radiation belts are essentially the high energetic electrons and protons trapped within the Earth's magnetosphere [155]. There are two distinct radiation belts of toroidal shape surrounding the earth where the high energy charged particles get trapped in the earth's magnetic field [156] as shown in figure 6.2.

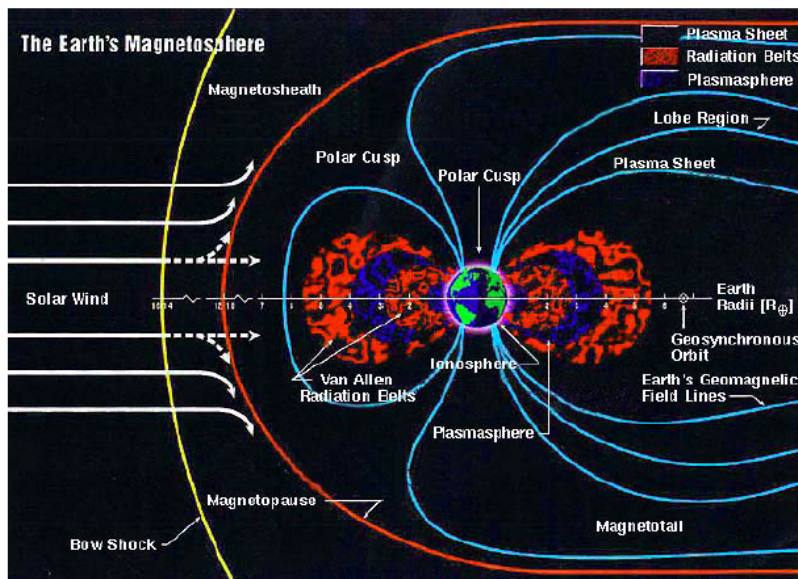


Fig. 6.2: Solar wind and radiation belt around the Earth [157].

The inner radiation belt mainly consists of protons having energies up to 400 MeV with particle flux reaching  $10^5$  particles  $\text{cm}^{-2} \text{s}^{-1}$ . The inner radiation belt extends typically from an altitude of 0.1 to 2 Earth radii. The outer radiation belt mainly consists of electrons which are highly variable with maximum energy of 10 MeV and the flux of  $\sim 10^6$  particles  $\text{cm}^{-2} \text{s}^{-1}$ . The inner radiation belt extends typically from an altitude of  $\sim 4$  to 9-10 Earth radii. Galactic cosmic rays incorporate a range of elements with atomic numbers ranging from 1 (Hydrogen) to 92 (Uranium), typically characterized with low flux levels and wide distribution of particle energies ranging from few MeV to several hundred GeV [154]. The compositions of the particles are determined to be  $\sim 85\%$  protons,  $\sim 14\%$  alpha particles and  $1\%$  heavy ions [158]. During solar flares, high energy protons, typically of the order of hundreds of MeV are involved and solar flares are typically observed in solar maximum conditions [154]. These radiation belts endanger satellites and systems and there should be adequate shielding to protect the sensitive components/devices if their orbit spends significant amount of time in the radiation belt. Planetary missions such as Chandrayaan-2 will be passing through these radiation belts during the transit to the Moon and hence it is necessary to study the radiation damage effects of the SDDs used in the spectrometer instruments. In the lunar orbit, the majority of the radiation is solar protons.

#### **6.4. THE RADIATION DAMAGE MECHANISMS:**

The interaction of energetic particles on a solid loses their energy due to ionizing and nonionizing process as they travel through a given material. The result of this energy loss is the production of e-h pairs (ionization) and displaced atoms (displacement damage). Figure 6.3 gives the flow diagram of some of the effects of these radiation damages [158].

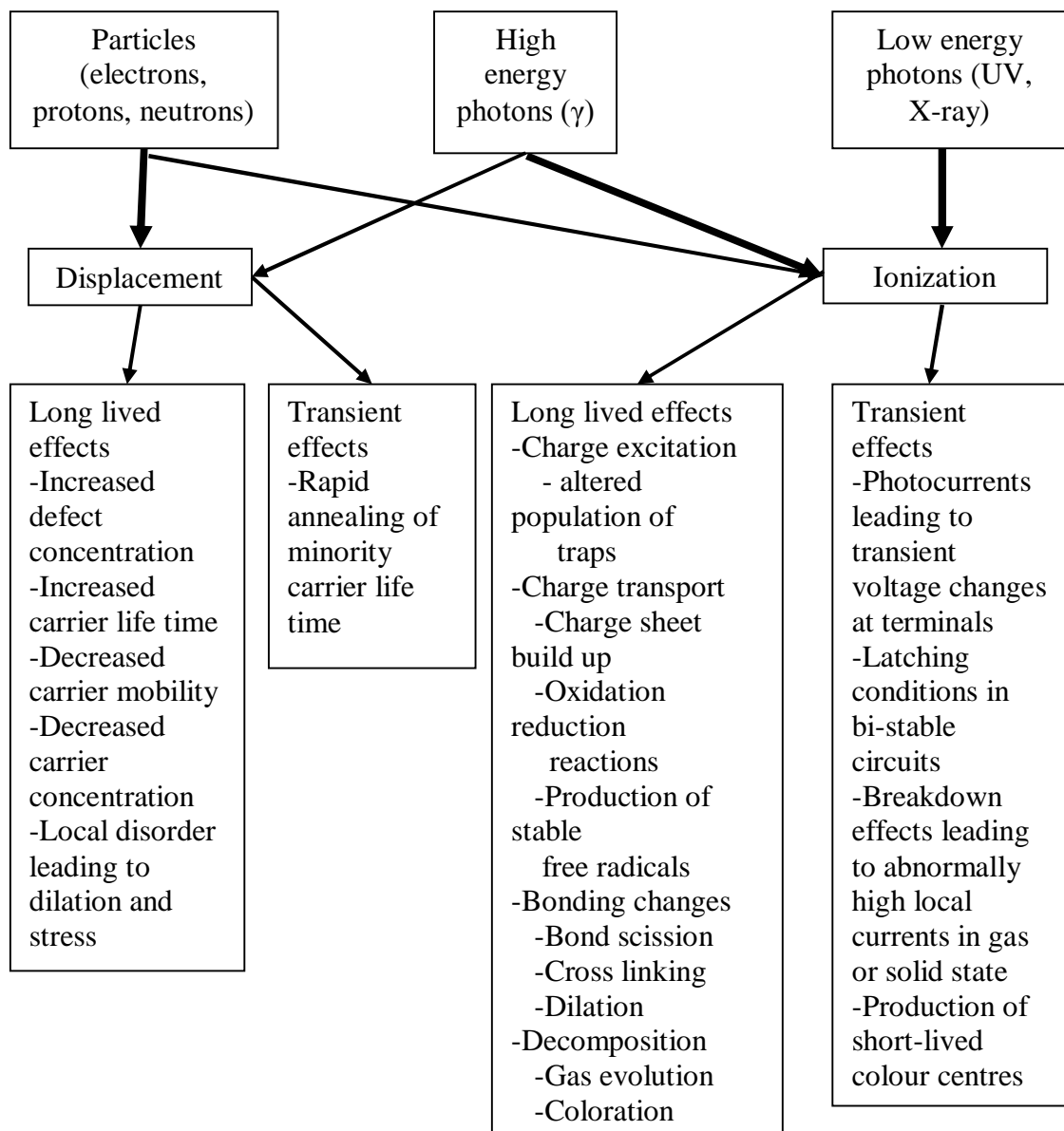


Fig. 6.3: Flow diagram of radiation damage effects for various radiations [158].

Incident radiation displaces silicon atoms from their lattice, resulting in creation of defects that alter the electronic characteristics of the crystal. The displacement damage is also known as non-ionizing damage. In ionization damage, the energy is absorbed by the ionization in the insulating layers, liberates charge carriers which diffuse or drift to the other locations leading to the charge build up and hence the parasitic fields.



## 6.5. DISPLACEMENT DAMAGE AND ITS EFFECTS:

### 6.5.1. Displacement Damage:

The interaction of particles in the silicon crystal depends on the type of particle and its energy. At lower energies, a big part of the particle energy is lost due to the ionization of silicon atoms in the lattice and it is fully reversible. If the incident particle displaces the lattice atoms through the non ionizing process such as Coulomb interaction, elastic and non elastic nuclear collisions [159] resulting in irreversible damage. The non ionizing energy loss for charged particles is mainly due to Coulomb interaction. In case of neutrons, the interaction is mainly via elastic scattering with the nucleus. Displacement damage is the ejection of an atom from its normal lattice position when the radiation strikes and the ejected atom is known as primary knock-on atom (PKA) as shown in figure 6.4.

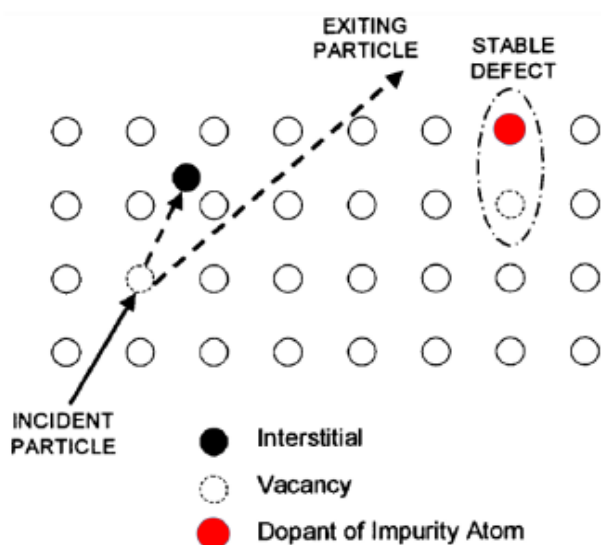


Fig. 6.4: Schematic representation of defect caused by damage from an incident particle [160].

The recoil energy of the PKAs can be up to  $\sim 133$  eV for neutrons, which in turn can remove other atoms from the lattice, giving rise to cascade of atomic displacements before eventually coming to rest as shown in figure 6.5. In case of gamma ray irradiation,

the displacement damage is due to Compton electrons that only can produce isolated single defects as shown in figure 6.6. The charged particles can produce both defect clusters and also isolated single defects.

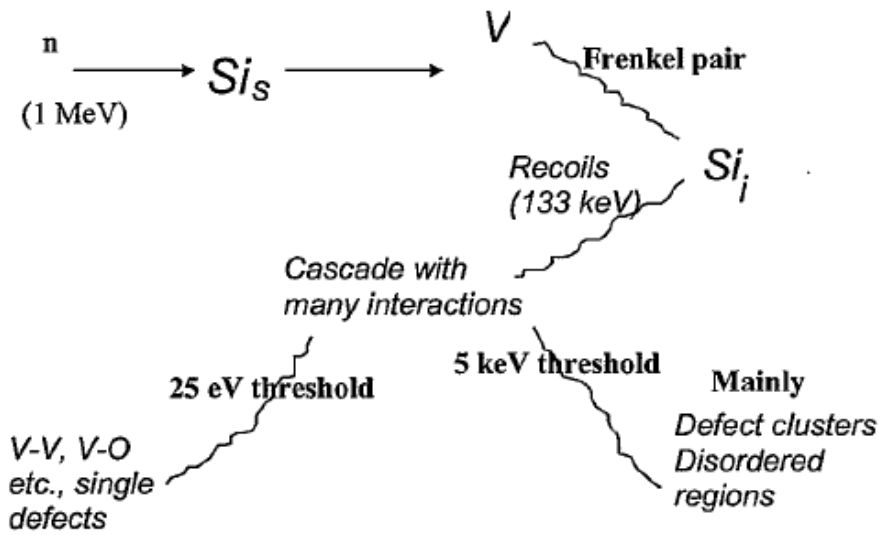


Fig. 6.5: The point and cluster defects in silicon due to fast neutrons [161].

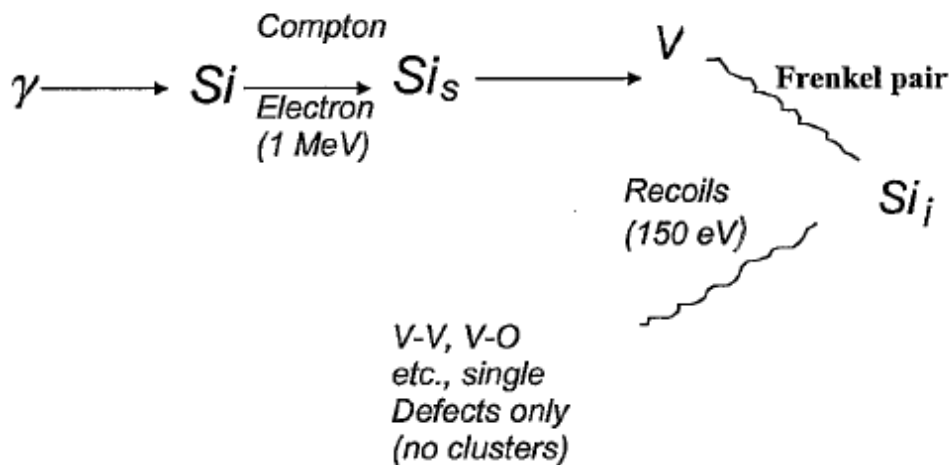


Fig. 6.6: The point defects in silicon due to gamma ray radiation [162].

It has been estimated that  $\sim 50\%$  of the energy of the recoil atom is deposited via ionization and the displacement dominates when the recoil atom loses its final 5-10 keV. The cascade effect resulting in the formation of two or three terminal clusters. The displaced atom becomes an interstitial and the position of the atom formerly occupied becomes a vacancy, together called as frenkel pair (stable defect). Vacancies within the

lattice are mobile and can combine with impurity atoms or with other vacancies. Combining of vacancies is known as cluster and they are electronically active depending on the vacancy and impurity. This can act same way as dopants and can also act as traps for carriers. For example, a 1 MeV neutron transfers  $\sim 50$  keV to the silicon recoil atom which in turn displaces about  $10^3$  additional atoms in the region. Compared to neutrons, protons are more likely to impart their energy in small fractions to the lattice because of Coulomb interaction and thereby creating more point defects than neutrons. Clusters are thought to be responsible for the significant differences between the damage created by light particles such as photons/low energy electrons and heavy particles. The schematic representation of cluster due to 50 keV recoil energy is shown in figure 6.7 and the simulated cluster defects is shown in figure 6.8.

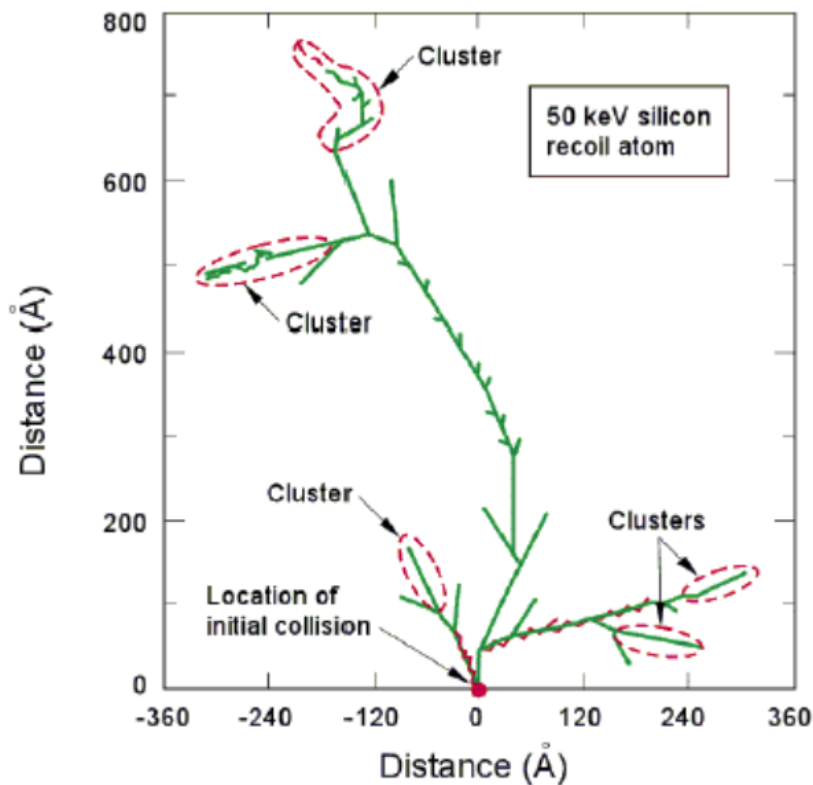


Fig. 6.7: Schematic representation of cluster defects created by an 1 MeV neutron imparting recoil energy of 50 keV on a silicon atom [163].

Electrons with energy up to few hundred keV can displace one or two atoms from their lattice site. In each interaction leading to displacement damage of a PKA, specific recoil energy  $E_R$  is produced. The displacement damage function can be expressed as in equation (6.1)

$$D(E) = \sum_v \sigma_v(E) \cdot \int_0^{E_R^{\max}} f_v(E, E_R) P(E_R) dE_R \quad (6.1)$$

where  $v$  indicates all possible interactions of the incoming particle with energy  $E$  with the silicon lattice leading to atom displacement.  $\sigma_v$  is the cross section and  $f_v(E, E_R)$  gives the probability for the generation of PKA with recoil energy  $E_R$ .

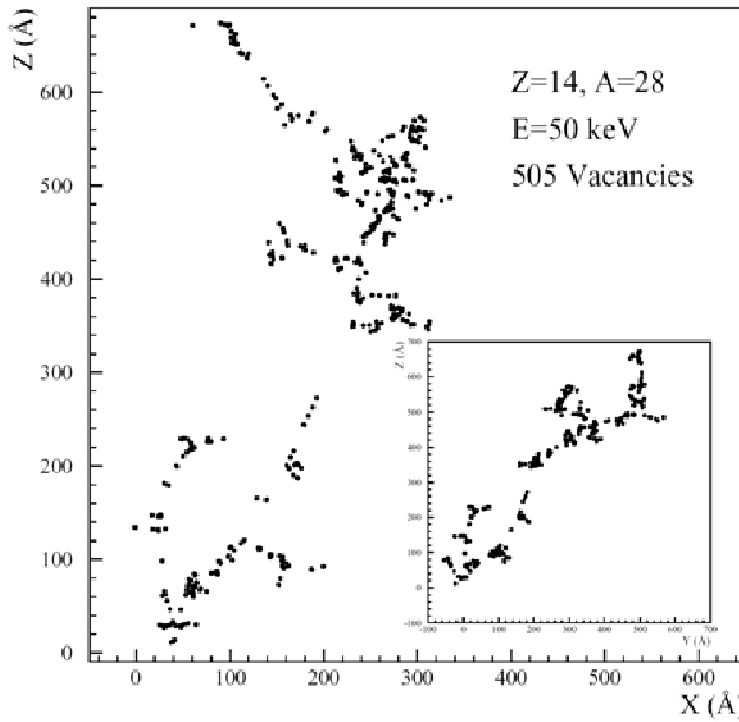


Fig. 6.8: Spatial distribution of vacancies created by a 1 MeV neutron imparting recoil energy of 50 keV on a silicon atom. The insert shows the traverse projection [163].

The total displacement damage energy per volume deposited in a crystal undergoing irradiation is given by (6.2)

$$T_d = N \cdot t_{ex} \int_0^{\infty} D(E) \phi(E) dE \quad (6.2)$$

where  $N$  is the number of silicon atoms per unit volume,  $\phi(E)$  is the differential particle flux spectrum and  $t_{ex}$  is the exposure time. An incident radiation imparting energy of about 25 eV [163] to a silicon atom can dislodge it from its lattice site. Displacement damage is proportional to non-ionizing energy loss which is not proportional to the total energy absorbed, but depends on the particle type and energy. Displacement damage can be quantified using the non-ionizing energy loss (NIEL) [164] and it is the energy lost to non-ionizing events per unit length (MeV/cm). Table-6.2 gives possible single defects and defect clusters created by the different radiations. The number of "X's" indicates the qualitative amount of defects of that particular type.

**Table-6.2:** Qualitative indication of defects created by different types of radiations [165].

Particle type	Single defects	Defects clusters
Neutron	X	XXXXX
Charged particles (p, $\pi$ , etc.)	XXXX	XX
Gamma rays and electrons	XXXXXX	

Non ionizing energy loss for various types of particles has been calculated over the large energy range [165]. Although these values are not verified quantitatively, but can be used to estimate the relative effects. X-rays do not cause displacement damage as the X-ray energy is less than the momentum conservation set threshold of about 250 keV for photons. Gamma rays can cause displacement damage through Compton scattered electrons. The neutron induced displacement damage with energy of 1 MeV is more than two orders of magnitude higher than the 1 MeV electron induced damage [166]. The relative displacement damage for various particles and energies are given in table-6.3.

**Table-6.3:** Relative displacement damage for various particles and energies [167].

Particle	Proton	Proton	Neutron	Electron	Electron
Energy	1 GeV	50 MeV	1 MeV	1 MeV	1 GeV
Relative damage	1	2	2	0.01	0.1

The displacement damage causes the following effects in the detector

1. Increased leakage current
2. Signal loss due to trapping because of reduced carrier life time
3. Change in the effective doping concentration increases the depletion voltage

The above factors result in the degradation of the energy resolution. The electronic effects of displacement damage are increase in generation current resulting in increased shot noise, recombination resulting in signal loss and charge buildup increasing the bias voltage required for full charge collection.

### 6.5.2. Increase in the Leakage Current:

Increase in the detector leakage current due to displacement damage is caused by the radiation induced deep level defects that act as generation which is given by the equation (6.3) [168]

$$\Delta I_o = \alpha \Phi_{eq} V \quad (6.3)$$

where  $\Phi_{eq}$  is the fluence of the incident particle, equivalent to 1 MeV neutron fluence and  $V$  is the detector volume in which the leakage current is measured and  $\alpha$  is the damage constant. The value of damage constant is  $\sim 11.1 \times 10^{-17}$  A/cm at  $-50^\circ\text{C}$  [168] and for high resistivity silicon (2-8 k $\Omega$ -cm), it is in the range of 4 - 6  $\times 10^{-17}$  A/cm at

room temperature [151]. The change in the leakage current is shown to be independent of type of silicon material; low or high resistivity, *p*- or *n*- type and low concentration of carbon and oxygen impurities [152], as shown in figure 6.9.

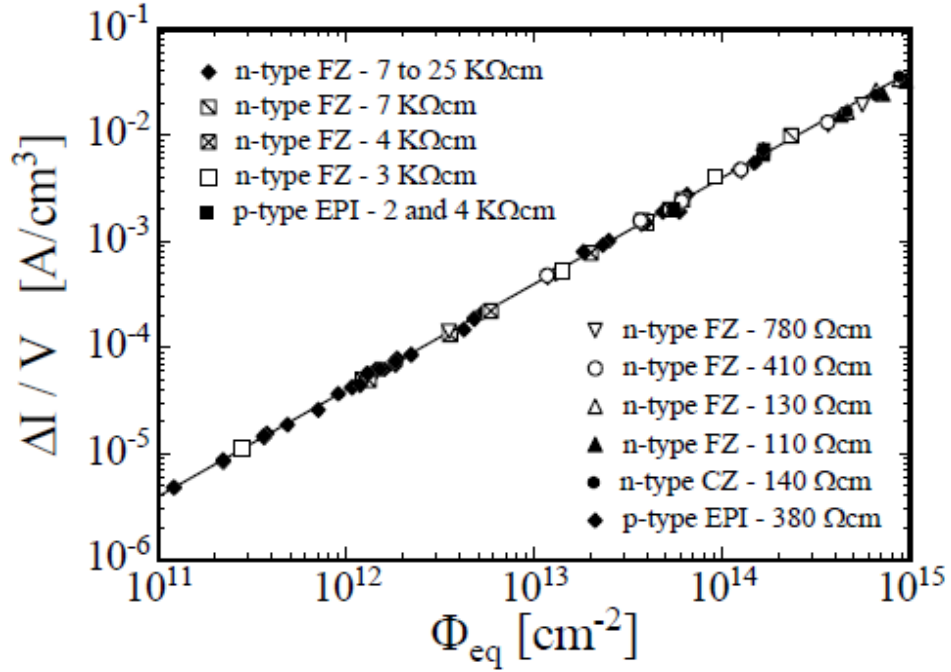


Fig. 6.9: Leakage current due to displacement damage as a function of particle fluence for different types of detectors [152].

The measured leakage current varies exponentially with the detector operating temperature and the value of  $\alpha$  is therefore generally normalized at room temperature. Therefore, the damage constant is a universal constant which does not depend on the material type and irradiating particle. It should be noted that the leakage current due to displacement damage strictly follows non ionizing energy loss scaling. The increase in the leakage current due to radiation damage (displacement damage) has same effect with temperature as that of non-irradiated detectors [169-170]. In both cases, the leakage current is originated by the thermal generation process.

### 6.5.3. Effect of Doping Concentration:

The change in the effective doping concentration ( $N_{eff}$ ) has been experimentally verified by many researchers [171-174] as a function of fluence  $\Phi$ . The empirical function of  $N_{eff}$  for n-type silicon is given in equation (6.4)

$$N_{eff} = \left| N_D e^{c\Phi} - N_A - \beta\Phi \right| \quad (6.4)$$

where  $N_D$  is the initial donor concentration,  $N_A$  is the initial acceptor concentration,  $c$  is the removal rate of initial donors and  $\beta$  is the parameter accounting for acceptor like defects. The radiation induced acceptor defects have been measured for the n-type silicon diode where the initial doping concentration decreases progressively with received fluence until the diode inverts to p-type. After inversion, the  $N_{eff}$  increases linearly with the fluence as shown in figure 6.10.

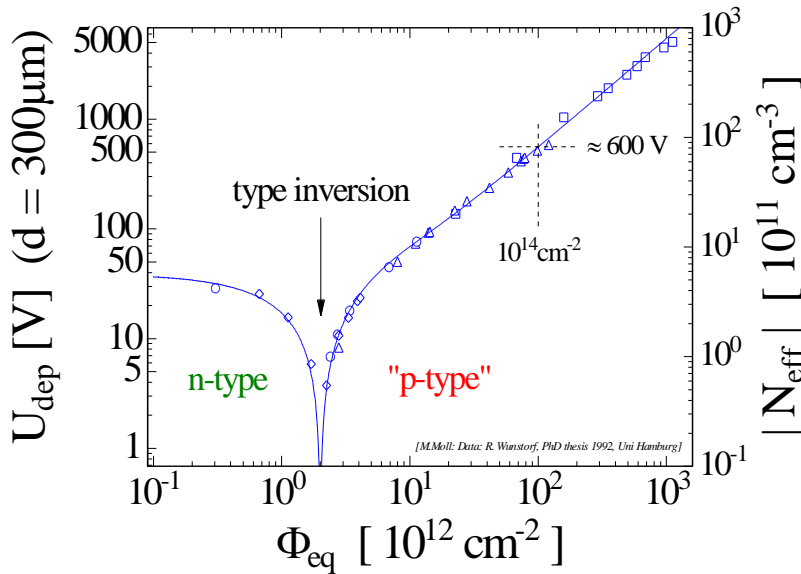


Fig. 6.10: Effect of doping concentration versus particle fluence [171].

The value of  $N_{eff}$  decreases with time until the minimum is reached after the irradiation and this is referred as beneficial annealing. The decay of active radiation induced acceptor sites back to neutral is believed to be responsible for the decrease in  $N_{eff}$  value. The  $N_{eff}$  starts increasing with time after the minimum value. This is due to the



creation of deep acceptor levels in the defects. This process is known as reverse annealing. Reverse annealing process is much slower than beneficial annealing.

#### 6.5.4. Charge Collection Efficiency:

The  $e-h$  pairs created by the ionizing radiation in the silicon bulk are collected in the detector electrodes by applying suitable bias voltage. The radiation induced defects introduce deep levels in the band gap of the silicon and acts as traps for the charge carriers. This effect increases the charge collection time. Subsequently if the detrapping time is larger than the signal processing time by the readout electronics, results in incomplete charge collection. The trapping effect results in the exponential decay of the number of charge carriers created as per the equation (6.5)

$$N_{e-h}(t) = N_0 e^{\left(-\frac{t}{\tau_{tr,e-h}}\right)} \quad (6.5)$$

where  $\tau_{tr,e-h}$  is the charge carrier life time of electrons and holes. As long as the collection time is much lower than  $\tau_{tr,e-h}$  and the measurement time is longer than the collection time, the number of collected charge pairs is  $\sim N_0$ . When the charge collection time is comparable with signal processing time, the reduction in the collected charge due to traps starts to be effective. Increase in the radiation level further increases the trap centers, reduces the charge collection efficiency and hence worsens the signal to noise ratio of the irradiated detector.

#### 6.5.5. Defects:

Silicon bulk crystals inherently possess imperfections or crystalline defects. The defects are classified in to various types such as point defects, line defects, two and three

dimensional defects or volume defects. The point defects usually happen in the localized regions of a crystal involving isolated atoms. The line defects involve rows of atoms such as dislocations. Volume defects in a crystal are known as bulk defects which include voids due to intrinsic and extrinsic point defects. There are different types of point defects that strongly affect the performance of the semiconductor device, which are classified as follows

***Vacancy:*** Created by the missing atom.

***Interstitial:*** Atom occupying interstitial site which is located in a non-lattice site.

***Frenkel defect pair:*** A complex formed by the host atom displaced from a lattice site to a nearby vacant interstitial site.

***Impurities:*** Defects involving impurities (foreign atoms), also referred as extrinsic defects.

***Substitutional:*** Impurity atom replacing the host atom.

***Antisite:*** It is a type of substitutional defect where a host atom occupies the site of another host atom.

## **6.6. IONIZATION DAMAGE:**

Ionization damage is also known as surface damage which is due to the ionizing energy loss in the  $SiO_2$  and  $Si - SiO_2$  interface resulting in increased surface leakage current in the detectors. The passage of ionizing radiation in the oxide layer causes charge build up of the trapped charges in the oxide layer of the detector. The e-h pair created in the oxide layer either recombines or moves in the oxide electric field. The electrons moves towards  $SiO_2 - Si$  layer interface and holes towards the metallic contact. The highly mobile electrons escaped from the recombination are injected in to the silicon bulk and the less mobile holes trapped in the  $SiO_2 - Si$  interface [175]. This results in the

increase of the positive charge in the oxide layer and thereby degrading the quality. In addition to the trapped charge, ionizing radiation also produces new energy levels in the band gap at the bulk and oxide interface. The schematic representation of the ionization damage is shown in figure 6.11.

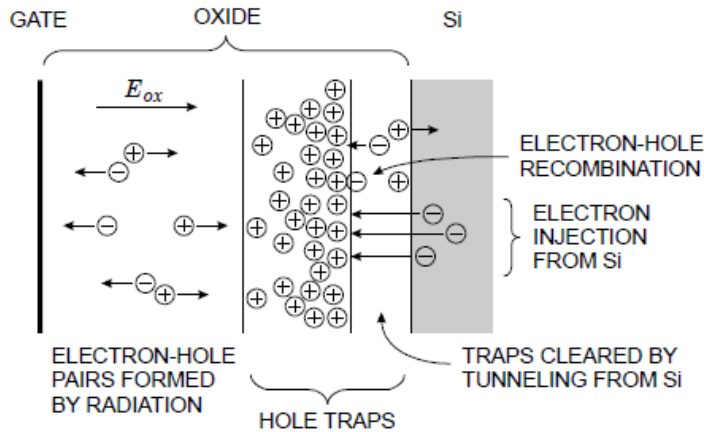


Fig. 6.11: Process of gate oxide under ionization radiation [175].

Although the primary radiation damage depends on the absorbed energy, the resulting effect depends on the rate of irradiation. The effects of the radiation damage on the oxide and the surface damage are dependent on the specific detector design.

## 6.7. THE NON IONIZING ENERGY LOSS (NIEL) SCALING HYPOTHESIS:

The proportionality between the non ionizing energy loss value and the damage caused by the particles is referred as NIEL scaling hypothesis. The NIEL scaling hypothesis is based on the assumption that the displacement damage is linearly dependent on the amount of energy imparted in displacing collisions which is independent of particle type. It is used to normalize the different radiation effects of various particles over large energy regions. Several experimental observations led to the assumption that the radiation damage produced in the silicon bulk due to the particle bombardment is proportional to the non ionizing energy loss.

To compare the damage produced by different types of particles at various energies, the particle fluence  $\Phi$  of particular irradiation is usually related to a reference value of 1 MeV neutrons (according to the ASTM - the international standards organization) by introducing a hardness factor  $\kappa$  and the 1 MeV equivalent particle fluence  $\Phi_{eq}$  is given in equation (6.6)

$$\Phi_{eq} = \kappa \Phi \quad (6.6)$$

The value of the hardness factor based on the NIEL scaling hypothesis is the ratio of damage displacement function  $\{D(E)\}$  for the particle with energy ( $E$ ) to the displacement damage function of 1 MeV neutrons [176]. The hardness factor for different particles with energy spectra  $\phi(E)$  by normalizing to that of 1 MeV neutron is given by the equation (6.7)

$$\kappa = \frac{\int D(E)\phi(E)dE}{D(E_n = 1MeV) \cdot \int \phi(E)dE} \quad (6.7)$$

The displacement damage function value caused by 1 MeV neutron is given in (6.8)

$$D_n(1MeV) = 95MeVmb \quad (6.8)$$

Figure 6.12 shows the displacement damage functions for protons, neutrons, electrons and pions in the energy range of  $10^{-4}$  MeV to  $10^4$  MeV [177-180]. From the above, one can see that the hardness factor is different for different types of particles. The 10 MeV proton equivalent radiation damage can be produced in the silicon detector with more than two orders of magnitude of 1 MeV electrons. There are experiments argue against the NIEL hypothesis [181-182]. Nevertheless, it is a useful tool for comparing the radiation damage due to various particles and energies in silicon detector.

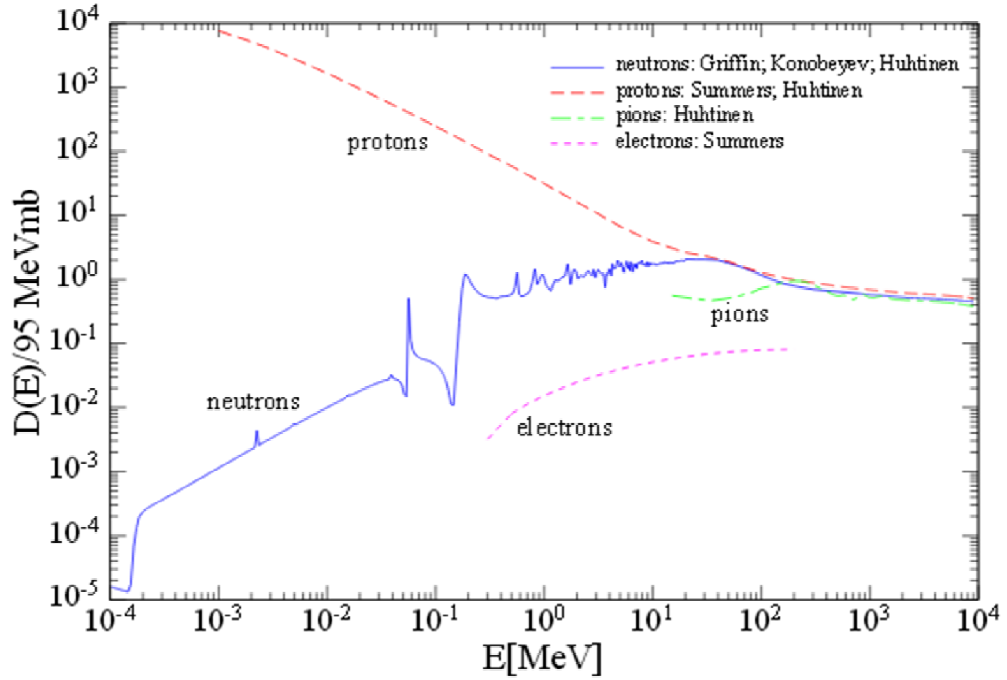


Fig. 6.12: Hardness factor for various radiations [177-180].

As discussed earlier, the semiconductor detector suffers from two types of damages. Some damages lead to catastrophic failure whereas the others show up as tolerable levels in the electrical parameters. In the later case, the radiation induced charges undergo redistribution and annihilation as time passes. The annealing in semiconductor device usually follows three different approaches namely rapid, slow and thermal annealing. In rapid annealing, it takes little time for device to recover from the damage and in case of slow annealing, it proceeds at room temperature. Thermal annealing takes places at elevated temperatures [183].

## 6.8. ESTIMATION OF TOTAL PROTON FLUENCE FOR CHANDRAYAAN-2 MISSION:

To estimate the expected particle fluence for the SDD onboard Chandrayaan-2 Mission, we have used the Chandrayaan-1 orbital profile (initially planned orbital

parameters), assuming that the Chandrayaan-2 mission will also follow the same launch strategy. The Chandrayaan-1 original orbital profile has two sections: a transfer orbit from the Earth to Moon of  $\sim 7$  days duration, and the 2 year circular orbit around the Moon at an altitude of 100 km. During the transfer orbit, the SDD detector onboard Chandrayaan-2 will encounter the trapped proton fluence in the Earth's radiation belt. The proton belt is located around 500 km above the Earth and extends up to an altitude of 20,000 km.

The fluence of trapped protons is estimated using the web-based European Space Agency (ESA) software suit SPENVIS (Space Environment Information System) [184]. In the estimation, we have adopted the AP-8 model of proton fluxes developed at NSSDC (National Space Science Data Center) of NASA/GSFC (Goddard Space Flight Center). The proton flux for each orbit is estimated individually and summed the proton flux for all orbits. The total estimated proton flux accumulated over the earth to moon transfer phase is  $\sim 7 \times 10^{12}$  protons  $\text{cm}^{-2}$  in the energy range of 0.1 MeV to 400 MeV under solar maximum conditions. The proton flux obtained for one sample Earth transfer orbit using SPENVIS AP-8 model is shown in figure 6.13. The electron flux obtained for the same orbit using SPENVIS AE-8 model is shown in figure 6.14.

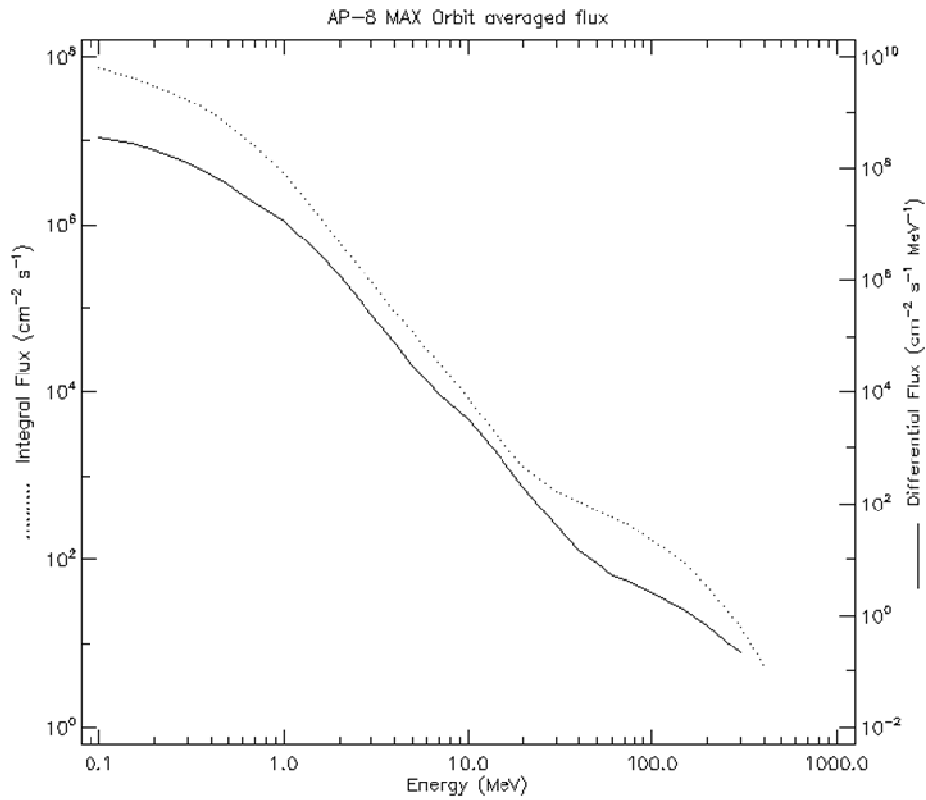


Fig. 6.13: Proton flux estimated using Ap-8 model for the Chandrayaan-1, Earth transfer orbit 299 km to 25481 km.

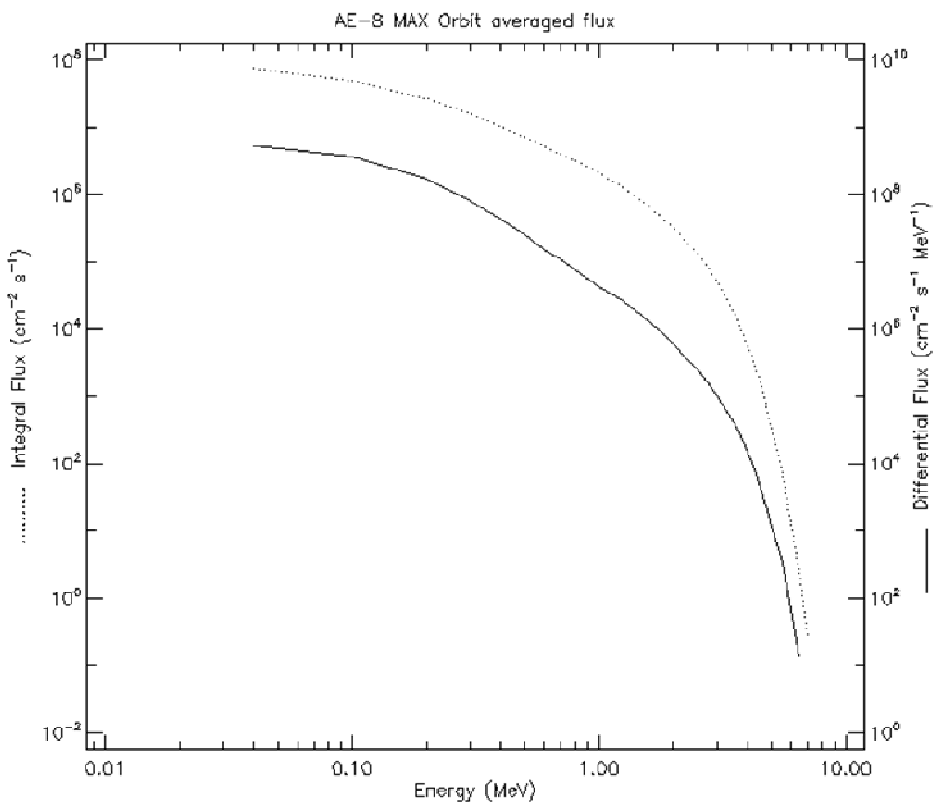


Fig. 6.14: Electron flux estimated using AE-8 model for the Chandrayaan-1, Earth transfer orbit 299 km to 25481 km.

Similarly the flux is calculated for all earth bound orbits and thereby the total flux is estimated by adding the flux from individual orbits during the transfer orbit to the moon. Once the satellite reaches the moon orbit, the radiation damage to the SDD is mainly due to the solar protons throughout the mission life of 2 years. To estimate the solar proton flux, we have adopted the JPL-91 solar fluence model which, with a confidence level of 95%. This gives the total solar proton flux of  $\sim 5 \times 10^{11}$  protons  $\text{cm}^{-2}$  in the energy range of 0.1 MeV to 400 MeV after the transfer orbit for the maximum solar activity.

The rover payload APXS is expected to receive much lower radiation dose compared to that of XSM payload which is in the orbiter craft. The APXS payload is mounted under the rover chassis and the whole rover is stored inside the lander craft during the earth to moon transit and hence the SDD is shielded by thick layers of lander and rover structures. APXS instrument is planned with life time of only one lunar day ( $\sim 14$  earth days) as there is no provision to control the rover subsystem environments during lunar night conditions where the temperatures could reach up to  $-200^\circ\text{C}$ . Hence the SDD onboard APXS is expected to receive very minimal radiation and hence no performance degradation is expected.

In case of the XSM payload, the instrument packages are mounted on the orbiting satellite and expected to see the radiation environment during the earth to moon transfer and also in the lunar orbit during the operating phase. The XSM payload packages are made of aluminum and the estimated thickness of aluminum layer around the SDD is about 2 mm except the field of view (FOV) which is  $\sim 0.2 \text{ mm}^2$ . The FOV of the SDD onboard XSM is covered with 2 mm thick aluminum filter during the earth to moon transfer and also during the non operating conditions in the lunar orbit.



After estimating the total proton flux in the transfer and lunar orbit phases, the proton flux reaching the SDD is estimated using the non ionizing energy loss function in SPENVIS. The NIEL function in SPENVIS provides 10 MeV equivalent proton fluence for various shielding thicknesses. Using this function, the 10 MeV equivalent trapped and solar proton fluxes were estimated as a function of various aluminum shielding thicknesses as shown in figure 6.15. This reduces the proton fluence to  $\sim 3.4 \times 10^7$  protons/40 mm<sup>2</sup> during the transit and to  $\sim 4 \times 10^9$  protons/40 mm<sup>2</sup> during the in-orbit lunar operation for 2 mm thick aluminum shield. We used <sup>60</sup>Co gamma ray chamber to simulate the proton induced radiation damage in the SDD as the particle accelerators are less accessible. The SDD irradiated using <sup>60</sup>Co with photon energies of 1.17 MeV and 1.33 MeV produces scattered Compton electrons having energies of a few hundred keV and these electrons cause displacement damage.

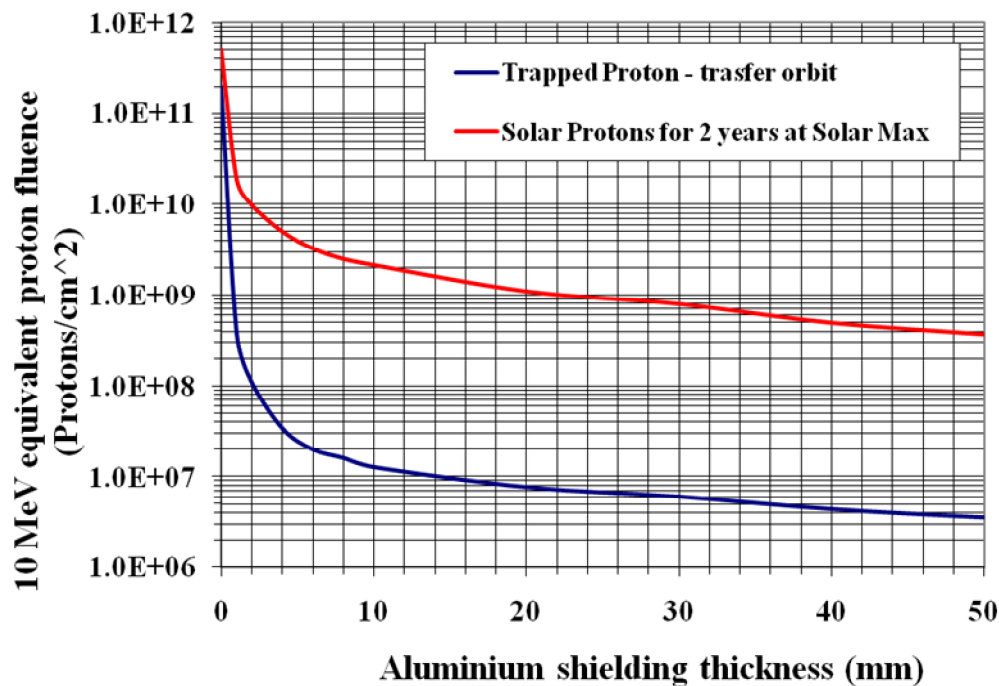


Fig. 6.15: The estimated 10 MeV equivalent trapped and solar proton fluence for various aluminum shielding thicknesses.

The correlation between the damage due to a gamma ray induced electron to that of a 1 MeV electron is given in ref. [180]. Based on the NIEL scaling hypothesis, the

hardness factor of more than 2 orders of magnitude lower for electrons at 1 MeV compared to that of a proton with energy at 10 MeV [179]. The values of hardness factor for various particles and energies are reported in refs [178-180].

## **6.9. ESTIMATION OF COMPTON ELECTRON SPECTRUM WITH GEANT4 SIMULATION:**

GEANT4 simulation is carried out to estimate the scattered Compton electron interactions in a 40 mm<sup>2</sup> area SDD. The SDD detector module is modeled with various materials as given by the manufacturer and the model is shown in figure 6.16.

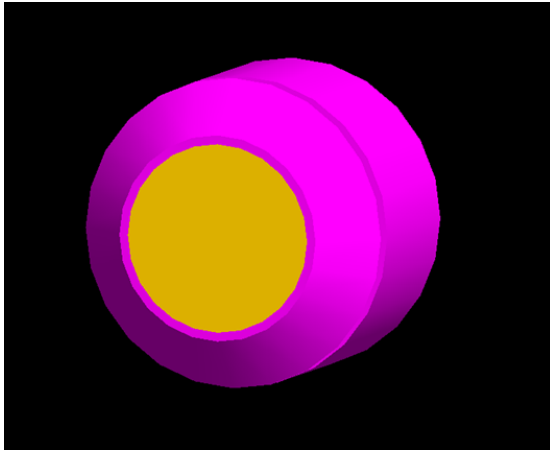


Fig. 6.16: SDD module modelled in GEANT4.

In the simulation, the SDD module is irradiated with gamma rays of 1.17 MeV and 1.33 MeV energies with total of  $10^9$  gamma ray photons as shown in figure 6.17. The Compton electron spectrum recorded for the given gamma interaction is shown in figure 6.18. This gives  $\sim 2.5 \times 10^5$  scattered Compton electron interactions with total energy of electrons is  $\sim 5.2 \times 10^{10}$  eV, depositing a total dose of  $\sim 0.025$  rads. The gamma ray chamber used in the irradiation experiment provides the dose of  $\sim 3.26$  rads / s and to achieve this,  $\sim 3.3 \times 10^7$  electron interactions/second are required.

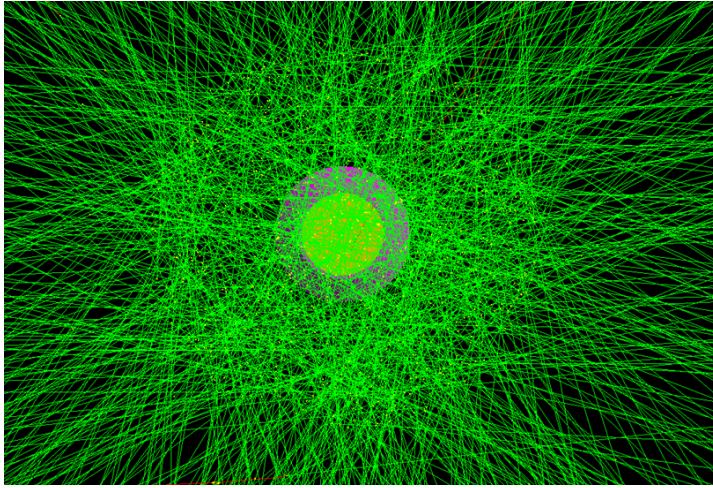


Fig. 6.17: GEANT4 simulation for  $10^3$  gamma ray photons using  $^{60}\text{Co}$  gamma ray source.

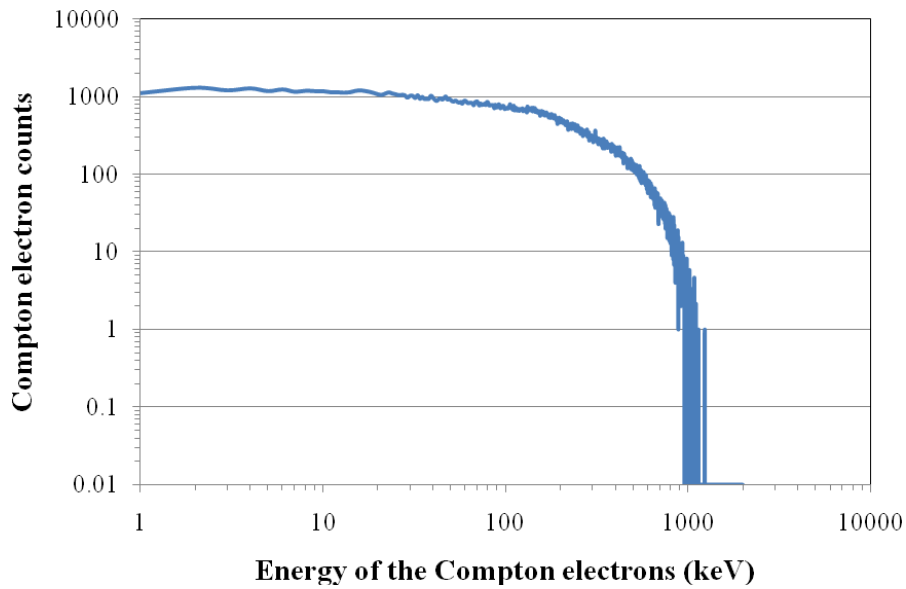


Fig.6.18: Scattered Compton spectrum observed for  $10^9$  gamma ray photon interactions with SDD detector using GEANT4.

The 10 MeV equivalent total proton fluence of  $\sim 4 \times 10^9$  protons/40 mm<sup>2</sup> provides the cumulative dose of  $\sim 10$  krad with each proton depositing  $\sim 5$  MeV in a 450 micron thick SDD. To achieve the same dose through gamma irradiation requires  $\sim 1 \times 10^{11}$  gamma induced Compton electron interactions.

## **6.10. GAMMA RAY AND X-RAY IRRADIATION:**

As discussed earlier, the interaction of protons, neutrons, electrons and gamma rays leads to displacement damage in silicon detectors. The displacement damage due to neutron irradiation results in defect clusters and in case of gamma irradiation, the displacement damage is due to isolated single defects. The displacement damage due to charged particles and protons are caused by the defect clusters as well as isolated single defects. In the present study, the SDD modules VS0592 and VS0629 (both with 40 mm<sup>2</sup> are with 450 micron thick silicon) are irradiated with various gamma ray (<sup>60</sup>Co) and X-ray (<sup>55</sup>Fe) doses to study any degradation in the spectroscopic performance and its suitability to use in the upcoming planetary mission. Gamma ray irradiation is carried out to study the space radiation effects on the SDD module and the degradation in the energy resolution. The gamma ray irradiation will also affect the characteristics of the electronic devices mounted inside the module along with the SDD chip as expected in the space environment.

The Solar X-ray Monitor (XSM) instrument onboard Chandrayaan-2 orbiter is expected to receive large intensities of solar X-rays during its operational period in the lunar orbit. In this regard, the X-ray irradiation using <sup>55</sup>Fe is carried out to study the fluence level up to which the SDD detector provides stable energy resolution.

### **6.10.1. Gamma Ray Facility and Experimental Procedure:**

The gamma chamber facility established at ISRO Satellite Centre (ISRO-Indian Space Research Organization) which was installed by Board of Radiation and Isotope Technology (BRIT) was used for testing. The GC 900 gamma chamber was loaded with 2 KCi of <sup>60</sup>Co activity on commissioning and calibrated at the time of installation.

Presently, this gamma chamber provides the dose rate of  $\sim 3.26$  rads/s. The schematic of the gamma ray irradiation experimental setup is shown in figure 6.19.

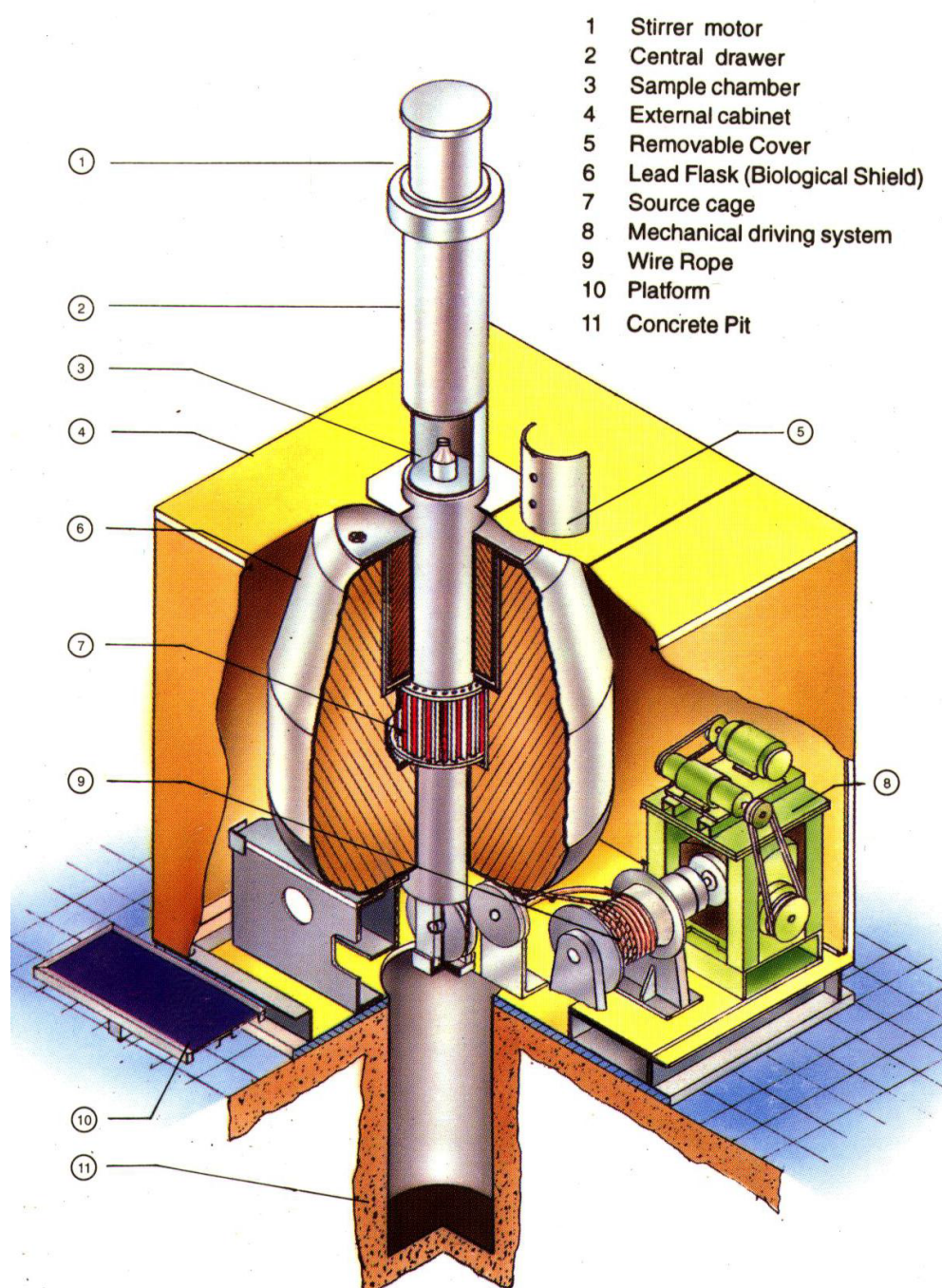


Fig. 6.19: Schematic representation of the cross sectional view of gamma ray irradiation chamber with  $^{60}\text{Co}$  (Courtesy BRIT).

The gamma chamber GC 900 is a motorized chamber with necessary shielding around the gamma source  $^{60}\text{Co}$ . The motor based mechanical driving system is used to

bring the sample mounted in the sample compartment in and out of the gamma radiation environment. The motor is controlled by a front panel where the irradiation timing duration can be set. In the gamma ray irradiation experiment, the SDD module mounted on a aluminum plate is (this assembly is part of the spectrometer) placed in a sample chamber by removing the cover. Subsequently, the irradiation time duration is set in the front panel based on the irradiation dose. During irradiation, the SDD module with aluminum plate is moved inside the lead (*Pb*) chamber to position the SDD module in the gamma ray radiation environment. After the set irradiation time, the motor based mechanism brings out the setup. Subsequently, the SDD module with aluminum plate is assembled with the readout electronics with necessary electrical interfaces. The SDD operating temperature is varied from room temperature to -40°C in steps of 10°C and measured the leakage current and the energy resolution. The leakage current is measured by counting the ramp signal frequency of CSPA with known value of feedback capacitance and the set ramps signal amplitude between -2 V to +4 V. Energy resolution is measured using  $^{55}\text{Fe}$  X-ray source. During these measurements, the room temperature is maintained at 20°C. This process is repeated for each desired gamma ray dose. This irradiation experiment was carried out over the period of ~ 5 days. Initially the irradiation dose level was aimed at 10 krad and subsequently extended to ~ 547 krad. SDD module is kept in passive mode (not powered) during irradiation.

#### **6.10.2. X-ray Irradiation Setup and Experimental Procedure:**

In case of X-ray irradiation, the SDD module VS0592 is mounted on a 1mm thick aluminum wall which is part of the spectrometer system. The  $^{55}\text{Fe}$  X-ray source is fixed in a source holder made of copper which is intern fixed on a movable aluminum assembly. The distance between the detector and the X-ray source is variable to maintain



the X-ray fluence rate falling on the SDD module. The detector assembly and the source are aligned such that the total SDD detector area views the source. The X-ray irradiation experimental setup is shown in figure 6.20. The activity of the  $^{55}\text{Fe}$  source used in the irradiation is  $\sim 5$  mCi. It is essential to estimate the X-ray fluence in order to determine the actual dose received by the SDD module under the test. Measuring the X-ray count rates by acquiring the spectral data is practically not feasible using the spectrometer system when the count rate exceeds  $10^5$  counts/s. Alternately, the fluence is estimated by counting the ramp signal frequency by placing  $^{55}\text{Fe}$  source at a desired distance from the SDD module. The  $^{55}\text{Fe}$  source has two X-ray lines with energies at 5.9 keV and 6.5 keV with the intensity of 83% and 17% respectively. With the known value of feedback capacitance and the set ramp signal amplitude, one can estimate the X-ray fluence.

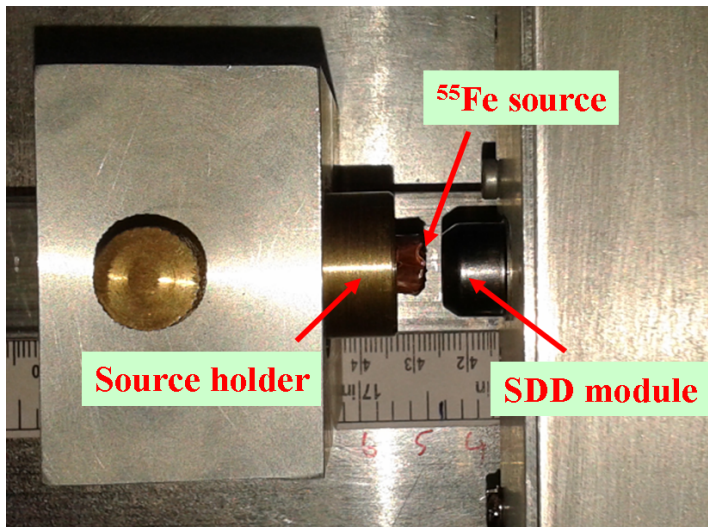


Fig. 6.20: X-ray irradiation experimental setup using  $^{55}\text{Fe}$  X-ray source [153].

The distance between the SDD module and the X-ray source is adjusted such that the ramp signal frequency is  $\sim 9$  kHz which is equal to the irradiation fluence rate of  $\sim 2 \times 10^6$  photons/ $40 \text{ mm}^2$  area SDD. The ramp signal frequency due to leakage current at  $-40^\circ\text{C}$  before irradiation is  $< 2$  Hz which is negligible compared to the 9 kHz due to the X-ray photons. The same fluence rate is maintained throughout the irradiation measurements by changing the source to detector distance at the desired time intervals by

counting the ramp signal frequency. It is experimentally verified that the ramp signal frequency increases by  $\sim 1$  Hz for the incident X-ray rate of  $\sim 220$  photons/s for the given ramp signal amplitude at  $-40^{\circ}\text{C}$ . This has been confirmed through independent measurements and also verified theoretically (discussed in chapter-5).

The irradiation time is estimated for the desired X-ray doses. After the each desired dose, the source is removed from the experimental setup and subsequently, the leakage current and the energy resolution is measured for various detector operating temperatures ranging from  $20^{\circ}\text{C}$  to  $-40^{\circ}\text{C}$  in the steps of  $10^{\circ}\text{C}$ . The room temperature is maintained at  $20^{\circ}\text{C}$  during the measurement. The experimental results are discussed in the next section. The irradiation is carried out in passive mode i.e., without powering the SDD module and the spectrometer system. The spectrometer system is powered at the desired time intervals to keep track of X-ray photon fluence.

## **6.11. EXPERIMENTAL RESULTS:**

### **6.11.1. Spectrometer Pperformance before Irradiation:**

The leakage current and the energy resolution are measured for both the SDD modules (VS0592 and VS0629) before gamma ray and X-ray irradiations. The measured value of feedback capacitance for these SDD modules are 66 fF and 60 fF respectively (as discussed in chapter-5). The measured leakage current is shown to be varying from  $\sim 0.1$  pA at  $-40^{\circ}\text{C}$  to  $\sim 70$  pA at  $10^{\circ}\text{C}$  for the SDD module VS0592 and incase of VS0629, the leakage current varies from  $\sim 0.3$  pA to  $\sim 300$  pA when the SDD temperature is varied from  $-40^{\circ}\text{C}$  to  $10^{\circ}\text{C}$ . The measured value of feedback capacitance and the leakage current for the SDD modules (VS0592, VS0629) used for the irradiation tests are given in table-6.4.



**Table-6.4:** Measured values of feedback capacitance and leakage current of the SDD modules before irradiation tests.

SDD module	Feedback capacitance	Leakage current at -40°C	Leakage current at 10°C
VS0592	~ 66 fF	~ 0.1 pA	~ 70 pA
VS0629	~ 60 fF	~ 0.3 pA	~ 300 pA

The measured energy resolution is shown to be varying from ~ 150 eV at 5.9 keV for the pulse shaping time of ~ 3.3  $\mu$ s at -40°C to ~ 180 eV at -10°C for the SDD module VS0592. For the SDD module VS0629, the energy resolution is ~ 160 eV at -40°C and increases to ~ 260 eV at -10°C. The spectral characteristics of the SDD module VS0592 is found to be superior compared to VS0629. The energy resolution as a function of temperature for both the SDDs is shown in figure 6.21.

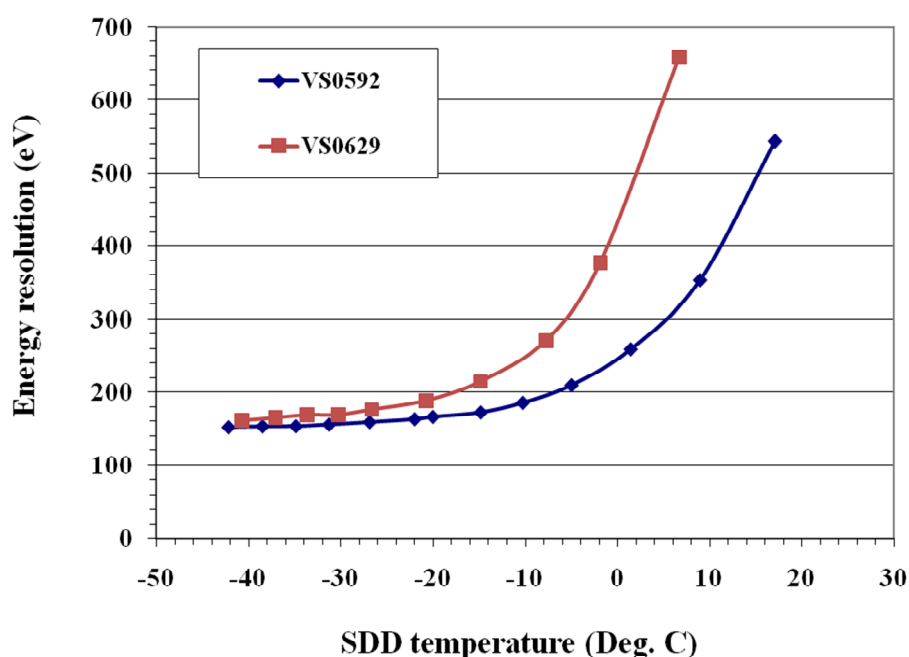


Fig. 6.21: Energy resolution measured for both the SDD modules (VS0592 and VS0629) before irradiation for various detector operating temperatures.

Energy resolution is also measured by changing the time constant of the pulse shaping amplifier (shaping time), to determine the optimal pulse shaping time. It is

observed that the developed SDD based X-ray spectrometer provides best energy resolution for the pulse peaking time of  $\sim 3.3 \mu\text{s}$ . Figure 6.22 shows the measured energy resolution for various shaping time constants of  $0.15 \mu\text{s}$ ,  $0.4 \mu\text{s}$ ,  $1 \mu\text{s}$ ,  $3.3 \mu\text{s}$  and  $10 \mu\text{s}$  for two different operating temperatures though the measurement is done for the temperature range of  $20^\circ\text{C}$  to  $-40^\circ\text{C}$ .

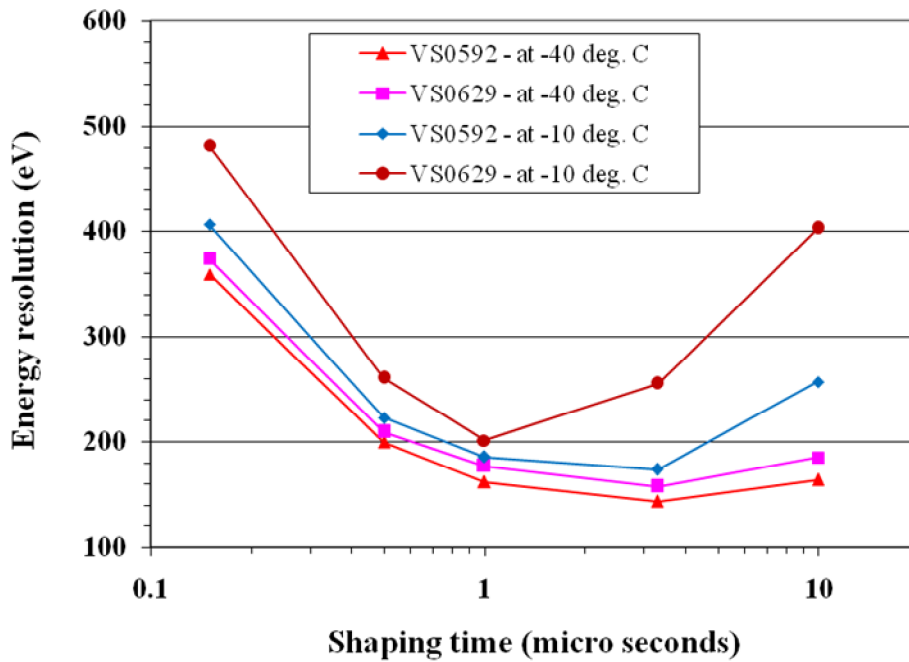


Fig. 6.22: Energy resolution measured for various shaping time constants at two temperatures for both VS0592 and VS0629 SDD modules [153].

### 6.11.2. Performance after Gamma Ray Irradiation:

It is shown in the earlier section that the  $40 \text{ mm}^2$  area SDD is expected to receive the total cumulative dose of  $\sim 10 \text{ krad}$  at the end of life (EOL) of the XSM instrument. It is essential to quantify the performance degradation of the SDD based X-ray spectrometer for these doses to meet the desired performance till EOL period. The space radiation will also affect the electronic components inside the SDD module. The SDD module VS0629 is irradiated with gamma rays in the passive mode with fluence rate  $\sim 3.23 \times 10^7$  gamma induced scattered Compton electron interactions/s. The initial

irradiation test is targeted up to 10 krad in steps for Chandrayaan-2 mission requirement. Later the irradiation test is extended up to  $\sim 547$  krad to quantify the performance for higher radiation levels. After each desired radiation dose, the leakage current and the energy resolution is measured. The measured leakage current is  $\sim 0.35$  pA at  $-40^\circ\text{C}$ ,  $\sim 50$  pA at  $0^\circ\text{C}$  and  $\sim 450$  pA at  $20^\circ\text{C}$  for the gamma ray dose of 10 krad and at  $\sim 547$  krad, the leakage current increased to  $\sim 4$  pA at  $-40^\circ\text{C}$ ,  $\sim 80$  pA at  $0^\circ\text{C}$  and 1 nA at  $20^\circ\text{C}$  as shown in figure 6.23.

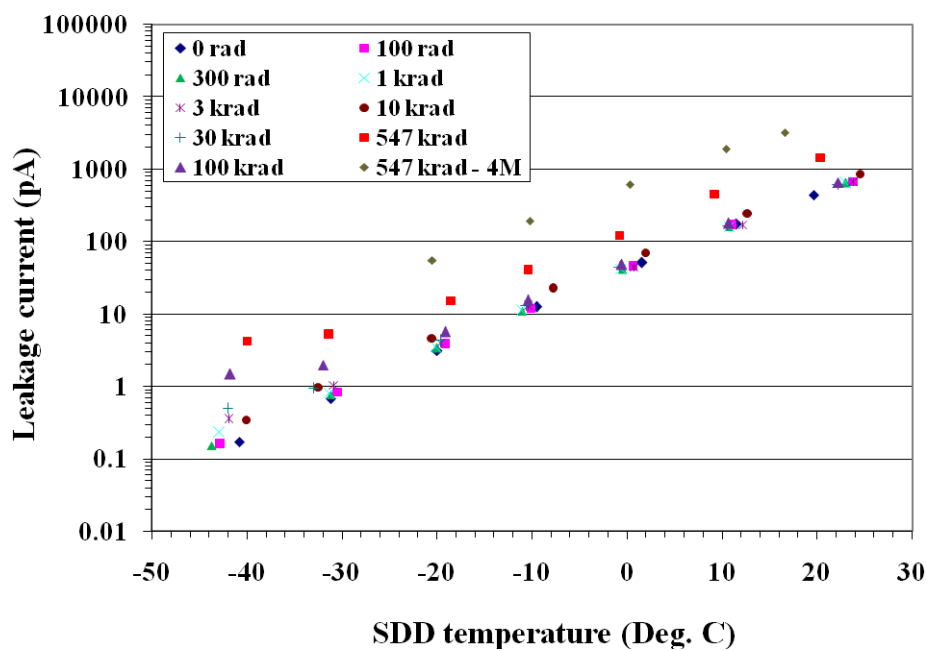


Fig. 6.23: Leakage current measured for various gamma ray doses versus detector operating temperatures [153].

It is also observed that the change in the magnitude of the leakage current is higher at lower detector operating temperatures compared to higher detector operating temperatures. Leakage current is also measured 4 months after irradiation by preserving the SDD module in the laboratory environment and found that the increase in the leakage current is  $\sim 40$  pA at  $\sim -20^\circ\text{C}$  compared to the leakage current measured just after irradiation of  $\sim 547$  krad. The measurement is limited to the detector operating temperature of  $-20^\circ\text{C}$  as the SDD module could not be cooled below  $-20^\circ\text{C}$  even though

the Peltier cooler consumes rated maximum power. This could be due to the degradation of Peltier cooler efficiency with the gamma ray irradiation. The increase in the leakage current could be due the irreversible damage to the SDD and the internal FET. It is observed that there is no significant degradation in the energy resolution (shaping time 3.3  $\mu$ s) for the gamma ray doses up to 3 krad, and the energy resolution degrades to  $\sim$  210 eV at 10 krad which is expected during the Chandrayaan-2 life time of two years. The energy resolution degrades to  $\sim$  250 eV at 100 krad and  $\sim$  340 eV at 547 krad for the detector operating temperature of  $\sim$  -40°C as shown in figure 6.24.

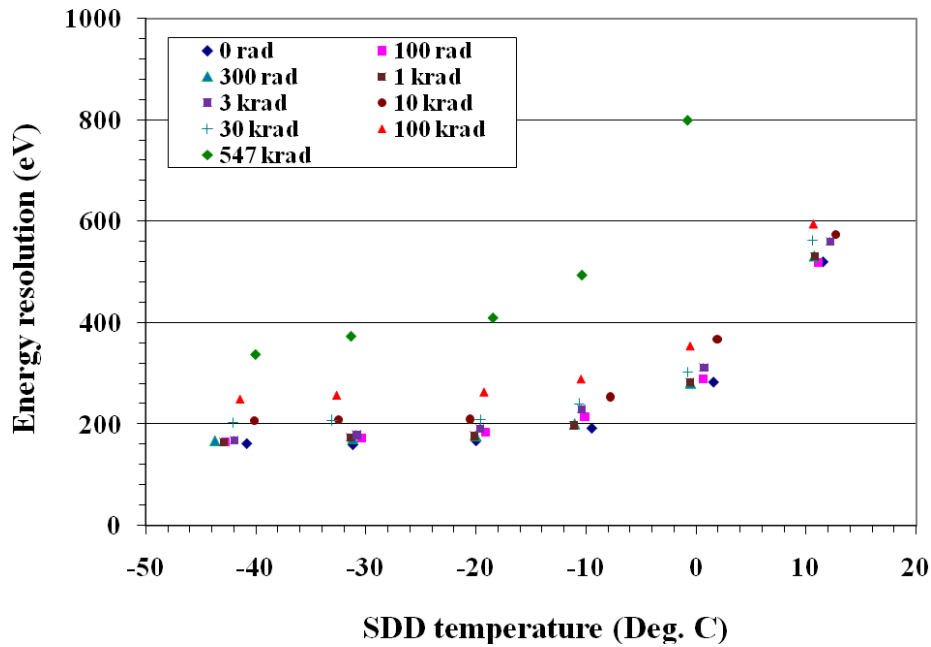


Fig. 6.24: Measured energy resolution for various gamma ray doses versus detector operating temperatures [153].

The energy resolution is measured for various pulse peaking time constants before gamma ray irradiation and compared with the energy resolution measured after 547 krad at -20°C. It is shown that the energy resolution after the gamma ray dose of 547 krad is worse than the energy resolution measured at 0°C before irradiation as shown in figure 6.25. Energy resolution is also measured for the pulse shaping time of  $\sim$  3.3  $\mu$ s

during the gamma ray irradiation and shown that the energy resolution degrades systematically with absorbed dose as shown in figure 6.26.

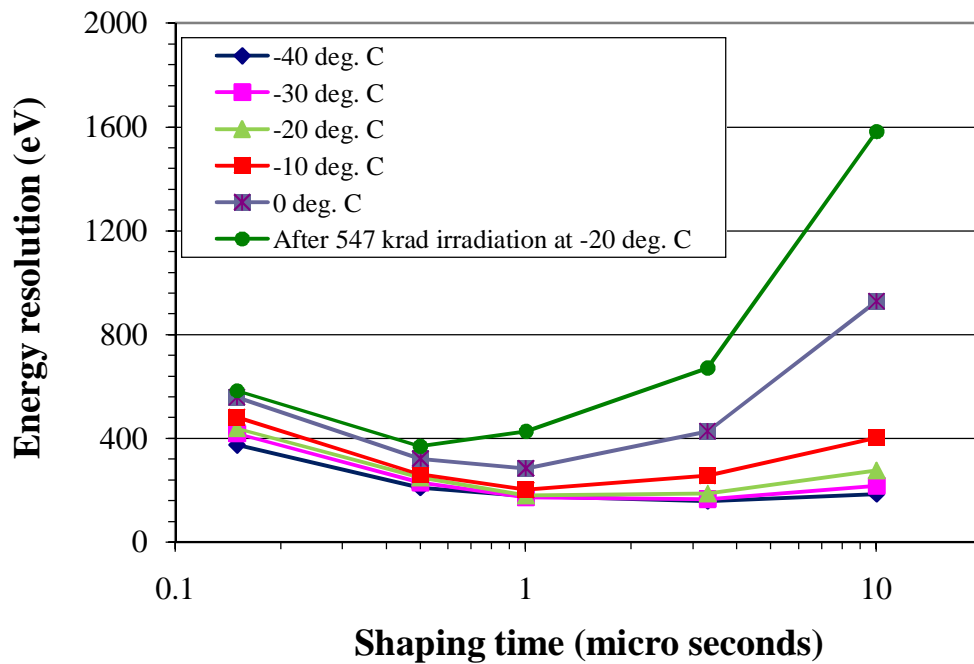


Fig. 6.25: Measured energy resolution for various detector operating temperatures and compared with gamma ray dose of 547 krad at  $-20^{\circ}\text{C}$ .

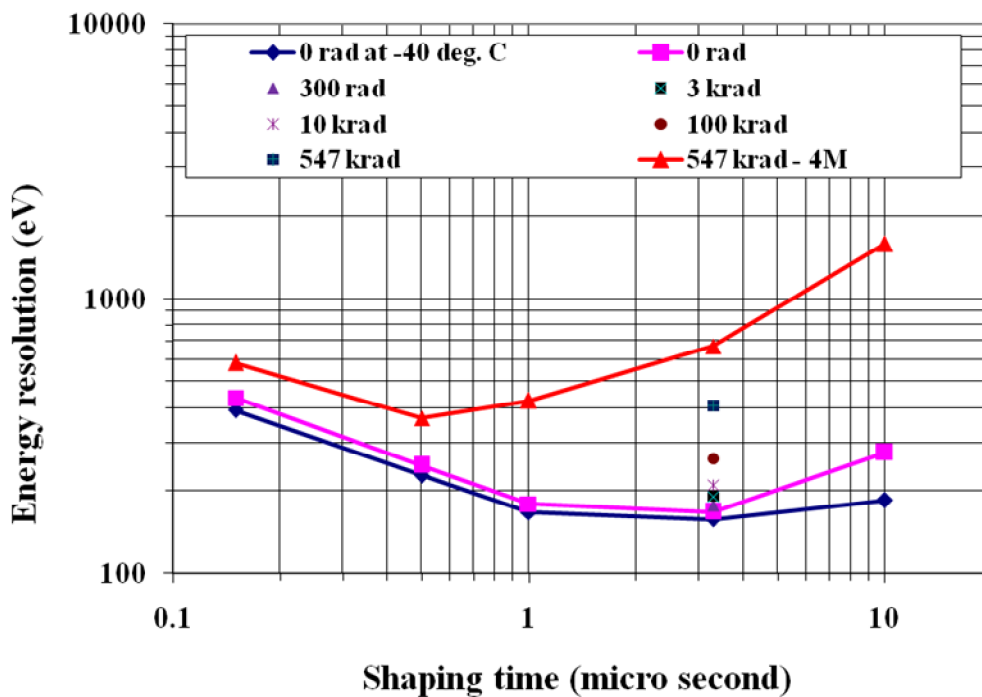


Fig. 6.26: Energy resolution measured before and after gamma ray irradiation for the detector operating temperature of  $-20^{\circ}\text{C}$  (4M - four months after gamma ray irradiation) compared with before irradiation at  $-40^{\circ}\text{C}$  [153].

The energy resolution of the detector is compared for the operating temperature of -20°C as the SDD module could not be cooled to lower temperatures though the energy resolution is measured at -40°C before and during the irradiation tests. The Solar X-ray Monitor instrument is designed with pulse shaping time of  $\sim 0.8 \mu\text{s}$  to accommodate the count rates close to  $\sim 70 \text{ kcts/s}$  with energy resolution of  $\sim 200 \text{ eV}$  at 5.9 keV. At 0.8  $\mu\text{s}$  shaping time, the degradation in the energy resolution could be around 210 - 220 eV after 10 krad. This meets the requirement of energy resolution of XSM which is  $< 250 \text{ eV}$  till EOL. In case of APXS, the SDD is expected to receive much lower dose as the instrument is well shielded by the lander craft during the transit and shorter operating life on the lunar surface. Rover chassis also provides additional shielding.

### **6.11.3. Performance after X-ray Irradiation:**

The Solar X-ray Monitor onboard Chandrayaan-2 mission is expected to receive high intensities of solar X-rays during its in orbit operation as this instrument is meant to provide real time solar X-ray spectrum to the companion instrument. In this direction, the SDD module VS0592 is subjected to various X-ray doses up to 64 krad in steps. The X-ray dose is applied in passive mode (without powering the SDD module and the readout electronics) with fluence rate of  $\sim 2 \times 10^6 \text{ photons/40 mm}^2$ . At each X-ray dose, the leakage current is measured by counting the ramp signal frequency and also the energy resolution for the shaping time of 3.3  $\mu\text{s}$ . It is observed that there is no significant change in the leakage current and the energy resolution for the detector operating temperatures  $< 0^\circ\text{C}$  as shown in figure 6.27. It is also observed that there is appreciable change in the leakage current and the energy resolution when the X-ray dose is increased from 30 krad to 64 krad for the detector operating temperatures  $> 0^\circ\text{C}$ .

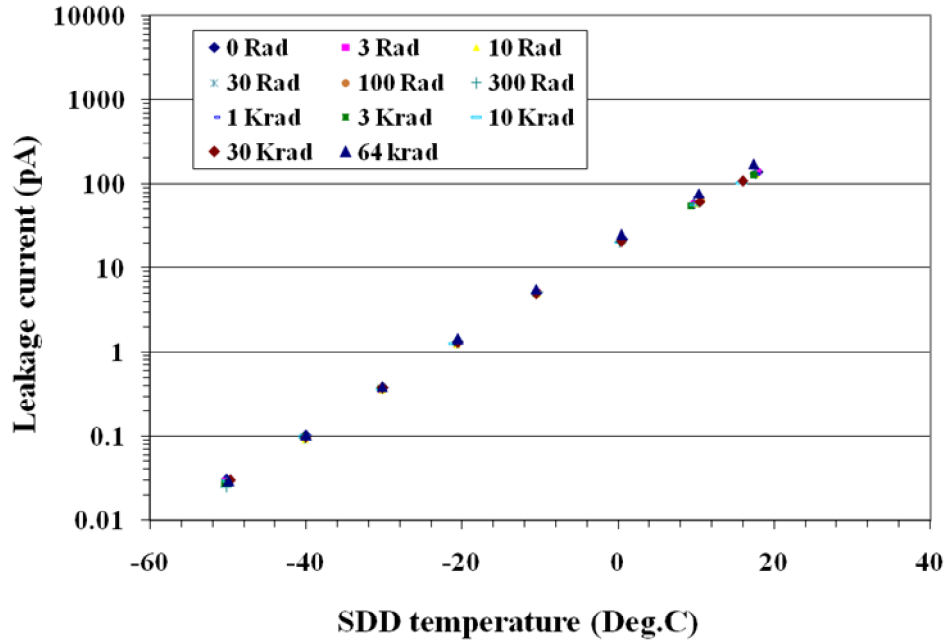


Fig. 6.27: Leakage current measured for various X-ray doses versus detector operating temperature [153].

Energy resolution degrades from  $\sim 340$  eV to  $\sim 410$  at  $10^\circ\text{C}$  and from  $\sim 500$  eV to  $\sim 620$  eV at  $20^\circ\text{C}$  when the X-ray dose is increased from 30 krad to 64 krad as shown in figure 6.28.

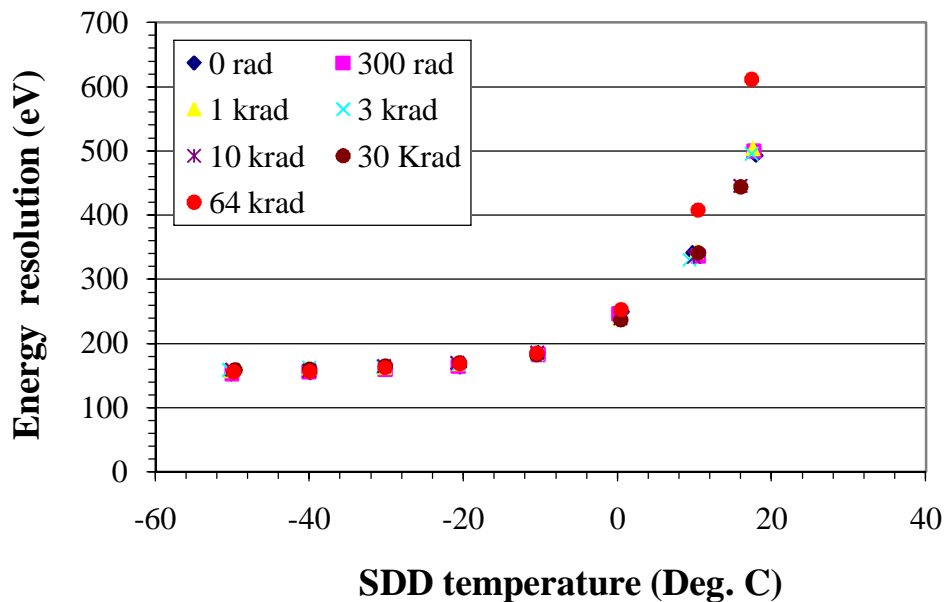


Fig. 6.28: Measured energy resolution (shaping time  $3.3 \mu\text{s}$ ) for various X-ray doses versus detector operating temperatures (Energy resolution is plotted for fewer doses for clarity).

This shows that the radiation damage is sensitive to temperature. The SDD module VS0592 is irradiated with total fluence of  $\sim 2 \times 10^{13}$  photons/40 mm<sup>2</sup> to get 64 krad cumulative dose on the silicon bulk. The energy resolution versus leakage current plot confirms the result presented in chapter-5, the potential use of leakage current as a calibration tool for onboard applications.

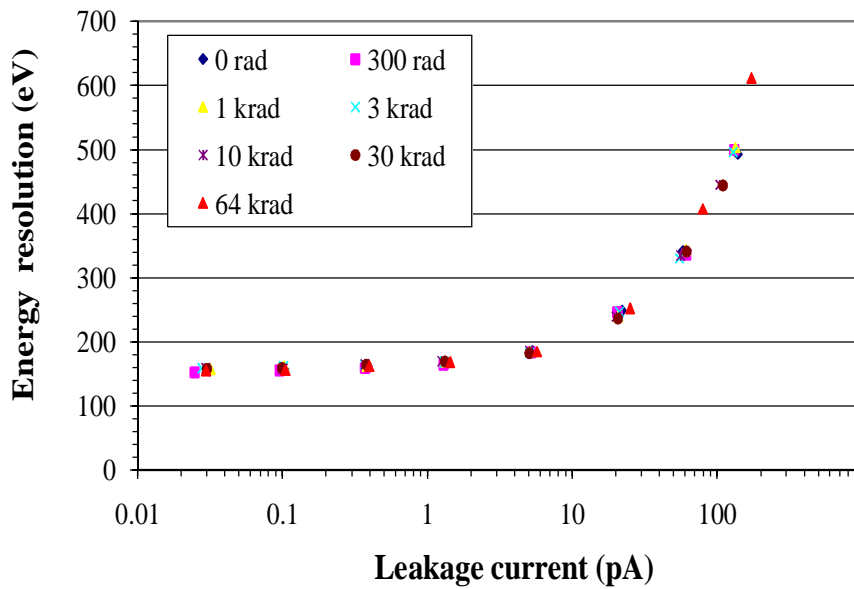


Fig. 6.29: Leakage current versus energy resolution for various X-ray doses.

This measurement confirms the earlier reported X-ray irradiation [185] on similar SDD detector with active area of 5 mm<sup>2</sup> irradiated with *Mo-K*, 18 keV X-ray photons for over several years in active mode for the fluence of  $10^{13}$  photons and shown no degradation in the energy resolution.



## 6.12. NOISE PERFORMANCE OF THE SPECTROMETER: PRE AND POST IRRADIATION TESTS:

### 6.12.1. Introduction to System Noise:

The energy resolution (FWHM) of the SDD based X-ray spectrometer depends on the charge carrier fluctuation during the photon interaction and the base line noise associated with the readout electronics. The charge carrier fluctuation is defined using Fano factor, which is also known as intrinsic energy resolution of the detector. The Fano factor for silicon detector is  $\sim 0.11$  and the intrinsic energy resolution is  $\sim 120$  eV at 5.9 keV [25]. The intrinsic energy resolution is due the lattice vibrations, quantized as photons whose excitation energy is much smaller (meV) than the band gap energy (eV). Therefore, many such excitations are involved and hence introduce statistical fluctuations in the signal charge.

In addition to the statistical fluctuations in the charge carrier generation, the readout electronics noise introduces the base line fluctuations which are superimposed on the signal and thereby altering the peak signal amplitude. The base line noise has random amplitude and time distributions and hence the base line noise alters the signal amplitude with time dependence. The schematic representation of signal, base line noise and the resultant signal is shown in figure 6.30.

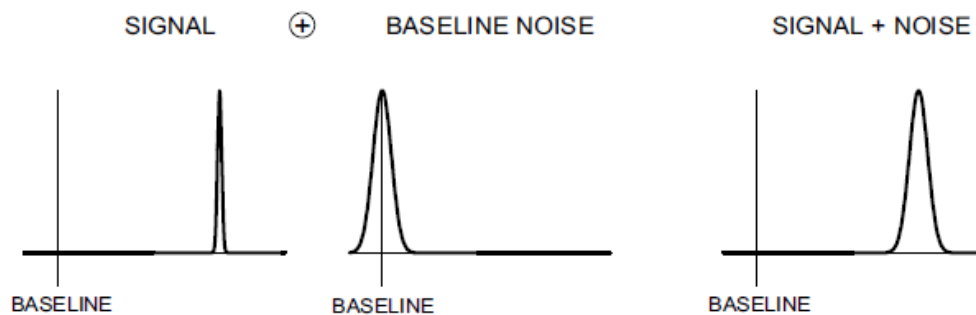


Fig. 6.30: Signal and base line fluctuation for small signal variance and large base line noise fluctuation [170].

The base line fluctuations are due to various factors such as artifacts due to imperfect readout electronics, interference from external sources, non optimized layout designs etc. In optimized spectrometer systems, the peak signal amplitude fluctuates above the average noise value and hence can be detected as a valid signal. Various charge readout techniques in recent years aimed to improve the signal to noise ratio by modifying the signal characteristics and hence the noise. In semiconductor detectors, the base line noise of the readout electronics is thought to be defining the system energy resolution. But in recent years, the advancement in the readout electronics systems, the energy resolution close to the intrinsic energy resolution is achieved [81]. For example, SDD with inbuilt FET or SDD with ASIC based readout as discussed in the chapter 3.

### 6.12.2. Basic Noise Mechanisms:

The current flown through the sample bounded by two electrodes depends on the number of charge carriers ( $n$ ), their velocity ( $v$ ) and the detector length ( $l$ ). The induced current detected at the readout electrode is given in equation (6.9).

$$I = \frac{nev}{l} \quad (6.9)$$

There are two mechanisms contribute to the total noise, one is velocity fluctuation (e.g. thermal noise) and the charge carrier number fluctuations (e.g. shot noise or 1/f noise). The fluctuation in the current is given by the total differential where the two terms are added in quadrature, which is given in equation (6.10)

$$\langle dI \rangle^2 = \left( \frac{ne}{l} \langle dv \rangle \right)^2 + \left( \frac{ev}{l} \langle dn \rangle \right)^2 \quad (6.10)$$

The two terms, velocity fluctuation and the number fluctuation are statistically uncorrelated and hence contribute to the total noise. The velocity fluctuation is due to the

thermal motion and known as thermal noise. The thermal noise is a white noise source and hence the power spectral density ie., the power per unit bandwidth is constant. The charge carrier number fluctuations occur in many circumstances such as carrier flow limited by the emission and the probability of carrier crossing the barrier is independent of other carriers being emitted. This current fluctuation noise is known as shot noise which also has white spectrum and hence the power spectral density is constant as given in (6.11) and (6.12).

$$\frac{dV_n^2}{df} = \text{const.} \quad (6.11)$$

or

$$\frac{dP_n}{df} = \text{const.} \quad (6.12)$$

#### 6.12.2.1. Thermal Noise:

Thermal noise in the resistor is the most common example of noise due to the velocity fluctuations. Thermal noise is also known as Johnson noise or Nyquist noise. This is due the thermal excitation of the charge carriers. The white spectral noise is proportional to the absolute temperature. Transforming the current fluctuations from time domain to frequency domain yields the spectral noise power density versus frequency which is given in equation (6.13)

$$\frac{dP_n}{df} = 4kT \quad (6.13)$$

where  $k$  is Boltzmann constant and  $T$  is the absolute temperature. The respective spectral noise voltage and current densities are given in equations (6.14) and (6.15).

$$\frac{dV_n^2}{df} \equiv e_n^2 = 4kTR \quad (6.14)$$

$$\frac{dI_n^2}{df} \equiv i_n^2 = \frac{4kT}{R} \quad (6.15)$$

The total noise is obtained by integrating over the desired frequency range or system bandwidth. The integrated voltage noise at the output of the amplifier is given in equation (6.16) with frequency dependent gain  $A(f)$

$$v_m^2 = \int_0^\infty e_n^2 A^2(f) df \quad (6.16)$$

The total noise increases with increase in the bandwidth. For smaller bandwidth amplifiers, the signal rise time is longer and hence limits the measurement rate with low noise. The amplifier with large bandwidth has fast signal rise time accommodating high measurement rate with increased noise contribution. The amplitude of the noise distribution is Gaussian and hence the noise superimposed with the signal also yields Gaussian distribution.

#### 6.12.2.2. Shot Noise:

Shot noise is also known as current noise which is the most commonly used example for carrier fluctuations. The spectral density of the shot noise is given in equation (6.17)

$$i_n^2 = 2q_e I \quad (6.17)$$

The spectral density of the shot noise is proportional to the average current  $I$ . where  $q_e$  is the electronic charge. The criterion for shot noise is that the carriers are

injected independent of one another. The current through the ohmic contact does not carry shot noise as the fluctuation in the charge carrier is compensated by the additional carriers in the field where the fluctuation is initiated.

#### 6.12.2.3. Flicker Noise:

Flicker noise is commonly referred as  $1/f$  noise. This arises usually due to traps in the semiconductor which is due to imperfections in the crystal where the charge carriers are trapped and released after some period. This noise phenomenon is the least understood. This leads to frequency dependent spectrum as given in equation (6.18)

$$\frac{dP_n}{df} = \frac{1}{f^\alpha} \quad (6.18)$$

where  $\alpha$  typically varies from 0.5 to 2.

#### 6.12.2.4. Detector Capacitance and Signal to Noise Ratio:

The noise manifests in the form of voltage or current fluctuations. The signal needs to be represented in the form of voltage or current for the purpose of comparison even though the signal from the detector is in the form of charge. The simple detector model shown in figure 6.31 has the detector capacitance  $C_{det}$  with input resistance of the readout amplifier  $R_i$  with input capacitance of  $C_i$ . The input time constant of the schematic is  $R_i (C_{det} + C_{in})$  and when the time constant is larger compared to the duration of the current pulse, the signal charge is integrated in to the input capacitance yielding the voltage signal output  $V_o = Q_i / (C_{det} + C_{in})$ . Then the signal to noise ratio is given in equation (6.19).

$$\frac{v_s}{v_n} = \frac{Q_i}{v_n (C_{\text{det}} + C_{\text{in}})} \quad (6.19)$$

where  $Q_i$  is the input charge. The peak amplitude of the signal is inversely proportional to the total input capacitance which is the sum of detector capacitance, input capacitance of the amplifier and the stray capacitances. This relationship holds when the time constant is ten times greater than the current pulse width and this is general feature that is independent of amplifier type.

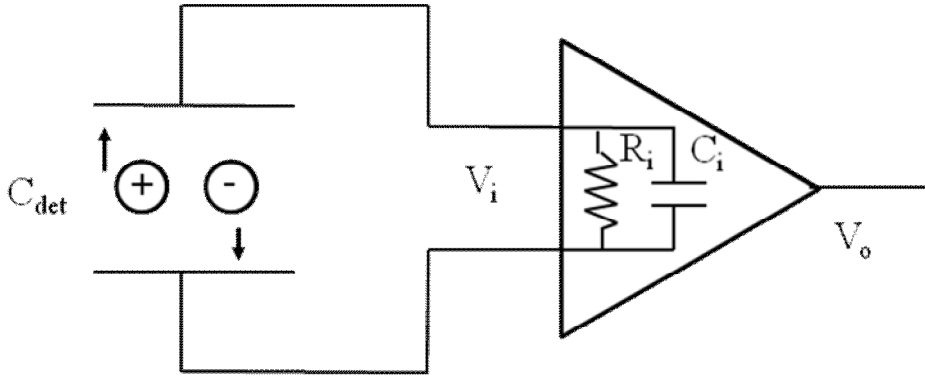


Fig. 6.31: Schematic representation of the detector capacitance and the charge readout amplifier.

In case of charge sensitive amplifier, the feedback cannot improve the signal to noise ratio, although the voltage signal output is constant. The signal charge to noise charge ratio is given in equation (6.20)

$$\frac{Q_i}{Q_n} = \frac{Q_i}{v_n (C_{\text{det}} + C_f)} \quad (6.20)$$

The feedback capacitance ( $C_f$ ) increases the noise due to increase in the total capacitance and hence the feedback capacitance should be kept as small as possible. In short, the signal to noise ratio is independent of whether the voltage, current or charge signal is sensed and S/N ratio cannot be improved by using feedback.

#### 6.12.2.5. Noise in JFET:

The noise sources in junction field-effect transistors are due to leakage current in the gate, thermal noise in the channel, gate resistance and the flicker noise in the channel. The gate leakage current is very small when the JFET is used in the spectroscopic applications and this current is generated due to reverse bias junction. The channel resistance can be expressed in the form of transconductance  $g_m$  and this gives at the drain, a noise current with spectral density. The noise coming from the JFET is mainly due to the gate resistance and the channel conductance. The noise voltage power spectral density is given in equation (6.21)

$$\frac{dV_n^2}{df} = 4kT \left( \frac{\Gamma}{g_m} + R_g \right) \quad (6.21)$$

where  $g_m$  is the transconductance of the JFET,  $R_g$  is the gate resistance and  $\Gamma$  is the excess noise parameter must be characterized for a given technology. Any change in the channel property will lead to change in the transconductance and hence the noise contribution. The value of transconductance can be estimated using the following relation given in equation (6.22)

$$g_m = \sqrt{2\mu C_{ox} I_{ds} \left( \frac{W}{L} \right)} \quad (6.22)$$

where  $C_{ox}$  is the capacitance of the oxide layer and  $I_{ds}$  is the drain current and  $W/L$  is the transistor width/length.

#### 6.12.2.6. Pulse Shaping and Noise:

The preamplifier converts the charge from the detector in to voltage signal. This voltage pulse is passed through the pulse shaping amplifier to improve the signal to noise

ratio by restricting the signal bandwidth. The pulse shaping transforms the narrow pulse into a broader pulse. The time taken to achieve the maximum signal amplitude is known as peaking time. The pulse amplifier is generally designed with high pass filter known as differentiator, which defines the fall time of the pulse. This pulse is then passed through the low pass filter which defines the rise time. The combination is known as *CR-RC* pulse amplifier or *CR-RC* shaper. To achieve the near Gaussian pulse, it is necessary to increase the number of *RC* stages. It is also important to constrain the pulse width so that the successive signal pulses can be measured without the overlap and also to allow the maximum possible signal rate. Increase in the signal rate increases the noise. Hence, one has to select the optimal shaping time and the signal bandwidth based on the application.

### **6.12.3. Equivalent Noise Charge (ENC):**

The most important feature limiting the performance of the spectrometer system is its inherent noise level. Noise is a measurable quantity and can be expressed in many ways. The signal to noise ratio indicates the ratio between the signal and the rms noise for the specific type of event. As most of the radiation detectors rely on the measurement of charge carriers produced by the ionization events and hence the most commonly used parameter to characterize the noise performance is by means of Equivalent Noise Charge (ENC). The ENC is defined as the input charge that produces the output signal amplitude equal to rms value of noise. It is the minimum charge detectable by the system, making the signal to noise ratio to 1. One can estimate the overall ENC of the spectrometer system by measuring the energy resolution. The energy resolution of the spectrometer system, expressed as Full Width at Half Maximum (FWHM) which is due to the statistical fluctuation in the number of  $e-h$  pairs created by the incident photon (Fano noise), detector leakage current and the noise contributed by the readout system. The



measured energy resolution is the quadrature sum of FWHM due to Fano statistics and the FWHM due to electronic noise [186], which is given by the equation (6.23)

$$FWHM(m) = \sqrt{FWHM^2(en) + FWHM^2(f)} \quad (6.23)$$

where  $FWHM(m)$  is the measured energy resolution,  $FWHM(en)$  is the energy resolution contributed by the electronics noise and  $FWHM(f)$  is the energy resolution of the detector due to Fano statistic. The Fano noise sets the lowest limit of spectrometer energy resolution, which is given by (6.24)

$$FWHM(f) = 2.355 \sqrt{\varepsilon FE} \quad (6.24)$$

where  $\varepsilon$  is the e-h pair production energy (3.6 eV for silicon at room temperature),  $F$  is the Fano factor ( $\sim 0.11$  for silicon) and  $E$  is the energy of the absorbed photon. This gives the theoretical limit of  $\sim 120$  eV for the detector based on silicon for the incident energy of  $Mn K\alpha$  line with energy of 5.9 keV. The energy resolution due to electronics noise is given by (6.25)

$$FWHM(en) = 2.355 \varepsilon \times ENC \quad (6.25)$$

By substituting the values of Fano noise and the electronics noise in equation (3.1), the equivalent noise charge in electrons rms of the spectrometer system can be derived, which is given by (6.26)

$$ENC_{rms} = \sqrt{\frac{FWHM^2(m) - FWHM^2(f)}{(2.355 \times \varepsilon)^2}} \quad (6.26)$$

The noise contribution by the first stage of the charge readout is the main source of noise as this part of the electronics circuit is directly interfaced with the detector. The subsequent signal processing electronics bandwidth can be optimized for improving the signal to noise ratio to achieve the better energy resolution. The equivalent noise charge contributed by the detector and the first amplification stage is given in equation (6.27),

which has three terms of electronic noises, the serial white noise,  $1/f$  noise of the JFET associated with the detector and the parallel short noise associated with the detector leakage current [79].

$$ENC_{ele} = \sqrt{\frac{4kT}{3g_m} C_T^2 A_1 \frac{1}{\tau} + 2\pi a_f C_T^2 A_2 + qI_o A_3 \tau} \quad (6.27)$$

where  $k$  is the Boltzmann's constant,  $T$  is the operating temperature,  $g_m$  is the transconductance of the JFET,  $a_f$  is the constant parameterizing the  $1/f$  noise of JFET,  $q$  is the charge of the electron,  $\tau$  is the pulse shaping time and  $A1$ - $A3$  are the noise coefficients (shape factors) which varies with the shape of the pulse. The shape factors characterize the type of the shaper such as  $CR$ - $RC$  or  $CR$ -( $RC$ )<sup>2</sup> or  $CR$ -( $RC$ )<sup>4</sup>. The shape factors depend on the ratio of time constant  $\tau_d$  (differentiator) and  $\tau_i$  (integrator), rather than the absolute magnitude of the signal. The first term combines all the noise voltage sources and decreases with shaping time. The second term is the contribution of excess  $1/f$  noise and increases with total capacitance which is the sum of the detector capacitance, feedback capacitance, JFET input capacitance and other parasitic capacitances exists at the input of the charge readout circuit [79]. The third term combines all the noise current sources and increases with shaping time. The generic plot indicating the noise sources and their contribution in terms of equivalent noise charge is shown in figure 6.32.

The serial white noise and the  $1/f$  noise depends strongly on the total capacitance ( $C_T$ ) at the input of charge readout system, the parallel noise is mainly determined by the magnitude of the leakage current. Any increase in the detector leakage current due to temperature or radiation damage will result in poor energy resolution at higher pulse shaping time constants. Increase in the total capacitance at the input of the spectrometer system increases the  $1/f$  noise and also the serial white noise. Decrease in the

transconductance increases the serial noise and hence degrades the energy resolution at lower pulse shaping time constants [187-188]. By measuring the energy resolution for various shaping times, before and after irradiation; one can estimate the noise contribution due leakage current, JFET and the total input capacitance on the spectrometer system resolution. It is also possible to optimize the shaping time for low noise performance where parallel and series noise components are equal.

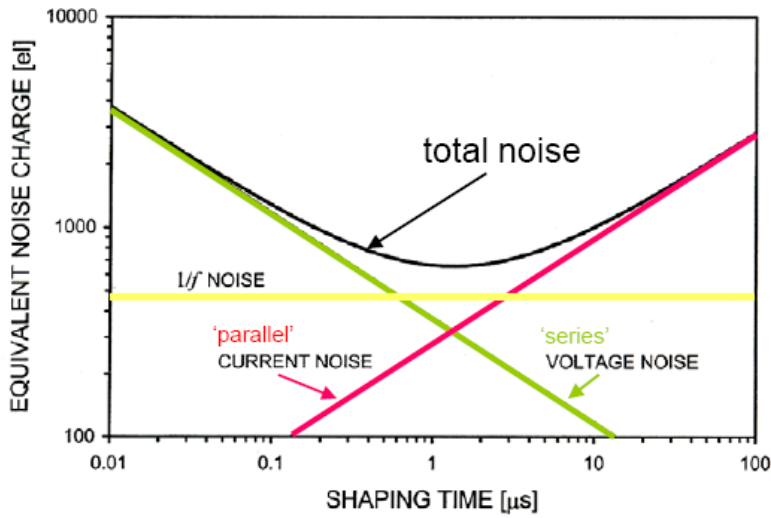


Fig. 6.32: Total equivalent noise charge and the contribution of series, parallel and  $1/f$  noises [170].

#### 6.12.4. Noise Performance before Irradiation:

The energy resolution is measured for both the SDD modules (VS0592 and VS0629) before irradiation for various pulse shaping time constants (0.15 μs, 0.4 μs, 1 μs, 3.3 μs and 10 μs) in the temperature range of +20°C to -40°C. The  $ENC_{rms}$  of the spectrometer system with these SDD modules is derived using equation (6.28) from the measured energy resolution. It is shown that the  $ENC_{rms}$  varies from ~ 10 electrons rms at -40°C to ~ 15 electrons rms at -10°C for the SDD module VS0592 and varies from ~ 12 electrons rms at -40°C to 27 electron rms at -10°C as shown in figure 6.33. It can be clearly seen that the ENC increases with increase in detector operating temperature at

higher shaping time constants which is due to increase in detector leakage current. The same effect is expected for the SDDs with radiation damage which is quantified in the subsequent subsections with gamma ray and X-ray irradiation. At lower pulse shaping time constants, the increase in ENC is due to the combined effect of change in the  $g_m$  and  $C_T$  with the operating temperature. In the present study, the change in the value of  $g_m$  could not be quantified individually as the FET is part of the SDD module and do not have access to the FET terminals for independent investigation for its characterization which includes temperature and the radiation effects. Hence we have used the  $C_T^2/g_m$  ratio to quantify the change in the  $g_m$  and  $C_T$  with temperature and also with radiation.

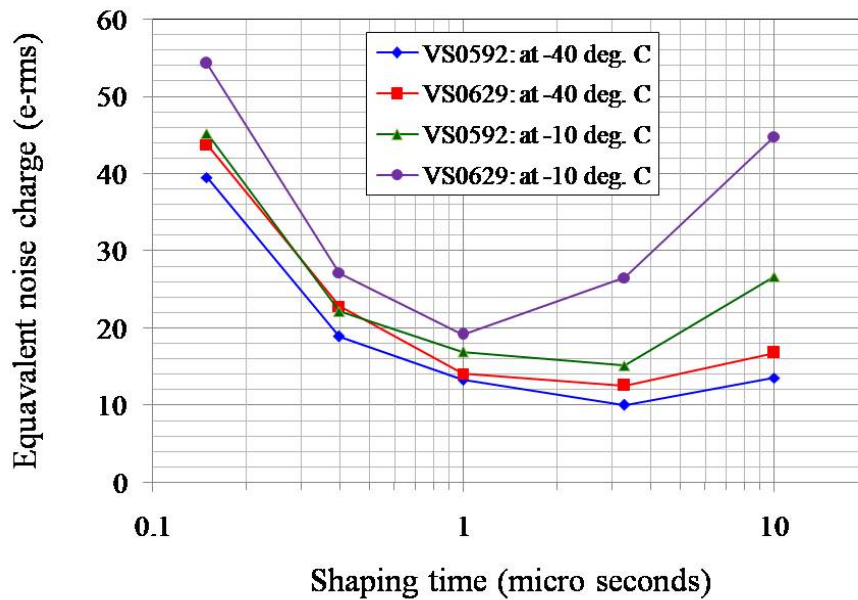


Fig. 6.33: Equivalent noise charge measured at 5.9 keV for various shaping time constants with temperature for both VS0592 and VS0629 SDD modules before irradiation [153].

The value of  $g_m$  is about 2.5 mS (obtained from the manufacturer through private email communication) The value of  $C_T^2/g_m$  is derived assuming  $a_f = 1 \times 10^{-14}$ , shape factors  $A_1 = 1.28$ ,  $A_2 = 0.426$ ,  $A_3 = 3.412$  [189] and using the measured leakage current. It is shown that the ratio changes from  $\sim 1 \times 10^{-21}$  to  $\sim 1.42 \times 10^{-21}$  for the SDD module VS0629 when the operating temperature is increased from  $-40^\circ\text{C}$  to  $-10^\circ\text{C}$ . In case of

VS0592, the ratio changes from  $\sim 0.8 \times 10^{-21}$  to  $\sim 1.03 \times 10^{-21}$  for the same operating temperature range.

#### 6.12.5. Noise Performance after Gamma Ray Irradiation:

The gamma ray irradiation affects the electronic devices mounted inside the module along with the detector SDD chip and hence the energy resolution. To quantify the radiation damage to the SDD chip and the internal JFET in terms of ENC, the energy resolution is measured for various pulse shaping time constants before and after irradiation (four months after 547 krad). The value of ENC is derived from the measured energy resolution is shown in figure 6.34.

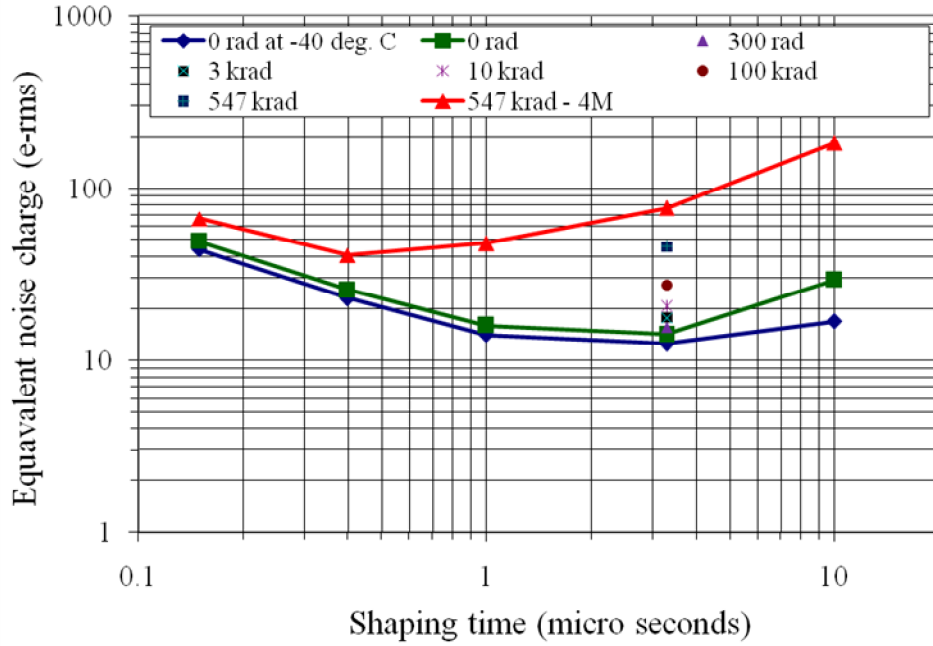


Fig. 6.34: ENC measured before and after gamma ray irradiation for a detector operating temperature of  $-20^{\circ}\text{C}$  (4M - four months after gamma ray irradiation) [153].

The value of  $C_T^2/g_m$  ratio is derived from the fit parameters and shown that the ratio increases from  $\sim 1.34 \times 10^{-21}$  to  $\sim 2.52 \times 10^{-21}$  for the operating temperature of  $-20^{\circ}\text{C}$  after the gamma ray dose of  $\sim 547$  krad. This shows that there is significant

radiation damage to the SDD which is shown in the form of increase in leakage current and the change in the JFET characteristics from  $C^2_T/g_m$  ratio value before and after gamma ray irradiation. The ENC before and after gamma ray irradiation for a detector operating temperature of  $-20^\circ\text{C}$  is shown in figure 6.35 and figure 6.36.

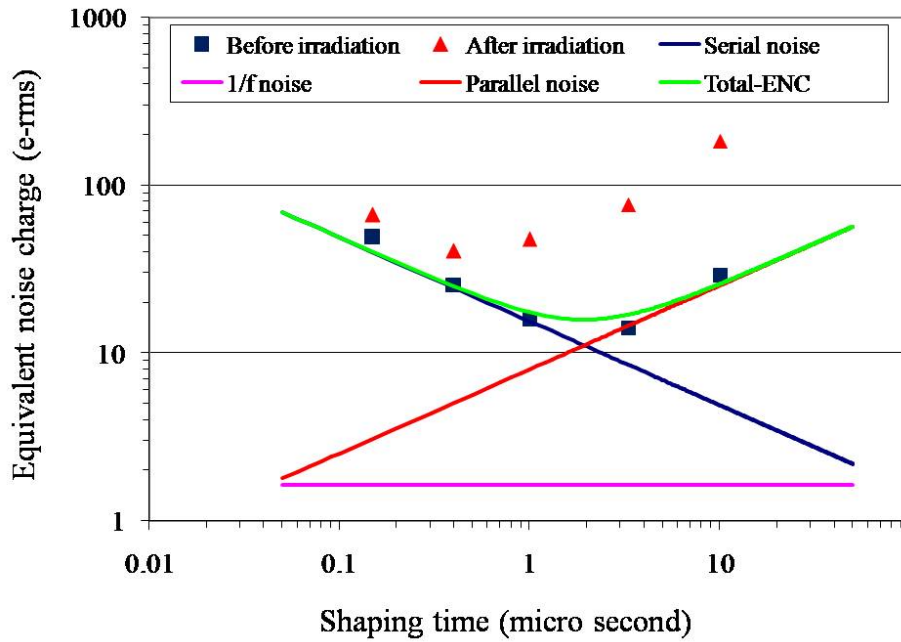


Fig. 6.35: The ENC in rms electrons derived from the measured energy resolution before irradiation for a detector operating temperature of  $-20^\circ\text{C}$  [153].

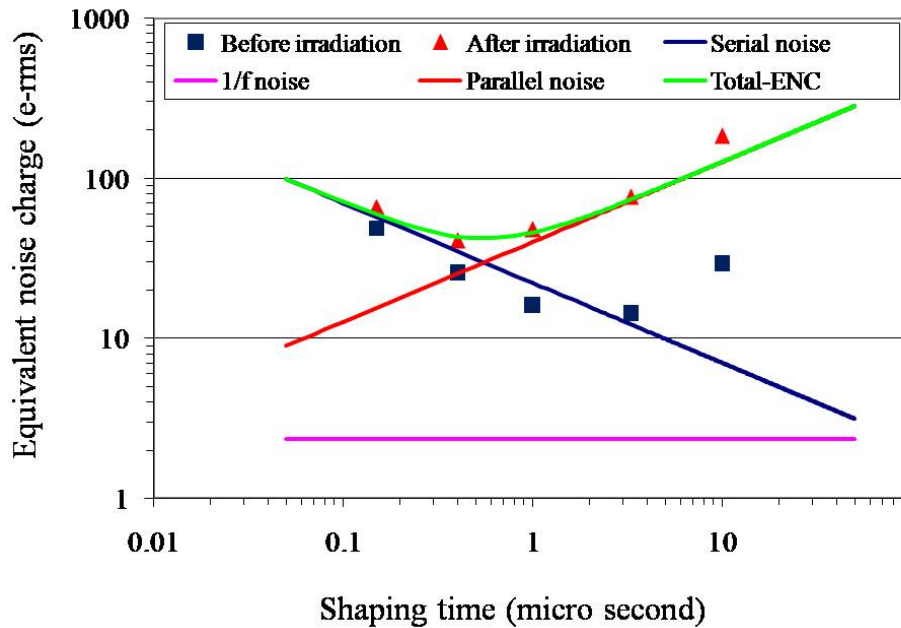


Fig. 6.36: The ENC in rms electrons derived from the measured energy resolution after irradiation for a detector operating temperature of  $-20^\circ\text{C}$  [153].

It is also shown that there is a systematic increase in the ENC with various gamma ray doses for a pulse shaping time of  $\sim 3.3 \mu\text{s}$  indicating an increase in detector leakage current with gamma ray dose.

#### 6.12.6. Noise Performance after X-ray Irradiation:

The value of ENC is derived from the measured energy resolution after the X-ray dose of 64 krad for various pulse shaping time constants with different SDD operating temperatures. It is shown that there is no significant change in the ENC for the detector operating temperature of  $\sim -40^\circ\text{C}$ . It is also observed that there is a systematic increase in the ENC at higher and lower shaping time constants with temperature as shown in figure 6.37.

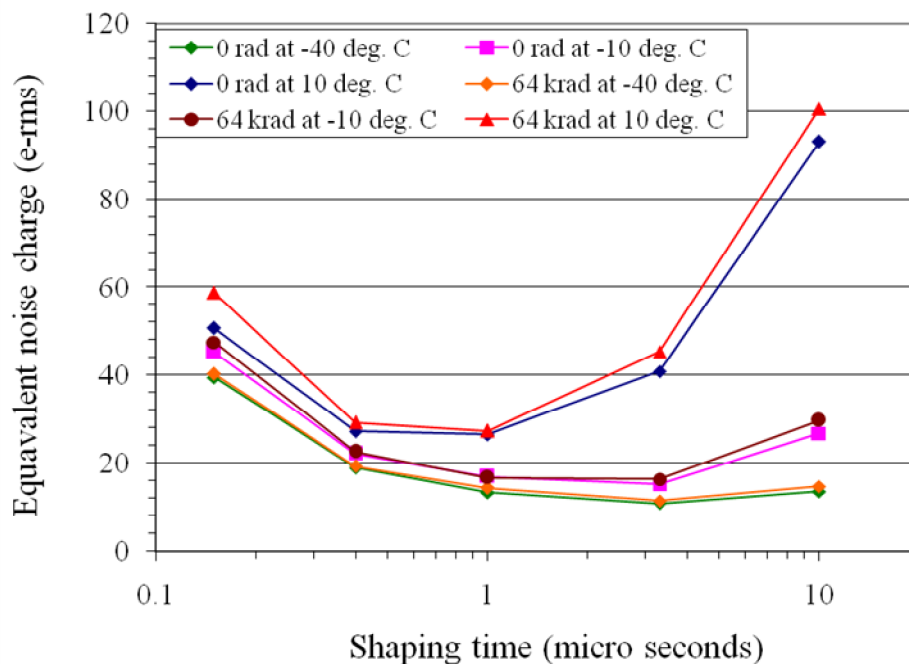


Fig. 6.37: Equivalent noise charge measured before and after X-ray irradiation for three different SDD operating temperatures [153].

It is observed that there is no increase in leakage current at  $-40^\circ\text{C}$  and the leakage current increased from  $\sim 5.1 \text{ pA}$  to  $\sim 5.7 \text{ pA}$  at  $-10^\circ\text{C}$  and  $\sim 61.2 \text{ pA}$  to  $\sim 77.6 \text{ pA}$  at

10°C. The  $C^2_T/g_m$  ratio is  $\sim 0.8 \times 10^{-21}$ ,  $\sim 1.03 \times 10^{-21}$  at -40°C and -10°C respectively and it increased from  $\sim 1.16 \times 10^{-21}$  to  $\sim 1.44 \times 10^{-21}$  at 10°C for the X-ray dose of 64 krad.

### 6.13. SUMMARY:

The SDD modules planned for Chandrayaan-2 mission has been tested to quantify any performance degradation due to space radiation using gamma rays. It is shown that there is no degradation in the energy resolution up to 3 krad and the resolution degrades to  $\sim 210$  eV at 5.9 keV for the gamma ray dose of 10 krad. This meets the Chandrayaan-2 performance requirement at the end of 2 year mission life. The extended irradiation tests show that the energy resolution degrades to  $\sim 250$  eV at 100 krad for the life time of  $\sim 20$  years. At 547 krad, the energy resolution degrades to  $\sim 340$  eV. From these measurements, it is shown that there is a significant radiation damage to the internal JFET which is quantified using ENC equation. The radiation damage to the internal JFET and the total input capacitance is quantified using measured leakage current and shown that  $C^2_T/g_m$  ratio increases from  $\sim 1.34 \times 10^{-21}$  to  $\sim 2.52 \times 10^{-21}$  for the operating temperature of -20°C after the gamma ray dose of  $\sim 547$  krad. Performance of the SDD based X-ray spectrometer is also tested for various X-ray doses as the XSM experiment is expected to detect the Solar X-rays continuously. The SDD module is irradiated for the X-ray dose up to 64 krad and shown that there is no degradation in the energy resolution for the detector operating temperature of -40°C. The total fluence is  $\sim 2 \times 10^{13}$  photons/40 mm<sup>2</sup> which corresponds to  $\sim 64$  krad of X-ray dose.



## **Chapter 7:**

### **SUMMARY AND FUTURE PLAN**

#### **7.1. SUMMARY OF THE RESEARCH WORK:**

The SDD based X-ray spectrometer has been developed using commercial equivalent of space qualified components. It is shown that the developed spectrometer provides energy resolution of  $\sim 150$  eV at 5.9 keV when the SDD is cooled to  $\sim -40^{\circ}\text{C}$  for the pulse peaking time of  $\sim 3.3$   $\mu\text{s}$ . This meets the performance requirement of APXS instrument. The energy resolution of the developed spectrometer is measured for various pulse shaping time constants to identify the suitable pulse shaping time for the XSM experiment. Also, it is essential to accommodate count rates close to  $\sim 10^5$  counts/s with reasonably good energy resolution of  $\sim 200$  eV at 5.9 keV which is required for the XSM experiment. Based on the experimental results, it is decided to have pulse shaping time of  $\sim 0.8$   $\mu\text{s}$  which gives stable energy resolution and peak energy position up to  $\sim 70$  kcts/s. The spectrometer performance is also characterized for various detector operating temperatures, pulse shaping time constants and for various incident X-ray rates (using X-ray source and X-ray gun). In both the instruments, the low energy threshold of  $< 1$  keV has been achieved.

In this research activity, a new and simple technique for measuring the leakage current in SDDs is proposed. The measurement technique involves by simply counting the ramp signal frequency at the output of CSPA with known values of charge integrating feedback capacitor and the ramp signal amplitude. The value of feedback

capacitance is estimated by independent measurements and the ramps signal amplitude is fixed electrically in the CSPA. The measured value of feedback capacitance is shown to be varying from  $\sim 60$  to  $66$  fF among the SDD modules under the test. Using this technique, the leakage current is measured for large sample of SDDs having two different active area of  $40 \text{ mm}^2$  and  $109 \text{ mm}^2$  for various detector operating temperatures. Simultaneously, the energy resolution is also measured for all the SDD modules at each point of leakage current measurement. It has been shown that the energy resolution is  $\sim 150$  eV at  $5.9$  keV for the detector leakage currents  $< 1$  pA and changes to  $\sim 200$  eV at  $10$  pA and  $\sim 400$  eV at  $100$  pA. For the leakage currents  $< 1$  pA, the electronics noise determines the energy resolution and at higher leakage currents, the leakage current is dominant. Using this technique, one can estimate the performance degradation of the space - borne SDD based X-ray spectrometer where the detector is expected to encounter very hostile space radiation environment. The radiation damage to the SDD leads to the increase in the leakage current and hence its energy resolution. This technique takes care of only the radiation damage to the SDD. It is expected that the components used in the readout electronics should be of space qualified in nature with certain dose levels. Any degradation to the electronic chain can be quantified separately by means of electronic calibration. The measured leakage current is also compared with theoretical values and shown to have good correlation with difference values of device constant ranges from  $\sim 1.5$  to  $2$ .

The SDD modules planned for Chandrayaan-2 mission has been tested to quantify any performance degradation due to space radiation using gamma rays. It is shown that there is no degradation in the energy resolution up to  $3$  krad and the resolution degrades to  $\sim 210$  eV at  $5.9$  keV for the gamma ray dose of  $10$  krad. This meets the Chandrayaan-2 performance requirement at the end of  $2$  year mission life. The

extended irradiation tests show that the energy resolution degrades to  $\sim 250$  eV at 100 krad for the life time of  $\sim 20$  years. At 547 krad, the energy resolution degrades to  $\sim 340$  eV. From these measurements, it is shown that there is significant radiation damage to the internal JFET which is quantified using ENC equation. The radiation damage to the internal JFET and the total input capacitance is quantified using measured leakage current and shown that  $C_T^2/g_m$  ratio increases from  $\sim 1.34 \times 10^{-21}$  to  $\sim 2.52 \times 10^{-21}$  for the operating temperature of  $-20^\circ\text{C}$  after the gamma ray dose of  $\sim 547$  krad.

Performance of the SDD based X-ray spectrometer is also tested for various X-ray doses as the XSM experiment is expected to detect the Solar X-rays continuously. The SDD module is irradiated for the X-ray dose up to 64 krad corresponding to the total fluence of  $\sim 2 \times 10^{13}$  photons/40 mm<sup>2</sup> and shown that there is no degradation in the energy resolution for the detector operating temperature at  $-40^\circ\text{C}$ .

## **7.2 FUTURE PLAN:**

The development of SDDs using silicon planar technology has reached to a level of some maturity in the last few decades. The SDD charge readout techniques has been improved vastly over last decade with discrete or Application Specific Integrated Circuit (ASIC) based readouts. With these improvements, it is shown that the SDD based X-ray spectrometer can provide energy resolution close to Fano limit. In the recent years, radiation hardness tests on the Silicon detectors gained importance as they are presently used in high energy physics experiments and also in the space satellite missions where the detectors are exposed to very harsh radiation.

The research activity can be extended in the following areas and we also have some plan to do research work in this direction. Proton irradiation tests on the SDD module could not be carried out due to lack of availability of proton irradiation facility

which will through some more light on the device characterization. Thus, more experiments are necessary in order to investigate the detector and its complete behaviour in the space. The proton irradiation study will be extended to larger area SDD modules to study the radiation damage effects to the SDD chip and the internal FET in collaboration with the manufacturer for its use in the future space/planetary missions. This is in view of the future plan to develop large area SDD based X-ray spectrometer with large number of such devices.

Hybridization/ASIC development for the SDD readout electronics will be another step forward in developing large area SDD based X-ray spectrometers for the future planetary/astronomy missions.

In recent times, the research is focused at developing thicker silicon detectors with large active area aimed to use in the future space missions for imaging applications. The present X-ray CCDs imaging systems has two major disadvantages: depletion thickness is small (50 micron) resulting in reduction in detection efficiency and low count rate capability due to frame readout. Alternate silicon technologies such as DEPFET and fully depleted pn-CCD also have issue of faster readout. To overcome these issues, multi-linear SDD configurations were proposed. One such SDD with one dimensional position sensing is planned in the LOFT mission with segmented anodes for linear electron drift. We propose to extend our future research towards the development of multi-linear SDDs with two dimensional readout with segmented anodes and cathodes in both the sides of the SDD for electron and hole signal readouts to accurately measure the position interaction. In this case, the readout will be faster with increased depletion thickness ranging from few hundreds of microns to  $\sim 1$  mm. This will be major device level research work. We also propose to develop ASIC based readout for these devices.

## REFERENCES:

- [1] D. Briggs and M. P. Seah, "Practical Surface Analysis by Auger and X-ray Photoelectron Spectroscopy", John Wiley and Sons, New York, 1983.
- [2] [http://www-physics.lbl.gov/~spieler/Heidelberg\\_Notes](http://www-physics.lbl.gov/~spieler/Heidelberg_Notes), 2001.
- [3] J. M. F. dos Santos et al., "The development of portable gas proportional scintillation counters for X-ray spectrometry", X-ray spectrometry, vol. 30, pp. 373-381, 2001.
- [4] G. F. Knoll, "Radiation Detection and Measurement", John Wiley & Sons, 3rd edition, 1999.
- [5] [https://www.hamamatsu.com/resources/pdf/etd/PMT\\_handbook\\_v3aE-Chapter7.pdf](https://www.hamamatsu.com/resources/pdf/etd/PMT_handbook_v3aE-Chapter7.pdf)
- [6] <https://www.science.mcmaster.ca/medphys/images/files/courses/4R06/note8.pdf>
- [7] P. Dorenbos, J. T. M. de Haas, C. W. E. van Eijk, "Gamma-Ray Spectroscopy with a  $19 \times 19 \text{ mm}^3$  LaBr<sub>3</sub>:0.5%Ce<sup>3+</sup> Scintillator", IEEE Transactions on Nuclear Science, vol. 51, no. 3, pp. 1289-1296, 2004.
- [8] S. Mukhopadhyay, "High-Resolution Room Temperature Spectroscopy with Lanthanum Halides", Nuclear Science and Engineering 151, 2005.
- [9] E. H. Seabury, J. C. Wharton, A. J. Caffrey, "Response of a LaBr<sub>3</sub>(Ce) Detector to 2-11 MeV Gamma Rays", IEEE Nuclear Science Symposium, October 2006.
- [10] <http://www.hamamatsu.com/jp/en/3001.html>.
- [11] <http://www.sensl.com/downloads/ds/TN%20-%20Intro%20to%20SPM%20Tech.pdf>
- [12] <http://www.ketek.net/products/sipm-technology/working-principle/>
- [13] <http://www.ketek.net/products/sipm/pm6660/>
- [14] G. Lutz, "Semiconductor Radiation Detectors", Springer, 1999.

- [15] Y. J. Wang, J. S. Iwanczyk, W. R. Graham, "Evaluation of HgI<sub>2</sub> detectors for lead detection in paint", IEEE Trans. on Nucl. Sci., vol. 40, no. 4, pp. 846-850, 1993.
- [16] M. R. Squillante, G. Entine, "New applications of CdTe nuclear detectors", Nucl. Instr. and Meth. A, vol. 322, no. 3, pp. 569-574, 1992.
- [17] M. L. McConnell et al., "Three-dimensional imaging and detection efficiency performance of orthogonal coplanar CZT strip detectors", proceedings of SPIE, vol. 4141, pp. 157-167, 2000.
- [18] G. Bertuccio et al, "Pixel X-ray detectors in epitaxial gallium arsenide with high-energy resolution capabilities", IEEE Trans. on Nucl. Sci., vol. 44, no. 1, pp.1-5,1997.
- [19] J. Kemmer, "Fabrication of low noise silicon radiation detectors by the planar process", Nucl. Instr. and Meth. A, vol. 169, no. 3, pp. 499 -502 , 1980.
- [20] J. A. Pantazis et al., "New, High Performance Nuclear Spectroscopy System Using Si- PIN Diodes and CdTe Detectors," IEEE Trans. on Nuc. Sci., vol. 41, no. 4, pp. 1004-1008, 1994.
- [21] W. R. Runyan and K. E. Bean, "Semiconductor Integrated Circuit Processing Technology", Reading, MA: Addison-Wesley, 1990.
- [22] S. M. Sze, "VLSI Technology", 2nd ed. New York: McGraw-Hill Book Company, 1988.
- [23] [http://physics.nist.gov/cgi-bin/Xcom/xcom3\\_1](http://physics.nist.gov/cgi-bin/Xcom/xcom3_1)
- [24] Y. P. Varshni, "Temperature dependence of the energy gap in semiconductors", Physica, vol. 34, no. 1, pp. 149-155, 1967.
- [25] U. Fano, "Ionization Yield of Radiations. II. The Fluctuations of the Number of Ions", Phys. Rev., vol. 72, no. 1, pp. 26-29, 1947.
- [26] A. Coche and P. Siffert, "Lithium drifted silicon and germanium detectors", Semiconductor detectors, Elsevier-North Holland, Amsterdam, 1968.

- [27] U. Kroth, T. Saito and E. Tegeler, "Quantum efficiency of a semiconductor photodiode in the VUV determined by comparison with a proportional counter in monochromatized synchrotron radiation", *Appl. Opt.*, vol. 29, no. 18, pp. 2659-2661, 1990.
- [28] R. G. Musket, "Detection of proton-induced boron X-rays with a Si (Li) detector", *Nucl. Instr. and Meth.*, vol. 117, no. 2, pp. 385-389, 1974.
- [29] R. Hartmann, K. H. Stephan, and L. Struder, "The quantum efficiency of pn-detectors from near infrared to the soft X-ray region", *Nucl. Instr. and Meth. A*, vol. 439, no. 2-3, pp. 216-220, 2000.
- [30] P. Lechner and L. Struder, "Ionization statistics in silicon X-ray detectors-new experimental results", *Nucl. Instr. and Meth. A*, vol. 354, no. 2-3, pp. 464-474, 1995.
- [31] <http://www-physics.lbl.gov/~spieler/>
- [32] <http://www.xglab.it/cube-cmos-low-noise-sdd-preamplifier.shtml>
- [33] <http://www.amptek.com/products/xr-100cr-si-pin-x-ray-detector/>
- [34] <http://www.amptek.com/si-pin-vs-cdte-comparison/>
- [35] C. S. Rossington, R. D. Giaque, J. M. Jaklevic, "A direct comparison of Ge na Si (Li) detectors in the 2-20 keV range", *IEEE Trans. on Nucl. Sci.*, vol. 39, no. 4, pp. 570-576, 1992.
- [36] F. Hartmann, "Evolution of Silicon Sensor Technology in Particle Physics", vol. 231 of *Springer Tracts in Modern Physics*, Springer, 2009.
- [37] J. Kemmer and G. Lutz, "New Structures for Position Sensitive Semiconductor Detectors", *Nucl. Instr. Meth. A*, vol. **273**, no. 2-3, pp. 588-598, 1988.
- [38] A. Peisert, "Silicon Microstrip Detectors", DELPHI 92-143 MVX 2, CERN, 1992.
- [39] R. Richter et al., "Strip detector design for ATLAS and HERA-B using two-dimensional device simulation", *Nucl. Instr. Meth. A*, vol. 377, no. 2-3, pp. 412-421, 1996.

- [40] CMS Tracker Collaboration, "Supply of Silicon Micro-Strip Sensors for The CMS Silicon Strip Tracker", IT-2777/EP/CMS, 2000.
- [41] F. Hartmut, W. Sadrozinski, "GLAST, a Gamma-Ray Large Area Space Telescope", Nucl. Instr. Meth. A, vol. 466, no. 2, pp. 292-299, 2001.
- [42] L. Rossi et al., "Pixel detectors, from fundamental to applications: Particle acceleration and detection", Springer, Edition 2006.
- [43] K. Mathieson et al., "Charge sharing in Silicon pixel detectors", Nucl. Instr. Meth. A, vol. 487, no. 1-2, pp. 113-122, 2002.
- [44] F. Hartmann, "Evolution of Silicon Sensor Technology in Particle Physics", Springer, volume 231, 2009.
- [45] J. Kemmer and G. Lutz, "New semiconductor detector concepts", Nucl. Instr. Meth. A, vol. 253, no. 3, pp. 365-377, 1987.
- [46] M. S. Alam and ATLAS team, "The ATLAS silicon pixel sensors", Nucl. Instr. Meth. A, vol. 456, no. 3, pp. 217-232, 2001.
- [47] D. Bortoletto [CMS collaboration], "The CMS Pixel system", Nucl. Instr. Meth. A, vol. 579, no. 2, pp. 669-674, 2007.
- [48] F. Meddi, "The ALICE silicon pixel detector (SPD)", Nucl. Instr. Meth. A, vol. 465, no. 1, pp. 40-45, 2001.
- [49] L. Struder et al., "Device Modelling of fully depletable CCDs", Nucl. Instr. Meth. A, vol. 253, no. 3, pp. 386-392, 1987.
- [50] L. Struder et al., "The MPI/AIT X-ray imager (MAXI) - High speed pn-CCDs for X-ray detection", Nucl. Instr. Meth. A, vol. 288, no. 1, pp. 227-235, 1990.
- [51] E. Pinotti et al., "The pn-CCD on-Chip Electronics", Nucl. Instr. Meth. A, vol. 326, no. 1-2, pp. 85-92, 1993.
- [52] <http://www.pnsensor.de/Welcome/Detectors/pn-CCD/index.php>



- [53] L. Struder et al., "The European photon imaging camera on XMM-Newton: The pn-CCD Camera", *Astronomy and Astrophysics*, vol. 365, pp. L18-L26, 2001.
- [54] L. Struder et al., "X-ray pn-CCDs on the XMM Newton Observatory", *Proc. SPIE*, vol. 4012, pp 342-352, 2000.
- [55] E. Gatti and P. Rehak, "Semiconductor drift chamber-An application of a novel charge transport scheme", *Nucl. Instr. and Meth. A*, vol. 225, no. 3, pp. 608-614, 1984.
- [56] P. Rehak et al., "Semiconductor drift chambers for position and energy measurements", *Nucl. Instr. Methods A*, vol. 235, no. 2, pp. 224-234, 1985.
- [57] J. Kemmer et al., "Low capacity drift diode", *Nucl. Instr. and Meth. A*, vol. 253, no. 3, pp. 378-381, 1987.
- [58] T. Pantazis et al., "The historical development of the thermoelectrically cooled X-ray detector and its impact on the portable and hand-held XRF industries," *X-ray Spectrometry*, vol. 39, no. 2, pp 90-97, 2009.
- [59] <http://www.pnsensor.de/Welcome/Detectors/SDD/>
- [60] G. A. Carini et al., "Performance of a thin-window silicon drift detector X-ray fluorescence spectrometer", *IEEE. Trans. Nucl. Sci.*, vol. 56, no. 5, pp. 2843-2849, 2009.
- [61] G. Zampa, A. Rashevsky and A. Vacchi, "The X-ray spectroscopic performance of a very large area silicon drift detector", *IEEE. Trans. Nucl. Sci.*, vol. 56, no. 3, pp. 832-835, 2009.
- [62] G. Bertuccio, M. Sampietro and A. Fazzi, "High resolution X-ray spectroscopy with silicon drift detectors and integrated electronics", *Nucl. Instrum. Meth. A*, vol. 322, no. 3, pp. 538-542, 1992.
- [63] P. Lechner, A. Pahlke and H. Soltau, "Novel high-resolution silicon drift detectors", *X-Ray Spectrometry*, vol. 33, no. 4, pp. 256-261, 2004.
- [64] <http://www.pnsensor.de/Welcome/Detectors/SDD/index.php>

- [65] G. Bertuccio et al., "New electrode geometry and potential distribution for X-ray drift detectors", Nucl. Instr. and Meth. A, vol. 312, no. 3, pp. 613-616, 1992.
- [66] P. Lechner et al., "Silicon drift detectors for high resolution room temperature X-ray spectroscopy, Nucl. Instr. and Meth. A, vol. 377, no. 2-3, pp. 346-351, 1996.
- [67] R. Hartmann et al., "Ultrathin entrance windows for silicon drift detectors", Nucl. Instr. and Meth. A, vol. 387, no. 1-2, pp. 250-254, 1997.
- [68] D. M. Schlosser et al., "Expanding the detection efficiency of silicon drift detectors", Nucl. Instr. and Meth. A, vol. 624, no. 2, pp. 270-276, 2010.
- [69] <http://www.amptek.com/products/xr-100sdd-silicon-drift-detector/>
- [70] P. Lechner et al., "Silicon drift detectors for high count rate X-ray spectroscopy at room temperature", Nucl. Instr. Meth. A, vol. 458, no. 1-2, pp. 281-287, 2001.
- [71] <http://www.esrf.eu/files/live/sites/www/files/events/conferences/2015/ParisSpectroscopy/PDF/Hoffman-Ketek.pdf>
- [72] V. Radeka et al., "Implanted Silicon JFET on completely depleted high-resistivity devices", IEEE Electron Device Letters, vol. 10, no. 2, pp. 91-94, 1989.
- [73] J. Kemmer et al., "Experimental confirmation of a new semiconductor detector principle", Nucl. Instr. and Meth. A, vol. 288, no. 1, pp. 92-98, 1990.
- [74] M. Sampietro et al., "Novel p-JFET Embedded in Silicon Radiation Detectors that avoids preamplifier feedback resistor", IEEE Elec. Dev. Let., vol. 16, no. 5, pp. 208-210, 1995.
- [75] E. Pinotti et al., "Room temperature, high-resolution X-ray spectroscopy with silicon drift chambers", IEEE Trans. Nucl. Sci., vol. 42, no. 1, pp. 12-16, 1995.
- [76] C. Fiorini and P. Lechner, "Continuous charge restoration in semiconductor detectors by means of the gate-to-drain current of the integrated front-end JFET", IEEE Trans. Nucl. Sci., vol. 46, no. 3, pp. 761-764, 1999.
- [77] G. Bertuccio et al., "Spectroscopy charge amplifier for detectors with integrated front-end FET", IEEE Trans. Nucl. Sci., vol. 42, no. 4, pp. 1399-1405, 1995.

- [78] C. Fiorini et al., "A cmos pulsed-reset preamplifier for silicon drift detectors with on-chip JFET", IEEE Nuclear Science Symposium Conference Record, vol. 4, pp. 2519-2521, 2007.
- [79] A. Niculae et al., "Optimized readout methods of silicon drift detectors for high-resolution X-ray spectroscopy", Nucl. Instr. and Meth. A, vol. 568, no. 1, pp. 336-342, 2006.
- [80] [http://pndetector.de/wp-content/uploads/2013/11/Brox\\_spreads\\_A4-pub.pdf](http://pndetector.de/wp-content/uploads/2013/11/Brox_spreads_A4-pub.pdf)
- [81] L. Bombelli et al., "Low-noise CMOS charge preamplifier for X-ray spectroscopy detectors", IEEE Nuclear Science Symposium Conference Record, pp. 135-138, 2010.
- [82] [http://www.thermoscientific.com/content/dam/tfs/ATG/CAD/CAD%20Documents/Application%20&%20Technical%20Notes/Microanalysis%20and%20Electron%20Microscopy/TN52342\\_E\\_0512M\\_SiliconDrift\\_H.pdf](http://www.thermoscientific.com/content/dam/tfs/ATG/CAD/CAD%20Documents/Application%20&%20Technical%20Notes/Microanalysis%20and%20Electron%20Microscopy/TN52342_E_0512M_SiliconDrift_H.pdf)
- [83] P. Lechner et al., "Silicon Drift Detector for high resolution, high count rate X-ray spectroscopy at room temperature", International Centre for Diffraction Data 2004, Advances in X-ray Analysis, vol. 47, pp. 53-59, 2004.
- [84] <http://www.xglab.it/cube-cmos-low-noise-sdd-preamplifier.shtml>
- [85] <http://www.ketek.net/products/vitus-sdd/>
- [86] [http://pndetector.de/wp-content/uploads/2014/07/The-Complete\\_Flyer.pdf](http://pndetector.de/wp-content/uploads/2014/07/The-Complete_Flyer.pdf)
- [87] <http://www.esrf.eu/files/live/sites/www/files/events/conferences/2015/ParisSpectroscopy/PDF/Hoffman-Ketek.pdf>
- [88] [http://pndetector.de/wp-content/uploads/2013/10/Flyer\\_extra-large-area.pdf](http://pndetector.de/wp-content/uploads/2013/10/Flyer_extra-large-area.pdf)
- [89] P. Lechner et al., "Multichannel silicon drift detectors for X-ray spectroscopy", Proc. SPIE, vol. 4012, pp. 592-599, 2000.
- [90] C. Fiorini et al., "A large-area monolithic array of silicon drift detectors for medical imaging", Nucl. Instr. and Meth. A, vol. 568, no. 1, pp. 96-100, 2006.

- [91] G. Zampa, A. Rashevsky and A. Vacchi, "The X-ray spectroscopic performance of a very large area silicon drift detector", *IEEE. Trans. Nucl. Sci.*, vol. 56, no. 3, pp. 832-835, 2009.
- [92] D. E. Newbury and N. W. M. Ritchie, "Elemental mapping of microstructures by scanning electron microscope energy dispersive X-ray spectrometry (SEM-EDS): Extraordinary advances with the silicon drift detector (SDD)", *J. Anal. At. Spectrom.*, vol. 23, no. 4, pp. 973-978, 2013.
- [93] C. Fiorini et al., "Silicon Drift Detector for Readout of Scintillators in Gamma-Ray Spectroscopy", *IEEE. Trans. Nucl. Sci.*, vol. 60, no. 4, pp. 2923-2933, 2013.
- [94] R. Rieder et al., "The new Athena alpha particle X-ray spectrometer for the Mars exploration rovers", *J. Geophys. Res.*, vol. 108, no. E12, pp. 8066-, 2003.
- [95] R. Gillert et al., "Chemistry of Rocks and Soils in Gusev Crater from the Alpha Particle X-ray Spectrometer", *Science*, vol. 305, no. 5685, pp. 829-832, 2004.
- [96] G. Klingelhofer et al., "The Rosetta Alpha Particle X-ray Spectrometer (APXS)", *Space Science Reviews*, vol. 128, pp. 383–396, 2007.
- [97] R. Gellert et al., "The Alpha-Particle-X-ray-Spectrometer (APXS) for the Mars Science Laboratory (MSL) Rover Mission", *Lunar and Planetary Science Conference*, abstract no. 2364, 2009.
- [98] Xiao-Hui Fu et al., "Data processing for the Active Particle-induced X-ray Spectrometer and initial scientific results from Chang'e-3 mission", *Research in Astronomy and Astrophysics*, vol. 14, no. 12, pp. 1595-1606, 2014.
- [99] M. Shanmugam et al., "Alpha Particle X-Ray Spectrometer (APXS) on-board Chandrayaan-2 rover", *J. Adv. Space Res.*, vol. 54, no. 10, pp. 1974-1984, 2014.
- [100] A. L. Turkevich, E. J. Franzgrote and J. H. Patterson, "Chemical analysis of the moon at the Surveyor 5 landing site", *Science*, vol. 158, no. 3801, pp. 635-637, 1967.
- [101] S. K. Goyal et al., "Laboratory XRF measurements using Alpha Particle X-ray Spectrometer of Chandrayaan-2 rover: Comparison with GEANT4 simulation

- results", IEEE Nuclear Science Symposium and Medical Imaging Conference, pp. 1-6, 2013.
- [102] S. V. Vadawale et al., "Solar X-ray Monitor (XSM) on-board Chandrayaan-2 orbiter", J. Adv. Space Res., vol. 54, no. 10, pp. 2021-2028, 2014.
- [103] M. Feroci and LOFT team, "The Large Observatory for X-ray Timing (LOFT)", Exp. Astr., vol. 34, no. 2, pp. 415-444, 2012.
- [104] S. Zane and LOFT team, "A Large Area Detector proposed for the Large Observatory for X-ray Timing (LOFT)", Proc. of SPIE, vol. 8443, 2012.
- [105] M. Shanmugam et al., "A new technique for measuring the leakage current in Silicon Drift Detector based X-ray spectrometer – Implications for on-board calibration", JINST 10 P02009, 2015 (doi:10.1088/1748-0221/10/02/P02009).
- [106] <http://www.ketek.net/news/news-archive/>
- [107] F. S. Goulding, J. T. Walton, R. H. Pehl, "Recent results on the optoelectronic feedback preamplifier," IEEE Trans. Nucl. Sci., vol. 17, no. 1, pp. 218-225, 1970.
- [108] Elad, E. "Drain Feedback - A Novel Feedback Technique for Low-Noise Cryogenic Preamplifiers", IEEE Trans. Nucl. Sci., vol. 19, no. 1, pp. 403-411, 1972.
- [109] M. Sampietro, L. Fasoli, G. Bertuccio, "Source Follower or Charge Amplifier? An Experimental Comparison Using a -Detector with Integrated Electronics", IEEE Trans. Nucl. Sci., vol. 43, no. 4, pp. 2413- 2418, 1996.
- [110] C. Fiorini, "A charge sensitive preamplifier for high peak stability in spectroscopic measurements at high counting rates", IEEE Trans. Nucl. Sci., vol. 52, no. 5, pp. 1603–1610, 2005.
- [111] F. Olschner, J. C. Lund, "Low Noise Charge Sensitive Preamplifier Using Drain Current Feedback", IEEE Nuclear Science Symposium and Medical Imaging Conference, vol. 1, pp. 378-380, 1992.

- [112] A. Fazzi et al., "Charge-Sensitive Amplifier Front-End with an nJFET and a Forward-Biased Reset Diode" , IEEE Trans. Nucl. Sci., vol. 43, no. 6, pp. 3218-3222, 1996.
- [113] C. Fiorini and P. Lechner, "Charge-sensitive pre-amplifier with continuous reset by means of the gate-to-drain current of the JFET integrated on the detector", IEEE Trans. Nucl. Sci., vol. 49, no. 3, pp. 1147-1151, 2002.
- [114] C. Fiorini, M. Porro, T. Frizzi, "An 8-Channel DRAGO Readout Circuit for Silicon Detectors With Integrated Front-End JFET", IEEE Trans. Nucl. Sci., vol. 53, no. 5, pp. 2998-3003, 2006.
- [115] T. Frizzi et al., "The SIDDHARTA chip: a CMOS multi-channel circuit for Silicon drift detectors readout in exotic atoms research", IEEE Nucl. Sci. Symp. Conf. Record, vol. 2, pp. 850-856, 2006.
- [116] T. Noulis et al., "Advanced Low Noise X-ray readout ASIC for Radiation Sensor Interfaces", IEEE Trans. on Circ. and Sys., vol. 55, no. 7, pp. 1854-1862, 2008.
- [117] M. Shanmugam et al., "Characterization of High Count Rate Capability of Solar X-ray Monitor on-board Chandrayaan-2: The second Indian mission to Moon", IEEE Nuclear Science Symposium and Medical Imaging Conference, pp. 1-7, 2013.
- [118] V. Radhakrishna and CLASS team, "The Chandrayaan-2 Large Area Soft X-ray Spectrometer (CLASS)", 42nd Lunar and Planetary Science Conference, abs. no. 1708, 2011.
- [119] B. G. Lowe and R. A. Sareen, "Semiconductor X-Ray Detectors", CRC Press, 2013.
- [120] E. Del Monte et al., "Measurement of the effect of Non Ionising Energy Losses on the leakage current of Silicon Drift Detector prototypes for the LOFT satellite", JINST, 2014 (doi:10.1088/1748-0221/9/07/P07016).
- [121] A. Chilingarov, "Temperature dependence of the current generated in Si bulk", JINST, vol. 8, no. 10, 2013 (10.1088/1748-0221/8/10/P10003).

- [122] P. Mehta et al., "Studies of the Silcion Drift Detector: Design, Technology development, Characterization and Physics simulations", *Armenian Journal of Physics*, vol. 4, no. 3, pp. 175-192, 2011.
- [123] K. Ohyu et al., "A mechanism and a reduction technique for large reverse leakage current in p-n junctions", *IEEE Trans. Elec. Dev.*, vol. 42, no. 8, pp. 1404-1412, 1995.
- [124] W. C. Zhang et al., "Design, Simulation and Testing of Large Area Silicon Drift Detectors and Detector Array for X-ray Spectroscopy", *IEEE Trans. Nucl. Sci.*, vol. 47, no. 4, pp. 1381-1385, 2000.
- [125] A. Vasic et al., "Study of increased temperature influence on the degradation of photo detectors through ideality factor", *Mat. Sci. Forum*, vol. 453-454, pp. 37-42, 2004.
- [126] W. Shockley, "The theory of p-n junction in semiconductors and p-n junction transistors", *Bell Syst. Tech. J.*, vol. 28, no. 3, pp. 435-489, 1949.
- [127] C. T. Sah, R. N. Noyce, W. Shockley, "Carrier generation and recombination in P-N junctions and P-N junction characteristics", *Proc. IRE.*, vol. 45, no. 9, pp. 1228-1243, 1957.
- [128] F. Iucolano et al., "Barrier in homogeneity and electrical properties of Pt/GaN Schottky contacts", *J. Appl. Phys.*, vol. 102, pp. 113701-113708, 2007.
- [129] H. C. Casey et al., "Dominance of tunneling current and band filling in InGaN/AlGaIn double heterostructure blue light-emitting diodes", *Appl. Phys. Lett.*, vol. 68, pp. 2867-2869, 1996.
- [130] D. J. Dumin, G. L. Pearson, "Properties of Gallium Arsenide Diodes between 4.2° and 300°K", *J. Appl. Phys.*, vol. 36, pp. 3418-3516, 1965.
- [131] M. El-Tahchi et al., "Degradation of the diode ideality factor of silicon n-p junctions", *Solar Energy Mat. & Solar Cells*, vol. 62, pp. 393-398, 2000.
- [132] J. Pallares et al., "Space charge recombination in P-N junctions with a discrete and continuous trap distribution", *Solid State Electron.*, vol. 41, no. 1, pp. 17-23, 1997.

- [133] H. J. Queisser, "Forward Characteristics and Efficiencies of Silicon Solar Cells", Solid-State Electronics, vol 5. no. 1, pp. 1-10, 1962.
- [134] M. Shanmugam et al., "Dependence of the Leakage Current on the Performance of the Silicon Drift Detector Based X-Ray Spectrometer", IEEE Nuclear Science Symposium and Medical Imaging Conference, pp. 1-6, 2013 (DOI: 10.1109/NSSMIC.2013.6829801).
- [135] C. W. Fischer, "Elementary technique to measure the energy band gap and diffusion potential of p-n junctions", American Journal of Physics, vol. 50, pp. 1103-1105, 1982.
- [136] H. Spieler, Semiconductor detector systems, Oxford science publications, New York (2005) 16.
- [137] <http://users.ece.gatech.edu/mleach/ece3040/notes/chap02.pdf>.
- [138] J. M. Shah et al., "Experimental analysis and theoretical model for anomalously high ideality factors ( $n \gg 2.0$ ) in AlGaIn/GaN p-n junction diodes", J. Appl. Phys., vo. 94, no. 4, pp. 2627-2630, 2003.
- [139] R. Singh et al., "Temperature dependence of current–voltage characteristics of Au/n-GaAs epitaxial Schottky diode", Bull. Mater. Sci., vol. 23, no. 6, pp. 471-474, 2000.
- [140] K. Ashish et al., "Temperature dependence of electrical characteristics of Pt/GaN Schottky diode fabricated by UHV e-beam evaporation", Nanoscale Research Letters, vol. 8, pp. 481-487, 2013.
- [141] J. Krustok et al., "Temperature dependence of  $\text{Cu}_2\text{ZnSn}(\text{Se}_x\text{S}_{1-x})_4$  monograin solar cells", Solar Energy, vol. 84, pp. 379-383, 2010.
- [142] U. Rau and H. W. Schock, "Electronic properties of Cu(In, Ga)Se<sub>2</sub> heterojunction solar cells—recent achievements, current understanding, and future challenges", Applied Physics A., vol. 69, pp. 131-147, 1999.
- [143] M. Altosaar et al., " $\text{Cu}_2\text{Zn}_{1-x}\text{Cd}_x\text{Sn}(\text{Se}_{1-y}\text{S}_y)_4$  solid solutions as absorber materials for solar cells", Physica Status Solidi A, vol. 205, pp. 167-170, 2008.



- [144] P. Singh et al., "Temperature dependence of I–V characteristics and performance parameters of silicon solar cell", *Solar Energy Materials & Solar Cells*, vol. 92, pp. 1611-1617, 2008.
- [145] E. Del Monte et al., "The effect of the displacement damage on the Charge Collection Efficiency in Silicon Drift Detectors for the LOFT satellite", *JINST*, 2015 (10.1088/1748-0221/10/05/P05002).
- [146] R. S. Harper et al., "Evolution of silicon microstrip detector currents during proton irradiation at the CERN PS", *Nucl. Instr. and Meth. A*, vol. 479, no. 2-3, pp. 548-554, 2002.
- [147] G. Kramberger et al., "Effective trapping time of electrons and holes in different silicon material irradiated with neutron, protons and pions", *Nucl. Instr. and Meth. A*, vol. 481, no. 1-3, pp. 297-305, 2002.
- [148] K. Hayashi and Team, "Radiation effects on the silicon semiconductor detectors for the ASTRO-H mission", *Nucl. Instr. and Meth. A*, vol. 699, pp. 225-229, 2013.
- [149] S. U. Pandey et al., "Studies of ionizing radiation effects on the silicon drift detectors", *Nucl. Instr. and Meth. A*, vol. 361, no. 3, pp. 457-460, 1995.
- [150] H. W. Kraner, Z. Li, K. U. Posnecker, "Fast neutron damage in silicon detectors", *Nucl. Instr. and Meth. A*, vol. 279, no. 1-2, pp. 266-271, 1989.
- [151] Z. Li et al., "Study of the long term stability of the effective concentration of ionized space charges Neff of neutron irradiated silicon detectors fabricated by various thermal oxidation processes", *IEEE. Nuclear Science Symposium and Medical Imaging Conference*, vol. 2, pp. 953-957, 1992.
- [152] M. Moll, E. Fretwurst, G. Lindstrom (ROSE/CERN-RD48 Collaboration), "Leakage current of hardon irradiated silicon detectors – material dependence", *Nucl. Instr. and Meth. A*, vol. 426, no. 1, pp. 87-93, 1999.
- [153] M. Shanmugam et al., "Radiation effects on Silicon Drift Detector based X-ray spectrometer on-board Chandrayaan-2 Mission", *JINST*, vol. 10, 2015 (doi:10.1088/1748-0221/10/09/P09005).

- [154] C. Claeys and E. Simoen, "Radiation Effects in Advanced Semiconductor Materials and Devices", Springer-Verlag, Berlin, 2002.
- [155] J. L. Barth, C. S. Dyer, and G. Stassinopoulos, "Space, atmospheric, and terrestrial radiation environments," IEEE Trans. Nucl. Sci., vol. 50, no. 3, pp. 466–482, 2003.
- [156] E. G. Stassinopolous et al., "Solar flare proton evaluation at geostationary orbits for engineering applications," IEEE Transactions on Nuclear Science, vol. 43, no. 2, pp. 369-382, 1996.
- [157] NASA Space Environments and Effects (SEE) Program "Technical Working Group-Ionosphere and Thermosphere," available online at <http://see.msfc.nasa.gov/pf/pf.htm>.
- [158] A. Holmes-Seidle, L. Adams, "Handbook of Radiation Effects", Oxford University Press (1993).
- [159] J. R. Srour, C. J. Marshall, and P. W. Marshall, "Review of displacement damage effects in silicon devices," IEEE Trans. Nucl. Sci., vol. 50, no. 3, pp. 653–670, 2003.
- [160] C. J. Marshall and P. W. Marshall, "Proton effects and test issues for satellite designers Displacement effects," 1999 NSREC Short Course, Section IVB, 1999.
- [161] V. A. J. van Lint, "The physics of radiation damage in particle detectors", Nucl. Instr. and Meth. A, vol. 253, no. 3, pp. 453-459, 1987.
- [162] Z. Li, "Radiation hardness/tolerance of Si sensors/detector for nuclear and high energy physics experiments", Pres. PIXEL 2002 Intl. Conf., Cannel, CA, 9-12, 2002.
- [163] M. Huhtinen, "Simulation of non-ionising energy loss and defect formation in silicon", Nucl. Instr. and Meth. A, vol. 491, no. 1-2, pp. 194-215, 2002.
- [164] E. A. Burke, "Energy Dependence of Proton-Induced Displacement Damage in Silicon," IEEE Trans. Nucl. Sci., vol. 33, no. 6, pp. 1276-1281, 1986.

- [165] A. Van Ginneken, "Non Ionizing Energy Deposition in Silicon for Radiation Damage Studies," FNAL FN 522, 1989.
- [166] J. R. Srour et al., "Radiation Damage Coefficients for Silicon Depletion Regions," IEEE Trans. Nucl. Sci., vol. 26, no. 6, pp. 4783-4791, 1979.
- [167] R. N. DeWitt, D. Duston and A. K. Hyder, "The Behavior of Systems in the Space Environment", NATO ASI Series, Applied Sciences, Springer, 1991.
- [168] G. Segneri et al., "Measurement of the Current Related Damage Rate at -50°C and Consequences on the Macropixel Detector Operation in Space Experiments", IEEE. Trans. Nucl. Sci., vol. 56, no. 6, pp. 3734-3742, 2009.
- [169] E. Verbitskaya, "Competition of generation channels in reverse current of irradiated silicon detectors", 3<sup>rd</sup> conference on Radiation Effects on Semiconductor Materials, Detectors and Devices, 28-30 June, Italy (2000).
- [170] H. Spieler, Semiconductor Detectors Systems, Oxford Science Publications, Oxford (2005).
- [171] D. Pitzl et al., "Type Inversion in Silicon Detectors", Nucl. Instr. and Meth. A, vol. 311, no 1-2, pp. 98-104, 1992.
- [172] P. Giubellino et al., "Study of the Effects of Neutron Irradiation on Silicon Strip Detectors," Nucl. Instr. and Meth. A, vol. 315, no. 1-3, pp. 156-160, 1992.
- [173] J. A. J. Matthews et al., "Bulk Radiation Damage in Silicon Detectors and Implications for ATLAS SCT," New Mexico Center for Particle Physics Note and ATLAS INDET-NO-118, 1995.
- [174] Z. Li, "Modeling and simulation of neutron induced changes and temperature annealing of Neff and changes in resistivity in high resistivity silicon detectors," Nucl. Instr. and Meth. A, vol. 342, no. 1, pp. 105-118, 1994.
- [175] <http://www-physics.lbl.gov/~spieler/USPAS>  
MSU\_2012/pdf/VII\_Radiation\_Effects.pdf.

- [176] A. Vasilescu and G. Lindstroem, Displacement damage in silicon, on-line compilation,
- [177] P. Griffin et al. SAND92-0094 (SANDIA Natl. Lab., Nov 1996), neutron cross sections taken from ENDF/B-VI, ORNL, unpublished but available from G. Lindström, Hamburg.
- [178] A. Y. Konobeyev, Y. A. Korovin and V. N. Sosnin, "Neutron displacement cross-sections for structural materials below 800 MeV", J. Nucl. Mater., vol. 186, no. 2, pp. 117-130, 1992.
- [179] M. Huhtinen and P.A. Aarnio, "Pion induced displacement damage in silicon devices", Nucl. Inst. and Meth. A, vol. 335, no. 3, pp. 580-582, 1993.
- [180] G. P. Summers et al., "Damage correlations in semiconductors exposed to gamma, electron and proton radiations", IEEE. Trans. Nucl. Sci., vo. 40, no. 6, pp. 1372-1379, 1993.
- [181] C. J. Dale et al., "High energy electron induced displacement damage in silicon", IEEE Trans. Nucl. Sci., vol. 35, pp. 1208–1214, 1988.
- [182] R. L. Pease et al., "Comparison of neutron and proton carrier removal rates", IEEE Trans. Nucl. Sci., vol. 34, pp. 1140–1146, 1987.
- [183] M. I. Gorlov and D. A. Litvinenko, "Annealing of Radiation and Electrostatic-Discharge Damages in Semiconductor Devices", Russian Microelectronics, vol. 31, no. 5, pp. 295-304, 2002.
- [184] M. Kruglanski et al., "Space Environment Information System (SPENVIS)", 38th COSPAR Scientific Assembly, 2010.
- [185] P. Lechner and Team, "The Silicon Drift Detector for the IXO High Time Resolution Spectrometer", Proc. of SPIE, 7742, 2010 (doi: 10.1117/12.857260).
- [186] B. Beckhoff et al., "Handbook of practical X-ray fluorescence analysis", Springer verlag, Berlin/Heidelberg, 2006.

- [187] J. Sonsky et al., "Novel low-temperature processing of low noise SDDs with on-detector electronics", Nucl. Instr. and Meth. A, vol. 517, no. 1-3, pp. 301-312, 2004.
- [188] Andreas Pahlke, Ph. D. Thesis, Technical University of Munich, Max Planck Institute for Extraterrestrial Physics, 2004.
- [189] Adrian Sorin Niculae, Ph. D. Thesis, Development of a low noise analog readout for a DEPFET pixel detector, 2003.

## PUBLICATIONS:

1. **M. Shanmugam**, Y. B. Acharya, H. S. Mazumdar and S. V. Vadawale, “Dependence of the Leakage Current on the Performance of the Silicon Drift Detector Based X-Ray Spectrometer”, IEEE NSS/MIC, Oct 27 – Nov 2, pp. 1-6, 2013. (DOI: 10.1109/NSSMIC.2013.6829801).
2. **M. Shanmugam**, A. R. Patel, S. V. Vadawale, Y. B. Acharya and S. K. Goyal, “Characterization of High Count Rate Capability of Solar X-ray Monitor on-board Chandrayaan-2: The second Indian mission to Moon”, IEEE NSS/MIC, Oct 27 – Nov 2, pp. 1-7, 2013 (10.1109/NSSMIC.2013.6829697).
3. **M. Shanmugam**, Y. B. Acharya, S. V. Vadawale and H. S. Mazumdar, “A new technique for measuring the leakage current in Silicon Drift Detector based X-ray spectrometer – Implications for on-board calibration”, JINST 10 P02009, 2015 (doi:10.1088/1748-0221/10/02/P02009).
4. **M. Shanmugam**, Y. B. Acharya, S. V. Vadawale and H. S. Mazumdar, “Radiation effects on Silicon Drift Detector based X-ray spectrometer on-board Chandrayaan-2 Mission”, JINST 10 P09005, 2015 (doi:10.1088/1748-0221/10/09/P09005).
5. **M. Shanmugam**, Y. B. Acharya, S. V. Vadawale and H. S. Mazumdar, “Experimental characterization of Silicon Drift Detector for X-ray spectrometry: Comparison with theoretical estimation”, Measurements, 2015 (Under review).